

# Geodätisch-geophysikalische Arbeiten in der Schweiz

(Fortsetzung der Publikationsreihe  
«Astronomisch-geodätische Arbeiten in der Schweiz»)

herausgegeben von der

Schweizerischen Geodätischen Kommission  
(Organ der Akademie der Naturwissenschaften Schweiz)

**Fünfundsiebzigster Band**  
**Volume 75**

**Mutual Validation of Satellite-  
Geodetic Techniques and its Impact  
on GNSS Orbit Modeling**

Claudia Flohrer

2008

Adresse der Schweizerischen Geodätischen Kommission:

ETH Zürich  
Institut für Geodäsie und Photogrammetrie  
Schafmattstr. 34  
CH-8093 Zürich, Switzerland

Internet: <http://www.sgc.ethz.ch>

ISBN 978-3-908440-19-2

Redaktion des 75. Bandes:  
Dr. C. Flohrer, Dr. B. Bürki  
Druck: Print-Atelier E. Zingg, Zürich

## VORWORT

Frau Claudia Flohrer-Urschl bearbeitet in der vorliegenden Publikation das Problem, aus Zeitreihen unterschiedlicher Satelliten-Beobachtungstechniken und entsprechenden Bahnrechnungen Aussagen über die Genauigkeit der Satellitenbahnen und über mögliche systematische Fehler in den Beobachtungen zu machen. Frau Flohrer nutzte dazu (a) Mikrowellen-Messungen der Globalen Navigations-Satelliten-Systeme (GNSS), insbesondere des amerikanischen GPS und des russischen GLONASS, (b) Laufzeitmessungen (SLR) zu GNSS-Satelliten, die mit Laser-Reflektoren ausgerüstet sind sowie zu spezialisierten Lasersatelliten und (c) astrometrische Beobachtungen dieser Satelliten. Damit musste sich Frau Flohrer mit allen Beobachtungsarten der modernen Fundamentalastronomie befassen (mit Ausnahme von Very Long Baseline Interferometry, der Beobachtung von Quasaren mit Radioteleskopen), insbesondere mit den Feinheiten aller Beobachtungsarten und den Eigenschaften und Eigenheiten der daraus abgeleiteten Resultate. Die wichtigsten Resultate der Arbeit sind:

**Validierung** der vom CODE-Rechenzentrum bestimmten GPS- und GLONASS-Satellitenbahnen mit Hilfe von SLR-Beobachtungen des weltweiten Netzes von SLR-Stationen (inklusive Zimmerwald). Frau Flohrer gelang erstmals der Nachweis, dass es nicht nur einen bereits von Tim Springer (SGK, Band 60, 2000) beschriebenen systematischen Offset von 3-5 cm zwischen SLR-Beobachtungen und den aus den GNSS-Bahnen abgeleiteten Distanzen, sondern auch umlaufperiodische systematische Fehler mit einer Amplitude von 5-10 cm gibt. Dadurch gelang es, Einsicht in die Struktur der Systematiken zu gewinnen und, was noch wichtiger ist, die „Schuld“ eindeutig den GNSS-Bahnen zuzuschreiben. Erst nach diesem Resultat war und ist es sinnvoll, die zur Modellierung der GNSS-Bahnen bei CODE (und anderen Zentren) verwendeten Modelle für die Kräfte in Frage zu stellen und gründlichen Prüfungen zu unterziehen.

**Überprüfung der CODE-Modelle:** Frau Flohrer hat eine eindruckliche Reihe von Experimenten mit unterschiedlichen Modellen mit langen Zeitreihen von GNSS-Beobachtungen (vier Jahre) durchgeführt. Keines der Modelle konnte die oben erwähnten Systematiken befriedigend erklären. Man hat aber aus ihren Experimenten sehr viel gelernt und wird bei Folgeuntersuchungen auf ihren Resultaten aufbauen können.

**Validierung der CCD-Beobachtungstechnik** mit GNSS und Laser-Satelliten. Hier konnten jahrelange Zeitreihen von Richtungsbeobachtungen zu Satelliten (schnell bewegten Objekten) mit Hilfe der mit GPS und Laser bestimmten Bahnen validiert werden. Alle verwendeten CCD-Beobachtungen (CCD = Charge-Coupled Devices = Halbleiter-Sensoren digitaler Kameras) stammen vom Observatorium Zimmerwald. Drei Resultate seien erwähnt: (a) Die auf anderem Weg geschätzte Beobachtungsgenauigkeit von etwa 0.2“ konnte unabhängig bestätigt werden, (b) gelegentlich auftretende systematische Fehler in der Registrierung der Beobachtungszeit konnten eindeutig lokalisiert und zum grösseren Teil sogar korrigiert werden, (c) ein systematischer deklinationsabhängiger Fehler konnte zweifelsfrei einem der verwendeten Sternkataloge zugewiesen werden. Aus (b) wurde auch ein Vorschlag für eine routinemässige Kalibrierung der CCD-Aufnahmen abgeleitet.

**Untersuchungen zur Kombination verschiedener Beobachtungstechniken** (insbesondere GNSS und SLR): Frau Flohrer konnte zeigen, dass SLR einen wichtigen Beitrag zur Bahnbestimmung von GNSS-Satelliten zu leisten vermag, falls genügend SLR-Beobachtungen zur Verfügung stehen.

Die SGK bedankt sich bei der Akademie der Naturwissenschaften Schweiz (scnat) für die Übernahme der Druckkosten.

**Prof. Dr. W. Gurtner**  
Direktor Observatorium Zimmerwald  
Universität Bern

**Prof. Dr. A. Geiger**  
ETH Zürich  
Präsident der SGK

## PREFACE

Dans cette présente publication, en se basant sur des séries temporelles de différent types d'observations satellitaires ainsi que sur le calcul des orbites correspondants, Claudia Flohrer-Urschl s'est principalement intéressée à la problématique de la validation de la précision des orbites des satellites et des possibles erreurs systématiques qui entachent les observations. Claudia Flohrer a notamment utilisé (a) des observations micro-ondes des systèmes globaux de navigation par satellites (GNSS), en particulier à celles des systèmes américains (GPS) et russes (GLONASS), (b) des mesures temps de vol (SLR) sur les satellites GNSS qui sont équipés de réflecteurs laser ainsi que sur les satellites laser spécialisés, et finalement, (c) des observations astrométriques de tous ces satellites. Par conséquent, Claudia Flohrer a dû travailler avec toutes les observables de l'astronomie fondamentale moderne (à l'exception de celles du système Very Long Baseline Interferometry, l'observation de quasars à l'aide de radiotélescopes), plus spécialement avec les subtilités des trois techniques d'observations, et des propriétés et particularités des résultats qui en découlent. Les résultats majeurs de ses recherches sont:

**Validation** des orbites des satellites GPS et GLONASS, déterminés par le centre de calcul CODE, à l'aide d'observations SLR du réseau global des stations SLR (y compris celles de Zimmerwald). Claudia Flohrer a pu prouver pour la première fois qu'il n'y a pas seulement un écart systématique de 3-5 cm entre les observations SLR et les distances dérivées des orbites micro-ondes GNSS, comme décrit par Tim Springer (CGS, volume 60, 2000), mais également des erreurs systématiques périodiques orbitales d'une amplitude de 5 à 10 cm. Cela a permis une meilleure compréhension de la structure de tels systématismes et plus important encore, cela a offert la possibilité de pouvoir assigner, sans ambiguïté, la source de ces erreurs aux orbites GNSS. C'est seulement une fois ce fait identifié, qu'il a été pertinent de remettre en question la modélisation des forces des modèles d'orbites GNSS utilisés par le CODE (et les autres centres de calculs) et de les soumettre à des analyses en profondeur.

**Examen des modèles du CODE.** Claudia Flohrer a réalisé une impressionnante série d'expériences avec différents modèles en utilisant de longues séries temporelles d'observations GNSS sur une durée d'environ quatre ans. Aucun modèle ne peut expliquer de manière satisfaisante les erreurs systématiques mentionnées plus haut. Nous avons toutefois beaucoup appris de ses expériences et pouvons nous baser sur ses résultats pour de futures investigations.

**Validation des techniques d'observations CCD** sur GNSS et satellites lasers. De longues séries temporelles d'observations directionnelles de satellites (objets en mouvement rapide) ont pu être validées à l'aide d'orbites estimées avec GPS et laser. Toutes les observations CCD utilisées (CCD = Charge-Coupled Devices = senseurs semi-conducteurs des caméras digitales) proviennent de l'observatoire de Zimmerwald. Trois résultats peuvent être mentionnés : (a) la précision des observations de 0.2 secondes d'arc obtenue par une autre méthode a pu être confirmée de façon indépendante ; (b) les erreurs systématiques occasionnelles des déterminations de l'époque des observations ont pu être confirmées et identifiées (et en grande partie corrigées) ; (c) une erreur systématique dépendante de la déclinaison a pu être assignée, sans aucun doute possible, à l'un des catalogues d'étoiles utilisé pour la détermination des positions des étoiles et des objets. De plus, une routine de calibration des images CCD est proposée sur la base de (b).

**Etudes sur la combinaison de différentes techniques d'observations** (en particulier GNSS et SLR): Claudia Flohrer a pu montrer que si un nombre suffisant d'observations SLR sont disponibles, le système SLR est en mesure d'apporter une importante contribution à la détermination des orbites des satellites GNSS.

La CGS remercie l'académie des sciences des sciences naturelles suisses (scnat) pour la prise en charge des frais d'impression.

**Prof. Dr. Werner Gurtner**  
Directeur de l'Observatoire de Zimmerwald  
Université de Berne

**Prof. Dr. A. Geiger**  
ETH Zürich  
Président de la CGS

## FOREWORD

In this publication Mrs. Claudia Flohrer-Urschl focuses on the problem of assessing the accuracies of time series from diverse satellite observation techniques and corresponding orbit computations about orbits and possible systematic errors within the observations.

Mrs. Flohrer's work is based on (a) Microwave observations to Global Navigation Satellite Systems (GNSS), (b) SLR measurements (SLR = Satellite Laser Ranging) to GNSS satellites equipped with laser retro-reflectors or to specialized laser satellites and (c) Astrometric observations to these satellites. Mrs. Flohrer had to deal with all types of observables of modern fundamental astronomy (with the exception of Very Long Baseline Interferometry, the observation of quasars by radio telescopes), especially with the subtleties of all observation techniques and the properties and peculiarities of the derived results. The most important results of her studies are:

**Validation** of the GPS and GLONASS satellite orbits, as determined by the CODE analysis center by means of SLR observations of the global network of SLR stations (including Zimmerwald). For the first time, Mrs. Flohrer proved that, in addition to the systematic offset of 3-5 cm between SLR observations and ranges derived from GNSS microwave orbits as already described by Tim Springer (SGC, Volume 60, 2000), there are also orbit-periodic systematic errors with an amplitude of 5 to 10 cm. This led to an improved comprehension of the structure of such systematics and, more important, to the possibility to unambiguously attribute the source of these errors to the GNSS orbits. Only now it made sense to question the underlying force models of the GNSS orbits used by CODE (and other analysis centers) and to perform an in-depth error analysis.

**Examination of the CODE models:** Mrs. Flohrer performed an impressive series of experiments with different force models using long time series of GNSS observations of about four years. However, none of the models could sufficiently explain the systematic errors mentioned above. But we have learned a lot from her experiments and we will be able to build on her results for subsequent future studies.

**Validation of the CCD observation technique** by GNSS and laser satellites. Multiple-year time series of optical position (direction) observations to satellites (fast moving objects) could be validated using orbits determined by microwave GPS and SLR observations. All optical CCD observations (CCD = charge-coupled device = semiconductor sensors of digital cameras) have been collected at the Zimmerwald observatory. Three results are worth to be mentioned: (a) The accuracy of optical observations estimated elsewhere to be about 0.2 arc seconds could be confirmed independently; (b) systematic errors occasionally showing up in the registration of the observation epoch could be confirmed and identified (and even corrected to a large extent); (c) a systematic declination-dependent error could be attributed to one of the star catalogues used for the derivation of the star and object positions. (b) led to a proposal for a routine calibration of CCD images.

**Investigations about the combination of various observation techniques** (especially GNSS and SLR): Mrs. Flohrer proved that SLR is capable to significantly contribute to the orbit determination of GNSS satellites provided there are sufficient SLR observations available.

The SGC is grateful to the Swiss Academy of Sciences (scnat) for covering the printing costs of this volume.

**Prof. Dr. W. Gurtner**  
Director Observatory Zimmerwald  
University of Bern

**Prof. Dr. A. Geiger**  
ETH Zürich  
President of SGC

# Contents

<b>Contents</b>	<b>i</b>
<b>List of Figures</b>	<b>v</b>
<b>List of Tables</b>	<b>xi</b>
<b>List of Acronyms</b>	<b>xiii</b>
<b>1. Introduction and Motivation</b>	<b>1</b>
<b>2. Modeling the Observables in Satellite Geodesy</b>	<b>5</b>
2.1 The Dynamic Orbit Model for Artificial Satellites . . . . .	5
2.1.1 Orbital Elements . . . . .	6
2.1.2 Equations of Motion of an Artificial Earth Satellite . . . . .	7
2.1.3 Perturbing Forces Acting on a Satellite . . . . .	8
2.1.4 Variational Equations . . . . .	15
2.2 Station Coordinates . . . . .	17
2.3 Reference Systems . . . . .	18
2.3.1 The Terrestrial Reference System . . . . .	19
2.3.2 The Celestial Reference Systems . . . . .	19
2.3.3 Earth Orientation Parameters . . . . .	21
2.4 Parameter Estimation . . . . .	22
2.4.1 Method of Least Squares . . . . .	22
2.4.2 Observation Equations . . . . .	24

<b>3. Observing GNSS Satellites</b>	<b>31</b>
3.1 Characteristics of the Global Navigation Satellite Systems (GNSS) . . . . .	31
3.1.1 GNSS Overview . . . . .	31
3.1.2 GNSS Satellite Attitude . . . . .	38
3.1.3 GNSS Solar Radiation Pressure Modeling . . . . .	43
3.2 GNSS Orbit Determination Based on Microwave Observations . . . . .	48
3.2.1 The IGS Orbit Products . . . . .	49
3.2.2 GNSS Orbit Determination at CODE . . . . .	49
3.2.3 GNSS Orbit Accuracy . . . . .	51
3.3 Astrometric CCD Observations of GNSS Satellites . . . . .	52
3.4 SLR Observations of GNSS Satellites . . . . .	56
<b>4. Mutual Validation of the Different Satellite-Geodetic Techniques</b>	<b>61</b>
4.1 Validating the Astrometric Observation Technique . . . . .	61
4.1.1 Validation Procedure for Astrometric Observations . . . . .	62
4.1.2 Validation Results for Astrometric Observations Using Microwave-based GNSS Orbits . . . . .	65
4.1.3 Validation Results for Astrometric Observations Using SLR-based Orbits	75
4.2 Validating Microwave-based GNSS Orbits Using SLR Observations . . . . .	79
4.2.1 SLR Validation Procedure . . . . .	80
4.2.2 SLR Validation Results . . . . .	82
<b>5. Improvement of the GNSS Orbit Model</b>	<b>89</b>
5.1 Different Solar Radiation Pressure Models . . . . .	90
5.2 Assessing the Quality of the Orbit Model . . . . .	94
5.2.1 . . . by Analyzing SLR Residuals . . . . .	94
5.2.2 . . . by Analyzing Orbit Differences . . . . .	98
5.2.3 . . . by Analyzing Orbit Predictions . . . . .	102
5.2.4 . . . by Analyzing Orbit Overlap Errors of One-day and Three-day Arcs	107
5.2.5 . . . by Analyzing the Geocenter Coordinates . . . . .	129
5.3 Estimating Different Sets of Dynamic Orbit Parameters . . . . .	130
5.4 Conclusions . . . . .	133

---

<b>6. Improving GNSS Orbits with SLR</b>	<b>137</b>
6.1 GNSS Orbit Determination Based on Combined Microwave and SLR Data Analysis . . . . .	137
6.1.1 Combination Strategy . . . . .	138
6.1.2 Combined Analysis of Microwave and SLR Observations . . . . .	138
6.1.3 Variance-Covariance Studies for the Combined Analysis of Microwave and SLR Observations of GPS and GLONASS Satellites . . . . .	152
6.1.4 Variance-Covariance Studies for the Combined Analysis of Microwave and SLR Observations of the GIOVE-A Satellite . . . . .	156
6.2 GIOVE-A Orbit Determination Based on SLR Observations . . . . .	159
<b>7. Conclusions and Recommendations</b>	<b>163</b>
<b>A. Observing GNSS Satellites</b>	<b>167</b>
A.1 GNSS Satellite Information . . . . .	167
A.2 SLR Sites . . . . .	172
<b>B. Mutual Validation of the Different Satellite-Geodetic Techniques</b>	<b>173</b>
B.1 SLR Residuals . . . . .	173
<b>C. Improvement of the GNSS Orbit Model</b>	<b>175</b>
C.1 Accelerations Due to Different Solar Radiation Pressure Models . . . . .	175
C.2 Overlap Errors of One-day and Three-day Arcs . . . . .	178



# List of Figures

2.1	Orbital elements . . . . .	6
3.1	Ground-tracks of 30 GPS satellites over two orbital revolutions . . . . .	32
3.2	GPS Block IIA and Block IIR satellite types . . . . .	33
3.3	Number of launched and operational GNSS satellites . . . . .	34
3.4	Laser retroreflector array mounted on two Block IIA GPS satellites . . . . .	34
3.5	Ground-tracks of 12 GLONASS satellites over 17 orbital revolutions . . . . .	36
3.6	GLONASS, GLONASS-M, and GLONASS-K satellite types . . . . .	37
3.7	GIOVE-A satellite . . . . .	37
3.8	GNSS satellite's body-fixed coordinate system (X, Y, Z) . . . . .	39
3.9	Angles $\beta_0$ , $\Delta u$ , and $E$ in the Sun-satellite-Earth system . . . . .	40
3.10	Geographical distribution of GNSS tracking stations . . . . .	50
3.11	The 1 m telescope ZIMLAT at the Zimmerwald Observatory . . . . .	53
3.12	CCD exposure of a GNSS satellite acquired with ZimSMART . . . . .	54
3.13	CCD observations of GPS satellites . . . . .	55
3.14	CCD observations of GLONASS satellites . . . . .	55
3.15	CCD observations of the two LAGEOS satellites . . . . .	55
3.16	Number of CCD observations of GNSS satellites . . . . .	56
3.17	Global distribution of the SLR stations that observe GNSS satellites . . . . .	57
3.18	Number of SLR observations for each SLR station observing GNSS satellites	58
3.19	Number of SLR observations of GNSS satellites . . . . .	58
4.1	Illustration of the LAGEOS-1 sphere with its retroreflectors . . . . .	62
4.2	Validation method for the astrometric observation technique . . . . .	64

List of Figures

---

4.3	Raw CCD residuals $\Delta\alpha^*$ and $\Delta\delta$ for the GNSS satellites as a function of time	65
4.4	CCD residuals in along-track and out-of-plane direction for the GNSS satellites as a function of time	66
4.5	CCD residuals $\Delta\alpha^*$ and $\Delta\delta$ for the GNSS satellites as a function of time corrected for time biases	67
4.6	CCD residuals $\Delta e$ for the GNSS satellites as a function of elevation $e$	69
4.7	Distribution of the CCD observations for the GNSS satellites in right ascension $\alpha$ and declination $\delta$	70
4.8	Distribution of the CCD observations for the GNSS satellites in azimuth $a$ and elevation $e$	70
4.9	CCD residuals $\Delta\delta$ for the GNSS satellites as a function of azimuth $a$ , elevation $e$ , right ascension $\alpha$ , and declination $\delta$	71
4.10	Number of reference stars used from the catalogs UCAC2, GSC, USNO-B1.0, Tycho2, and Hipparcos	72
4.11	Number of observations (%) of GNSS satellites as a function of the usage of USNO-B1.0 reference stars (%) from a total of USNO-B1.0 and UCAC reference stars	73
4.12	CCD residuals $\Delta\delta$ for the GNSS satellites as a function of declination $\delta$ ; all reference stars are from USNO-B1.0	74
4.13	CCD residuals $\Delta\delta$ for the GNSS satellites as a function of declination $\delta$ ; all reference stars are from UCAC2	74
4.14	CCD residuals $\Delta\delta$ for the GNSS satellites as a function of declination $\delta$ ; more than 80% of the reference stars are from UCAC2	74
4.15	Raw CCD residuals $\Delta\alpha^*$ and $\Delta\delta$ for the LAGEOS satellites as a function of time	76
4.16	Distribution of the CCD observations for LAGEO-1 and LAGEOS-2 satellites in $\Delta\alpha^*$ and $\Delta\delta$	76
4.17	CCD residuals $\Delta\alpha^*$ and $\Delta\delta$ for the LAGEOS satellites as a function of time corrected for time bias	77
4.18	SLR validation method	80
4.19	SLR residuals $\Delta r$ derived from CODE final orbits for the GPS satellite G06 outside and during eclipse as a function of time	81
4.20	SLR residuals $\Delta r$ derived from CODE final orbits for the GPS satellites G05 and G06 as a function of time	83
4.21	SLR residuals $\Delta r$ derived from CODE final orbits for the GLONASS satellites R03, R22, R24, and R07 as a function of time	83

4.22	SLR residuals $\Delta r^*$ derived from CODE final orbits for the GPS satellites G05 and G06 as a function of time . . . . .	85
4.23	SLR residuals $\Delta r^*$ derived from CODE final orbits for the GPS satellites G05 and G06 in the $(\Delta u, \beta_0)$ coordinate system . . . . .	85
4.24	Station-specific SLR residuals $\Delta r^*$ derived from CODE final orbits for the GPS satellite G05 in the $(\Delta u, \beta_0)$ coordinate system . . . . .	86
4.25	SLR residuals $\Delta r^*$ derived from CODE final orbits for the GLONASS satellites R03, R22, R2, and R07 in the $(\Delta u, \beta_0)$ coordinate system . . . . .	86
5.1	Accelerations due to SRP acting on the GPS satellite G06, derived from the SRP models ROCK and CODE . . . . .	92
5.2	Estimated accelerations due to SRP acting on the GPS satellite G06, derived from parameter adjustment using the SRP models ROCK, CODE, and NONE . . . . .	93
5.3	SLR residuals $\Delta r^*$ derived from reprocessed orbits using the ROCK SRP model for the GPS satellites G05 and G06 in the $(\Delta u, \beta_0)$ coordinate system . . . . .	95
5.4	SLR residuals $\Delta r$ derived from microwave-based orbits using the ROCK and the CODE SRP model for the GPS satellites G05 and G06 as a function of time . . . . .	95
5.5	SLR residuals $\Delta r^*$ derived from reprocessed orbits using the CODE SRP model for the GPS satellites G05 and G06 in the $(\Delta u, \beta_0)$ coordinate system . . . . .	96
5.6	SLR residuals $\Delta r^*$ derived from reprocessed orbits using the NONE SRP model for the GPS satellites G05 and G06 in the $(\Delta u, \beta_0)$ coordinate system . . . . .	96
5.7	Radial orbit differences between orbits estimated using the ROCK and the CODE SRP model for the GPS satellites in 2005 . . . . .	99
5.8	Radial orbit differences between orbits estimated using the CODE and the NONE SRP model for the GPS satellites in 2005 . . . . .	100
5.9	Orbit differences for the GPS satellites between the 15 <sup>th</sup> day of prediction and the estimated orbit for all three SRP models used . . . . .	103
5.10	Orbit differences for the GPS satellites between the 15 <sup>th</sup> day of prediction and the estimated orbit for all three SRP models used . . . . .	104
5.11	Orbit differences for the GLONASS satellites between the 15 <sup>th</sup> day of prediction and the estimated orbit for all three SRP models used . . . . .	105
5.12	RMS of 73 orbit differences for the GPS satellites between the 15 <sup>th</sup> day of prediction and the estimated orbit for three SRP models . . . . .	106
5.13	RMS of 73 orbit differences for the GLONASS satellites between the 15 <sup>th</sup> day of prediction and the estimated orbit for two SRP models . . . . .	106
5.14	Orbit overlap errors of the GPS satellite G05 derived from one-day arcs . . . . .	108
5.15	Orbit overlap errors in along-track direction of 24 GPS satellites derived from one-day arcs . . . . .	110

List of Figures

---

5.16	Y-biases of 24 GPS satellites derived from one-day arcs . . . . .	113
5.17	Y-biases as a function of $\beta_0$ of 24 GPS satellites derived from one-day arcs . .	114
5.18	Amplitude spectra of GPS orbit overlap errors derived from one-day arcs using the CODE SRP model . . . . .	115
5.19	Orbit overlap errors of the GPS satellite G05 derived from three-day arcs . . .	117
5.20	Orbit overlap errors in along-track direction of 24 GPS satellites derived from three-day arcs . . . . .	118
5.21	Amplitude spectra of GPS orbit overlap errors derived from three-day arcs using the NONE SRP model . . . . .	119
5.22	Orbit overlap errors of the GLONASS satellite R22 derived from one-day arcs	120
5.23	Orbit overlap errors of the GLONASS satellite R22 derived from one-day arcs using the relative and the absolute antenna PCC model . . . . .	121
5.24	Orbit overlap errors in along-track direction of 10 GLONASS satellites derived from one-day arcs . . . . .	123
5.25	Amplitude spectra of GLONASS orbit overlap errors derived from one-day arcs using the NONE SRP model . . . . .	124
5.26	Amplitude spectra of GLONASS orbit overlap errors derived from one-day arcs using the NONE SRP model (zoomed) . . . . .	125
5.27	Orbit overlap errors of the GLONASS satellite R22 derived from three-day arcs	126
5.28	Orbit overlap errors in along-track direction of 10 GLONASS satellites derived from three-day arcs . . . . .	127
5.29	Amplitude spectra of GLONASS orbit overlap errors derived from three-day arcs using the NONE SRP model . . . . .	128
5.30	Amplitude spectra of the geocenter Z-coordinate derived from daily orbit so- lutions using three different SRP models . . . . .	129
5.31	SLR residuals $\Delta r$ for the GPS satellite G06 derived from microwave-based orbits generated by estimating five and nine SRP parameters . . . . .	132
5.32	SLR residuals $\Delta r$ for the GLONASS satellite R22 derived from microwave- based orbits generated by estimating five and nine SRP parameters . . . . .	133
6.1	SLR and GNSS sites . . . . .	139
6.2	SLR normal points of the GNSS satellites over the considered time interval . .	139
6.3	SLR residuals derived from one-day arc orbit solutions $A1, B1, C1$ , and $D1$ for the GPS satellite G05 . . . . .	142
6.4	Orbit overlap errors in radial direction of the one-day arc orbit solutions $A1, B1$ , $C1$ , and $D1$ for the GPS satellite G05 and the GLONASS satellite R22 . . . .	145

6.5	Pass-specific range residuals of the GLONASS satellite R24 observed by the SLR site 7090 for the orbit solutions $A1$ , $B2$ , and $C2$ . . . . .	146
6.6	Orbit overlap errors in radial direction of the one-day arc orbit solutions $A1$ , $B3$ , and $C3$ for the GPS satellite G05 and the GLONASS satellite R22 . . . . .	150
6.7	Formal errors of the radial orbit component for the GPS satellite G05 . . . . .	153
6.8	SLR site distribution for SLR data simulation . . . . .	154
6.9	Formal errors of the radial orbit component for the GPS satellite G05, derived from simulated data . . . . .	154
6.10	Formal errors of the semi-major axis for the GPS satellite G06, derived from simulated data for a different number of SLR sites . . . . .	155
6.11	Formal errors of the semi-major axis for the GLONASS satellite R03, derived from simulated data for a different number of SLR sites . . . . .	155
6.12	GIOVE-A microwave and SLR tracking sites . . . . .	157
6.13	Formal orbit errors for a GIOVE-A three-day arc . . . . .	158
6.14	Geographical location of the 11 SLR sites used for GIOVE-A orbit determination	159
6.15	SLR data coverage of the GIOVE-A SLR tracking campaign . . . . .	160
6.16	Overlapping 9-day arcs . . . . .	160
6.17	Orbit overlap differences of SLR-based 9-day arcs of GIOVE-A . . . . .	161
6.18	Range residuals derived from SLR-based 9-day arcs of GIOVE-A . . . . .	161
6.19	Orbit overlap differences of 5-day predictions based on GIOVE-A 9-day arcs .	162
B.1	SLR residuals $\Delta r^*$ derived from GFZ final orbits for the GPS satellites G05 and G06 in the $(\Delta u, \beta_0)$ coordinate system . . . . .	173
B.2	SLR residuals $\Delta r^*$ derived from JPL final orbits for the GPS satellites G05 and G06 in the $(\Delta u, \beta_0)$ coordinate system . . . . .	174
B.3	SLR residuals $\Delta r^*$ derived from IGS final orbits for the GPS satellites G05 and G06 in the $(\Delta u, \beta_0)$ coordinate system . . . . .	174
C.1	Accelerations due to SRP acting on the GPS satellite G16, derived from the SRP models ROCK and CODE . . . . .	176
C.2	Estimated accelerations due to SRP acting on the GPS satellite G16, derived from parameter adjustment using the SRP models ROCK, CODE, and NONE	177
C.3	Orbit overlap errors in radial direction of 24 GPS satellites derived from one-day arcs . . . . .	179
C.4	Orbit overlap errors in radial direction of 24 GPS satellites derived from three-day arcs . . . . .	180

*List of Figures*

---

C.5	Orbit overlap errors in out-of-plane direction of 24 GPS satellites derived from one-day arcs . . . . .	182
C.6	Orbit overlap errors in out-of-plane direction of 24 GPS satellites derived from three-day arcs . . . . .	183
C.7	Orbit overlap errors in radial direction of 10 GLONASS satellites derived from one-day arcs . . . . .	185
C.8	Orbit overlap errors in radial direction of 10 GLONASS satellites derived from three-day arcs . . . . .	186
C.9	Orbit overlap errors in out-of plane direction of 10 GLONASS satellites derived from one-day arcs . . . . .	187
C.10	Orbit overlap errors in out-of-plane direction of 10 GLONASS satellites derived from three-day arcs . . . . .	188

# List of Tables

2.1	Accelerations acting on GPS satellites due to perturbing forces . . . . .	15
3.1	Selected revolution periods of the GPS satellites . . . . .	33
3.2	Selected revolution periods of the GLONASS satellites . . . . .	35
3.3	IGS orbit products . . . . .	49
4.1	Procedure for the validation of the astrometric observation technique in program ORBTRA . . . . .	63
4.2	Statistical information of the CCD residuals for the GNSS satellites . . . . .	68
4.3	Statistical information of the CCD residuals for the LAGEOS satellites . . . . .	75
4.4	Summary of the validated orbits . . . . .	79
4.5	Retroreflector offsets for the used GNSS satellites . . . . .	81
4.6	Statistical information of the SLR residuals . . . . .	82
5.1	Statistical information of the SLR residuals for GNSS orbits using different SRP models . . . . .	97
5.2	Overlap time series analyzed for one-day and three-day arc orbit solutions . . . . .	107
5.3	Statistical information for along-track orbit overlap errors of 24 GPS satellites derived from one-day and three-day arcs . . . . .	111
5.4	Statistical information for along-track orbit overlap errors of 10 GLONASS satellites derived from one-day and three-day arcs . . . . .	122
6.1	Listing of orbit solution IDs . . . . .	141
6.2	Mean values and standard deviations of the SLR residuals derived from the solutions $A1$ , $B1$ , $C1$ , and $D1$ . . . . .	142
6.3	Mean values and standard deviations of the Helmert transformation parameters averaged over 41 days between the solutions $A1 - B1$ , $A1 - C1$ , and $A1 - D1$ . . . . .	143
6.4	Standard deviations of orbit differences of 41 days between the solutions $A1 - B1$ , $A1 - C1$ , and $A1 - D1$ . . . . .	144

List of Tables

---

6.5	Mean values and standard deviations of the SLR residuals derived from the solutions <i>B2</i> and <i>C2</i> . . . . .	147
6.6	Standard deviations of orbit differences of 41 days between the solutions <i>A1</i> – <i>B2</i> and <i>A1</i> – <i>C2</i> . . . . .	147
6.7	Estimated satellite retroreflector offset correction in radial direction and formal RMS for GPS and GLONASS satellites from solutions <i>B3</i> and <i>C3</i> . . . . .	148
6.8	Mean values and standard deviations of the SLR residuals derived from the solutions <i>B3</i> and <i>C3</i> . . . . .	148
6.9	Standard deviations of orbit differences of 41 days between the solutions <i>A1</i> – <i>B3</i> and <i>A1</i> – <i>C3</i> . . . . .	149
A.1	List of GPS satellites, providing satellite-specific information as per January 29, 2008 . . . . .	169
A.2	List of GLONASS satellites, providing satellite-specific information as per January 29, 2008 . . . . .	171
A.3	Listing of SLR sites . . . . .	172
C.1	Statistical information for radial orbit overlap errors of 24 GPS satellites derived from one-day and three-day arcs . . . . .	181
C.2	Statistical information for out-of-plane orbit overlap errors of 24 GPS satellites derived from one-day and three-day arcs . . . . .	184
C.3	Statistical information for radial orbit overlap errors of 10 GLONASS satellites derived from one-day and three-day arcs . . . . .	189
C.4	Statistical information for out-of-plane orbit overlap errors of 10 GLONASS satellites derived from one-day and three-day arcs . . . . .	189

# List of Acronyms

AC	Analysis Center
ACC	Analysis Center Coordinator
AIUB	Astronomical Institute of the University of Bern
BIH	Bureau International de l'Heure
BTS	BIH Terrestrial System
CODE	Center for Orbit Determination in Europe, Bern, Switzerland
CCD	Charge Coupled Device
CCRS	Conventional Celestial Reference System
CDP	Crustal Dynamics Project
CNSS	Compass Navigation Satellite System
CPF	Consolidated Prediction Format
CIP	Celestial Intermediate Pole
CODE	Center for Orbit Determination in Europe
CQSSP	Coupled Quasar, Satellite, and Star Positioning
CRF	Celestial Reference Frame
CRS	Celestial Reference System
CTRS	Conventional Terrestrial Reference System
DGFI	Deutsches Geodätisches Forschungsinstitut, Munich, Germany
DOF	Degree of freedom
DORIS	Doppler Orbitography and Radiopositioning Integrated by Satellite
DoY	Day of year
ESA	European Space Agency
EAP	Earth albedo radiation pressure
EOP	Earth orientation parameters
ERP	Earth rotation parameters
ESOC	European Space Operations Centre, Darmstadt, Germany
FoV	Field of view
FK5	The Fifth Fundamental Catalog
GCRS	Geocentric Celestial Reference System
GFZ	GeoForschungsZentrum, Potsdam, Germany
GIOVE	Galileo In Orbit Validation Element
GLONASS	GLOBAL'naya NAVigatsionnaya Sputnikovaya Sistema
GNSS	Global Navigation Satellite System
GPS	Global Positioning System

## List of Acronyms

---

HIP	Hipparcos catalog
HTSI	Honeywell Technical Services, Inc.
IAG	International Association of Geodesy
ICRF	International Celestial Reference Frame
ICRS	International Celestial Reference System
IDS	International DORIS Service
IERS	International Earth rotation and Reference system Service
IRM	IERS Reference Meridian
IRP	IERS Reference Pol
IGEX	International GLONASS EXperiment
IGLOS	International GLONASS Service
IGS	International GNSS Service
ILRS	International Laser Ranging Service
ITRF	International Terrestrial Reference Frame
ITRS	International Terrestrial Reference System
IVS	International VLBI Service
JPL	Jet Propulsion Laboratory, Pasadena, U.S.A.
LEO	Low Earth Orbiter
LRA	Laser retroreflector array
LLR	Lunar Laser Ranging
LOD	Length of day
mas	Milliarcsecond
MIT	Massachusetts Institute of Technology, Cambridge, U.S.A.
NAPEOS	Navigation Package for Earth Orbiting Satellites
NAVSTAR GPS	NAVigation Signal Timing And Ranging Global Positioning System
PCC	Phase center correction
PCO	Phase center offset
PCV	Phase center variation
PRN	Pseudo-random noise
PS	Pixel scale
RMS	Root mean square
RW	Reaction wheel
SBV	Space-Based Visible telescope
SIO	Scripps Institution of Oceanography, San Diego, U.S.A.
SLR	Satellite Laser Ranging
SNR	Signal-to-noise ratio
SRP	Solar radiation pressure
SSN	Space Surveillance Network
SVN	Satellite vehicle number
TAI	International atomic time
TLE	Two Line Elements
TRR	Thermal reradiation
UTC	Coordinated universal time

VLBI	Very Long Baseline Interferometry
ZIMLAT	Zimmerwald Laser ranging and Astrometry Telescope
ZimSMART	Zimmerwald Small Aperture Robotic Telescope

*List of Acronyms*

---

# 1. Introduction and Motivation

Global Navigation Satellite Systems (GNSS) provide positioning and timing on a global scale. For a broad range of scientific and commercial applications the GNSS observation technique is preferentially used because of its weather independency, its global coverage, and its availability at any time.

GNSS have been build up since the 1960's. Currently, the best-known constellation is the Global Positioning System (GPS), which has been deployed by the U.S. Department of Defence since the late 1970's. Today, the GPS constellation consists of more than 30 satellites. It is the only fully operational GNSS. The Russian counterpart GLObal'naya NAvigatsionnaya Sputnikovaya Sistema (GLONASS) has been developed in the 1980's and is expected to reach full orbit constellation and full availability in 2010. The European Union together with the European Space Agency is building-up the navigation satellite system Galileo, which will be the first GNSS under civil control. The first Galileo test-bed satellite has been launched in 2007, a second one will follow in 2008. China plans to implement an independent GNSS, the Compass Navigation Satellite System (CNSS).

During the last decades GNSS have become indispensable in satellite geodesy. Satellite geodetic techniques are used to determine the Earth's shape, to observe the Earth's gravity field, and to monitor the Earth's rotational motion. Together with the other space-geodetic techniques, i.e., Very Long Baseline Interferometry (VLBI), Satellite and Lunar Laser Ranging (SLR/LLR), and Doppler Orbitography and Radiopositioning Integrated by Satellite (DORIS), the GNSS technique contributes to the determination and maintenance of a global terrestrial reference frame under the auspices of the International Earth Rotation and Reference Systems Service (IERS). The main objective of the IERS is to provide the astronomical, geodetic and geophysical communities with the International Celestial Reference System (ICRS) and its realization the International Celestial Reference Frame (ICRF), with the International Terrestrial Reference System (ITRS) and its realization the International Terrestrial Reference Frame (ITRF), and with Earth orientation parameters as transformation parameters between the ICRF and the ITRF (McCarthy and Petit, 2004).

These well-defined reference frames are the basis for precise positioning used in scientific applications, e.g., for the detection of geophysical signals down to the millimeter level, or millimeter/year level. Such strong requirements on absolute position and velocity accuracy may only be met if the available orbits of the GNSS satellites are highly accurate. Orbits of GPS satellites are routinely computed by different analysis centers of the International GNSS Service (IGS), and are known to be consistent at the 1 – 2 cm level. Using the microwave-based

technique GNSS alone does not, however, allow it to assess the “true” orbit accuracy. If there are any systematic biases in the GNSS orbits due to, e.g., modeling errors, they will affect the estimated positions and velocities of the site coordinates. As such, technique-specific biases may become indistinguishable from geophysical signals.

Only the comparison of the GNSS observation technique with other techniques allows it to assess the absolute accuracy of GNSS orbits and to reveal possible technique-specific systematic biases. The GNSS satellites are well suited for such comparison studies as they are observable by different satellite-geodetic techniques, namely by GNSS microwave observations, SLR, and optical astrometry. The mutual validation of these three observation techniques using GNSS satellites is subject of this work. The results are used to improve the modeling of GNSS satellite orbits.

Chapter 2 introduces the observation models used in satellite geodesy. The focus is on modeling the orbits of artificial Earth satellites. We shortly review the principles of orbit determination. The force model used to account for the different forces acting on a satellite is presented. The definitions of the terrestrial and the celestial reference system, and of the Earth orientation parameters (necessary to transform between both systems) are outlined. Furthermore, we briefly review the method of least squares used for parameter estimation, and the observation equations for the three different techniques relevant in our context: GNSS microwave observations, SLR, and optical astrometry.

Chapter 3 is dedicated to the GNSS satellites. First, we discuss the characteristics of the existing and future Global Navigation Satellite Systems. Then, each of the three observation techniques is discussed in detail concerning its capability of determining GNSS satellite positions. The technique-specific error sources, which have to be treated with in the data analysis, are addressed.

Chapter 4 contains the key elements of our work, namely the mutual validation of the three satellite-geodetic techniques. We validate the astrometric observation technique by comparing optical observations of GNSS or Laser satellites with satellite positions derived from the microwave- or SLR-based orbits. The optical observations were acquired at the observatory in Zimmerwald of the Astronomical Institute of the University of Bern (AIUB). The validation method allows the calibration of the optical observation system and accordingly the assessment of the accuracy of astrometric observations for GNSS and Laser satellites. We then validate GNSS orbits based on microwave-phase observations by using SLR range measurements. SLR data are obtained through the International Laser Ranging Service (ILRS). The analysis of the resulting residuals allows the assessment of the GNSS orbit accuracy mainly in radial direction, as well as the detection of systematic errors in the GNSS and SLR observation technique.

Chapter 5 looks for potential improvements of the GNSS orbit models, based on the validation results of Chapter 4. The impact of different solar radiation pressure models on GNSS orbits is studied in particular.

Chapter 6 addresses the aspects of combining the observations of different techniques. GNSS satellites can be used for linking the observation techniques in space. If the location of the technique-specific sensors at the satellite are precisely known the observations from different

---

techniques can be combined for the determination of orbit parameters. Assuming that individual technique-specific modeling problems are solved beforehand, technique-independent parameters (as, e.g, the orbit parameters) benefit from the combination, i.e., from the strengths of each observations technique. Results of combined analyses of GNSS microwave and SLR data for GNSS orbit determination are presented in this chapter.

The last Chapter 7 summarizes the results, draws conclusions, and recommends further investigations.

Our work is a contribution to a central goal in space geodesy: the comparison and combination of the major space-geodetic techniques in order to improve the consistency of the geodetic products, to ensure long-term reliability and to contribute to a better understanding of (global) geophysical processes.



## 2. Modeling the Observables in Satellite Geodesy

In Sect. 2.1 we review the orbit models relevant for our work. Section 2.2 describes the models related to stations, which are the observing sites or receiving antennas on the Earth's surface. To specify the positions of objects in space or on the Earth, reference systems are needed. Both, the celestial and terrestrial reference systems, as well as the transformation parameters to connect the systems are discussed in Sect. 2.3. Finally, Sect. 2.4 briefly reviews the method of least squares used for parameter estimation and the observation equations for the three techniques relevant for this work.

### 2.1 The Dynamic Orbit Model for Artificial Satellites

According to Newton's law of gravitation, the acceleration of a satellite of negligible mass, compared to the mass  $M$  of the Earth, is given as a first approximation by

$$\ddot{\mathbf{r}} = -\frac{GM}{r^2} \frac{\mathbf{r}}{r} \quad (2.1)$$

where  $\ddot{\mathbf{r}}$  ... Geocentric acceleration vector of the satellite  
 $G$  ... Newtonian gravitational constant  
 $M$  ... Total mass of the Earth  
 $\mathbf{r}$  ... Geocentric position vector of the satellite  
 $r = |\mathbf{r}|$  ... Distance Earth-satellite.

Equation (2.1) describes the motion of a satellite in the gravity field of one central body - the Earth, which is assumed to be spherically symmetric. The differential equation (2.1) characterizes the unperturbed two-body problem. The magnitude of the acceleration is proportional to  $1/r^2$ , the inverse of the squared distance from the satellite to the Earth's center of mass. The gravitational coefficient  $GM$  (including the mass of the Earth's atmosphere) may be determined by using SLR observations of artificial Earth satellites (Ries et al., 1989). The value of  $GM$  may slightly differ for different Earth gravity models.

The equations of motion (a generalization of Eq. (2.1)) together with initial conditions, as, e.g., the orbital elements, uniquely specify the orbit of a satellite. The orbital elements will be introduced in the following section. The equations of motion for an artificial Earth satellite are

presented in Sect. 2.1.2. We will see that Eq. (2.1) has to be expanded to take into account perturbing forces acting on the satellite, due to, e.g., the non-sphericity of the Earth's gravitational potential. A more detailed description may be found, e.g., in (Beutler, 2005). The perturbing forces acting on an Earth satellite are discussed in Sect. 2.1.3. In Sect. 2.1.4, the variational equations are presented, which allow to solve for parameters characterizing the satellite's orbit.

## 2.1.1 Orbital Elements

The values of the Cartesian components of the satellite's position and velocity vector,  $\mathbf{r}$  and  $\dot{\mathbf{r}}$ , fully define a particular Keplerian (unperturbed) orbit, referring to a particular epoch  $t$ . Therefore, a set of orbital elements consists always of six parameters, although there are multiple ways of parameterizing an orbit.

We use the following set of orbital elements and call them Keplerian elements

- $a$  ... Semi-major axis
- $e$  ... Eccentricity
- $i$  ... Inclination with respect to the equatorial plane
- $\Omega$  ... Right ascension of the ascending node
- $\omega$  ... Argument of perigee
- $T_0$  ... Perigee passing time.

Instead of  $T_0$  we use  $u_0$ , the argument of latitude of the satellite at the initial time of arc  $t_0$ .

The first two elements,  $a$  and  $e$ , define the size and the shape of the orbit (e.g., ellipse). The argument of perigee  $\omega$  defines the orientation of the orbit in the orbital plane. The orientation

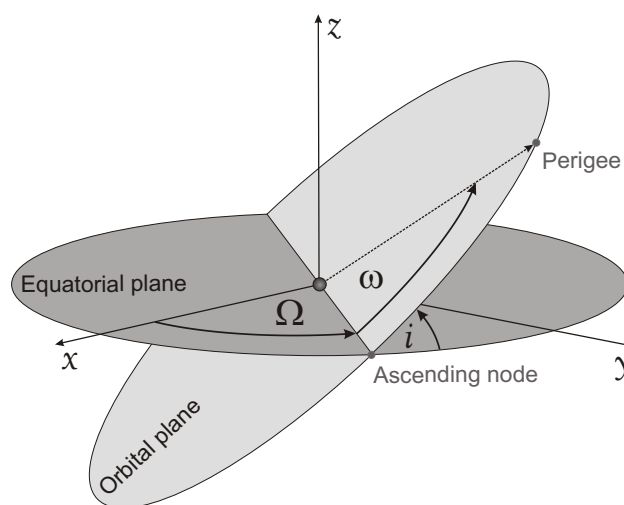


Figure 2.1: Orbital elements  $i, \Omega, \omega$

of the orbital plane in the inertial system is given by the angles  $i$  and  $\Omega$ . Figure 2.1 shows the three orbital elements,  $i$ ,  $\Omega$ , and  $\omega$ , which are known as the Eulerian angles.

The Keplerian elements can be easily transformed into the satellite's position and velocity vectors  $\mathbf{r}$  and  $\dot{\mathbf{r}}$  (and vice-versa), which are also referred to as state vectors of the orbital motion at epoch  $t$

$$\{\mathbf{r}(t), \dot{\mathbf{r}}(t)\} \leftrightarrow \{a, e, i, \Omega, \omega, u_0\}. \quad (2.2)$$

In an unperturbed two-body problem, the Keplerian elements parameterize a conic section type of orbit (i.e., an ellipse for artificial Earth satellites). The orbit of an Earth satellite is, however, subject to perturbing forces, which makes the actual orbit differ from the Keplerian orbit. The perturbed trajectory may be represented as a sequence of instantaneous Keplerian orbits, that are always tangential to the real trajectory. The set of orbital elements assigned to the satellite's state vector at each epoch  $t$  is called the set of osculating elements

$$\{\mathbf{r}(t), \dot{\mathbf{r}}(t)\} \leftrightarrow \{a(t), e(t), i(t), \Omega(t), \omega(t), u_0(t)\}, \quad (2.3)$$

where  $t$  is the osculation epoch.

### 2.1.2 Equations of Motion of an Artificial Earth Satellite

The equations of motion of an artificial satellite orbiting the Earth may be written in a geocentric quasi-inertial system as

$$\ddot{\mathbf{r}} = -GM \frac{\mathbf{r}}{r^3} + \mathbf{a}(t; \mathbf{r}, \dot{\mathbf{r}}, d_1, d_2, \dots, d_m) \quad (2.4)$$

where  $\ddot{\mathbf{r}}$  ... Geocentric acceleration vector of the satellite  
 $G$  ... Newtonian gravitational constant  
 $M$  ... Total mass of the Earth  
 $\mathbf{a}$  ... Perturbing acceleration  
 $\mathbf{r}$  ... Geocentric position vector of the satellite  
 $\dot{\mathbf{r}}$  ... Geocentric velocity vector of the satellite  
 $d_j$  ... Dynamical parameters,  $j = 1 \dots m$ .

The first term represents the central gravity term, whereas vector  $\mathbf{a}$  includes the sum of all perturbing accelerations acting on an artificial Earth satellite. A particular solution of the second order differential equation system (2.4) is given by adding, e.g., initial conditions at time  $t_0$

$$\begin{aligned} \mathbf{r}(t_0) &= \mathbf{r}_0 \doteq \mathbf{r}(a, e, i, \Omega, \omega, u_0; t_0) \\ \dot{\mathbf{r}}(t_0) &= \dot{\mathbf{r}}_0 \doteq \dot{\mathbf{r}}(a, e, i, \Omega, \omega, u_0; t_0). \end{aligned} \quad (2.5)$$

A set of osculating elements  $a, e, i, \Omega, \omega$ , and  $u_0$  and a set of dynamical parameters  $d_j$ , characterizing the force field, define a particular solution of the equations of motion (2.4). The differential equation system can be solved by using numerical integration algorithms. Approximate values  $a_0, e_0, i_0, \Omega_0, \omega_0, u_{00}$  and  $d_{j0}$  allow the computation of an a priori orbit, which may serve as a reference orbit for the orbit improvement.

### 2.1.3 Perturbing Forces Acting on a Satellite

An artificial Earth satellite experiences a number of accelerations caused by the gravitational attraction by celestial bodies but also by non-gravitational forces. Some of the accelerations might be negligible considering the achievable orbit accuracy, which also depends on the measurement accuracy of the satellite's position. The most important perturbations are caused by the actual (and time varying) Earth's figure and mass distribution, the gravitational attractions from Moon and Sun, the Earth's tidal potential, and the direct solar radiation pressure, depending on the area to mass ratio of the spacecraft. The perturbing acceleration caused by atmospheric drag has to be considered for Low Earth Orbiters (LEOs). In the following the different kinds of perturbing forces are presented. The section concludes with a summary of the various accelerations acting on a satellite, including their orders of magnitude.

#### Gravitational Forces

The gravitational acceleration acting on an artificial Earth satellite due to the Earth, Moon, Sun, and planets is given by the equations of motion. Assuming Moon, Sun and planets being point masses, the equation of motion of a satellite in the inertial system reads as (see, e.g., Beutler, 2005)

$$\ddot{\mathbf{x}} = -GM \int_{V_e} \rho_{pr} \frac{\mathbf{x} - \mathbf{x}_p}{|\mathbf{x} - \mathbf{x}_p|^3} dV_e - G \sum_{j=1}^n m_j \frac{\mathbf{x} - \mathbf{x}_j}{|\mathbf{x} - \mathbf{x}_j|^3} + \sum \mathbf{a}_{ng} \quad (2.6)$$

- where
- $\ddot{\mathbf{x}}$  ... Acceleration vector of the satellite in the inertial system
  - $\mathbf{x}$  ... Position vector of the satellite in the inertial system
  - $\mathbf{x}_e$  ... Position vector of the Earth's center of mass in the inertial system
  - $\mathbf{x}_j$  ... Position vector of the point mass  $j$  in the inertial system
  - $\mathbf{x}_p$  ... Position vector of a particular volume element of the Earth in the inertial system
  - $V_e$  ... Volume of the Earth
  - $\rho_{pr}$  ... Relative density function (i.e., density in units of the Earth's mass)
  - $m_j$  ... Mass of the point mass  $j$  (e.g., Moon, Sun, planets)
  - $\mathbf{a}_{ng}$  ... Non-gravitational accelerations.

Equation (2.6) refers to the inertial system, in which the Earth is also subject to an acceleration caused by the Moon and planets

$$\ddot{\mathbf{x}}_e = -G \sum_{j=1}^n m_j \frac{\mathbf{x}_e - \mathbf{x}_j}{|\mathbf{x}_e - \mathbf{x}_j|^3}. \quad (2.7)$$

Subtracting Eq. (2.7) from Eq. (2.6) leads to the equations of motion of the satellite in the geocentric system, also referred to as quasi-inertial system, as its axes are parallel to the axes of the inertial system

$$\ddot{\mathbf{r}} = \ddot{\mathbf{x}} - \ddot{\mathbf{x}}_e = -GM \int_{V_e} \rho_{pr} \frac{\mathbf{r} - \mathbf{r}_p}{|\mathbf{r} - \mathbf{r}_p|^3} dV_e - G \sum_{j=1}^n m_j \left( \frac{\mathbf{r} - \mathbf{r}_j}{|\mathbf{r} - \mathbf{r}_j|^3} + \frac{\mathbf{r}_j}{r_j^3} \right) + \sum \mathbf{a}_{ng} \quad (2.8)$$

where  $\mathbf{r}$  ... Geocentric position vector of the satellite,  $\mathbf{r} = \mathbf{x} - \mathbf{x}_e$   
 $\mathbf{r}_j$  ... Geocentric position vector of the point mass  $j$ ,  $\mathbf{r}_j = \mathbf{x}_j - \mathbf{x}_e$   
 $\mathbf{r}_p$  ... Geocentric position vector of a volume element of the Earth,  $\mathbf{r}_p = \mathbf{x}_p - \mathbf{x}_e$ .

The first term in the equation of motion (2.8) describes the gravitational acceleration acting on an artificial Earth satellite due to the Earth's gravity potential. The second term includes the (tidal) accelerations caused by point masses (as, e.g., Moon, Sun, and planets), whereas the third term represents the sum of all remaining accelerations due to non-gravitational forces.

Assuming a spherically symmetric Earth, the first part of the Eq. (2.8) becomes

$$\ddot{\mathbf{r}} = -GM \frac{\mathbf{r}}{r^3} \quad (2.9)$$

representing the gravity field of a spherically symmetric Earth. This term is also called the **Earth's monopole**, and it is the largest acceleration influencing the satellite's motion. This acceleration is the quantity to which the various perturbing accelerations have to be compared, in order to study how much they perturb the actual orbit with respect to an unperturbed Keplerian orbit.

The most important perturbing force acting on a satellite is caused by the non-spherical part of the **Earth's gravity potential**, due to the non-spherical mass distribution within the Earth. Usually the gravity potential of the Earth (geopotential)  $V$  is represented by a spherical harmonic expansion

$$V(r, \lambda, \phi) = \frac{GM}{r} \sum_{n=0}^{\infty} \frac{R^n}{r^n} \sum_{m=0}^n P_{nm}(\sin \phi) \{C_{nm} \cos(m\lambda) + S_{nm} \sin(m\lambda)\} \quad (2.10)$$

where  $\lambda, \phi$  ... Geocentric longitude and latitude of the satellite  
 $R$  ... Mean equatorial radius of the Earth  
 $n, m$  ... Degree and order of the geopotential term  
 $P_{nm}$  ... Associated Legendre function of degree  $n$  and order  $m$   
 $C_{nm}, S_{nm}$  ... Geopotential coefficients of degree  $n$  and order  $m$ .

The coefficients  $C_{nm}$  and  $S_{nm}$  are functions of the Earth's internal mass distribution. We distinguish between zonal ( $m = 0$ ), sectorial ( $m = n$ ), and tesseral ( $0 < m < n$ ) coefficients. Note that  $S_{n0} \doteq 0$ . The terms  $C_{n0}$  are also referred to as

$$J_n = -C_{n0}. \quad (2.11)$$

For a spherically symmetric Earth the gravitational potential would neither depend on longitude nor on latitude ( $n = m = 0$ ). With  $C_{00} = 1$  the first term in the geopotential expansion corresponds to the two-body potential  $V = GM/r$ . The first order terms  $C_{10}$ ,  $C_{11}$ , and  $S_{11}$  are zero, if the origin of the coordinate system is the center of mass.

The perturbing acceleration caused by the Earth's gravity potential can be written as the gradient of the gravity potential

$$\mathbf{a} = \nabla V. \quad (2.12)$$

The **Earth's oblateness**, represented by the zonal term  $C_{20}$  (or  $-J_2$ ), is the largest contribution to the perturbing accelerations. This term causes, e.g., the precession of the nodal line of the satellite orbit.

As the internal mass distribution of the Earth is not known, the coefficients of the Earth's gravity field cannot be calculated directly, they rather have to be determined from, e.g., the perturbations seen in the orbits of so-called Low Earth Satellites (LEOs), or from surface gravity data, or from altimetry, which measures the height of a satellite above the sea surface level. Most of the global gravity field models combine the data derived from LEO tracking, terrestrial gravimetry, and altimetry.

The gravitational attraction of Moon and Sun do affect the satellite's motion, but also the gravity potential of the Earth. The periodic deformations of the solid Earth caused by Moon and Sun are called **solid Earth tides**. The oceans' response to lunisolar tidal perturbations is known as **ocean tides**. The Earth's gravity potential exhibits small periodic variations, due to solid Earth tides and ocean tides, which in turn influence the satellite's motion. The changes of the geopotential may be modeled as time-dependent variations of the geopotential coefficients  $C_{nm}, S_{nm}$  (McCarthy and Petit, 2004).

### Non-Gravitational Forces

Non-gravitational forces arise from the interaction of the spacecraft with particles (e.g. air drag) and electromagnetic radiation emitted by the Sun and reflected by the Earth. The corresponding perturbing accelerations depend on the satellites area-to-mass ratio, where the area corresponds to the cross-section of the satellite normal to the line Sun-satellite (for the direct solar radiation pressure).

**Solar radiation pressure** The primary source of radiation affecting the satellite's orbit is the Sun. The solar radiation pressure (SRP) acting on an artificial Earth satellite can be characterized by the pressure

$$P_{\odot} = \frac{S}{c} \quad (2.13)$$

where  $S$  ... Solar constant  
 $c$  ... Speed of light.

The value of the solar constant is

$$S = 1367 \frac{\text{Watt}}{\text{m}^2} \quad (2.14)$$

(McCarthy, 1996), which corresponds to the total amount of radiated flux from the Sun on a square meter area, measured on the outer surface of Earth's atmosphere in a plane perpendicular to the rays at the mean Sun to Earth distance  $a_e$ . The mean distance  $a_e$  is the Astronomical Unit

$$a_e = 149,597,870.691 \text{ km} \quad (2.15)$$

(Standish, 1998). As the Sun to Earth distance varies during the year between  $147 \cdot 10^6$  km and  $152 \cdot 10^6$  km, due to the eccentricity of the Earth's orbit ( $e \approx 0.016$ ), the incoming solar radiation shows annual variations of about  $\pm 3.3\%$ , since the solar flux decreases with the square of the distance to the Sun (Montenbruck and Gill, 2000). To account for this effect, the SRP has to be scaled by  $\frac{a_e^2}{|\mathbf{r} - \mathbf{r}_\odot|^2}$ , where  $|\mathbf{r} - \mathbf{r}_\odot|$  is the instantaneous distance between satellite and Sun.

The impact of SRP on the satellite depends also on the satellite's area-to-mass ratio  $\frac{A}{m}$ , where  $A$  is the cross-section of the satellite normal to the direction satellite-Sun. Let us now assume a flat satellite with surface  $A'$ , whose normal is inclined by an angle of  $\theta$  to the direction satellite-Sun.

Depending on the optical properties of the surface, the incoming solar radiation is partly absorbed, specularly and diffusely reflected. We denote the absorbed fraction of the incoming radiation with  $\alpha$ , the specularly and diffusely reflected fractions with  $\rho$  and  $\delta$ , respectively. The fractions are also referred to as absorption, reflection, and diffusion coefficients and they are related by

$$\alpha + \rho + \delta = 1. \quad (2.16)$$

For each surface component of the satellite three acceleration components  $\mathbf{a}_\alpha$ ,  $\mathbf{a}_\rho$ , and  $\mathbf{a}_\delta$  can be identified, the components due to the absorbed, specularly reflected, and diffusely reflected part of the incoming solar radiation. For a flat surface one obtains

$$\mathbf{a}_\alpha = \alpha C \mathbf{e}_\odot \quad (2.17)$$

$$\mathbf{a}_\rho = \rho C 2 \cos \theta \mathbf{e}_n \quad (2.18)$$

$$\mathbf{a}_\delta = \delta C \left( \mathbf{e}_\odot + \frac{2}{3} \mathbf{e}_n \right) \quad (2.19)$$

with

$$C = -\frac{a_e^2}{|\mathbf{r} - \mathbf{r}_\odot|^2} P_\odot \cos \theta \frac{A'}{m} = -\frac{a_e^2}{|\mathbf{r} - \mathbf{r}_\odot|^2} P_\odot \frac{A}{m} \quad (2.20)$$

- where
- $\mathbf{e}_\odot$  ... Unit vector pointing from the satellite to the Sun
  - $\mathbf{e}_n$  ... Unit vector perpendicular to the satellite's surface
  - $\alpha$  ... Absorption coefficient
  - $\rho$  ... Reflection coefficient (specularly reflected fraction)
  - $\delta$  ... Diffusion coefficient (diffusely reflected fraction)
  - $\theta$  ... Angle between the incident radiation  $\mathbf{e}_\odot$  and the normal to the surface  $\mathbf{e}_n$
  - $a_e$  ... Astronomical unit
  - $\mathbf{r}$  ... Geocentric position vector of the satellite
  - $\mathbf{r}_\odot$  ... Geocentric position vector of the Sun
  - $P_\odot$  ... Solar radiation pressure
  - $A'$  ... Satellite surface element
  - $m$  ... Satellite mass.

The resulting perturbing acceleration caused by solar radiation for a flat surface  $A'$  is the sum of the three acceleration components  $\mathbf{a}_f = \mathbf{a}_\alpha + \mathbf{a}_\rho + \mathbf{a}_\delta$  and reads as

$$\mathbf{a}_f = C \left[ (\alpha + \delta) \mathbf{e}_\odot + \left( 2\rho \cos \theta + \frac{2}{3} \delta \right) \mathbf{e}_n \right]. \quad (2.21)$$

For a cylindric surface, with  $A'$  being the cross-section area presented to an observer whose line of sight is perpendicular to the axis of the cylinder, the acceleration can be derived with the expression

$$\mathbf{a}_c = C \left[ (\alpha + \delta) \mathbf{e}_\odot + \left( \frac{4}{3} \rho \cos \theta + \frac{\pi}{6} \delta \right) \mathbf{e}_n \right]. \quad (2.22)$$

For a spherical surface the resulting acceleration depends only on the diffusion coefficient

$$\mathbf{a}_s = C \left( 1 + \frac{4}{9} \delta \right) \mathbf{e}_\odot. \quad (2.23)$$

The optical surface properties of a spacecraft are also often described by two optical parameters  $v$  and  $\mu$ . The reflectivity  $v$ , ranging between 0 (black) and 1 (white), is the fraction of the incoming light that is reflected. The specularity  $\mu$ , ranging between 0 (diffuse) and 1 (specular), denotes the fraction of the reflected light that is specularly reflected. The following relations hold

$$v = \rho + \delta, \quad \mu = \frac{\rho}{\rho + \delta}. \quad (2.24)$$

The surface of Earth orbiting satellites may consist of surface elements with different optical properties. For each surface element a corresponding acceleration vector may be calculated. The sum of the individual vector accelerations gives the total perturbing acceleration acting on the satellite. The knowledge of the instantaneous attitude of the satellite (see Sect. 3.1.2) is necessary for accurate radiation pressure modeling (except for spherically symmetric satellites).

Eclipsing periods, i.e., periods when the satellite passes the shadow cast by the Earth (or the Moon), have to be considered for modeling the impact of SRP on the satellite. We may account for this shadow effect by using an eclipse factor for scaling the resulting acceleration in Eqs. (2.21, 2.22, 2.23) (see Sect. 3.1.2).

**Earth albedo radiation pressure** Incident solar radiation is reradiated by the Earth and/or its atmosphere and may produce a perturbing acceleration on a satellite. This effect is referred to as Earth albedo radiation pressure (EAP). The resulting perturbing acceleration on a satellite is difficult to model, as it varies significantly due to the Earth's changing surface characteristics and the cloud coverage. In a simple model approach (see, e.g., (Beutler et al., 1994)) a spherical Earth is assumed, divided into  $n \times m$  surface elements with the same surface area  $ds$ . Only the diffuse reradiation, derived from Lambert's law, which is emitted by each surface element of the Earth, is considered. The energy reradiated by a surface element is proportional to the surface area  $ds$  and the Sun's zenith angle  $z_\odot$  with respect to the surface element. The perturbing acceleration caused by a surface element of area  $ds$  that is acting on a flat satellite surface of

area  $A'$  may be written in an analogous way as to the equations developed for the solar radiation pressure (Eqs. (2.21, 2.22, 2.23)). For a flat, cylindrical or spherical surface we have

$$\mathbf{a}_f = B \left[ (\alpha + \delta) \mathbf{e}_s + \left( 2\rho \cos \phi + \frac{2}{3}\delta \right) \mathbf{e}_n \right] \quad (2.25)$$

$$\mathbf{a}_c = B \left[ (\alpha + \delta) \mathbf{e}_s + \left( \frac{4}{3}\rho \cos \phi + \frac{\pi}{6}\delta \right) \mathbf{e}_n \right] \quad (2.26)$$

$$\mathbf{a}_s = B \left( 1 + \frac{4}{9}\delta \right) \mathbf{e}_s \quad (2.27)$$

with

$$B = -\frac{a_e^2}{|\mathbf{r} - \mathbf{r}_\odot|^2} P_\odot \cos \phi \frac{A'}{m} k(ds) \cos z_s \cos z_\odot ds \quad (2.28)$$

where  $a_e$  ... Astronomical unit  
 $\mathbf{r}$  ... Geocentric position vector of the satellite  
 $\mathbf{r}_\odot$  ... Geocentric position vector of the Sun  
 $P_\odot$  ... Solar radiation pressure  
 $A'$  ... Satellite surface element  
 $m$  ... Satellite mass  
 $ds$  ... Area of the Earth surface element  
 $k(ds)$  ... Albedo radiation of the surface element  
 $z_\odot$  ... Zenith distance of the Sun with respect to the surface element  
 $z_s$  ... Zenith distance of the satellite with respect to the surface element  
 $\mathbf{e}_s$  ... Unit vector pointing from the satellite to the surface element  
 $\mathbf{e}_n$  ... Unit vector perpendicular to the satellite's surface  $A'$   
 $\phi$  ... Angle between incident radiation  $\mathbf{e}_s$  and normal to the satellite's surface  $\mathbf{e}_n$ .

As opposed to Eqs. (2.21, 2.22, 2.23) the factor  $B$  instead of  $C$  is used and the direction of the incident radiation acting on the satellite's surface is no longer stemming directly from the Sun but from the surface element of the Earth. Thus, the angle  $\phi$  between the incident radiation and the surface normal, is the angle between  $\mathbf{e}_s$  (unit vector pointing from the satellite to the Earth surface element) and  $\mathbf{e}_n$  (normal of satellite's surface). A simple approximation for the albedo radiation  $k(ds)$  is a constant value for all surface elements  $ds$  of the Earth

$$k(ds) = k = 0.3 = const. \quad (2.29)$$

The total acceleration due to EAP is obtained as the sum of the EAPs over all surface elements of the Earth, which are illuminated by the Sun and which are in the field of view of the satellite.

As the acceleration caused by EAP is much smaller than the one caused by SRP, perturbations due to EAP are often ignored. Although the EAP effect on a GNSS satellite is less than 1% of the perturbing acceleration caused by SRP, it may have to be considered for precise orbit determination.

**Thermal reradiation** Most of the solar energy absorbed by the satellite is reradiated as heat by the same surface having absorbed the radiation. The accelerations acting on a satellite orbit due to thermal reradiation (TRR) is much larger for the spacecraft body than for the solar panel arrays. The solar panels are thin and the back and front surface temperatures are nearly the same. Thus, the resulting TRR force from the solar panels nearly cancels out and is only about 1% of the total SRP force acting on the satellite. The TRR force from the spacecrafts body is around 3.9% of the SRP force for Block I, and around 5% for Block II/IIA satellites and Block IIR satellites (Fliegel et al., 1992), but it may reach up to 10% due to the blackened multi-layered insulation covering most of the satellite bus (Ziebart et al., 2005).

According to Fliegel et al. (1992), the absorbed and reradiated energy of the spacecraft body is proportional to  $(1 - v)$  (assuming that there is no thermal conduction). We may account for thermal reradiation by adapting the reflectivity and specularity coefficients  $v \rightarrow \tilde{v}$  and  $\mu \rightarrow \tilde{\mu}$  with

$$\tilde{v} = 1, \quad \tilde{\mu} = \mu v, \quad (2.30)$$

or by adapting the absorption, reflection and diffusion coefficients correspondingly  $\alpha \rightarrow \tilde{\alpha}$ ,  $\rho \rightarrow \tilde{\rho}$ , and  $\delta \rightarrow \tilde{\delta}$  with

$$\tilde{\alpha} = 0, \quad \tilde{\rho} = \rho, \quad \tilde{\delta} = 1 - \rho \quad (2.31)$$

in Eqs. (2.21, 2.22, 2.23).

**Atmospheric Drag** Perturbing accelerations caused by atmospheric drag, i.e., the interaction of the spacecraft with particles of the atmosphere, depend on the atmospheric density at the satellite height. Atmospheric drag is negligible for the high orbiting GNSS satellites. For LEOs, atmospheric drag becomes, however, the most important non-gravitational force influencing the satellite's motion. A detailed discussion may be found in (Montenbruck and Gill, 2000).

## General Relativistic Correction

The correction to the Newtonian equation of motion due to the theory of general relativity is called general relativistic correction. As the differences between the relativistic and the Newtonian motion of an artificial satellite are small, the relativistic correction to the acceleration of an artificial Earth satellite due to the main relativistic effects described by the Schwarzschild field of the Earth may be approximated by the simple formula (McCarthy and Petit, 2004)

$$\mathbf{a} = \frac{GM}{c^2 r^3} \left\{ \left[ 4 \frac{GM}{r} - \dot{\mathbf{r}}^2 \right] \mathbf{r} + 4(\mathbf{r} \cdot \dot{\mathbf{r}}) \dot{\mathbf{r}} \right\}. \quad (2.32)$$

It is based on the parameterized post-Newtonian (PPN) approximation of the correct general-relativistic formulations of the equations of motion and on the assumption of a spherically symmetric Earth. The perturbing force lies in the instantaneous orbital plane and generates, among others, a small rotation of the satellite's perigee. The effects of Lense-Thirring precession and geodesic (de Sitter) precession have been neglected here, as the impact of those effects on GNSS satellite orbits is one or two orders of magnitude smaller than that of the Schwarzschild term.

### Summary of Perturbing Forces

Table 2.1 shows the order of magnitude of accelerations caused by the perturbing forces for GNSS satellites. The values have been computed for GPS satellites, orbiting the Earth at about 20 200 km altitude, by Beutler (2005). The accelerations are given in decreasing order. In addition, the impact on the satellite's orbit after one day is shown.

Perturbing force	Acceleration (m/s <sup>2</sup> )	Orbit error after one day (m)
Earth's monopole	0.57	330 000 000
Earth's oblateness	$5.1 \cdot 10^{-5}$	35 500
Lunar attraction	$4.5 \cdot 10^{-6}$	1 800
Solar attraction	$2.0 \cdot 10^{-6}$	1 300
Geopotential harmonics (higher terms)	$4.2 \cdot 10^{-7}$	450
Direct solar radiation pressure	$9.7 \cdot 10^{-8}$	200
Y-bias	$1.0 \cdot 10^{-9}$	8
Solid Earth tides	$5.0 \cdot 10^{-9}$	0.4

Table 2.1: Accelerations acting on GPS satellites due to perturbing forces

The dominant perturbation for GNSS satellites is due to the Earth's oblateness ( $C_{20}$ -term), followed by the gravitational attraction by Moon and Sun and the higher terms of the Earth's gravity field. Accelerations due to the direct solar radiation pressure are of considerable size causing orbit errors at the level of 100 – 200 meters after one day. Although the Y-bias (acceleration along the solar panel axis due to solar radiation pressure, see Sect. 3.1.2) is much smaller, it has to be considered for precise orbit determination, as well as accelerations due to solid Earth tides and general relativistic effects. Accelerations due to thermal reradiation and Earth albedo may cause orbit errors at the decimeter level after one day, whereas accelerations caused by the gravitational attraction of planets and ocean tides may cause orbit errors at the centimeter level.

#### 2.1.4 Variational Equations

Within the scope of this work, orbit determination actually means orbit improvement of a known a priori orbit  $\mathbf{r}_0(t)$ . The positions of Earth, Sun, Moon, and planets are assumed to be known (e.g., from the Jet Propulsion Laboratory (JPL) ephemerides). Currently the Development Ephemerides DE200 (Standish, 1990) and the latest version DE405 (Standish, 1998) are widely used. They are necessary for the computation of the satellite's motion, in order to model tidal deformations of the Earth and third body effects, when computing the gravitational attraction acting on a satellite. In addition, some of the dynamical parameters  $d_j$  describing the force field are known a priori with high accuracy (e.g., gravity field coefficients), but others have to be determined.

For each orbit determination process, at least six initial conditions have to be determined, i.e., the satellite position and velocity vectors  $\mathbf{r}$  and  $\dot{\mathbf{r}}$ , or the orbital elements  $a$ ,  $e$ ,  $i$ ,  $\Omega$ ,  $\omega$ , and  $u_0$ .

In addition  $m$  dynamical parameters may be taken into account. This leads to a total number of  $n = 6 + m$  parameters  $p_i$  ( $i = 1, \dots, n$ ) defined by, e.g.,

$$\{p_1, p_2, \dots, p_n\} = \{\mathbf{r}, \dot{\mathbf{r}}, d_1, d_2, \dots, d_m\} \quad (2.33)$$

or by

$$\{p_1, p_2, \dots, p_n\} = \{a, e, i, \Omega, \omega, u_0, d_1, d_2, \dots, d_m\}. \quad (2.34)$$

As the geocentric position vector of the satellite is a non-linear function of the orbital elements  $a, e, i, \Omega, \omega, u_0$  and the dynamical parameters  $d_j$ , the unknown satellite position  $\mathbf{r}(t)$  has to be linearized, in order to solve for the orbit parameters using least squares algorithms. The satellite position vector can be written as a linear function of the unknown parameters  $p_i$ , by developing it into a Taylor series truncated after the first-order terms

$$\mathbf{r}(t) = \mathbf{r}_0(t) + \sum_{i=1}^n \mathbf{z}_{p_i}(p_i - p_{i0}) \quad (2.35)$$

where

$$\mathbf{z}_{p_i}(t) = \frac{\partial \mathbf{r}_0(t)}{\partial p_i} \quad (2.36)$$

denotes the partial derivatives of the known a priori orbit  $\mathbf{r}_0(t)$  with respect to the orbit parameters  $p_i \in \{p_1, p_2, \dots, p_n\}$ .

To obtain the partial derivatives  $\mathbf{z}_{p_i}$ , the total derivative of the equation of motion (2.4) with respect to the unknown orbit parameters has to be computed. The equations of motion are also called the primary equations in this context. They may be written also as

$$\ddot{\mathbf{r}} = \mathbf{f}(t; \mathbf{r}, \dot{\mathbf{r}}, d_1, d_2, \dots, d_m) = \mathbf{f}(t; p_1, p_2, \dots, p_n). \quad (2.37)$$

They yield to the following differential equation system for each unknown parameter  $p_i$

$$\ddot{\mathbf{z}}_{p_i} = \mathbf{A}_0 \frac{\partial \mathbf{r}_0(t)}{\partial p_i} + \mathbf{A}_1 \frac{\partial \dot{\mathbf{r}}_0(t)}{\partial p_i} + \frac{\partial \mathbf{f}}{\partial p_i}. \quad (2.38)$$

Using the  $3 \times 3$  matrices  $\mathbf{A}_0$  and  $\mathbf{A}_1$  with the elements  $i, k$

$$\mathbf{A}_{0_{ik}} = \frac{\partial f_i}{\partial r_{0_k}(t)} \quad i, k = 1, 2, 3 \quad (2.39)$$

$$\mathbf{A}_{1_{ik}} = \frac{\partial f_i}{\partial \dot{r}_{0_k}(t)} \quad i, k = 1, 2, 3 \quad (2.40)$$

the Eq. (2.38) may be simplified to

$$\ddot{\mathbf{z}}_{p_i} = \mathbf{A}_0 \mathbf{z}_{p_i} + \mathbf{A}_1 \dot{\mathbf{z}}_{p_i} + \frac{\partial \mathbf{f}}{\partial p_i}. \quad (2.41)$$

The differential equations (2.41) are called the variational equations. The corresponding initial conditions of the variational equations,  $\mathbf{z}_{p_i}(t_0)$  and  $\dot{\mathbf{z}}_{p_i}(t_0)$ , are obtained by taking the partial derivatives of the initial conditions (Eq. (2.5)) of the primary equations

$$\mathbf{z}_{p_i}(t_0) = \frac{\partial \mathbf{r}_0(t_0)}{\partial p_i} \quad \text{and} \quad \dot{\mathbf{z}}_{p_i}(t_0) = \frac{\partial \dot{\mathbf{r}}_0(t_0)}{\partial p_i}. \quad (2.42)$$

The variational equations are a system of linear differential equations of second order and of dimension three. For parameters  $p_i$  ( $i \leq 6$ ) the system is even homogeneous, as the partial derivative of the force field with respect to the initial conditions is a zero vector

$$\frac{\partial \mathbf{f}}{\partial p_i} = \mathbf{0} \quad \text{for} \quad i \leq 6. \quad (2.43)$$

For  $p_i$  ( $i > 6$ ) the opposite holds

$$\frac{\partial \mathbf{f}}{\partial p_i} \neq \mathbf{0} \quad \text{for} \quad i > 6, \quad (2.44)$$

but the initial conditions do not depend on the force field

$$\mathbf{z}_{p_i}(t_0) = \dot{\mathbf{z}}(t_0) = \mathbf{0} \quad \text{for} \quad i > 6. \quad (2.45)$$

The homogenous part of the variational equations ( $\mathbf{A}_0 \mathbf{z}_{p_i} + \mathbf{A}_1 \dot{\mathbf{z}}_{p_i}$ ) is common to all parameters  $p_i$ .

This means in summary that for each orbit improvement step one system of the non-linear primary equations (2.4, 2.5), and one system of the linear variational equations (2.41, 2.42) have to be solved for each parameter  $p_i$ , in order to obtain the partial derivative  $\mathbf{z}_{p_i}$  of the orbit position  $\mathbf{r}(t)$  with respect to the parameter  $p_i$ . Due to the linearization of the orbit (see Eq. (2.35)) orbit improvement is in principle an iterative process, where the orbit parameters estimated in one step have to be used as new a priori values for the next orbit improvement step.

## 2.2 Station Coordinates

Station positions on the Earth's surface are changing over time with respect to an Earth-fixed reference system (or a Tisserand system in the case of deformable bodies) due to various reasons. Plate motions cause station drifts up to several centimeters per year. This effect is accounted for by assigning velocities to each station. Tidal forces due to Moon and Sun deform the Earth and are responsible for solid Earth tides and ocean tides. Site displacements caused by solid Earth tides may reach amplitudes up to 40 cm and should be modeled when estimating station positions (McCarthy and Petit, 2004). They also produce (as already mentioned) temporal variations of the Earth's gravity field.

In addition, ocean tides induce temporal variations of the ocean mass distribution. The associated periodic deformation of the Earth's crust is known as ocean tide loading. Vertical site displacements due to ocean tide loading may reach values of several centimeters for coastal sites (Baker et al., 1995). In geodetic analysis, ocean tide loading models are used to account for these displacements.

Deformations of the Earth may be also induced by other than tidal loading effects, e.g., by atmospheric pressure loading. Atmospheric pressure loading is caused by the redistribution of air masses due to atmospheric circulation. The associated vertical crust displacements may reach up to 20 mm (Van Dam and Wahr, 1987). Thus, atmospheric pressure loading should also be accounted for in high precision geodetic analysis.

Due to the fact that the Earth is not rigid and has fluid components, there is a relative motion between the Earth's center of mass and a network of observing sites. This motion is often referred to as geocenter motion.

In general, positions of geodetic reference points fixed to the Earth's crust, which are mainly tracking instruments or geodetic markers, are expressed in a terrestrial reference frame (see Sect. 2.3.1). According to McCarthy and Petit (2004), the instantaneous actual position of a point on the Earth's surface at epoch  $t$ ,  $\mathbf{X}(t)$ , can be written as a sum of a regularized position  $\mathbf{X}_R(t)$  and position corrections  $\Delta\mathbf{X}_i(t)$  that add various time changing effects

$$\mathbf{X}(t) = \mathbf{X}_R(t) + \sum_i \Delta\mathbf{X}_i(t). \quad (2.46)$$

Thus, a position with time variations  $\mathbf{X}(t)$  is obtained. The modeled time variations include effects of, e.g., solid Earth tides (the full correction including the permanent tide), ocean tides, tidal and non-tidal loading, post-glacial rebound, and geocenter motion.

The position  $\mathbf{X}_R(t)$  at epoch  $t$  is modeled as linear function of the site position at a reference epoch  $t_0$  and the site velocity

$$\mathbf{X}_R(t) = \mathbf{X}_0 + \sum_i \Delta\dot{\mathbf{X}}_i(t - t_0). \quad (2.47)$$

The linear motions may be derived from tectonic plate motion models.

## 2.3 Reference Systems

In order to define positions of objects in space or on the Earth's surface the definition of reference systems is essential. The equations of motion for artificial Earth satellites are described in a celestial reference system, whereas a terrestrial reference system rotating with the Earth is used for the description of site positions. We have to distinguish between the terms reference system and reference frame. A reference system is the set of prescriptions and conventions together with the modeling required to define at any time a triad of axes (IERS2000). A reference frame

is the realization of the reference system by means of either station coordinates and velocities (for a terrestrial reference frame) or by means of coordinates of quasars or other celestial objects (for a celestial reference frame). To relate the celestial to the terrestrial reference frame Earth orientation parameters are required.

### 2.3.1 The Terrestrial Reference System

The International Terrestrial Reference System (ITRS) is a particular terrestrial reference system. It is a right-handed orthogonal coordinate system. Its orientation is equatorial, i.e., the z-axis is the direction of the IERS Reference Pole (IRP). The x-axis is the line of intersection between the Earth's equator and the IERS Reference Meridian (IRM), which is close to the Greenwich meridian. The y-axis completes the system.

The ITRS follows these criteria (McCarthy and Petit, 2004):

- The ITRS origin is geocentric at the center of mass of the whole Earth, including atmosphere and oceans.
- Its unit of length is the meter (SI), defined in a geocentric local frame as governed by the relativistic theory of gravitation.
- The orientation of its axes is consistent with that of the Bureau International de l'Heure (BIH) System at epoch 1984.0. BIH was the forerunner of the IERS and transferred its activities to the IERS at the start of 1988 (Boucher and Altamimi, 1996). The IRP and the IRM are consistent with the corresponding directions in the BIH Terrestrial System (BTS) (McCarthy, 1996).
- The time evolution of the system is ensured by using a no-net-rotation condition with regard to horizontal tectonic motions over the whole Earth.

The ITRS is realized by the International Terrestrial Reference Frame (ITRF), formerly known as the IERS Terrestrial Reference Frame, that was established and is maintained by the IERS. The ITRF consists of lists of coordinates and velocities for a selected number of IERS sites (i.e., tracking stations or related ground markers) observed by VLBI, SLR, LLR, GPS, and DORIS. The construction of the ITRF is based on the combination of the individual TRF solutions provided by the combination centers of each observation technique.

The first ITRF solution was published in 1988. ITRF solutions are published by the IERS Product Center in the "Technical Notes" (cf. (Boucher et al., 2004)).

### 2.3.2 The Celestial Reference Systems

An ideal celestial reference system would provide an inertial frame that could be used for all frequencies of the electro-magnetic spectrum, and for objects of all magnitudes. However, there

are no celestial reference sources radiating at all frequencies such that the position determined at one frequency can be accurately related to those determined at another frequency. Thus we have to deal with different sets of reference sources in the optical, radio, and X-ray frequencies. In addition the dynamical range for all observing systems is limited. Therefore it is difficult to realize a reference frame observable at all frequencies (Seidelmann, 1992).

We distinguish between stellar and extragalactic reference systems, both realizing a celestial reference system (i.e., a reference frame), but based on different sources. The International Celestial Reference System is based on extragalactic radio sources that are observed by VLBI.

### **The Extragalactic Reference System**

The celestial reference system provided and maintained by the IERS is called the International Celestial Reference System (ICRS). The ICRS origin is the barycenter of the solar system and the directions of the axes are fixed with respect to the quasars. Its fundamental plane is defined to coincide (as closely as possible) with the mean equator at J2000.0. The x-axis of the ICRS is the intersection of the mean planes of the ecliptic and the equator of the dynamical equinox at J2000.0, being the origin of right ascension.

According to McCarthy and Petit (2004), the ICRS is materialized by the International Celestial Reference Frame (ICRF). The ICRF is a set of precise polar coordinates (right ascension  $\alpha$ , declination  $\delta$ ) referring to the mean equator and equinox at J2000.0 of about 600 extragalactic radio sources determined from VLBI observations. These sources are sufficiently far away to ignore their expected proper motions. A first ICRF was provided in 1995 by a reanalysis of the available VLBI observations. VLBI is used for the maintenance of the primary frame, as this technique provides the most precise directions to the quasars. Access to the ICRS is provided by the catalog of source coordinates published in the IERS annual reports, cf. (Dick and Richter, 2001).

The celestial reference system used for satellite geodesy is not a barycentric, but a geocentric celestial reference system (GCRS), which is also called a quasi-inertial reference system (because the origin performs an accelerated motion). The orientation of the GCRS is identical to that of the ICRS, but its origin is shifted from the barycenter to the geocenter.

### **The Stellar Reference System**

A stellar reference system is realized by a stellar reference frame that can be determined optically. The Fifth Fundamental Catalog FK5 (Fricke et al., 1988) is a star catalog realizing a celestial reference frame based on optical observations of stars. The FK5 catalog provides positions and proper motions of about 4600 fundamental stars and serves as a reference frame for measurements of other stellar positions and proper motions. Its fundamental plane is the equatorial plane referring to a particular epoch. Its origin is a meridian of zero right ascension. The zero points of right ascension and declination, given implicitly by the star positions and

proper motions, coincides (as closely as possible) with the mean equator and equinox referred to a particular epoch.

FK6, the successor of FK5, includes observations provided by the Hipparcos catalog (HIP) (Perryman and ESA, 1997) resulting from the Hipparcos mission (1989-1993). The HIP star positions and proper motions are much more accurate than those of the FK5. In addition, coordinates from a few extragalactic radio sources are included, providing a direct link to the extragalactic reference system. Until now, the FK6 star catalog represents the most accurate realization of the CRF in the optical domain.

Other star catalogs providing many more stellar positions and proper motions with different levels of accuracies are, e.g., the Tycho catalogs Tycho and Tycho2 (also gained from the Hipparcos mission) with about 1 and 2 million stars, respectively, or the USNO-B1.0 catalog from the U.S. Naval Observatory with about one million stars. These catalogs are defined within the Hipparcos and the FK5 reference frames, respectively, but not used for reference frame realization.

### 2.3.3 Earth Orientation Parameters

The ITRS is related to the ICRS as a function of time by rotation matrices between the two systems describing the Earth's rotation (McCarthy and Petit, 2004). In principle the Earth's orientation can be expressed by three independent angles, the Euler angles. However, for routine monitoring of the Earth's orientation five Earth orientation parameters (EOP) are used, giving corrections to the uniform diurnal rotation and the model for precession and nutation.

The gravitational attraction of Moon, Sun, and planets exert torques on the oblate Earth, which cause the equatorial plane to precess with respect to an inertial system. This motion is reflected by a precession of the equatorial plane. In astronomy, the lunisolar precession, which is a long-periodic motion of the mean pole of the equatorial plane around the pole of the ecliptic plane with a period of about 26 000 years, is distinguished from nutation, which denotes the periodic motion of the true pole around the mean pole. The main period at 18.6 years is due to the precession of the lunar orbital plane around the pole of the ecliptic plane.

The EOPs refer to a fictitious axis, the Celestial Intermediate Pole (CIP) (formerly known as Celestial Ephemeris Pole (CEP)), which is defined by the precession-nutation model and its corrections (the celestial pole offsets  $d\psi$ ,  $d\epsilon$ ). The diurnal rotation of the rotating system around the CIP is given by the Earth rotation angle  $\theta$  defining the sidereal rotation of the Earth. For common use, the IERS does not provide  $\theta$  but its associated time scale UT1 (universal time) given in mean solar time. The excess of the rotation period with respect to the mean period is called the excess of the length of day (LOD). The CIP is referred to the polar axis of the terrestrial reference frame by two small rotation angles (polar motion), called the polar coordinates  $(x_p, y_p)$ .

Thus the five EOPs measured by space-geodetic techniques and provided by the IERS are the celestial pole offsets  $(d\psi, d\epsilon)$ , the correction to the universal time showing the variations of the Earth's angular velocity  $(UT1 - UTC)$ , and the polar coordinates  $(x_p, y_p)$ . The Earth orientation

is then obtained by inserting these parameters into the transformation matrices used to relate the ITRS to the ICRS. According to McCarthy and Petit (2004) the following transformation has to be applied to transform coordinates from the ITRS into the ICRS at epoch  $t$

$$\mathbf{X}_C = \mathbf{P}(t)\mathbf{N}(t)\mathbf{R}(t)\mathbf{W}(t)\mathbf{X}_T \quad (2.48)$$

where  $\mathbf{X}_T$  ... Vector in the ITRS  
 $\mathbf{X}_C$  ... Vector in the ICRS  
 $\mathbf{P}$  ... Transformation matrix containing precession parameters  
 $\mathbf{N}$  ... Transformation matrix containing nutation parameters  
 $\mathbf{R}$  ... Transformation matrix containing the Earth rotation angle  
 $\mathbf{W}$  ... Transformation matrix containing the polar coordinates .

In practise, the term Earth Rotation Parameters (ERP) is often used, meaning three of the EOPs specifying the motion of the rotation axis with respect to the ITRF, which are the polar coordinates  $(x_p, y_p)$  and the universal time (UT1-UTC) or LOD, respectively.

## 2.4 Parameter Estimation

For the estimation of model parameters (e.g., orbit parameters, EOP, coordinates, tropospheric parameters, etc.) the method of least squares was used throughout this work. First we briefly review the basic algorithms of least squares adjustment. Then the observation equations for all three observation types – GNSS microwave, SLR, and astrometric CCD observations – are presented.

### 2.4.1 Method of Least Squares

Each observation may be expressed as a function of parameters of a given mathematical model. Based on the vectorial model function  $\mathbf{F}$  the system of observation equations can be formulated in the presence of observation errors as

$$\mathbf{L} + \mathbf{v} = \mathbf{F}(\mathbf{X}), \quad (2.49)$$

or in its linearized form as

$$\mathbf{L} + \mathbf{v} = \mathbf{F}(\mathbf{X}_0) + \mathbf{A}\mathbf{x} \quad (2.50)$$

where  $\mathbf{L}$  ... Vector of actual observations  
 $\mathbf{v}$  ... Vector of observation corrections (residual vector)  
 $\mathbf{F}(\mathbf{X})$  ... Vector of the model function  
 $\mathbf{X}$  ... Vector of unknown model parameters to be adjusted,  $\mathbf{X} = \mathbf{X}_0 + \mathbf{x}$   
 $\mathbf{X}_0$  ... Vector of approximate model parameters  
 $\mathbf{x}$  ... Vector of model parameter corrections (solution vector)  
 $\mathbf{A}$  ... First design matrix (Jacobi matrix).

The first design matrix contains the derivatives of the function  $F$  with respect to the model parameters

$$\mathbf{A} = \left. \frac{\partial \mathbf{F}(\mathbf{X})}{\partial \mathbf{X}} \right|_{\mathbf{X}=\mathbf{X}_0} \quad (2.51)$$

Solving the linearized observation equations (2.50) for the residual vector  $\mathbf{v}$  leads to the system of correction equations

$$\mathbf{v} = \mathbf{A}\mathbf{x} - (\mathbf{L} - \mathbf{F}(\mathbf{X}_0)) = \mathbf{A}\mathbf{x} - \mathbf{l} \quad (2.52)$$

where  $\mathbf{l} \doteq \mathbf{L} - \mathbf{F}(\mathbf{X}_0)$  corresponds to the term “observed-minus-computed” (O-C).

The observation errors are described by the stochastic model

$$\mathbf{P} = \mathbf{Q}_{ll}^{-1} = \sigma_0^2 \mathbf{C}_{ll}^{-1} \quad (2.53)$$

where  $\mathbf{P}$  ... Weight matrix of observations  
 $\mathbf{Q}_{ll}$  ... Cofactor matrix of observations  
 $\mathbf{C}_{ll}$  ... Covariance matrix of observations  
 $\sigma_0$  ... A priori standard deviation of unit weight.

If the observations are uncorrelated, the weight matrix  $\mathbf{P}$  is a diagonal matrix with elements

$$P_{ll} = \frac{\sigma_0^2}{\sigma_l^2} \quad (2.54)$$

where  $\sigma_l^2$  is the a priori variance of the corresponding observation.

To solve the system of correction equations (2.52) the method of least squares sets up a condition that minimizes the sum of the squared weighted residuals  $\mathbf{v}^T \mathbf{P} \mathbf{v}$ . The resulting normal equation system reads as

$$(\mathbf{A}^T \mathbf{P} \mathbf{A}) \mathbf{x} = \mathbf{A}^T \mathbf{P} \mathbf{l} \quad (2.55)$$

or by substituting  $\mathbf{N} = \mathbf{A}^T \mathbf{P} \mathbf{A}$  and  $\mathbf{b} = \mathbf{A}^T \mathbf{P} \mathbf{l}$  as

$$\mathbf{N} \mathbf{x} = \mathbf{b} \quad (2.56)$$

where  $\mathbf{N}$  ... Normal equation matrix  
 $\mathbf{b}$  ... Right hand side of the normal equation system.

The normal equation matrix  $\mathbf{N}$  is a quadratic and symmetric matrix. By inverting  $\mathbf{N}$  the solution vector  $\mathbf{x}$  is obtained

$$\mathbf{x} = (\mathbf{A}^T \mathbf{P} \mathbf{A})^{-1} \mathbf{A}^T \mathbf{P} \mathbf{l} = \mathbf{N}^{-1} \mathbf{b}. \quad (2.57)$$

The estimated standard deviation of unit weight  $m_0$  is computed as

$$m_0 = \sqrt{\frac{\mathbf{v}^T \mathbf{P} \mathbf{v}}{f}} \quad \text{if } f > 0 \quad (2.58)$$

where  $f = n - u$  ... Degree of freedom (DOF) for the least squares adjustment  
 $n$  ... Number of observation  
 $u$  ... Number of unknowns (adjusted model parameters).

The covariance matrix of adjusted model parameters is given by

$$\mathbf{C}_{xx} = m_0^2 \mathbf{Q}_{xx} = m_0^2 \mathbf{N}^{-1} \quad (2.59)$$

where  $\mathbf{C}_{xx}$  ... Covariance matrix of adjusted model parameters  
 $\mathbf{Q}_{xx}$  ... Cofactor matrix of adjusted model parameters.

The diagonal elements of  $\mathbf{C}_{xx}$  contain the estimated standard deviations of the individual model parameters that can be computed as

$$m_x = \sqrt{C_{xx}} = m_0 \sqrt{Q_{xx}}, \quad (2.60)$$

whereas from the off-diagonal elements of  $\mathbf{C}_{xx}$  the correlation coefficient  $\rho$  between two model parameters can be derived

$$\rho = \frac{C_{xy}}{m_x m_y} \quad (2.61)$$

where  $m_x$  ... Standard deviation of a model parameter  $x$   
 $C_{xx}$  ... Diagonal element of  $\mathbf{C}_{xx}$   
 $Q_{xx}$  ... Diagonal element of  $\mathbf{Q}_{xx}$   
 $\rho$  ... Correlation coefficient between model parameters  $x$  and  $y$   
 $m_y$  ... Standard deviation of a model parameter  $y$   
 $C_{xy}$  ... Off-diagonal element of  $\mathbf{C}_{xx}$ .

For special applications, as, e.g., data analysis over longer time spans or combination of different observation types, it is convenient to combine solutions on the normal equation level. If the arrays  $\mathbf{N}$ ,  $\mathbf{b}$ ,  $\mathbf{X}_0$ ,  $\mathbf{l}^T \mathbf{P} \mathbf{l}$ ,  $n$ ,  $u$  and the associated parameter characterization for each individual normal equation system are saved, a set of normal equation systems can be subsequently stacked as, e.g., described by Brockmann (1997). The stacked solution is comparable with the solution that would be obtained by setting up only one big normal equation system. Correlations in time between observations are usually unknown and thus neglected. It is generally assumed that there are no correlations in time between parameters of consecutive days.

## 2.4.2 Observation Equations

### GNSS Microwave Observations

We will briefly review the GNSS code and phase observation equations. For a detailed discussion we refer to the GPS literature, e.g., (Teunissen and Kleusberg, 1998) or (Hofmann-Wellenhof et al., 1992).

GNSS observations are based on microwave signals transmitted by the GNSS satellites and recorded by receivers located on (or near) the Earth's surface. The GNSS observables are understood as ranges derived from measured time or phase differences between received signals and receiver-generated signals. Two carrier frequencies are transmitted by the GNSS satellites. Pseudo-random noise (PRN) codes are generated and modulated on the carriers. The satellite clock reading at emission time  $T^s$  is transmitted via the PRN code. The difference between the receiver clock reading at signal reception time  $T_r$  and the satellite clock reading at signal emission time  $T^s$  corresponds to the propagation time if satellite and receiver clocks would be synchronized. The difference between the two clock readings ( $T_r - T^s$ ) multiplied by the speed of light yields the pseudorange.

As different clocks are involved, a common reference time – the GPS system time – must be defined. This time is aligned to the coordinated universal time UTC (USNO) without taking into account the leap seconds. The GPS time therefore corresponds in essence to the international atomic time TAI with a constant offset of  $-19$  s. The delays of the clocks with respect to GPS system time are termed  $\Delta t_r$  and  $\Delta t^s$ . As two clocks, the satellite and the receiver clock, are used, the ranges are biased by satellite and receiver clock errors and thus denoted as pseudoranges. The code observation equation reads as

$$P = c(T_r - T^s) = \rho + c(\Delta t_r - \Delta t^s) + \Delta \rho_{trop} + \Delta \rho_{ion} + \epsilon \quad (2.62)$$

where

- $P$  ... Code pseudorange
- $c$  ... Speed of light
- $\rho$  ... Range between observer at  $t_r$  and satellite at  $t^s$ ,  $\rho = c(t_r - t^s)$
- $T_r$  ... Receiver clock reading at signal reception time,  $T_r = t_r + \Delta t_r$
- $T^s$  ... Satellite clock reading at signal transmission time,  $T^s = t^s + \Delta t^s$
- $t_r$  ... GPS time at signal reception
- $t^s$  ... GPS time at signal transmission
- $\Delta t_r$  ... Receiver clock error
- $\Delta t^s$  ... Satellite clock error
- $\Delta \rho_{trop}$  ... Signal delay due to troposphere
- $\Delta \rho_{ion}$  ... Signal delay due to ionosphere
- $\epsilon$  ... Signal delay due to unmodeled effects.

The range  $\rho$  corresponds to the geometric distance between the position of the satellite at signal transmission time  $t^s$  and the position of the receiver's antenna at signal reception time  $t_r$ , both epochs measured in GPS system time.

The pseudoranges are affected by systematic errors and random noise. The systematic errors can be modeled and give rise to additional terms in the observation equation – the clock offsets  $\Delta t_r$ , and  $\Delta t^s$ , and the path delays  $\Delta \rho_{trop}$  and  $\Delta \rho_{ion}$  due to tropospheric refraction and ionospheric refraction. Remaining unmodeled effects, as observation noise and multipath effects, which occur due to multiple reflections of the signal near the receiving antenna, are summarized in the residual term  $\epsilon$ .

Satellite and receiver specific hardware delays have to be taken into account as well. They are not explicitly listed in Eq. (2.62) as they cannot be separated from the clock offsets. Consequently the clock offsets are implicitly compensating for the hardware delays.

The geometric range term  $\rho$  includes antenna phase center offsets and variations. Antenna phase center offsets describe the difference between the antenna phase center (the point to which the microwave measurement is referred to) and the physical antenna center.

The phase of the received carrier with respect to the phase of a carrier generated by the receiver is far more precise than the code pseudorange. The phase observation equation for an electromagnetic wave of wavelength  $\lambda$  as observed at the receiving site yields

$$L = \lambda (\phi_r - \phi^s + N) \quad (2.63)$$

where  $L$  ... Phase pseudorange  
 $\lambda$  ... Carrier wavelength  
 $\phi_r$  ... Carrier phase of the reference signal at receiving time  $T_r$   
 $\phi^s$  ... Carrier phase of the transmitted signal at transmission time  $T^s$   
 $N$  ... Initial carrier phase ambiguity expressed in integer cycles of  $\lambda$ .

The receiver generates a reference signal (nominally) of the same wavelength as the satellite. Thus, the basic phase observable is the difference between the reference phase  $\phi_r$  at receiving time  $T_r$  and the phase  $\phi^s$  generated by the satellite at transmission time  $T^s$  multiplied by the wavelength  $\lambda$ . The initial integer number of cycles or ambiguity  $N$  between receiver and satellite is unknown and must be estimated together with the other unknowns.  $N$  remains constant as long as there is no loss of the signal lock.

In analogy to Eq. (2.62), Eq. (2.63) may be written in the following form

$$L = \rho + c(\Delta t_r - \Delta t^s) + \Delta\rho_{trop} - \Delta\rho_{ion} + \lambda B + \epsilon \quad (2.64)$$

where  $\phi$  ... Phase pseudorange  
 $B$  ... Ambiguity term expressed in cycles of  $\lambda$   
 $\lambda$  ... Carrier wavelength.

The bias term  $B$  is a real-valued number containing the initial carrier phase ambiguity  $N$  as well as satellite and receiver hardware delays, which cannot be separated from  $N$ . The major difference between phase and code pseudorange are the phase ambiguities. In addition, the effect of polarization induced phase-windup (Wu et al., 1993) is effecting carrier phase observations. Furthermore the ionospheric correction has the opposite sign compared to the code pseudorange (phase advance as opposed to signal delay).

In principle, one bias parameter  $B$  has to be determined per satellite pass, receiver, and frequency. Discontinuities in the carrier phase observations due to a loss of signal lock, resulting in so-called cycle-slips, have to be compensated by the set up of additional bias parameters  $B$ .

Systematic effects can be eliminated by differencing the observables. Differencing observations to the same satellite that are acquired quasi-simultaneously by two receivers eliminates satellite-specific biases. This receiver difference is called (station) single-difference. Differencing two single-differences, thus including the difference between two satellites – called double-difference – eliminates satellite-specific biases. In addition linear combinations of different frequencies may be formed at each level of differentiation in order to eliminate specific error sources. The most frequently used linear combination is the ionosphere-free linear combination, which eliminates the ionospheric refraction term. For more information on GNSS data combinations the reader is referred to Hofmann-Wellenhof et al. (1992).

For high-precision geodetic applications the carrier phase observables are used primarily, as the code observations are up to three orders of magnitude less accurate than the phase observations. Carrier phase observations exhibit a thermal noise of the receiver at the millimeter level. In addition carrier phases are much less affected by multipath effects than code observations.

### Astrometric CCD Observations

Astrometric CCD observations are optical observations based on Charge Coupled Device (CCD) sensors. Astrometric observations provide the astrometric direction of an observed object (e.g., a satellite). Usually this direction is measured relative to reference stars, the coordinates of which are available in an inertial reference frame. The observables are right ascension  $\alpha$  and declination  $\delta$  describing the apparent topocentric place of an object at time  $t$ . They are defined as follows

$$\rho \doteq \left| \mathbf{r}\left(t - \frac{\rho}{c}\right) - \mathbf{R}(t) \right| \quad (2.65)$$

$$\mathbf{e} \doteq \frac{\mathbf{r}\left(t - \frac{\rho}{c}\right) - \mathbf{R}(t)}{\rho} \quad (2.66)$$

$$\alpha = \arctan \frac{e_y}{e_x} \quad (2.67)$$

$$\delta = \arcsin e_z \quad (2.68)$$

- where  $\rho$  ... Distance between the observatory at time  $t$  and the satellite at time  $t - \Delta t$  (slant range)
- $\mathbf{r}\left(t - \frac{\rho}{c}\right)$  ... Geocentric position vector of the satellite at time  $t - \Delta t \doteq t - \frac{\rho}{c}$
- $\mathbf{R}(t)$  ... Geocentric position vector of the observatory at time  $t$
- $t$  ... Observation time
- $c$  ... Speed of light
- $\mathbf{e}$  ... Unit vector pointing from the observatory to the satellite in the equatorial system
- $\alpha$  ... Right ascension
- $\delta$  ... Declination.

In order to derive the observables from the raw data represented by a CCD exposure several reduction steps are necessary. The raw observations are given in a detector coordinate system.

This system is related to the celestial sphere by transformations, which are in general described by a model (mapping model). The model may take into account the various characteristics of the optical system and the orientation of the detector system with respect to the optical system and may thus become rather complex. For the estimation of the transformation parameters, observations to neighboring objects (e.g., reference stars), which are linked to the celestial reference frame, are used.

During the reduction process, several effects contributing to the error budget of astronomical observations have to be considered. The following overview is based on (Schildknecht, 1994). The error values given here refer to astrometric observations of the ZIMLAT telescope, the 1 m laser ranging and astrometry telescope located at the Zimmerwald Observatory. A description of the ZIMLAT CCD system is given in Sect. 3.3.

Radial non-linear deformations stemming from imperfect optics cause deviations from the linear projection model. Depending on the detector size these deviations may reach values up to  $0.3''$  for ZIMLAT. These deformations are taken into account in the actual mapping model.

To compute the center of light of an observed object, moment centroiding algorithms (see, e.g., Verdun (1993)) are used. The centroiding error for bright objects, as GNSS satellites, is about 0.1 pixel. The pixel scale for the ZIMLAT camera is about  $1''/\text{pixel}$ , i.e., one pixel corresponds to  $1''$  of the mapped sky. With a centroiding error of 0.1 pixel the precision of the measured astrometric positions is supposed to be at the level of  $0.1''$  per angular coordinate with respect to the stellar catalog reference frame (Schildknecht, 1994).

The effect of atmospheric refraction has to be considered, too. The astronomical refraction is the angle between the apparent direction of an object as seen by the observer and the “true direction” of the object, i.e., the direction that would be observed in the absence of the atmosphere. As an exposure maps only a small section of the celestial sphere, the main part of refraction is similar for all objects within one frame. The remaining differences in refraction are called differential refraction and have to be reduced. The error in differential refraction for zenith distances below  $60^\circ$  may reach about 3 mas for an absolute refraction error of  $1''$ , in the worst case (Schildknecht, 1994). For finite distances  $\rho < 10^5$  km, as for Earth orbiting satellites, the so-called parallactic refraction correction has to be added in addition. This correction characterizes the differences in refraction between an object observed at infinite and at finite distances.

Atmospheric turbulences may cause variations of the apparent brightness and/or color of objects (scintillation), variations of the point spread function (PSF) producing a blurring of objects, and variations of the centroid position. As these seeing conditions are high-frequency effects their impact on the measured object position may be assumed as random with expected mean values of zero.

The epoch registration accuracy is limited by the mechanical and electronic shutter timing technique. Epoch registration errors may be of stochastic but also of systematic nature. Depending on the velocity of the observed object a shuttering error leads to position errors of different size (i.e., larger position errors for faster objects).

The precision of astrometric CCD measurements is dominated by the quality of the optical system, the seeing conditions, the pixel scale, the signal-to-noise ratio (SNR), and the integration

interval, i.e., the time interval used for an exposure. All these effects contribute to the error budget, which gives a theoretical value for the measurement precision.

The formal error of the astrometric reduction process is a first estimate of the actual precision of the astrometric positions. The astrometric reduction for ZIMLAT data is done with ZimControl, the software system used for data acquisition and data processing (Flohrer et al., 2007). The astrometric error estimated by ZimControl is about 0.2'' for observations of GNSS satellites acquired with ZIMLAT. This precision results from the analysis of reference stars only. Reduction errors with respect to the satellite as well as position errors of the reference stars do not show up. Star position errors produce a systematic bias depending on the catalog accuracy including star positions and proper motions.

In order to assess the value for the CCD measurement accuracy, an external calibration by comparing the satellite's position derived from the astrometric observation with the satellite's precise ephemeris may be used, see Sect. 4.1.

### SLR Observations

SLR observations are based on the round trip time of flight measurements of short light pulses. These pulses are generated by a laser and directed by a telescope to a given satellite. Corner cube retroreflectors mounted on the satellite reflect the pulses and send them back to the telescope. A time interval counter records the flight time  $\Delta t$  of the pulses. The measured light travel time of a transmitted pulse multiplied by the velocity of the pulse, which travels with the speed of light, leads to twice the distance  $\rho$  from the observing station to the satellite at time  $t_m$

$$\rho(t_m) = \frac{c\Delta t}{2} + \Delta\rho_{sro} + \Delta\rho_{trop} + \Delta\rho_{bias} \doteq |\mathbf{r}(t_m) - \mathbf{R}(t_m)| \quad (2.69)$$

where

- $\rho(t_m)$  ... One-way range between the observatory and the satellite at time  $t_m$
- $c$  ... Speed of light
- $\Delta t$  ... Light travel time
- $\mathbf{r}(t_m)$  ... Geocentric position vector of the satellite at time  $t_m$
- $\mathbf{R}(t_m)$  ... Geocentric position vector of the observatory at time  $t_m$
- $\Delta\rho_{sro}$  ... Satellite retroreflector offset
- $\Delta\rho_{trop}$  ... Signal delay due to the troposphere
- $\Delta\rho_{bias}$  ... Signal delay due to various biases.

The time  $t_m$  is derived from the pulse emission time  $t_1$  and the pulse reception time  $t_2$ , recorded by, e.g., an event timer

$$t_m = \frac{t_1 + t_2}{2}. \quad (2.70)$$

Note that Eq. (2.69) is “only” a good approximation as it neglects the non-linear part of the station motion during the time interval  $\Delta t$  (due to Earth rotation).

The satellite retroreflector offset  $\Delta\rho_{sro}$  is the optical distance from the satellite's center of mass to the center of reflection of the laser retroreflector array (LRA). This offset has to be added to

the measured range, as the orbit determination conventionally refers to the satellite's center of mass. For GNSS satellites, the center of mass of the satellite is expected to move over the life of the mission due to the loss of mass (fuel), i.e. for GPS satellites by about 4.6 mm (Degnan and Pavlis, 1994). Thus, the retroreflector offset is changing slightly over time and the offset values used in SLR data analysis always represent an average position.

The atmospheric delay  $\Delta\rho_{trop}$  is influenced mainly by the dry component of the troposphere. Traditionally, the correction of the atmospheric delay at optical wavelengths was derived from the formulation of Marini and Murray (1973). The model includes the zenith delay of a signal and the mapping function, in order to project the zenith delay to a given elevation angle. In 2002 Mendes et al. (2002) have developed new mapping functions for optical wavelengths using a large data base of ray tracing radiosonde profiles. These mapping functions can be combined with different zenith delay models and represent a significant improvement over other (older) mapping functions (McCarthy and Petit, 2004). Therefore the ILRS recommends the use of the Mendes-Pavlis refraction model.

Systematic errors in the measured distance to the satellite may be caused by the SLR tracking system or by external factors introduced by the atmosphere or the satellite. Such error sources cause biases, characterized by  $\Delta\rho_{bias}$  in Eq. (2.69).

Station-dependent range biases may exist, which are (hopefully) constant over a satellite pass or any other period of time. They might be caused by instrumental problems (e.g., ranging electronics), or incorrect calibration measurements. Satellite-specific range biases depend on the satellite signature and the detection mode of the laser system. In the multi-photon detection mode, the measured range might be too short, if the LRA is very large and the inclination angle of the reflected light is very small as for low elevation observations (Otsubo et al., 2001). For single-photon detection the noise level will be increased. Range biases may reach values of several millimeters up to few centimeters.

Systematic time errors due to epoch registration can cause station- and pass-specific time biases. Scale biases may occur due to frequency errors of the event timer. Errors in the temperature measurement or the barometer readings cause troposphere biases or pressure biases, respectively. These kinds of biases are very difficult to separate from range biases. For a detailed discussion of SLR systematic biases we refer to Degnan (1993) and Pearlman (1984).

The individual SLR observations are known as fullrate data. In SLR data analyses so-called normal points are used that are generated on-site by averaging the individual range measurements over a certain time interval (e.g., over 5 min for GNSS satellites). The standard deviation of these normal points is at the 5 – 10 mm level for GNSS satellites.

The main advantages of SLR observations (compared to microwave observations) are

- essentially unbiased measurements with mm- to cm-accuracy, and
- much better knowledge (mm to cm) of the atmospheric delays when standard meteorological measurements (temperature, pressure, humidity) are available.

These advantages make the SLR technique a calibration tool for microwave observation techniques.

## 3. Observing GNSS Satellites

The models described in Chapter 2 are valid for satellite geodetic analyses in general. Let us now in particular focus on the GNSS satellites, which can be observed by various techniques. The primary observation type is the GNSS microwave observation technique. We describe the GNSS orbit products based on the microwave data. Furthermore, GNSS satellites may be also observed with optical telescopes. The astrometric CCD observations acquired for this work are introduced. As two of the GPS satellites and all GLONASS satellites are equipped with laser retroreflector arrays (LRAs), these satellites may also be tracked by the SLR technique. We present the SLR observations of GNSS satellites that were used in our studies.

### 3.1 Characteristics of the Global Navigation Satellite Systems (GNSS)

This section introduces the two existing and two future Global Navigation Satellite Systems. The American GPS was the first GNSS with full operational capacity in 1994. The Russian counterpart GLONASS started operation in 1983, and was fully operational for a short time period (1995 and 1996). Today, it is not yet fully completed. The European Galileo System, which is the first GNSS under civil control, is currently being developed. China is deploying an independent GNSS, the Compass Navigation Satellite System (CNSS).

#### 3.1.1 GNSS Overview

##### GPS – the American GNSS

The American GNSS, officially designated as NAVSTAR GPS (NAVigation Signal Timing And Ranging Global Positioning System), is commonly known as Global Positioning System, GPS. The GPS configuration nominally consist of 24 satellites, but actually more than 24 satellites are available since 1994. The spacing of the GPS satellites is arranged in such a way that at each point of the Earth's surface and at each epoch  $t$  a minimum of four satellites is in view. Nominally, four satellites, actually on the average five, are in each orbital plane. The six orbital planes have an inclination of  $55^\circ$  with respect to the Earth's equator and are separated in the

equator by  $60^\circ$ . The satellites orbit the Earth at about 20,200 km altitude above the Earth's surface in almost circular orbits. The sidereal revolution period of the GPS satellites is  $11^{\text{h}}58^{\text{m}}02^{\text{s}}$ , which is precisely half a sidereal day. Consequently, the Earth-satellite constellation repeats itself every  $23^{\text{h}}56^{\text{m}}$ . This in turn brings the GPS satellites into a deep (2:1) resonance with the Earth rotation, causing resonance perturbations (Beutler, 1998). Due to the perturbing forces the GPS satellite constellation is not stable. In order to maintain the satellite configuration so-called station keeping maneuvers have to be performed approximately once per year for each of the GPS satellites.

Figure 3.1 shows the “ground-tracks” (the projection of the satellite's position on the Earth) of 30 GPS satellites in October 2006. After two revolutions the ground-tracks repeat almost perfectly for all GPS satellites. As long as the constellation stays the same, the same ground-track pattern results for each day. This in turn improves the day-to-day repeatability for GPS site coordinates, but it might also be a weakness of the GPS by probably causing systematics in the estimated parameters (e.g, orbit parameters, site coordinates), as each satellite is always observed by the same subset of sites.

As opposed to the Earth-satellite constellation, the same Sun-Earth-satellite constellation repeats itself only after about 352.4 days due to the regression of the nodes of the orbital planes. After that time period the satellite is observed over the same point of the Earth's surface at the same time of the day. This period is called the draconitic GPS year. The draconitic revolution period is the time that elapses between two passages of the satellite through its ascending node, the point of its orbit where it crosses the equator from the southern to the northern hemisphere. It differs from the sidereal period because the satellite's line of nodes typically recesses slowly.

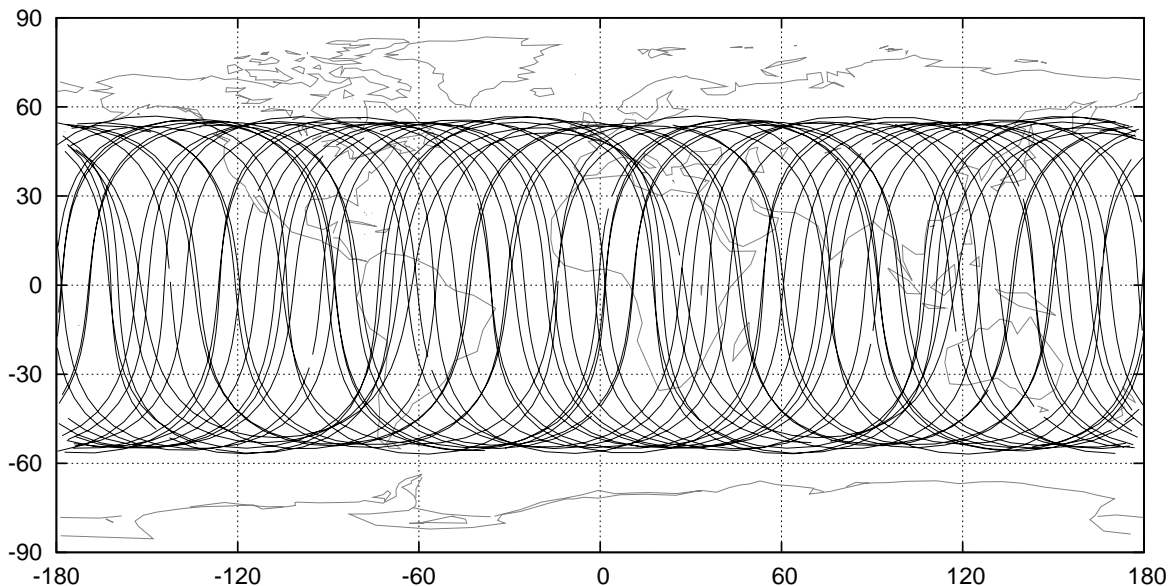


Figure 3.1: Ground-tracks of 30 GPS satellites over two orbital revolutions, for October 28, 2006

### 3.1 Characteristics of the Global Navigation Satellite Systems (GNSS)

Revolution periods of the GPS satellites	
Sidereal period	11 <sup>h</sup> 58 <sup>m</sup> 02 <sup>s</sup>
Draconitic period	11 <sup>h</sup> 57 <sup>m</sup> 57 <sup>s</sup>
Synodic period	11 <sup>h</sup> 59 <sup>m</sup> 01 <sup>s</sup>

Table 3.1: Selected revolution periods of the GPS satellites

The regression rate of the ascending node is about  $-0.039^\circ/\text{d}$  for GPS satellites. Thus the differences between sidereal and draconitic revolution period are very small (a few seconds, see Table 3.1) for the GPS satellites. The synodic revolution period is larger by about one minute. This period is the average time that elapses between two successive epochs with equal right ascension of the satellite and the mean Sun.

Up to now, four generations of GPS satellites have been put in orbit. The satellite vehicle numbers SVN 1 through 11 are designated as Block I, which have been put in orbit from 1978 to 1985. The Block I satellites have been experimental satellites to validate the space-based navigation concept. As the mean mission duration is about ten years, all Block I satellites already have been decommissioned. The operational GPS satellites are designated as Block II (SVN 13-21), Block IIA (SVN 22-40), and Block IIR (SVN 41-62), see Fig. 3.2. The first modern Block II satellite was launched in February 1989, whereas the system achieved full operational capability in January 1997, when the Block IIR satellites started replacing the older Block II/IAs. The Block IIR satellites are now going to be modernized to transmit the new military (M-Code) signal as well as the more robust civil signal L2C. The first modernized Block IIR satellite, designated as Block IIR-M, was launched in September 2005. Figure 3.3 (left) shows the steadily increasing number of GPS satellites since 1978 as well as the number of operational GPS satellites. The graph is based on the satellites launch and decommission dates. Altogether 54 GPS satellites have been launched until mid 2007. There have been 31 operational satellites at the beginning of 2008. Two of the Block IIA satellites (SVN 35 and 36) are equipped

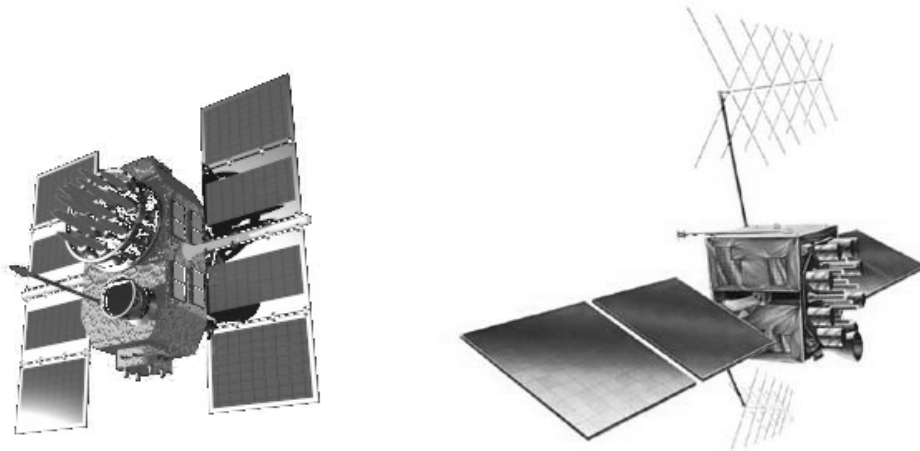


Figure 3.2: GPS Block IIA and Block IIR satellite types

### 3 Observing GNSS Satellites

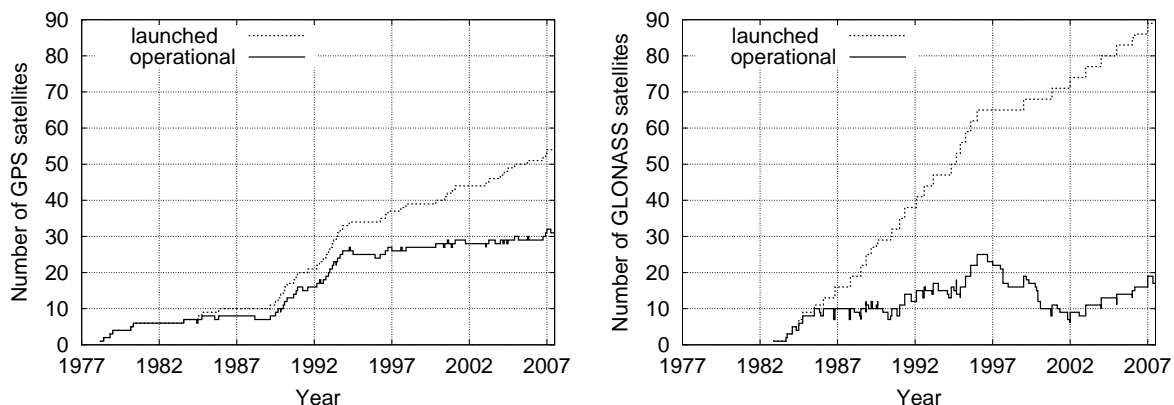


Figure 3.3: Number of launched and operational GNSS satellites, **left: GPS, right: GLONASS**

with LRAs of about 20 cm diameter in order to calibrate the GNSS measurement technique by measuring optical ranges to the satellites using SLR (see Fig. 3.4).

The next generation of GPS satellites, Block IIF, will transmit a new civil signal on a third frequency (L5). The launch of the first Block IIF satellite is expected in 2008. The next GPS satellite generation is already under development. The designated Block III satellites will have two more channels providing navigation signals for civil use. The first Block III satellite is scheduled for launch in 2012. The entire constellation is expected to remain fully operational through at least 2030. New satellites, additional frequencies, and signals will turn the GPS into a triple frequency system within the next few years. The equipment of all Block III satellites with LRAs is currently under consideration.

Table A.1 in the Appendix A provides a list of all GPS satellites (as per January 29, 2008) including the following satellite-specific information: PRN number, SVN, Block type, COSPAR-ID, launch and decommissioning date, satellite mass, and number of the orbital plane. The PRN numbers are preceded by a one-character system identifier (G for GPS, R for GLONASS), as used in the RINEX (Receiver Independent Exchange Format) observation files. This satellite numbering is also used throughout this work for the indication of the satellites. Note that the PRN numbers are only valid for the corresponding time window (as given in Table A.1).



Figure 3.4: Laser retroreflector array mounted on two Block IIA GPS satellites (Courtesy of HTSI)

### GLONASS – the Russian GNSS

The system design of the Russian GLONASS is similar to that of the GPS. The complete nominal GLONASS constellation consists also of 24 satellites. Each of the three orbital planes contains eight satellites, equally spaced by a  $45^\circ$  shift in the argument of latitude. The orbital planes are separated by  $120^\circ$  and inclined by about  $64.8^\circ$  with respect to the equator. Thus the high latitude regions are better covered by GLONASS than by GPS. The orbits are almost circular at an altitude of 19 100 km above the Earth’s surface, which is 1 100 km lower than the GPS constellation. The sidereal period needed for one orbital revolution is  $11^{\text{h}}15^{\text{m}}48^{\text{s}}$ , corresponding to 8/17 of a sidereal day. Therewith the deep (2:1) resonance perturbations (with respect to the Earth rotation) are avoided and station keeping maneuvers are not necessary as they are for the GPS satellites. The GLONASS satellites perform  $2\frac{1}{8}$  revolutions per sidereal day, causing a (17:8) commensurability with the Earth rotation (whereas the GPS satellites perform precisely 2 revolutions within the same time). As there are eight equally-spaced satellites in each orbital plane the GLONASS constellation repeats itself after one sidereal day with the individual satellites shifted by  $45^\circ$  (assuming a complete constellation). The Earth-satellite constellation repeats after eight sidereal days, which corresponds to 17 orbital revolutions. The Sun-Earth-satellite constellation repeats only after about 354.4 days, which is the draconitic GLONASS year, caused by the regression of the orbital node in the equator with a regression rate of about  $-0.033^\circ/\text{d}$ .

Figure 3.5 shows the ground-tracks of 12 GLONASS satellites, active in October 2006, for 17 orbital revolutions. Within 8 days (or 17 revolutions) a GLONASS satellite will be observed from every tracking site of a given latitude. Thus, possibly occurring systematics in the estimated parameters due to an unchanged satellite-site constellation are avoided, which might be a strength of the GLONASS compared to the GPS. In October 2006 only two of the three orbital planes (planes 1 and 3) have been occupied. The ground-tracks of all satellites of orbital plane 1 interfere with those of plane 3 (as opposed to the GPS satellites). Even the ground-tracks of the six new GLONASS satellites that have been placed in plane 2 (in December 2006 and 2007) would not change the figure, as these ground-tracks also interfere with those of the other planes.

In October 1982 the first three test satellites have been put into orbit. The first operational satellites were launched in December 1983. Initially, the system was intended to be fully operational in 1991, but it reached this status only for a short time period during 1995-1996. Today, there are altogether more than 90 GLONASS satellites in orbit, but due to the lifetime of about three years, the majority of them has been already decommissioned (see Fig. 3.3, right). Since March 2008, there are 16 operational GLONASS satellites in orbit. In September as well as in

Revolution periods of the GLONASS satellites	
Sidereal period	$11^{\text{h}}15^{\text{m}}48^{\text{s}}$
Draconitic period	$11^{\text{h}}15^{\text{m}}44^{\text{s}}$
Synodic period	$11^{\text{h}}16^{\text{m}}47^{\text{s}}$

Table 3.2: Selected revolution periods of the GLONASS satellites

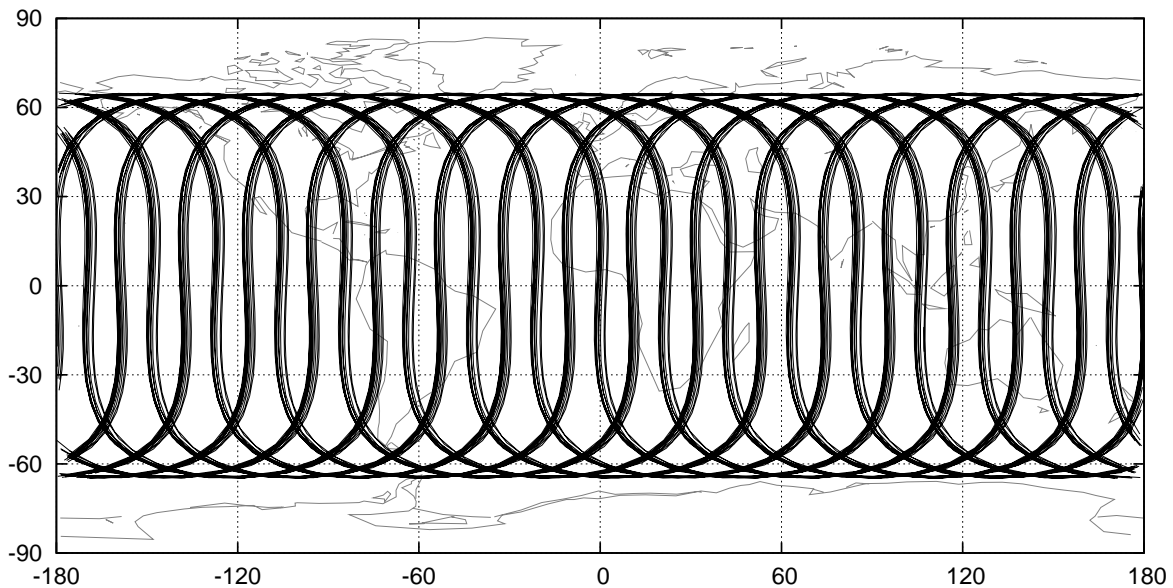


Figure 3.5: Ground-tracks of 12 GLONASS satellites over 17 orbital revolutions, for October 28 - November 4, 2006

December 2008 the next GLONASS satellite launches, of three GLONASS-M satellites each, are expected.

With the nominal configuration of 24 satellites, a minimum of five satellites would be in view at any given time anywhere on the globe. Today, at least four satellites are visible approximately 95% of the time. As opposed to the GPS, all satellites of the GLONASS constellation are equipped with LRAs for calibrating the radio signals by optical range measurements (SLR). With about 60 cm diameter the GLONASS LRAs are three times larger than the LRAs on GPS satellites and therefore much easier to track by the SLR technique.

Figure 3.6 shows the different GLONASS satellite types. The new modernized GLONASS satellites are called GLONASS-M satellites with a planned mission time of seven years. The first GLONASS-M satellite was launched in December 2003. Today, 13 GLONASS-M satellites are in orbit. The next satellite generation, GLONASS-K, is further improved with a reduced weight and an extended operational lifetime of 10-12 years. Its development costs are shared with India. A third frequency for civil use is introduced. The first GLONASS-K launch is scheduled for 2008. The configuration is proposed to become fully operational in 2010. The next long-term plan is the construction and deployment of the GLONASS-MK satellite generation.

A list of all GLONASS satellites (as per January 29, 2008) is provided in Table A.2 in the Appendix A including the following satellite-specific information: PRN number, SVN, GLONASS type, COSPAR-ID, launch date, status or decommissioning date, satellite mass, number of the orbital plane and slot number. The satellites are identified by their slot number, which defines the corresponding orbital plane and the satellite's position within the plane. For the three planes,

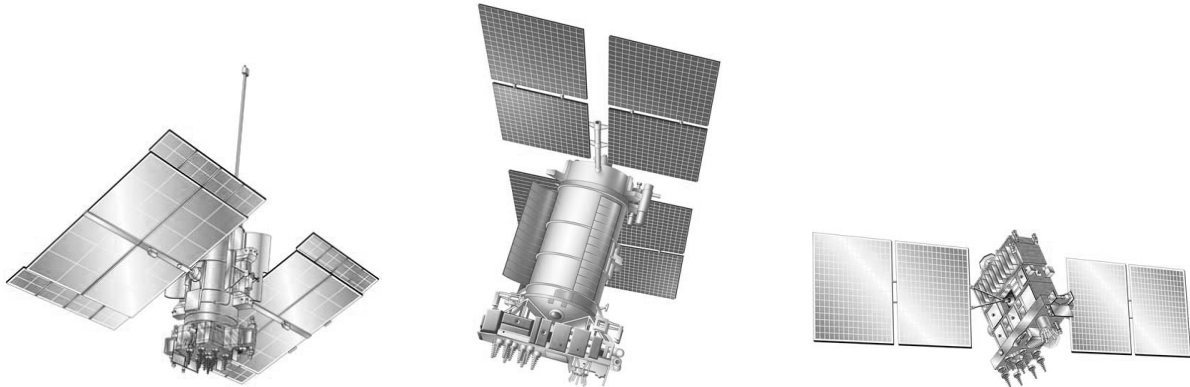


Figure 3.6: GLONASS, GLONASS-M, and GLONASS-K satellite types

the numbers 1-8, 9-16, and 17-24 are used. Hence, if an old satellite is replaced by a new one, it gets an “old” number. The slot number together with the system identifier “R” is used in the RINEX format for the satellite identification. In this work, this number is referred to as “PRN number” (although there is no “PRN” for GLONASS) to be consistent with the notation of the GPS satellites.

### Galileo – the European GNSS

Galileo, Europe’s GNSS, is currently under development. Unlike GPS and GLONASS, both of which are (at least partly) under military control, Galileo will be under civil control. The first experimental Galileo satellite GIOVE-A (Galileo In Orbit Validation Element) was launched in December 2005. The second satellite GIOVE-B is supposed to be deployed in April 2008. The Galileo constellation is scheduled to reach full operational capability within the time frame 2010-2013.

The nominal Galileo satellite constellation will be a so-called Walker 27/3/1 constellation consisting of 30 satellites, of which three are spares. The satellites will orbit at an altitude of 23,222 km, which is 3000 km higher than the GPS constellation. In each of the three orbital planes there will be nine operational satellites separated by 40°, and one spare. The inclination

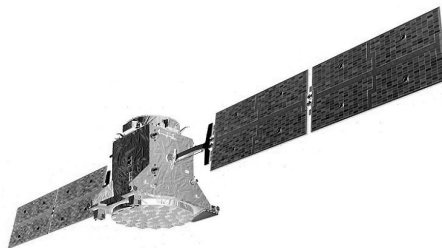


Figure 3.7: GIOVE-A satellite

of the orbital planes is  $56^\circ$  with respect to the equatorial plane. The satellites draconitic period is about  $14^h$ , which avoids resonance perturbations due to Earth rotation. The Earth-satellite constellation repeats after 17 orbital revolutions corresponding to 10 sidereal days, which causes a (10:17) commensurability with Earth rotation.

## Compass – the Chinese GNSS

China is developing the Compass Navigation Satellite System (CNSS), also known as Beidou-2. The current Beidou-1 system (consisting of four satellites) is experimental and has limited coverage and application. The new Compass system will be a constellation of 35 satellites, which includes five satellites in the geostationary orbit (GEO) and 30 satellites in the medium Earth orbit (MEO) that will offer complete coverage of the globe. Two levels of service will be provided: a free service and a licensed service for the military. Two Compass satellites were launched early in 2007. In the next few years, China plans to continue experimentation and system setup operations. The system is scheduled to be fully operational in 2010.

With GPS, GLONASS, Galileo, and Compass a total number of more than 100 GNSS satellite may become available to the user community within the next 10 years. Combined receivers are currently developed, which will be able to receive the signals from GPS, GLONASS, and Galileo.

### 3.1.2 GNSS Satellite Attitude

As the GNSS satellites are not of spherical shape but rather complex with large solar panels, the attitude of the satellite with respect to Sun and Earth is important for modeling the non-gravitational forces (e.g., solar radiation pressure or Earth albedo) acting on the satellite orbits (as well as for the knowledge of the location of the microwave antenna and the laser retroreflector array at any time).

The satellite's body-fixed coordinate system (X, Y, Z) is a right-handed system. Figure 3.8 illustrates the (X, Y, Z) system of a simplified GNSS satellite model, consisting of a box-like body and two solar panels. The system origin is the satellite's center of mass. The X-axis points into the hemisphere containing the Sun. The Y-axis points along the solar panel axis, and the Z-axis points to the Earth's center. For GPS satellites of type Block IIR the orientation of the X-axis, specified by the manufacturer, is in opposite direction (-X). But we will always refer to the X-axis as defined above for all GNSS satellite types.

An on board attitude system maintains the nominal pointing of the satellite through yaw and pitch control. Yaw rotates the satellite around the Z-axis, whereas pitch rotates the solar panels around the Y-axis. The navigation antennas along the positive Z-axis are supposed to always point towards the geocenter. The solar panel arrays mounted on the Y-axis should remain perpendicular to the incoming solar radiation, i.e., the normal vector of the solar panel surfaces should always point to the Sun when the satellite is not in eclipse. To meet these two conditions the satellite has to yaw and pitch continuously.

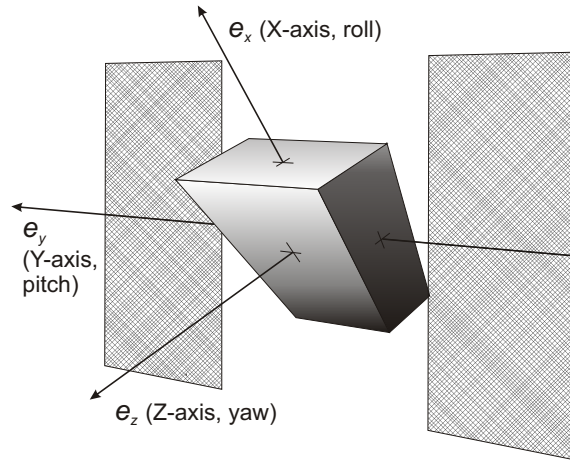


Figure 3.8: GNSS satellite's body-fixed coordinate system (X, Y, Z)

The nadir pointing attitude is determined by static Earth sensors that are mounted on the +Z surface and measure the IR detection of the Earth's horizon. A pair of Sun sensors mounted on each solar panel determine the yaw attitude. Data from these sensors are processed and any measured attitude error is corrected by applying torques using one of two sets of actuators. For GPS satellites, the three-axis stabilized attitude control is provided by a system of four reaction wheels (RW). In most cases attitude errors are corrected by commanding changes in the RW speeds. The RWs are designed to maintain spacecraft pointing within  $\pm 0.5^\circ$  in the roll, pitch, and yaw axis (Violet et al., 1999). For GLONASS satellites the attitude is maintained in a similar way by means of controlling flywheel engines. The Earth orientation is maintained with a maximum error of  $3^\circ$ , and the deviation of the normal to the solar panel surface from the direction to the Sun is at maximum  $5^\circ$  (Roscosmos, 2004).

In addition to the body-fixed satellite system, we have to define a Sun-oriented satellite system (D, Y, B) for solar radiation pressure (SRP) modeling. The system origin is in the satellite's center of mass. The D-axis points towards the incoming solar radiation. The Y-axis is already known as axis along the solar panels. The third axis B points into the hemisphere containing the geocenter and complements the right-handed system.

### Yaw bias

The yaw attitude is singular at two points, the intersection of the satellite orbit with the Earth-Sun line. At the point where the satellite is closest to the Sun any yaw angle allows optimal view of the Sun, whereas at the other singularity, when the satellite is in the Earth's shadow, the Sun sensor output is zero. But even a small amount of noise may trigger an unpredictable yaw rotation.

To allow modeling of the yaw attitude of GPS Block II/IIA satellites, the Sun sensors are biased by a small, but fixed, amount, which was set to  $0.5^\circ$  on all Block II/IIA satellites since November 1995 (Bar-Sever, 1996). As a result the yaw attitude is always about  $0.5^\circ$  in error

with respect to the nominal orientation. During shadow periods the satellite will yaw at full speed in the direction of the bias. Thus the yaw attitude upon shadow exit can be calculated and the Sun recover maneuver can be modeled, as well. The yaw maneuvers from shadow entry until nominal attitude is reached again are referred to as midnight maneuvers. At the opposite side, when the satellite is closest to the Sun, a similar maneuver takes place referred to as noon maneuver, starting when the nominal yaw rate gets larger than the maximal yaw rate and ending when the nominal yaw gets below the maximal yaw rate again.

The yaw bias  $b_1$  is an angle describing the rotation of the solar panel surface around an axis perpendicular to the panel axis Y and lying in the panel surface. The resulting yaw angle bias (i.e., the correction of the yaw angle due to the yaw bias)  $\Delta\Psi$  is given by

$$\sin \Delta\Psi = \frac{\sin b_1}{\sin E} \quad (3.1)$$

where  $\Delta\Psi$  ... Yaw angle bias induced by the yaw bias  
 $b_1$  ... Yaw bias  
 $E$  ... Phase angle referred to the geocenter, angle Sun-satellite-geocenter .

The elongation angle  $E'$ , being the angle Sun-geocenter-satellite, is given by

$$\cos E' = \cos \beta_0 \cos \Delta u \quad (3.2)$$

where  $\beta_0$  ... Elevation of the Sun above the orbital plane  
 $\Delta u$  ... Argument of latitude of the satellite w.r.t. the argument of latitude of the Sun .

As the distance satellite-Sun is much larger than the distance satellite-Earth, we assume that the unit vector pointing from the geocenter to the Sun is parallel to the unit vector pointing from the satellite to the Sun. Thus, the elongation angle is set equal to  $E' = 180^\circ - E$ , where  $E$  is the

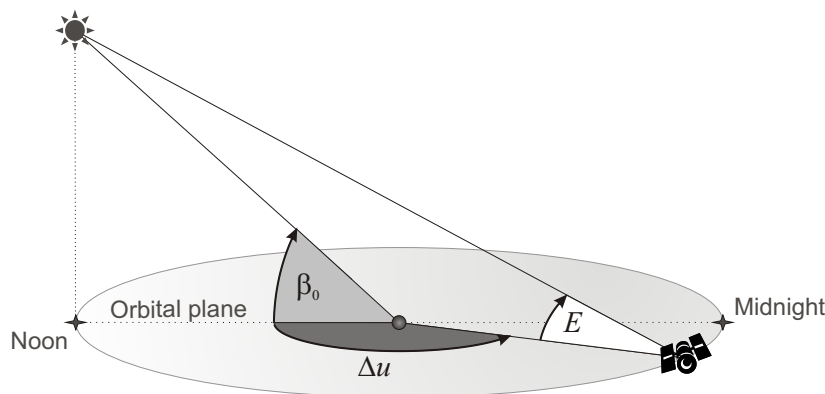


Figure 3.9: Angles  $\beta_0$ ,  $\Delta u$ , and  $E$  in the Sun-satellite-Earth system

phase angle referred to the geocenter, i.e., the angle Sun-satellite-geocenter (see Fig. 3.9). This approximation neglects an angle difference of about  $0.01^\circ$ . Hence, angle  $E$  can be approximated by

$$\cos E = -\cos \beta_0 \cos \Delta u. \quad (3.3)$$

The yaw angle bias induced by  $b_1$  may reach significant values only for small values of  $\sin E$ . At noon maneuver entry, when  $E \sim 5^\circ$  the yaw angle bias  $\Delta\Psi$  reaches  $6^\circ$ . Midnight maneuvers already start at  $E = 13^\circ$ , which results in  $\Delta\Psi = 2^\circ$ .

If the angle  $E$  is smaller than the yaw bias ( $E < 0.5^\circ$ ) Eq. (3.1) becomes undefined. Then the nominal orientation of the satellite can no longer be achieved by a yaw rotation. But this has no effect on the actual yaw rotation because for small values of  $E$  the satellite is in a midnight or noon maneuver and already yawing at full rate.

For Block IIR satellites no yaw bias is introduced. For angles  $|\beta| < 1.6^\circ$  Block IIR satellites switch from yaw steering to a fixed yaw mode (Bar-Sever, 1997). In this regime, the spacecraft does not perform a midnight or noon turn and is commanded to travel in a fixed yaw orientation aligning the negative X-axis roughly parallel to the velocity vector.

## Y-bias

Assuming nominal attitude, the solar radiation force vector is strictly confined to the body-fixed X-Z plane. In the 1980s, an unmodeled along-track acceleration was observed for the GPS satellites, produced by a force (per mass) along the solar panel axis direction. This acceleration (or force per satellite mass) is referred to as Y-bias. It is of the order of  $10^{-9} \text{ m/s}^2$  and it is different for each GPS satellite and changes slowly over a few weeks. Its physical nature is still unclear. Three possible explanations have been proposed by Fliegel et al. (1992): (1) the solar panel center beams are not perfectly straight and/or normal to the spacecraft body median plane, (2) the solar sensors are not perfectly aligned with the Z-axis, or (3) heat generated in the spacecraft body is reradiated from louvres on just one Y-side. A misalignment of the solar sensors between  $0.5^\circ$  and  $1^\circ$  would account for the observed Y-bias. The reported yaw bias ( $b_1 = 0.5^\circ$ ) is the most likely explanation.

For radiation pressure modeling, it is recommended to estimate for each satellite a scale factor  $D0$  for the direct radiation force and a Y-bias  $Y0$ , as quantities that may change slowly over days and weeks.

## Eclipses

During eclipse phases, when the direct solar radiation is blocked by the Earth or the Moon, no SRP force is acting on the satellite. Although the effect of partial shadowing of the sunlight by the Moon on the satellite orbit is very small, it must be taken into account for precise orbit modeling. Here we will, however, focus on the shadowing of the sunlight by the Earth only.

For GNSS satellites, eclipsing seasons caused by the Earth's shadow occur twice per year and last for about 30 days, during which a satellite passes the shadow once per revolution. For orbit modeling, the impact of SRP is switched off at shadow entry and switched on again at shadow exit in the Bernese GPS Software. Thus, the eclipse factor used to scale the accelerations caused by SRP (Eqs. (2.21, 2.22, 2.23)) is set either to zero (inside the shadow) or to one (outside the shadow).

The shadow modeling is based on the following simplifying assumptions. We assume a spherical Earth with radius  $r_e$ . We further assume that the solar radiation is parallel within the Earth's environment. Thus, the shadow boundary in space is assumed to be a cylinder with radius  $r_e$ . Its axis coincides with the line Sun-Earth. As the angular diameter of the Sun is about  $0.5^\circ$ , two shadow cones, one for umbra and one for penumbra should be used instead of a cylinder. Umbra is the region of total shadow, whereas penumbra specifies the region of partial shadow where the total solar irradiance is partially occluded by the Earth. The cylindrical approximation is, however, a sufficient approximation, as the penumbra period for GNSS satellites is only about 1 minute and the neglected accelerations before and after crossing the cylinder boundaries almost compensate each other (Beutler, 2005). The Earth's atmosphere causing refraction effects is not taken into account.

The longest duration of the eclipse phase results if the Sun lies in the orbital plane, i.e., if the elevation angle of the Sun above the orbital plane is  $\beta_0 = 0$ . This is the case if the Sun is near the ecliptic node of the orbital plane. For the GNSS satellites the longest eclipse period is about 55 minutes. Eclipses occur for  $|\beta_0| \leq 14^\circ$ , which is the angular radius of the Earth at the distance of the GNSS satellites.

For GPS the satellite's rotational behavior during shadow periods is well known, whereas for GLONASS satellites the behavior is not known. For GPS Block II/IIA satellites the yaw direction is always the same within the shadow given by the sign of the yaw bias  $b_1$ . But outside the shadow the yaw direction may be changing. Thus, the satellite might have to reverse its yaw rotation upon shadow entry. During the shadow phase, if the satellite is in yaw rate mode (see Sect. 3.1.2), the GPS Block II/IIA satellites rotate around the Z-axis with maximum rate of about  $0.12^\circ/\text{s}$  (Bar-Sever, 1994). The actual maximum rotation rates may slightly differ from that value. After shadow exit, the satellites may need up to 30 minutes to reach their nominal attitude.

For SLR analysis the position of the LRA with respect to the satellite's center of mass and thus the satellite's attitude have to be known precisely. As opposed to the GLONASS satellites, the LRA of the GPS satellites is not centered on the Z-axis, which results in biased SLR range measurements during the eclipse phase, if the rotation rate is not modeled correctly. Therefore, we apply the rotation rates provided by JPL for eclipsing GPS satellites in our SLR analysis (see Sect. 4.2.2).

### GPS Satellite Maneuvers

In general, station-keeping maneuvers for GPS satellites are performed 1-2 times a year using thruster firings. These satellite maneuvers are necessary for active GPS satellites to keep them in

their nominal positions in the orbital planes. The satellites leave their nominal positions due to resonance effects of the satellites motion with terms of the geopotential, as the orbital periods of the GPS satellites are in 2:1 commensurability with the rotation period of the Earth. According to Hugentobler (1998), the most important geopotential terms responsible for resonance for circular orbits with non-zero inclination are the terms  $C_{32}$  and  $S_{32}$ , followed by  $C_{44}$  and  $S_{44}$ . These terms give raise to resonance perturbations of the semi-major axis. In addition, the Y-bias (a force acting perpendicular to the direction to the Sun) induces a long-periodic drift in the semi-major axis of up to nearly 20% of the effect stemming from geopotential terms.

#### 3.1.3 GNSS Solar Radiation Pressure Modeling

Solar radiation pressure is the most important non-gravitational force acting on GNSS satellites. Therefore, the SRP effect has to be modeled with high accuracy for generating most accurate GNSS orbits. Improved models of all effects, which have an impact on the satellite's position, help to reduce the uncertainty in other parameters derived from GNSS analysis (e.g., troposphere parameters). In recent years, various techniques for SRP modeling were developed, ranging from purely empirical approaches to purely analytical models. In the following sections we present three of them, a very simple as well as a more sophisticated analytical model, and an empirical model.

From the scientific point of view, it is important to understand the physical effects affecting the dynamics of a satellite. The ROCK radiation pressure models are based on a purely physical model, but for easy use they were represented by Fourier series as a function of the phase angle  $E$  between the Sun and the Z-axis of the spacecraft. Thus the physical parameters of the model, as optical or surface properties, are not available. They cannot be established by estimating parameter improvements from the observations. Possible model errors cannot be removed from the Fourier series.

As opposed to a physical model, the CODE radiation pressure model is based on an empirical approach. This is particularly effective, if a long time series of data is available from a dense, globally distributed network. However, the use of empirical parameters to absorb unmodeled effects provides no insight into the physical mechanism responsible for these effects.

A simple boxwing model allows the estimation of the optical properties of the spacecraft's surfaces. Various surface components may be specified by the user. In this way, different body shapes, ranging from very simple shapes to more complex shapes, can be modeled.

More sophisticated purely analytical models, which take care, e.g., of secondary intersection effects when light is reflected from one surface and then strikes another, have been developed by Ziebart et al. (2005).

#### Rock Models

The ROCK models have been developed by Rockwell International for the GPS Block I and Block II satellites (Fliegel et al., 1992). The Fortran computer subroutine that implemented the

Rockwell solar radiation pressure models became known as ROCK4 (Fliegel et al., 1985) and ROCK42 (Fliegel and Gallini, 1989) for the Block I and Block II satellites, respectively. There are two different model types, the standard model (S) and the thermal model (T) including accelerations due to reradiated heat. For Block I satellites the models are denoted as S10 and T10, for Block II satellites as S20 and T20, and for Block IIR satellites a S30 and T30. The Rock models treat a satellite as a set of flat or cylindrical surfaces. First, the contribution of all major surfaces to the accelerations caused by solar radiation pressure are computed. Input parameters are the shape, area, and optical parameters  $(\mu, \nu)$  of the various surfaces. First order shadowing effects are considered, as, e.g., the shadow caused by an antenna on the satellite's body. The resulting accelerations are expressed in the satellite's body-fixed coordinate system (see Sect. 3.1.2). The acceleration components can be represented as Fourier series (with few terms) as a function of the phase angle  $E$ , that is the angle between the direction to the Sun and the positive  $Z$ -axis. If the attitude of the satellite is nominal, the acceleration due to solar radiation pressure always lies in the  $(X,Z)$  plane.

As it is recommended in the IERS conventions (McCarthy and Petit, 2004) to use the T-models due to the inclusion of thermal reradiation (TRR), we repeat only the resulting formulas for the T10 and T20 models from (Fliegel et al., 1992) and for the T30 model from (Fliegel and Gallini, 1996). The SRP force acting on a GPS satellite is given in  $X$ -, and  $Z$ -components using units of  $10^{-5}\text{N}$  and angle  $E$  in radians.

For Block I satellites the T10 model reads

$$\begin{aligned} f_X &= -4.55 \sin E + 0.08 \sin(2E + 0.9) - 0.06 \cos(4E + 0.08) + 0.08 \\ f_Z &= -4.54 \cos E + 0.20 \sin(2E - 0.3) - 0.03 \sin(4E). \end{aligned} \quad (3.4)$$

For Block II/IIA satellites the T20 model reads

$$\begin{aligned} f_X &= -8.96 \sin E + 0.16 \sin(3E) + 0.10 \sin(5E) - 0.07 \sin(7E) \\ f_Z &= -8.43 \cos E. \end{aligned} \quad (3.5)$$

For Block IIR satellites the T30 model reads

$$\begin{aligned} f_X &= -11.0 \sin E - 0.2 \sin(3E) + 0.2 \sin(5E) \\ f_Z &= -11.3 \cos E + 0.1 \cos(3E) + 0.2 \cos(5E). \end{aligned} \quad (3.6)$$

The resulting acceleration is the sum of the two components divided by the satellite's mass  $m$

$$\mathbf{a}_{rock} = \frac{(f_X \mathbf{e}_X + f_Z \mathbf{e}_Z)}{m} \quad (3.7)$$

where  $\mathbf{e}_X \dots$  Unit vector in the satellite's body-fixed coordinate system in  $X$ -direction  
 $\mathbf{e}_Z \dots$  Unit vector in the satellite's body-fixed coordinate system in  $Z$ -direction.

The Eqs. (3.4, 3.5, 3.6) represent the ROCK4 and ROCK42 output with a maximum error of about 1.5%, which occurs only during eclipse seasons, when  $E$  is close to  $180^\circ$ . The more important contribution to model errors are given by the ROCK4 and ROCK42 models themselves. According to Fliegel et al. (1992), there remain about 3% error in the force components, caused by spacecraft components that are not modeled, second order shadowing effects, or aging effects of the optical properties. This error can be accounted for by estimating a scale factor ( $D0$ ) in addition to the use of the a priori radiation pressure models T10, T20, and T30. It is also recommended to estimate a Y-bias ( $Y0$ ) (see Sect. 3.1.2).

### CODE Models

CODE (introduced in Sect. 3.2.2), developed a SRP model for GPS Block II and Block IIA satellites in 1998.

The CODE SRP model is not based on a physical model, as the Rock model is, but rather on empirical parameters (Springer, 2000). GPS orbits, generated by using the Rock SRP models, were used as pseudo-observations for orbit determination. For the orbit determination step no a priori SRP model was introduced. A set of six orbit parameters consisting of three constant and three periodic terms was estimated for each orbital arc

$$\begin{aligned} \text{Constant terms: } & D0, Y0, B0 \\ \text{Periodic terms: } & Z1 \sin(\Delta u), X1 \sin(\Delta u), X3 \sin(3\Delta u), \end{aligned}$$

where angle  $\Delta u = u - u_0$  is the argument of latitude of the satellite relative to the argument of latitude of the Sun. Thus, the dependency on the Sun's position with respect to the orbital plane is taken into account. The orbital arc-length is of five days each.

A long time series covering almost six years starting in 1996 of estimates for the six selected orbit parameters was generated. Analyzing the time series yields a new deterministic SRP model. For each of the six parameters a  $\beta_0$ -dependent function was derived. The angle  $\beta_0$  is the elevation of the Sun above the orbital plane. Significant periodic terms were found for the constant terms  $D0, Y0, B0$ , and the once-per-revolution terms  $Z1, X1$ , and  $X3$ . The resulting functions read as

$$\begin{aligned} D0(\beta_0) &= D0_0 + D0_{C2} \cos(2\beta_0) + D0_{C4} \cos(4\beta_0) \\ Y0(\beta_0) &= Y0_0 + Y0_{C2} \cos(2\beta_0) \\ B0(\beta_0) &= B0_0 + B0_{C2} \cos(2\beta_0) \\ Z1(\beta_0) &= Z1_0 + Z1_{C2} \cos(2\beta_0) + Z1_{S2} \sin(2\beta_0) + Z1_{C4} \cos(4\beta_0) + Z1_{S4} \sin(4\beta_0) \\ X1(\beta_0) &= X1_0 + X1_{C2} \cos(2\beta_0) + X1_{S2} \sin(2\beta_0) \\ X3(\beta_0) &= X3_0 + X3_{C2} \cos(2\beta_0) + X3_{S2} \sin(2\beta_0). \end{aligned} \tag{3.8}$$

Thus, the perturbing acceleration on a Block II/IIA GPS satellite due to SRP may be written as

$$\begin{aligned} \mathbf{a}_{code} &= D0(\beta_0)\mathbf{e}_D + Y0(\beta_0)\mathbf{e}_Y + B0(\beta_0)\mathbf{e}_B + Z1(\beta_0) \sin(\Delta u) \mathbf{e}_Z \\ &\quad + [X1(\beta_0) \sin(\Delta u) + X3(\beta_0) \sin(3\Delta u)]\mathbf{e}_X \end{aligned} \tag{3.9}$$

where  $e_D$  ... Unit vector pointing from the satellite to the Sun  
 $e_Y$  ... Unit vector along the spacecraft's solar panel axis  
 $e_B$  ... Unit vector completing the system (D, Y, B):  $e_B = e_D \times e_Y$   
 $e_X$  ... Unit vector completing the system (X, Y, Z):  $e_X = e_Y \times e_Z$   
 $e_Z$  ... Unit vector pointing from the satellite to the geocenter.

Remember that X and Z are the axes of the body-fixed coordinate system (X, Y, Z) (see Fig. 3.8), whereas D and B correspond to the Sun-oriented coordinate system (D, Y, B). The direction of Y is defined such that X points into the hemisphere containing the Sun and B into the hemisphere containing the geocenter.

The constant terms  $D0_0$ ,  $Y0_0$ , and  $B0_0$  are satellite-specific, whereas  $Z1_0$  is block-specific. For the values of all CODE SRP model parameters we refer to Springer (2000).

In 2006, the model coefficients were checked and improved based on six years of GPS data starting in 2000. The time series included Block IIR satellites, which were not available before. New values for the coefficients and slightly changed model parameters were estimated. The acceleration derived from the improved CODE SRP model is given by

$$\mathbf{a}_{code} = D0(\beta_0)\mathbf{e}_D + Y0(\beta_0)\mathbf{e}_Y + B0(\beta_0)\mathbf{e}_B + Z1(\beta_0) \sin(\Delta u) \mathbf{e}_Z \quad (3.10)$$

with the coefficients

$$\begin{aligned} D0(\beta_0) &= D0_0 + D0_{C2} \cos(2\beta_0) + D0_{C4} \cos(4\beta_0) \\ Y0(\beta_0) &= Y0_0 + Y0_{C2} \cos(2\beta_0) \\ B0(\beta_0) &= B0_0 + B0_{C2} \cos(2\beta_0) + B0_{C4} \cos(4\beta_0) \\ Z1(\beta_0) &= Z1_0 + Z1_{C2} \cos(2\beta_0) + Z1_{S2} \sin(2\beta_0) + Z1_{C4} \cos(4\beta_0) + Z1_{S4} \sin(4\beta_0). \end{aligned} \quad (3.11)$$

Note that there are no longer any X1- and X3-terms as for the previous model.

In addition, a similar approach was used for deriving for the first time a SRP model for GLONASS satellites. The resulting acceleration reads as

$$\mathbf{a}_{code} = D0(\beta_0)\mathbf{e}_D + Y0(\beta_0)\mathbf{e}_Y + Z1(\beta_0) \sin(\Delta u) \mathbf{e}_Z \quad (3.12)$$

with the coefficients

$$\begin{aligned} D0(\beta_0) &= D0_0 + D0_{C2} \cos(2\beta_0) \\ Y0(\beta_0) &= Y0_0 + Y0_{C2} \cos(2\beta_0) \\ Z1(\beta_0) &= Z1_0 + Z1_{C2} \cos(2\beta_0) + Z1_{C6} \cos(6\beta_0). \end{aligned} \quad (3.13)$$

There are no accelerations in Y-direction, except for one specific GLONASS satellite (R18), for which the function  $Y0(\beta_0)$  was estimated. The coefficient  $Z1_0$  is satellite-specific.

### Boxwing Model

We developed a simple boxwing radiation pressure model, consisting of a six-sided box and a flat-plate wing representing the satellite's body and the solar panel arrays. Each of the satellite's surfaces has two optical properties, reflectivity  $\nu$  and specularity  $\mu$ , which might be transformed into three coefficients each for the absorbed, the specularly reflected and the diffusely reflected fraction of the incoming solar radiation. The surfaces are assumed to be flat. The model does not only account for solar radiation pressure, but also for thermal reradiation effects (neglecting thermal conduction).

For each of the satellite surfaces a perturbing acceleration due to solar radiation pressure can be derived from Eq. (2.21) in Sect. 2.1.3. The formula is repeated here for better readability

$$\mathbf{a}_f = C \left[ (\alpha + \delta) \mathbf{e}_\odot + \left( 2\rho \cos \theta + \frac{2}{3}\delta \right) \mathbf{e}_n \right] \quad (3.14)$$

with

$$C = -\frac{a_e^2}{|\mathbf{r} - \mathbf{r}_\odot|^2} P_\odot \frac{A}{m}. \quad (3.15)$$

From Eq. (2.16) we form the relation  $\alpha = 1 - \delta - \rho$ . Replacing  $\alpha$  changes Eq. (3.14) accordingly

$$\mathbf{a}_f = C \left[ (1 - \rho) \mathbf{e}_\odot + \left( 2\rho \cos \theta + \frac{2}{3}\delta \right) \mathbf{e}_n \right]. \quad (3.16)$$

Including thermal reradiation effects by using relations (2.31) yields

$$\mathbf{a}_f = C \left[ (1 - \rho) \mathbf{e}_\odot + \left( 2\rho \cos \theta + \frac{2}{3}(1 - \rho) \right) \mathbf{e}_n \right]. \quad (3.17)$$

The total acceleration is derived by accumulating the accelerations of all illuminated surfaces. For a spacecraft consisting of flat surfaces only we get the following expression

$$\mathbf{a}_{bw} = \sum \mathbf{a}_{f_i} = \sum C_i \left[ (1 - \rho_i) \mathbf{e}_\odot + \left( 2\rho_i \cos \theta_i + \frac{2}{3}(1 - \rho_i) \right) \mathbf{e}_{n_i} \right] \quad (3.18)$$

with

$$C_i = -\frac{a_e^2}{|\mathbf{r} - \mathbf{r}_\odot|^2} P_\odot \frac{A_i}{m}. \quad (3.19)$$

Only surfaces actually illuminated by the Sun are taken into account.

The model input parameters for the a priori model have to be specified, which are the properties of the surfaces: shape, area, and the specularity and reflectivity coefficients. The orientation of each surface is given by two angles each, defining the surface normal. Components belonging

to the spacecraft's body are treated as body fixed surfaces, whereas the solar panels are rotating in the body-fixed coordinate system. The solar panel normal is assumed to be aligned with the direction to the Sun. A misorientation of the solar panels can be described by two angles  $b_1$  and  $b_2$ , where the yaw-bias  $b_1$  reflects the rotation of the solar panel around an axis lying in the panel plane and perpendicular to the Y-axis, and  $b_2$  reflects the rotation of the solar panel around the Y-axis. The yaw bias angle  $b_1$  has a nominal value of  $0.5^\circ$  for GPS Block II/IIA satellites and is related to the yaw bias  $\Delta\Psi$  (see Sect. 3.1.2).

Within the scope of this work, the boxwing model was implemented in a development version of the Bernese GPS Software. It is possible to define an arbitrary number of surfaces with the corresponding optical properties for each of the GNSS satellites and to compute a satellite-specific a priori radiation pressure model.

In contrast to other radiation pressure models, the boxwing model may be used not only as a priori model but also to improve the model parameters  $\mu$  and  $\nu$ , or  $\delta$  and  $\rho$  respectively, for each surface specified. The corresponding implementation of the parameter estimation process could not be completed within the scope of this work. It should be possible to estimate the yaw bias  $b_1$  in addition to the optical parameters. The angle  $b_2$  cannot be estimated together with  $b_1$  in one parameter estimation process, as it linearly depends on  $b_1$ . Also the estimation of the albedo parameter  $k$  would be of interest. Once the parameter estimation is implemented, the main problem will be the correct interpretation of the estimated parameter values.

Spherical satellites will be much easier to deal with than boxwing satellites. The acceleration due to SRP and EAP for a spherical satellites is given by

$$\mathbf{a}_s = \left(1 + \frac{4}{9}\delta\right)(B\mathbf{e}_s + C\mathbf{e}_\odot), \quad (3.20)$$

and including thermal reradiation by

$$\mathbf{a}_s = \left(\frac{13}{9} - \frac{4}{9}\rho\right)(B\mathbf{e}_s + C\mathbf{e}_\odot). \quad (3.21)$$

Modeling SRP for spherical Laser satellites as, e.g., LAGEOS, will be of interest for orbit determination based on SLR observations.

## 3.2 GNSS Orbit Determination Based on Microwave Observations

High precision GNSS orbits are a fundamental product of the International GNSS Service (IGS). GNSS microwave data and orbits, as well as other IGS products, are made available to the IGS user community through the internet. They support a wide range of scientific and engineering applications. Within the IERS GNSS data and products contribute to the improvement and densification of the geodetic reference frames and to the determination of Earth rotation parameters.

This section introduces the IGS orbit products and their quality. The orbit generation at the Center for Orbit Determination in Europe (CODE), which is one of ten IGS Analysis centers, is presented in more detail.

GNSS Satellite Ephemerides		Accuracy	Latency	Updates
GPS	final	< 5 cm	~ 13 days	weekly
	rapid	< 5 cm	17 hours	daily
	ultra-rapid (observed part)	< 5 cm	3 hours	four times daily
	ultra-rapid (predicted part)	≤ 10 cm	real time	four times daily
GLONASS	Final	15 cm	2 weeks	weekly

Table 3.3: IGS orbit products

### 3.2.1 The IGS Orbit Products

The IGS is an approved service of the International Association of Geodesy (IAG). It began routine operations on January 1, 1994. Among other GNSS products, the IGS provides the official IGS orbits based on contributions from the IGS Analysis Centers (ACs). The required microwave tracking data are collected by an international network of over 300 continuously operating dual-frequency GPS stations and about 50 GNSS stations, the latter tracking GPS as well as GLONASS satellites. The ACs analyze the IGS station data and submit the derived orbit solutions to the Analysis Center Coordinator (ACC), who combines the ACs' submissions to form the official IGS orbit products. Currently, there are three official IGS product lines, namely the IGS final-, the IGS rapid-, and the IGS ultra-rapid products (see Table 3.3). The IGS final orbits have the highest quality of all IGS orbits. They are generated on a weekly basis with a 2 weeks delay. The IGS rapid products have a quality comparable to that of the final products. They are made available on a daily basis with 17 hours delay after the end of the observation day. The ultra rapid products are available for real time use. They contain an orbit part based on real data and a predicted orbit part. As the ultra rapid products are provided twice per day, the average age of the predictions is reduced to 9 hours.

The orbit products are satellite ephemerides given in the International Terrestrial Reference System (ITRS) with a 15 min spacing. The IGS orbit accuracies specified in Table 3.3 are, except for the predicted orbits, based on comparisons with independent SLR measurements. For GLONASS orbits only final products are generated, as the constellation is not yet fully operational.

### 3.2.2 GNSS Orbit Determination at CODE

CODE, the Center for Orbit Determination in Europe, is one of the ten IGS Analysis Centers. It is a joint venture of the Federal Office of Topography (swisstopo) in Wabern, Switzerland; the Federal Agency of Cartography and Geodesy (BKG) in Frankfurt, Germany; and the Astronomical Institute of the University of Bern (AIUB) in Bern, Switzerland. CODE is located at the AIUB.

CODE contributes to all official IGS orbit products. The orbit solutions are generated with the latest development version of the Bernese GPS Software (Dach et al., 2007). The models

used are those provided by the IERS Conventions (McCarthy and Petit, 2004). They contain conventional models, constants and standards. Changes in the IERS conventions are taken over by CODE as soon as possible.

At present, the CODE orbit is based on the following foundation: The JPL Development Ephemeris (DE405) are used to compute the positions of Sun and Moon, both of which are treated as point masses. The geopotential is modeled with the JGM-3 model (Tapley et al., 1996) up to degree and order 12. Ocean tidal forces are treated by the CSR 3.0 ocean tide high model (Eanes and Bettadpur, 1992).

CODE uses the Extended Orbit Model (ECOM) described by Beutler et al. (1994). The acceleration of a satellite due to solar radiation pressure (SRP) is defined as

$$\mathbf{a}_{srp} = \mathbf{a}_{srp0} + D(u)\mathbf{e}_D + Y(u)\mathbf{e}_Y + B(u)\mathbf{e}_B \quad (3.22)$$

with the coefficients

$$\begin{aligned} D(u) &= D0 + DC \cos u + DS \sin u \\ Y(u) &= Y0 + YC \cos u + YS \sin u \\ B(u) &= B0 + BC \cos u + BS \sin u \end{aligned} \quad (3.23)$$

where  $\mathbf{a}_{srp}$  ... Acceleration due to the SRP  
 $\mathbf{a}_{srp0}$  ... Acceleration derived from the a priori SRP model  
 $u$  ... Argument of latitude of the satellite .

The SRP a priori model used for the computation of  $\mathbf{a}_{srp0}$  is the CODE SRP model for GPS satellites since November 2005 (the ROCK model was used before). From November 2005 until November 2007 the CODE SRP model was used for the GLONASS satellites. Since November 2007 no SRP model is used for the GLONASS satellites. The estimated orbit parameters are a set of six osculating elements (referring to the initial epoch) plus five solar radiation pressure parameters, namely the three constant accelerations ( $D0, Y0, B0$ ) in D-, Y-, and B-direction as well as periodic once-per-revolution terms ( $BS, BC$ ) in B-direction. The Earth shadow is

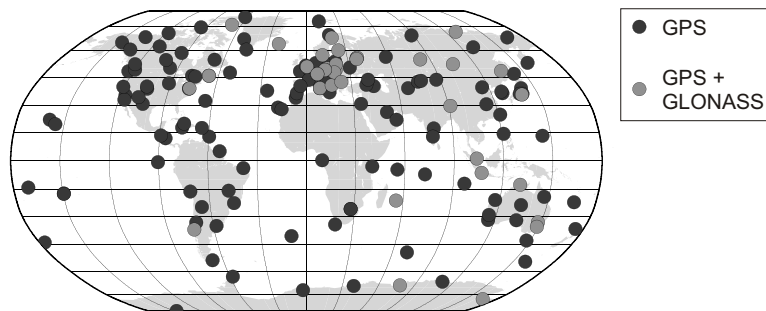


Figure 3.10: Geographical distribution of GNSS tracking stations

assumed to be cylindrical. The Moon shadow model takes umbra and penumbra into account. Pseudo-stochastic pulses (small velocity changes) are estimated once per revolution. The numerical integration algorithms used for orbit integration were developed by Beutler (2005). The integration step size is one hour. Within hourly time intervals, the orbit is represented by a polynomial of degree 10, which in turn approximates the true solution of the equations of motion on the sub-millimeter level.

General relativistic corrections are taken into account. The arc length of rapid and final orbit products is 72 hours or three solar days.

It is worth-while to mention that CODE generates consistent GPS and GLONASS satellite orbits from a combined analysis since mid 2003. Data of about 30 GPS/GLONASS tracking IGS sites are analyzed for that purpose together with about 150 GPS-only sites. Figure 3.10 shows the geographical distribution of the GPS-only and GPS/GLONASS tracking sites in July 2007.

The geodetic datum definition of the site coordinates is realized by a subset of up to 100 IGS core sites. Three no-net-rotation conditions are imposed with respect to the adopted IGS reference frame.

### 3.2.3 GNSS Orbit Accuracy

In order to assess the quality of the microwave-based GNSS orbits, independent measurements are necessary. SLR observations are very useful for such an independent orbit validation (see Sect. 3.4). As all GLONASS satellites carry LRAs on board, inter-technique comparisons are possible, whereas for GPS they are limited with only two satellites carrying LRAs.

The microwave technique alone does not allow it to assess the “true” orbit accuracy but to study the internal consistency of the orbits. The formal errors of the estimated orbit parameters are indicators of the orbit quality. Furthermore, orbits derived from microwave data, but obtained with different modeling approaches or different data sets may be compared.

#### Formal Orbit Errors

One result of the least square adjustment process is the variance-covariance matrix  $C$ . The diagonal elements  $C_{xx}$  contain the formal errors  $m_x$  of the estimated parameter, e.g. the osculating elements, whereas the off-diagonal elements  $C_{xy}$  characterize the correlations between individual parameters  $x$  and  $y$

$$C_{xx} = m_x^2, \quad C_{xy} = \rho_{xy} m_x m_y. \quad (3.24)$$

The formal errors of satellite positions at any given epoch may be computed through error propagation formulas from the variance-covariance matrix. The analysis of orbit errors over time shows the typical development of orbit precision over the entire arc: The orbit is well defined in the center of the arc, whereas it gets weaker towards the arc boundaries. This is expected as there are no stabilizing observations at the boundaries. For detailed studies we refer to Rothacher (1992).

#### Orbit Comparisons

Orbit comparisons are routinely performed by the IGS ACC. The individual contributions of the ACs are compared to the official IGS orbit products. It is important to note that these comparisons do not assess the accuracy of the orbits but only the consistency of the individual contributions. GPS final and rapid orbits of the individual ACs are proven to be consistent at the 1 – 2 cm level, and the GLONASS orbits at the 5 cm level. GLONASS orbits have a lower precision than GPS orbits, because the number of combined GPS/GLONASS tracking receivers (and therefore the number of GLONASS observations available for the parameter estimation process) is much smaller than that available for the GPS satellites.

Orbits derived from different data sets may be compared as well. Orbit overlap studies analyze the differences between two orbital parts stemming from two different orbits, which overlap in time, i.e., partly similar data sets have been used for the determination of both orbital arcs. In general, the middle of an orbital arc is better defined than the arc boundaries. Overlap differences derived from the central part of an arc and a boundary part of another arc, both of which were estimated with the same orbit model, are an indicator for the quality of the orbit model. If the orbit model is not sufficient to perfectly represent the orbit given by the measurements, the overlap differences become larger with increasing arc length, in particular if long-periodic effects were neglected.

Similar information may be gained from the differences of satellite position at the arc boundaries derived from two consecutive arcs. A systematic behavior of satellite positions at arc boundaries of successive arcs was reported by Slabinski (2006). Large along-track discontinuities of several centimeters are not randomly distributed but show a systematic pattern in time. Such comparisons indicate that the accuracy of the microwave-based orbits is lower than the precision (derived from the formal errors) and the consistency between orbits from different ACs let us expect.

### 3.3 Astrometric CCD Observations of GNSS Satellites

Observation of GNSS satellites are acquired for different reasons by optical telescopes. One principle reason is the generation and maintenance of a catalog of orbital elements of artificial satellites (active and passive satellites, fragments, and rocket bodies) for space surveillance and space situational awareness purposes. On the other hand, GNSS satellites may be used for the calibration of optical observation facilities (e.g., for the calibration of the telescope pointing, or of the epoch registration), as for GNSS satellites very precise ephemerides data are available from GNSS orbit determination based on microwave measurements. In principle any satellite with precise ephemerides is suited for this purpose.

The build-up and maintenance of a catalog of orbits is the main aim of space surveillance networks (SSN). Today, there are two operating SSNs, the U.S. SSN (Johnson, 1993) and the Russian SSN. A European SSN is currently under study (Donath et al., 2005). Orbital data from the U.S. SSN are published as so-called Two Line Elements (TLE), which are mean orbital

elements over a certain time period. The U.S. TLE catalog includes all GNSS satellites (active or inactive, see [www.space-track.org](http://www.space-track.org)).

Satellites with well known ephemerides may be used for the calibration and validation of optical observations. The sensitivity of the optical telescope has to be at the level of about 14-16 mag depending on the phase angle of the satellite, in order to observe GNSS satellites. The Space-Based Visible (SBV) telescope, a space-based sensor contributing to the U.S. SSN, tracks GPS satellites for the estimation of its sensor accuracy (Gaposchkin et al., 2000). The ESA (European Space Agency) space debris telescope at Tenerife, a 1 m telescope dedicated to space debris surveys (Schildknecht, 2007; Flury et al., 2000) makes also use of GPS satellites for calibration purposes.

At the Zimmerwald observatory there are two telescopes, ZIMLAT (Zimmerwald Laser Ranging and Astrometry Telescope) and ZimSMART (Zimmerwald Small Aperture Robotic Telescope), capable of tracking GNSS satellites for the calibration of the epoch registration biases and for the verification of the astrometric accuracy. ZIMLAT (see Fig. 3.11) is a 1 m telescope designed as a multi-purpose instrument that may be used to perform SLR observations to artificial satellites as well as astrometric observations using CCD detectors. The astrometric observations of ZIMLAT are primarily acquired to maintain the orbits of faint space debris objects (Flohrer et al., 2007; Schildknecht et al., 1999). Within the scope of this work astrometric observations of GNSS satellites were acquired covering about four years.

Using ZIMLAT's  $f/4$  focal station the effective field of view (FoV) on the CCD detectors is about  $20' \times 20'$ . Since November 2004, a CCD camera from Astrocam with E2V42-40 CCD



Figure 3.11: The 1 m telescope ZIMLAT at the Zimmerwald Observatory

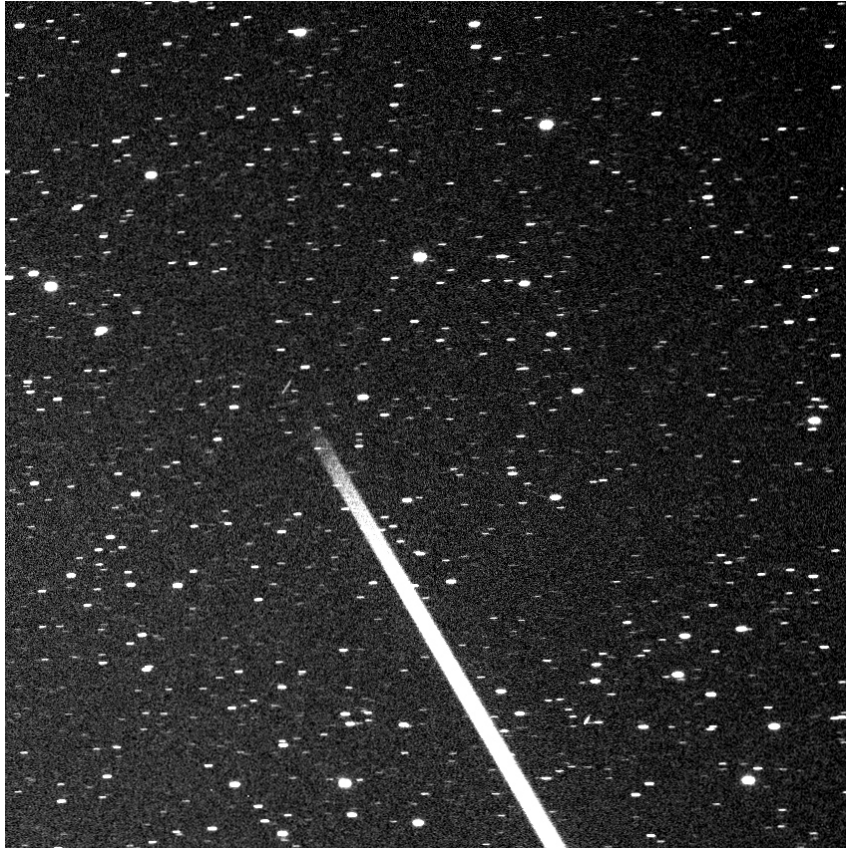


Figure 3.12: CCD exposure of a GNSS satellite, which is tracked by laser, acquired with ZimSMART; the prominent white line is the laser beam generated by ZIMLAT, at the upper end of the beam is a small streak visible that is the laser-tracked GNSS satellite

chips has been used. Its predecessor was the Photometrics camera equipped with a PM1024B CCD chip. The PM1042B consists of  $1024 \times 1024$  pixels, which have a size of  $24\mu \times 24\mu$  each. The E2V42-40 CCD is an array of  $2048 \times 2048$  pixels of  $13.5\mu \times 13.5\mu$ . In the case of the Astrocam camera pixel binning (combination of pixels) is applied during readout, which reduces the effective number of pixels to  $1024 \times 1024$ .

Since 2006 ZimSMART is operational and used to monitor objects in high-altitude regions. Figure 3.12 shows a very interesting exposure acquired with ZimSMART illustrating both, SLR tracking (ZIMLAT) and astrometric observation (ZimSMART) of a GNSS satellite at the Zimmerwald Observatory. The satellite is indicated by the small narrow line at the upper end of the laser beam. The exposure was, as a matter of fact, not intended to track the GNSS satellites, but to search for an object in the geostationary orbit region. Therefore, the satellite as well as the reference stars are mapped as streaks. When observing GNSS satellites, ZIMLAT tracks the satellite. Then the satellite appears as a point and the reference stars as streaks on the CCD frame.

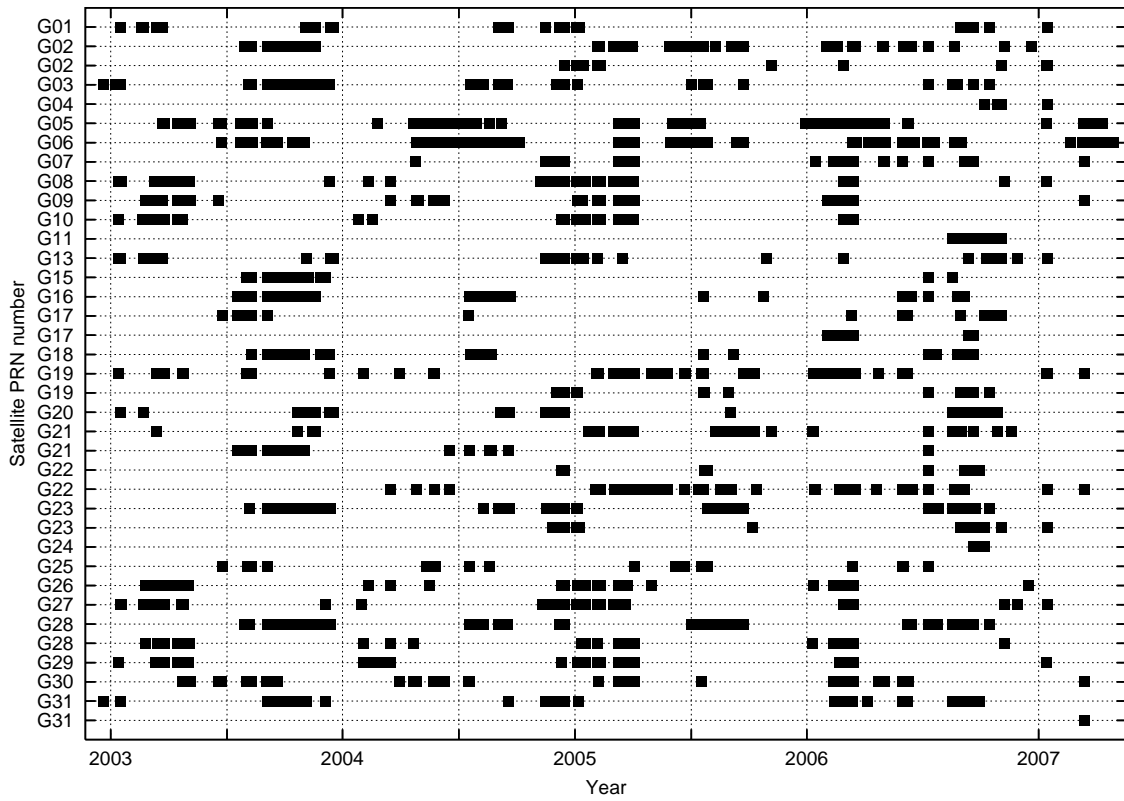


Figure 3.13: CCD observations of GPS satellites

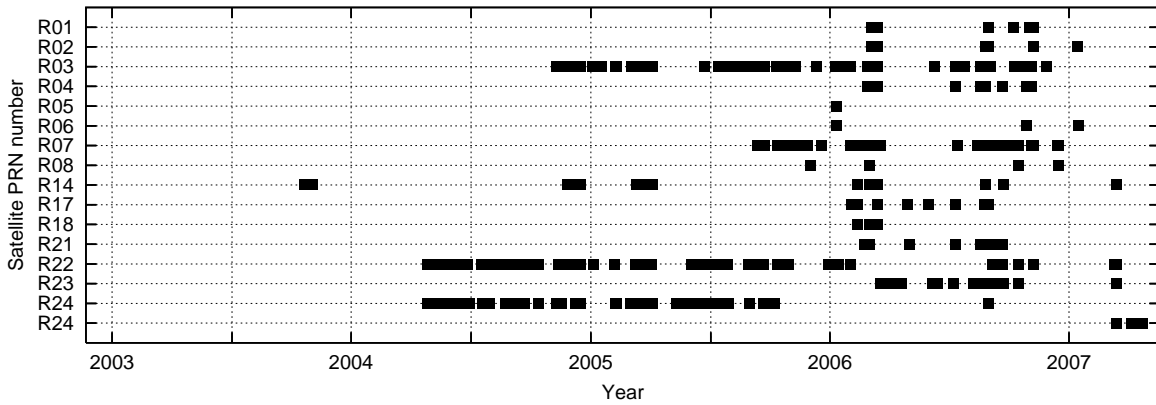


Figure 3.14: CCD observations of GLONASS satellites

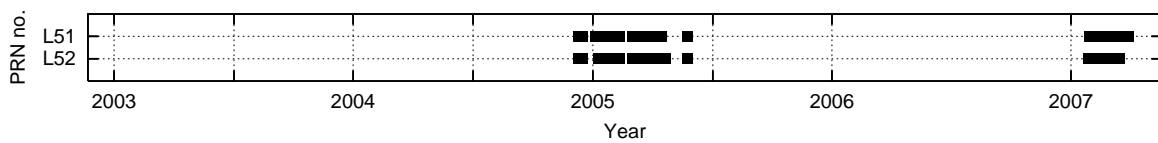


Figure 3.15: CCD observations of the two LAGEOS satellites

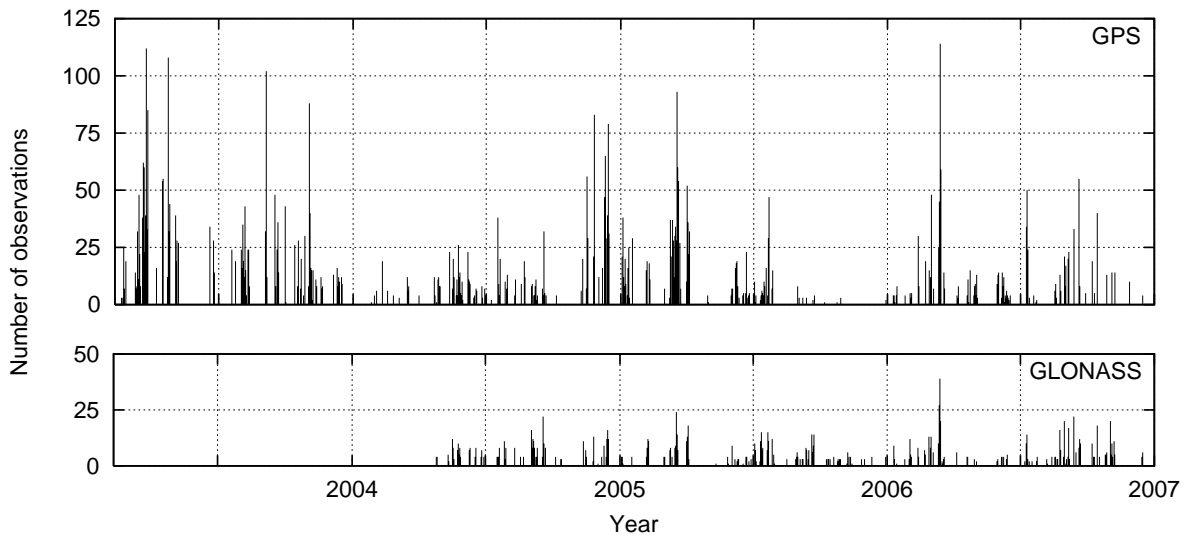


Figure 3.16: Number of CCD observations of GNSS satellites

### Astrometric CCD Observations Acquired at the Zimmerwald Observatory

Figures 3.13-3.15 show the distribution of CCD observations from 2003 to 2007 for the GPS, GLONASS, and LAGEOS satellites. The satellites are labeled by the identification used in the RINEX format. If a satellite of a GNSS constellation is replaced by a new one, both satellites may get the same number. Therefore a doubling of numbers, as, e.g., visible in the GPS observation plot (Fig. 3.13), is possible.

Figure 3.16 provides the number of observations as a function of time. It shows large variation, as the number of observations depends on the available observation time, which is limited by weather conditions and the length of the night, by the (quasi-simultaneous) acquisition of SLR observations, and by the GNSS campaign priority. The time interval chosen (day of year (DoY): 040/2003 - 365/2006) is the time interval used for the validation of the CCD observations using microwave-based GNSS orbits (see Sec. 4.1).

## 3.4 SLR Observations of GNSS Satellites

SLR observations of GNSS satellites are provided by the International Laser Ranging Service (ILRS) for a subset of those satellites carrying LRAs. GNSS orbit determination based on SLR data is quite possible, but those SLR-based orbits do not reach the accuracy of pure microwave-based orbits, due to the sparse tracking network and the comparably low number and uneven distribution of observations. For the validation of GNSS orbits the SLR data are, however, very useful. This section introduces the ILRS activities related to GNSS tracking. The orbit validation method and validation results are reported in Chapter 4.2.

### The ILRS Support for GNSS Satellites

The ILRS is one of the space geodetic services of the IAG. One of its main objectives is to support geodetic and geophysical research activities through satellite laser ranging data (Gurtner et al., 2004). Since 1993 and 1994 the two GPS satellites G05 and G06, equipped with LRAs, are routinely tracked by the ILRS network, in order to provide independent, high-precision measurements of satellite positions (Degnan and Pavlis, 1994).

The ILRS support for GLONASS satellites started in the early 1990's. Up to now, SLR data have been obtained of more than 25 different GLONASS satellites. In October 1998 the ILRS support of the International GLONASS EXperiment (IGEX-98) started and was scheduled for three months (and a five months extension). IGEX-98 was the first global GLONASS observation campaign for geodetic and geodynamics applications. It was followed by the International GLONASS Service (IGLOS), a service of the IGS to track and analyze data of the GLONASS constellation. In May 1999 the ILRS decided to continue its support of IGLOS "indefinitely", but the number of GLONASS satellites observed by the ILRS was reduced from nine to three. Currently, three of the GLONASS satellites (R07, R15, R24) are tracked in support of IGLOS.

Today, the ILRS tracking network consists of about 40 sites, of which about 15 are tracking the GNSS satellites routinely, including a number of 11 ILRS core sites. Figure 3.17 shows the geographical distribution of the SLR sites tracking GNSS satellites. Unfortunately, most of the sites are on the Northern hemisphere. The number of observations greatly varies from station to station, as the SLR systems but also the weather conditions are very different. Stations in dry regions (e.g., in Australia) may have a much better performance than others. SLR sites indicated by black triangles in Fig. 3.17 have a very good performance in tracking GPS as well as GLONASS satellites. Sites with gray triangles are mostly tracking GLONASS satellites, whereas white triangles indicate stations with very few GNSS observations.

Figure 3.18 shows the total number of SLR observations per day for GPS and GLONASS satellites separately. These numbers refer to the time interval used for the validation of the microwave-based GNSS orbits (DoY: 040/2003-365/2006) and only for the SLR sites marked with black and gray triangles. The SLR station ID is the so-called Crustal Dynamics Project

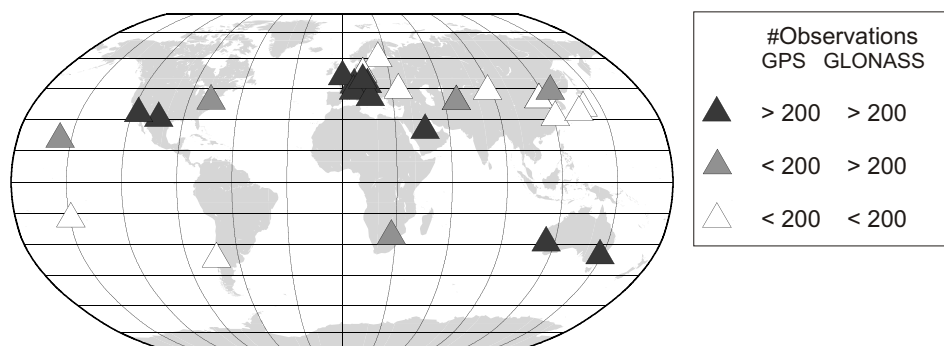


Figure 3.17: Global distribution of the SLR stations that observe GNSS satellites

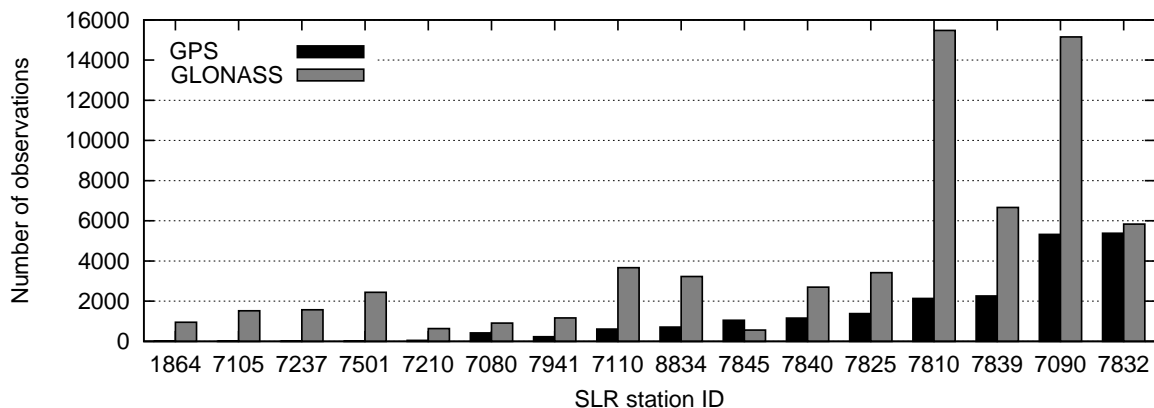


Figure 3.18: Number of SLR observations for each SLR station observing GNSS satellites (with more than 200 observation within the analyzed time interval of four years (DoY: 040/2003-365/2006))

(CDP) number, a 4-digit code. The corresponding site locations can be found in the SLR site listing in Table A.3, given in the Appendix A. The station ID 7810 corresponds to the observatory in Zimmerwald. It is one of the ILRS core sites and shows a very good performance with more than 15 000 observations of GNSS satellites within four years.

Figure 3.19 shows the number of SLR observations for GNSS satellites of all SLR sites as a function of time. As most SLR systems can track the GNSS satellites only during the night, the SLR observation statistic has a daily period. The size of the LRAs impacts the SLR measurement. For larger arrays the number of successful laser range measurements, but also their scatter, is higher. GPS satellites are equipped with LRAs of 32 corner cubes arranged in a flat panel of  $19 \times 24$  cm. The LRAs on the GLONASS satellites are larger; 132 corner cubes are

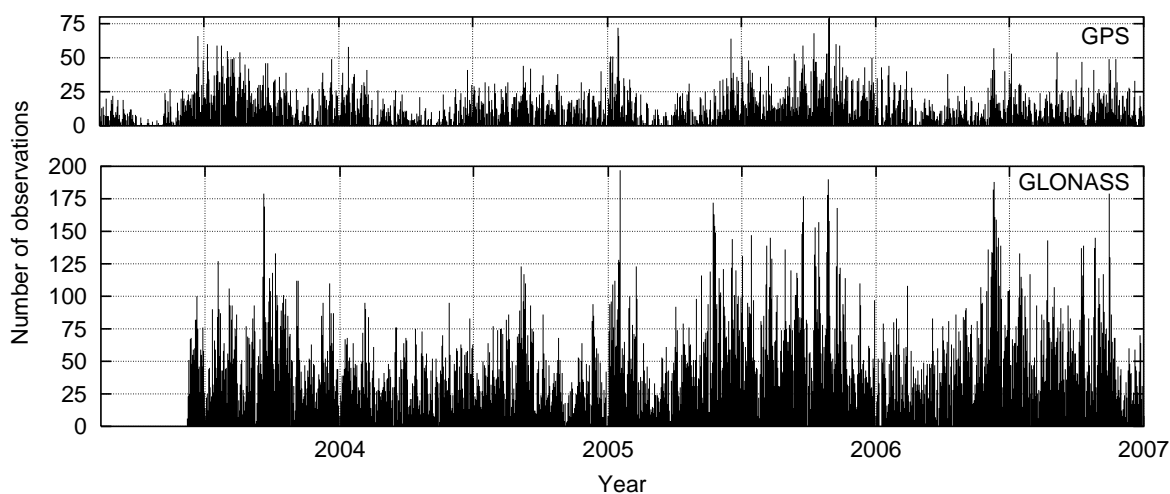


Figure 3.19: Number of SLR observations of GNSS satellites

mounted on a circular area of 66 cm diameter (ILRS, 2008). Therefore, the GLONASS satellites are much easier to track and consequently the number of SLR observations of GLONASS satellites is higher than that of GPS satellites. But a larger scatter of the range measurements is expected for GLONASS. In addition, if multi-photon laser measurements are used, the satellite signature may cause a maximum range bias of 8 cm for GLONASS satellites at low elevation.

SLR observations (normal points) of GNSS satellites are formed by averaging the differences of the individual range measurements to an a priori orbit over 5-min intervals. On a daily average, only 5 to 20 normal points for each GPS satellite and about 10 to 40 normal points for each GLONASS satellite are available.

For satellite tracking, CPF prediction files are used by the SLR stations. The CPF files for GNSS satellites are provided by the CODE AC, and based on the orbit predictions derived from microwave data. The accuracy of the predicted orbits is about 20 – 50 cm for the first prediction day. If CODE orbit predictions are not available due to, e.g., microwave tracking problems, SLR-based predictions from the Honeywell Technical Services, Inc. (HTSI) may be used instead.



## 4. Mutual Validation of the Different Satellite-Geodetic Techniques

This chapter presents the mutual validation of three satellite-geodetic techniques: GNSS, SLR, and optical astrometry using CCDs. First, we validate the astrometric observation technique by comparing the astrometric observations of GNSS or Laser satellites, acquired at the observatory in Zimmerwald, with the satellite orbits estimated either from GNSS or SLR data. This method allows the calibration of the optical observation system and the validation of the processed data. The accuracy of astrometric observations for GNSS or Laser satellites can be assessed.

Furthermore, we validate GNSS orbits based on microwave-phase observations by using SLR range measurements. The analysis of the resulting residuals allows the assessment of the GNSS orbit accuracy in radial direction, as well as the detection of systematic errors in the GNSS and/or SLR observation technique.

All computations have been performed using a development version of the Bernese GPS Software (Dach et al., 2007).

### 4.1 Validating the Astrometric Observation Technique

The directions given by the astrometric CCD observations of GNSS satellites are compared with the directions derived from microwave-based GNSS orbits. We use astrometric observations acquired with ZIMLAT at the Zimmerwald Observatory during four years (2003-2006). This data set is presented in Sect. 3.3. The microwave-based orbits are three-day arcs generated with the CODE orbit model (see Sect. 3.2.2).

In addition SLR-based orbits of the two LASER GEODynamics Satellites LAGEOS-1 and LAGEOS-2 are used for the validation of the astrometric CCD observations. Both satellites are aluminium-covered brass spheres with a diameter of 60 cm and a mass of about 400 kg, entirely covered with 462 retroreflectors (see Fig. 4.1). They orbit at an altitude of 5900 km and 5600 km, respectively. The inclination of the two orbital planes is  $109.8^\circ$  for LAGEOS-1 and  $52.6^\circ$  for LAGEOS-2. We use LAGEOS SLR-based orbits with an arc length of seven days, provided by DGFI (Deutsches Geodätisches Forschungsinstitut, Munich, Germany).



Figure 4.1: Illustration of the LAGEOS-1 sphere with its retroreflectors

### 4.1.1 Validation Procedure for Astrometric Observations

In order to compare an astrometric direction to a satellite with the direction derived from a microwave-based or SLR-based orbit, both directions have to be given in the same reference frame. The astrometric CCD observations are topocentric directions, given in the polar coordinates right ascension  $\alpha_{CCD}$  and declination  $\delta_{CCD}$ , and refer to the celestial reference system (CRS) of the mean equator and equinox J2000.0. This CRS is a local inertial system moving with the Earth's geocenter.

As a matter of fact, the topocentric directions to the satellite are measured in a celestial reference frame (CRF), i.e., a realization of the CRS defined by the set of used reference stars (the star catalog). The positions of the reference stars given by the catalog have to be transformed into the detector coordinate system. First, corrections for proper motion, precession, nutation, annual and diurnal aberration, and refraction are applied. Using these corrected star positions the transformation parameters, describing the mapping model (which maps the detector coordinate system to the celestial sphere, see Sect. 3.3), are estimated. The position of the satellite can now be determined with respect to the reference star positions in the detector coordinate system. In order to transform the satellite position into the CRS, corrections for refraction, diurnal aberration, nutation, and precession are applied again. Thus the resulting topocentric astrometric directions of the satellite are already corrected for annual aberration effects.

We developed a FORTRAN program named ORBTRA in the environment of the Bernese GPS Software to compute the residuals in right ascension and in declination between the astrometric directions from a topocentric observer to a satellite and the corresponding directions derived from the microwave-based or SLR-based orbits. The program ORBTRA performs the necessary transformations.

Table 4.1 gives the corresponding procedure of transformations and corrections, which are applied to the Cartesian coordinates  $\mathbf{X}_{ORB}$  (indicated by ↓) and to the astrometric directions  $\alpha_{CCD}, \delta_{CCD}$  (indicated by ↑). The coordinates  $\mathbf{X}_{ORB}$  are the geocentric satellite position at observation time derived from the microwave-based or SLR-based orbit and defined in the ITRF. The numbers given in the first column refer to the following transformation and correction

CRD	Reference system	Observer	Correction	Transformation
$\mathbf{X}_{ORB}$	ITRF	geocentric		
↓ <sup>1</sup>				polar motion, UT1
	CRF – ToD	geocentric		
↓ <sup>2</sup>				nutations, precession
	CRF – J2000	geocentric		
↓ <sup>3</sup>			geocentric parallax	
↓ <sup>4</sup>			correction for light time	
★	CRF – J2000	topocentric		
↑ <sup>5</sup>			parallactic refraction	
$\alpha, \delta_{CCD}$	CRF – J2000	topocentric		

Table 4.1: Procedure of coordinate transformations and corrections for the validation of the astrometric observation technique in program ORBTRA

steps. Steps 1-4 are applied to the geocentric position  $\mathbf{X}_{ORB}$ , whereas step 5 is applied to the astrometric directions  $\alpha_{CCD}, \delta_{CCD}$ :

1. Polar motion and Earth rotation (see Sect. 2.3.3) are applied to transform the coordinates from the ITRF into the GCRF of true system of date (ToD), i.e., the system of true equator and equinox at observation epoch.
2. Nutation and precession are applied according to Eq. (2.48), to transform the coordinates from ToD into the mean system J2000.0 (i.e., referring to the mean equator and equinox J2000.0).
3. The geocentric parallax is applied to transform the geocentric coordinates to the topocenter by

$$\mathbf{X}_{ORB}^* = \mathbf{X}_{ORB} - \mathbf{X}_{STA} \quad (4.1)$$

where the site coordinates of the observing telescope  $\mathbf{X}_{STA}$  were also transformed from the ITRF into the GCRF using the transformation steps 1 and 2.

4. The correction for light-time is applied by

$$\mathbf{X}_{ORB}^{**} = \mathbf{X}_{ORB}^* - \dot{\mathbf{X}}_{ORB}^* \frac{r}{c} \quad (4.2)$$

where  $r$  ... Topocentric distance of the satellite  
 $c$  ... Speed of light.

This correction takes into account the time  $\Delta t$  required for the light to travel from the object to the observer. The measured position therefore corresponds to the position of the object at time  $t - \Delta t$  and the observer at time  $t$ , where  $t$  is the epoch of measurement.

5. The parallactic refraction correction  $\Delta\gamma$  (see Sect. 2.4.2) is applied to the observed zenith distance  $z$ , which is derived from the astrometric direction. This correction has to be taken into account for objects at distances  $\rho \lesssim 10^5$  km. Assuming a satellite with height  $h \ll r$  and a standard atmosphere, the parallactic refraction correction (in radians) may be approximated, according to Schildknecht (1994) by

$$\Delta\gamma = -\frac{2.34 \tan z}{h \cos z}, \quad (4.3)$$

where  $h$  is given in meters. It is, of course, also possible to apply the parallactic refraction correction (with opposite sign) to the satellite position derived from the orbit.

At point  $\star$  in Tab. 4.1 both coordinate sets refer to the same system. The Cartesian coordinates  $\mathbf{X}_{ORB}^{**}$  are then transformed into polar coordinates  $\alpha_{ORB}, \delta_{ORB}$ . The CCD residuals  $\Delta\alpha^*, \Delta\delta$  are computed as

$$\Delta\alpha^* \doteq (\alpha_{CCD} - \alpha_{ORB}) \cos \delta = \Delta\alpha \cos \delta \quad (4.4)$$

$$\Delta\delta \doteq \delta_{CCD} - \delta_{ORB}. \quad (4.5)$$

Figure 4.2 shows the resulting residuals. For  $\Delta\alpha^*$  the differences in right ascension  $\Delta\alpha$  have to be multiplied with  $\cos \delta$ , assuming that  $\Delta\delta$  is small and that the observations do not occur close to the celestial pole. For ZIMLAT at Zimmerwald the maximum possible declination  $\delta$  of GNSS satellites is about  $72^\circ$ .

For test purposes it is possible to introduce a time bias in program ORBTTRA, which is added to the CCD observation epoch. In addition to the computation of residuals, ORBTTRA may also be used to transform Cartesian coordinates derived from orbit positions into astrometric directions.

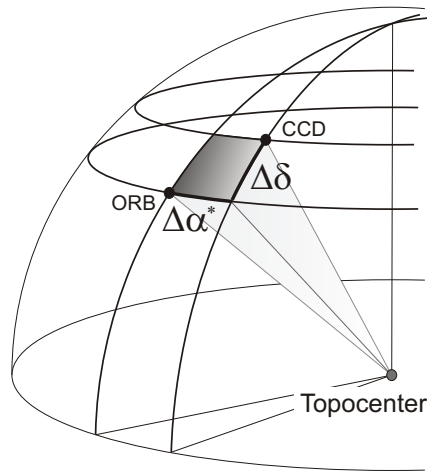


Figure 4.2: Validation method for the astrometric observation technique

### 4.1.2 Validation Results for Astrometric Observations Using Microwave-based GNSS Orbits

With the validation procedure outlined in Sect. 4.1.1 we generated two time series of CCD residuals  $\Delta\alpha^*$  and  $\Delta\delta$  over a time interval of about four years (DoY: 40/2003 - 365/2006) for GPS and GLONASS satellites. The data set is described in detail in Sect. 3.3. Altogether about 7300 observations are available within this time interval. Figure 4.3 shows the residuals (in arcseconds) as a function of time. Outliers due to object misidentifications have been removed previously. Misidentifications may be caused, e.g., by star occultation, when the object image partly coincides with a star, or by reflection effects within the optical components of the telescope.

A significant offset in the  $\Delta\alpha^*$  residuals and a significant change in the scattering of the  $\Delta\delta$  residuals is noticeable in November 2004. Both effects can be traced back to a problem at the epoch registration. A time bias will produce such an offset in right ascension, as the GNSS satellites are always moving in positive direction of right ascension, whereas in declination different

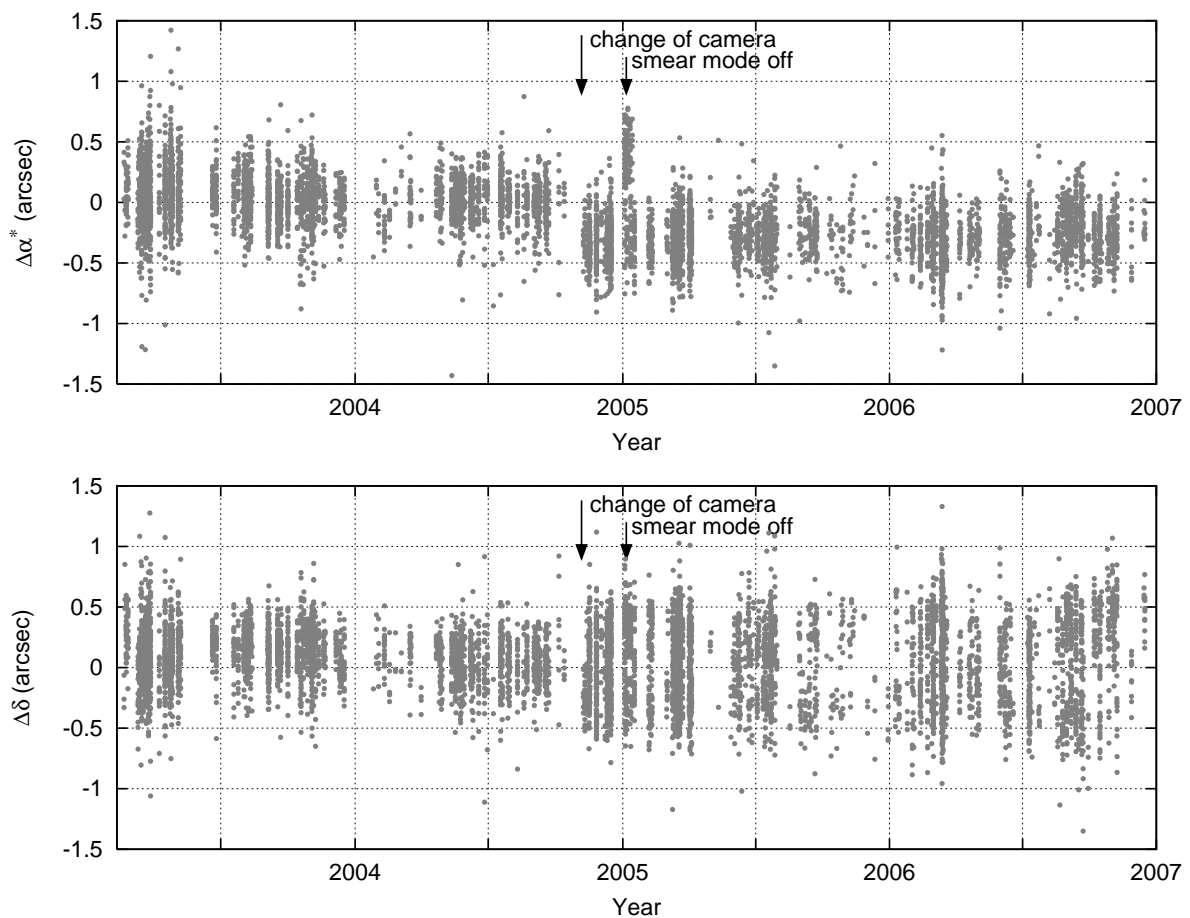


Figure 4.3: Raw CCD residuals  $\Delta\alpha^*$  and  $\Delta\delta$  for the GNSS satellites as a function of time

directions of movement are possible, in positive direction before the culmination and in negative direction after the culmination (in the  $(\alpha, \delta)$  system). A time bias thus increases the scattering of the residuals in declination. In addition, a time bias is always clearly reflected in the residuals in along-track direction, which will show a constant offset, whereas the out-of-plane residuals should not show any biases.

Figure 4.4 shows both series of residuals (in along-track and out-of-plane) as a function of time. The points in dark gray correspond to the observation, which are not affected by any time biases, whereas the black dots correspond to the observations affected by a time bias. The mean value of the along-track residuals is about 41 meters, corresponding to a time bias of  $-0.01$  seconds. We found this time bias of  $-0.01$  seconds starting from DoY 313/2004 for the presented time series of residuals. The problem is correlated in time with the change of the camera and the

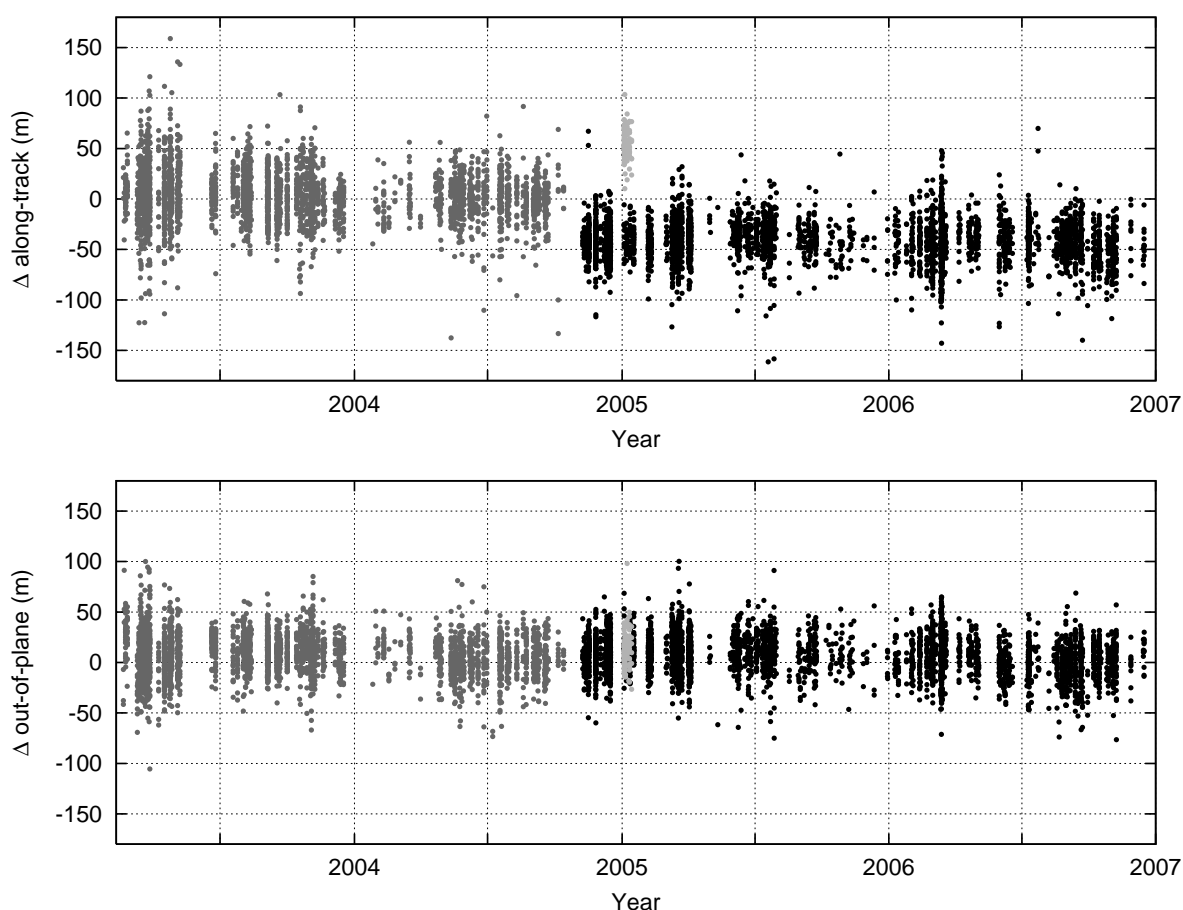


Figure 4.4: CCD residuals in along-track and out-of-plane direction for the GNSS satellites as a function of time; gray dots indicate residuals without any time bias; black dots indicate residuals with negative time bias (negative mean value in along-track direction) due to camera change; light gray dots indicate residuals with positive time bias (positive mean value in along-track direction) due to smear mode problems

CCD chip (see Sec. 3.3) and the corresponding change in the epoch registration technique for ZIMLAT in November 2004. Indeed the problem was detected in the electronics of the epoch registration of the new camera in December 2007. A determined correction of  $-0.0084$  seconds has to be applied to all observation epochs. This value corresponds nicely to the time bias found in our analysis.

In addition there was a known problem with the smear mode for some observations acquired in January 2005. The smear mode is a built-in function of the CCD camera used at that time and allows small row shifts of the register at start and end of each exposure, indicating start and end epochs with small streaks at the exposure (see Schildknecht, 1994). For the time intervals where the smear mode was erroneously turned off, we found a time offset of 0.015 seconds. It is also clearly visible in the along-track residuals (see Fig. 4.4) indicated by the light gray dots.

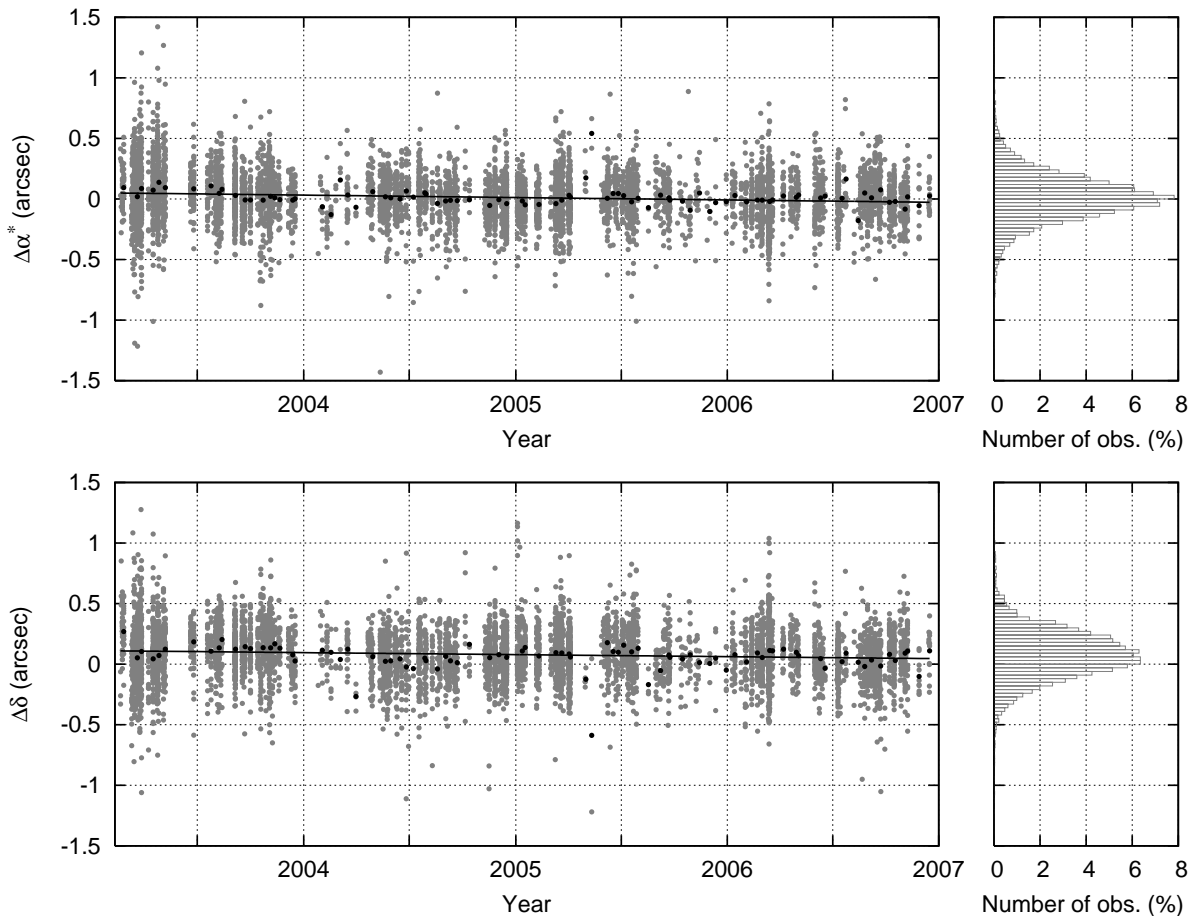


Figure 4.5: CCD residuals  $\Delta\alpha^*$  and  $\Delta\delta$  for the GNSS satellites as a function of time corrected for time biases due to camera change and smear mode problems; mean values over ten day intervals (black dots); regression line (black line); the distribution of the residuals is shown in the histogram

Both estimated time offsets due to camera change and the smear mode problem were added to the epoch of the CCD observations for the further validation. The recomputed residuals are shown in Fig. 4.5 as a function of time. The statistical information of the residual series is summarized in Table 4.2. The first column specifies the considered residuals (as a function of a specific parameter, as, e.g., time  $t$ ). The standard deviation  $\sigma$  is given in the second column, the mean value  $\bar{x}$  with its formal error in the third column. The slope  $m$  of the regression line, which is derived by least squares adjustment from the single residual values, is specified in the fourth column. All values are given in arcseconds. Column five lists the approximate number of CCD residuals #res. The last column provides the figure numbers with the corresponding residual series.

The standard deviations of both series of residuals  $\Delta\alpha^*$  and  $\Delta\delta$  decrease from  $0.3''$  (for the uncorrected residuals) to about  $0.2''$  (for the residuals corrected for time offsets). Also the mean values decrease to about  $0.02''$  and  $0.08''$  for  $\Delta\alpha^*$  and  $\Delta\delta$ , respectively. The black dots in Fig. 4.5 represent mean values of the residuals over time intervals of ten days. The black horizontal line is the regression line. There is no significant slope of the regression line for the CCD residuals as a function of time. The  $\Delta\alpha^*$  residuals are normally distributed, centered at a mean value of zero, which is shown by the histogram in Fig. 4.5. For  $\Delta\delta$  there is, however, an offset of about  $0.1''$ . Also, the histogram indicates that the  $\Delta\delta$  residuals are not normally distributed.

We try to understand this systematic behavior of the  $\Delta\delta$  residuals. First we check the residuals in elevation as a function of elevation, which would indicate an error in the applied refraction model. Such refraction errors might be reflected in the residuals in declination. Figure 4.6

Residuals	$\sigma (")$	$\bar{x} (")$	$m ("/\text{deg})$	#res	Fig.
$\Delta\alpha^*(t)$ uncorrected	0.268	$-0.132 \pm 0.003$		7300	4.3
$\Delta\delta(t)$ uncorrected	0.301	$0.058 \pm 0.004$		7300	4.3
$\Delta\alpha^*(t)$	0.198	$0.015 \pm 0.002$	0.000	7300	4.5
$\Delta\delta(t)$	0.208	$0.081 \pm 0.002$	0.000	7300	4.5
$\Delta e(e)$	0.213	$0.006 \pm 0.002$	0.000	7300	4.6
$\Delta\delta(a)$	0.208	$0.081 \pm 0.002$	0.000	7300	4.9
$\Delta\delta(e)$	0.208	$0.081 \pm 0.002$	0.003	7300	4.9
$\Delta\delta(\alpha)$	0.208	$0.081 \pm 0.002$	0.000	7300	4.9
$\Delta\delta(\delta)$	0.208	$0.081 \pm 0.002$	0.003	7300	4.9
$\Delta\delta(\delta)$ 100% USNO-B1.0	0.180	$0.172 \pm 0.004$	0.002	2570	4.12
$\Delta\delta(\delta)$ 100% UCAC2	0.184	$-0.002 \pm 0.007$	0.000	640	4.13
$\Delta\delta(\delta)$ $\geq 80\%$ UCAC2	0.177	$0.005 \pm 0.003$	0.001	3000	4.14

Table 4.2: Statistical information of the CCD residuals for the GNSS satellites: standard deviation  $\sigma$ , mean value  $\bar{x}$  with formal errors, slope of the regression line  $m$ , approximate number of CCD residuals #res; the last column specifies the corresponding figures

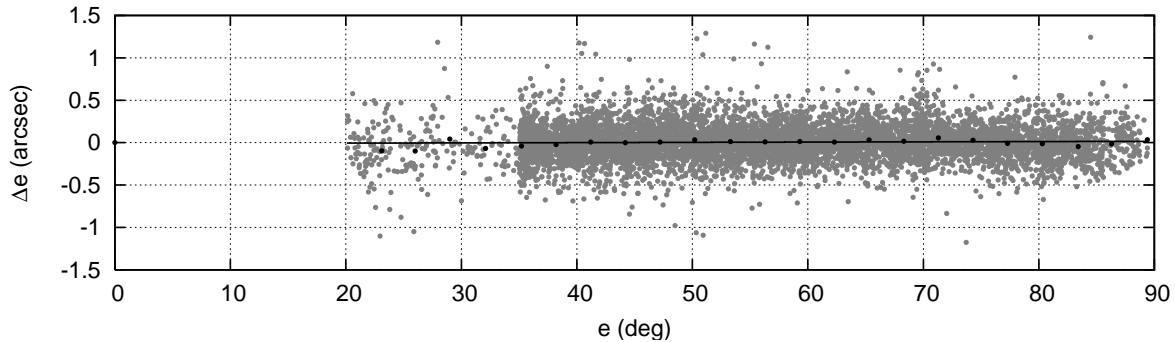


Figure 4.6: CCD residuals  $\Delta e$  for the GNSS satellites as a function of elevation  $e$ ; mean values over  $3^\circ$  intervals (black dots); regression line (black line)

shows the residuals in elevation  $\Delta e$  as a function of the elevation. There is no significant offset or pattern. The standard deviation of about  $0.2''$  is similar to that of the  $\Delta\alpha^*$  and  $\Delta\delta$  residuals. This leads to the conclusion that there are no significant systematic errors in the refraction modeling.

In order to explain the offset in the  $\Delta\delta$  residuals we examine now the  $\Delta\delta$  residuals as a function of azimuth  $a$ , elevation  $e$ , right ascension  $\alpha$ , and declination  $\delta$ . Therefore, we first have a look at the distribution of the observations in right ascension and declination and in azimuth and elevation.

Figure 4.7 gives the declination for each observation as a function of the right ascension. Observations of GPS satellites are represented by gray dots, those of GLONASS satellites by black dots. The differences in maximum declination are due to the different inclinations of the orbital planes of about  $55^\circ$  and  $64^\circ$ , respectively. For the GPS satellites we note a slight degrading of the maximum declination with increasing right ascension, which is due to small differences in the inclinations of the six orbital planes.

The two large areas without observations are due to restrictions set by the location of the Milky Way. No exposures were acquired for regions of galactic latitude  $|l| < 20^\circ$ , as in these regions the very large number of stars could likely cause that the object appears in front of a star and thus prevent the object identification.

The distribution of the observations in each coordinate is given by the histograms. Most of the observations are located at high declinations between  $50^\circ$ – $60^\circ$ . These observations at high declination map into right ascensions between 6–8 hours and 14–18 hours.

Figure 4.8 shows the elevation for each observation as a function of the azimuth and the corresponding histograms, giving the distribution of the observations. The regions of high declination correspond to ‘caustics’ in the azimuth-elevation plot. The caustics are at azimuths of about  $0^\circ$ – $60^\circ$  and about  $300^\circ$ – $360^\circ$ , and at elevations of  $40^\circ$ – $90^\circ$ .

Let us now check the residuals shown in the four subfigures of Fig. 4.9, which show the  $\Delta\delta$  residuals as a function of azimuth, elevation, right ascension, and declination, respectively. Mean

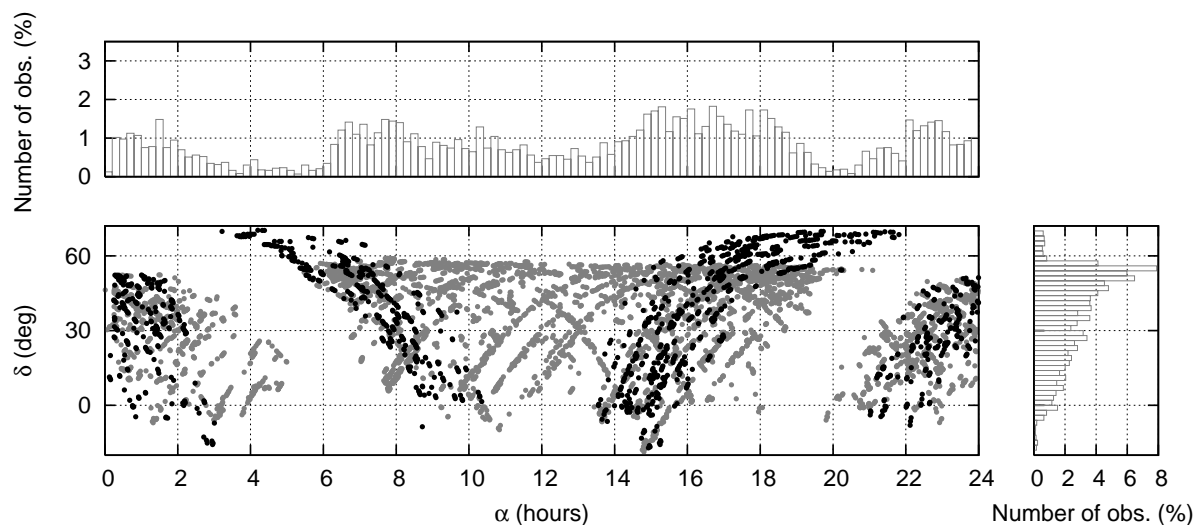


Figure 4.7: Distribution of the CCD observations for the GPS (in gray) and the GLONASS (in black) satellites in right ascension  $\alpha$  and declination  $\delta$ ; the distribution of the observations is shown in the histograms

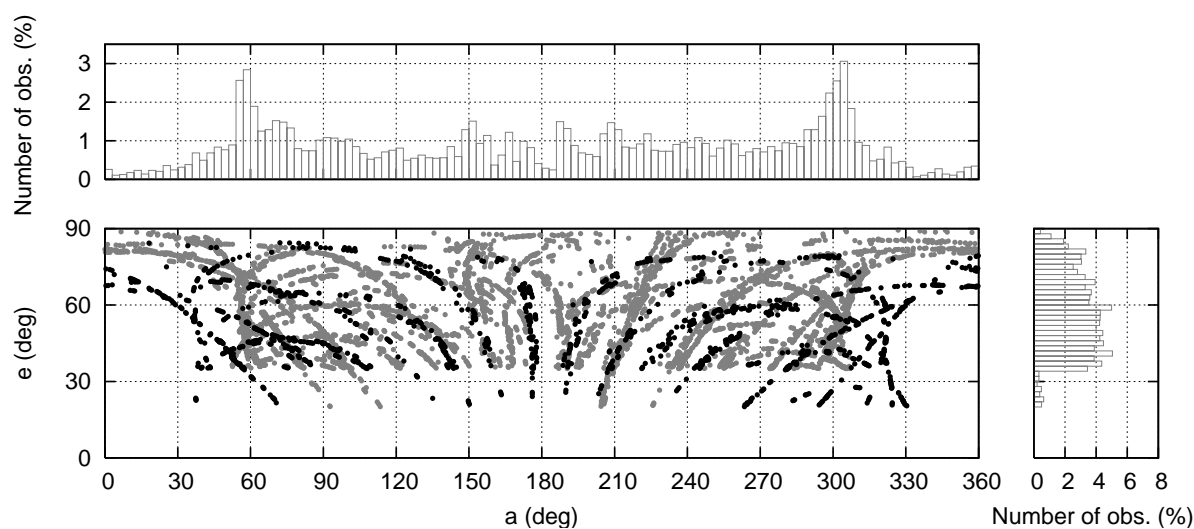


Figure 4.8: Distribution of the CCD observations for the GPS (in gray) and the GLONASS (in black) satellites in azimuth  $a$  and elevation  $e$ ; the distribution of the observations is shown in the histograms

values and regression lines are provided in addition. The corresponding statistical information is contained in Table 4.2.

The residuals in  $\delta$  as a function of the declination (fourth plot in Fig. 4.9) show a strong dependency on the declination. The slope of the regression line is about  $0.003''/\circ$ , which corresponds to  $0.27''/90^\circ$ . In addition, we see in all figures that significant positive mean values of the  $\Delta\delta$  residuals occur for high declinations ( $50^\circ-60^\circ$ ). In this region of high declination the largest

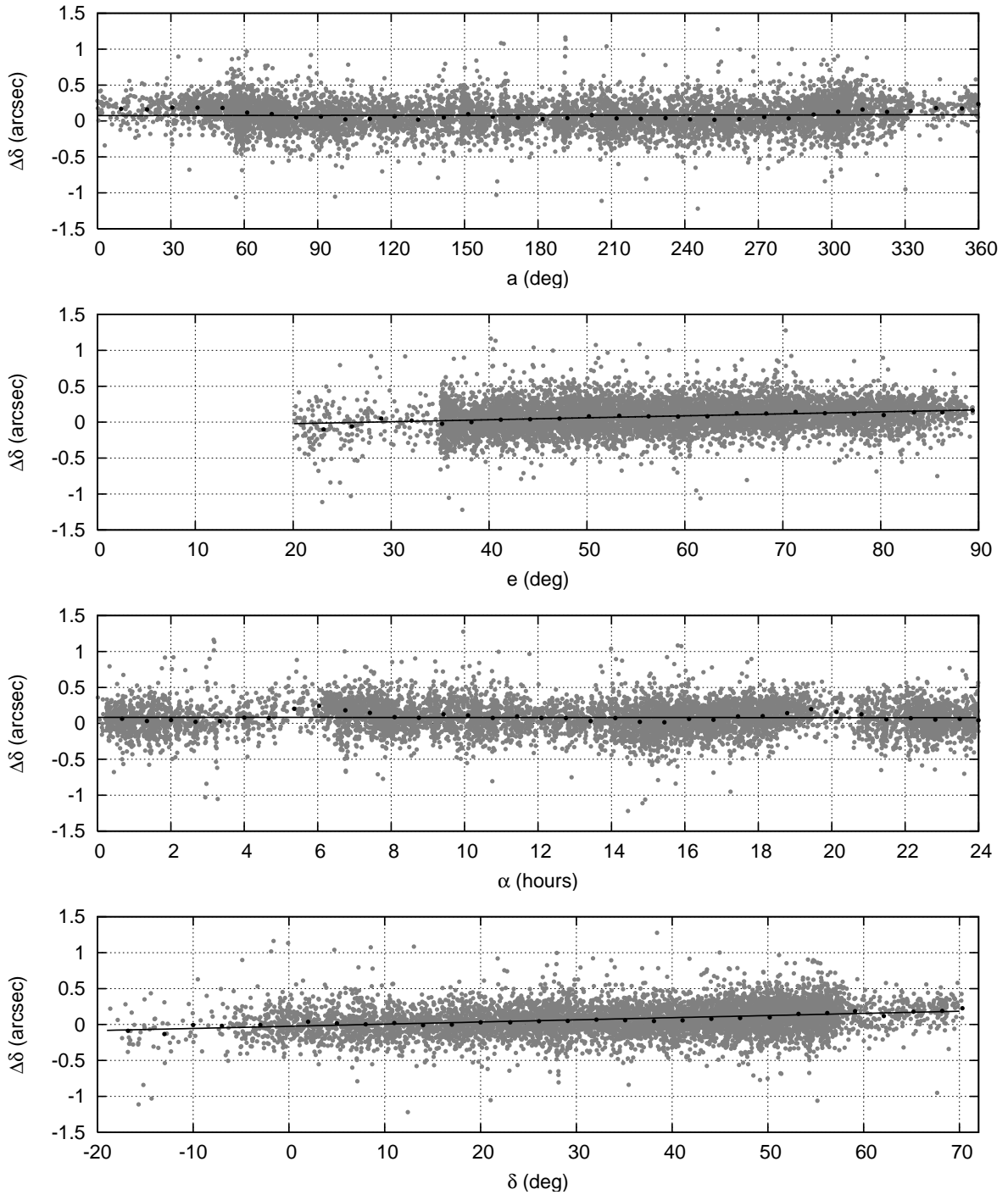


Figure 4.9: CCD residuals  $\Delta\delta$  for the GNSS satellites as a function of azimuth  $a$ , elevation  $e$ , right ascension  $\alpha$ , and declination  $\delta$ ; mean values over  $3^\circ$  (for  $a$  and  $\alpha$ ) and  $10^\circ$  (for  $e$  and  $\delta$ ) intervals (black dots); regression lines (black lines)

amount of observations were acquired, which map, as explained before, in different regions of right ascension, azimuth and elevation.

We now know that there is a systematic positive offset for  $\Delta\delta$  residuals corresponding to observations at high declinations. This dependency is reflected in the residuals  $\Delta\delta$  as a function of right ascension, declination, azimuth, and elevation. The strongest dependency is that on declination. A declination-specific effect is very unlikely caused by systematic orbit errors. Hence we concentrate on the analysis of the astrometric observations as other possible source. The corrections applied in the astrometric reduction process are not declination-specific. But the catalogs used for the reference star positions have different limits of their declination coverage.

Five different catalogs were used for the reference star positions: Hipparcos, Tycho2, UCAC2, USNO-B1.0, and GSC. The catalogs are listed in decreasing order of astrometric accuracy. The most accurate star positions and proper motions are provided by the Hipparcos catalog. As the star catalogs cover different areas of the celestial sphere with different spatial density and different magnitude ranges, a mixture of the five catalogs is used for processing each CCD exposure, where the catalog providing the highest accuracy is preferred. All reference star positions of an exposure are used with the same weight for the estimation of the transformation parameters, independently of the catalog accuracy.

Figure 4.10 shows the number of reference stars used for each exposure as a function of time. The number of Hipparcos reference stars is limited to 2–3. Also the number of Tycho2 reference stars is rather small with 10–20 for one CCD exposure. The GSC catalog was used only in 2003. It is not as accurate as the other catalogs, which explains the larger scattering of the CCD residuals in the first two quarters of 2003. Most reference star positions (up to 150) are taken from the UCAC2 catalog, which became available in July 2003. It covers the area  $-90^\circ \leq \delta \leq 40^\circ$ , going up to  $52^\circ$  in some areas (Zacharias et al., 2004). Its position accuracy at

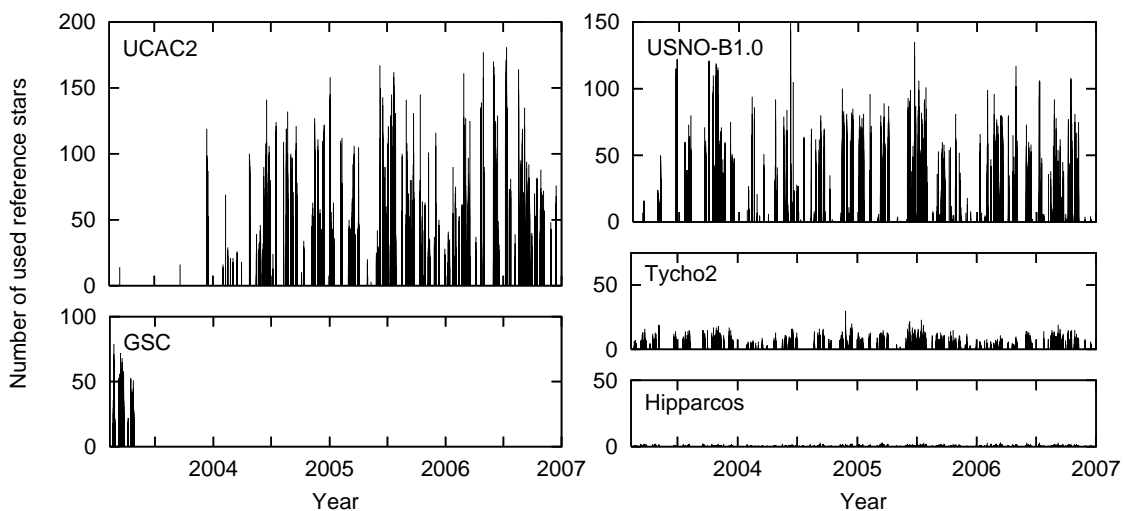


Figure 4.10: Number of reference stars used from the catalogs UCAC2, GSC, USNO-B1.0, Tycho2, and Hipparcos

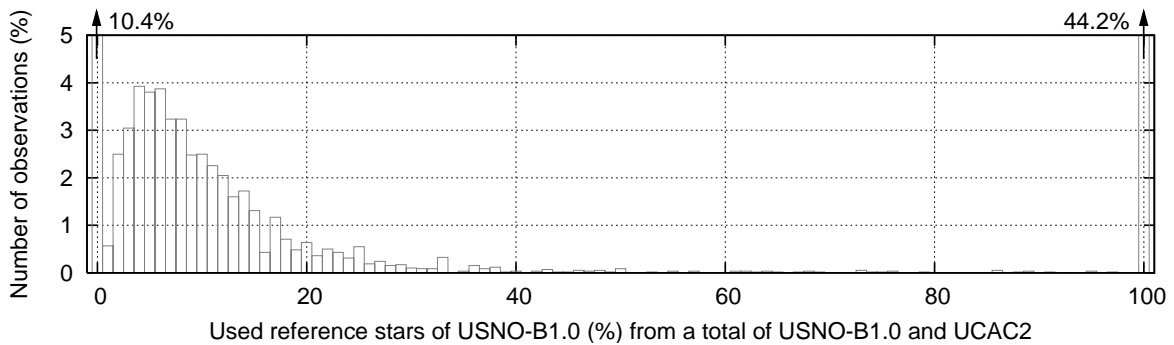


Figure 4.11: Number of observations (%) of GNSS satellites as a function of the usage of USNO-B1.0 reference stars (%) from a total of UNSO-B1.0 and UCAC reference stars

J2000 is  $0.015'' - 0.070''$ , depending on the star magnitude. But also USNO-B1.0 star position are frequently used with up to 100 positions per exposure. The position accuracy at J2000 of the USNO-B1.0 catalog is, however, limited to  $0.2''$  (Monet et al., 2003).

Let us now focus on the two most frequently used star catalogs UCAC2 and USNO-B1.0. The histogram in Fig. 4.11 shows the number of reference stars used from USNO-B1.0 (in percentage) from a total of UCAC2 and USNO-B1.0 reference stars. The other three catalogs are not considered. For about 44% of the CCD exposures the USNO-B1.0 catalog was used exclusively, whereas for about 10% of observations, the UCAC2 catalog was used exclusively. For the remaining 45% both catalogs were used, but the larger part of reference stars (up to 80%) was taken from the UCAC2 catalog. Thus the number of used reference stars is well separated, either the USNO-B1.0 catalog is used or the UCAC2 catalog together with a small percentage (up to 20%) of USNO-B1.0.

The residuals  $\Delta\delta$  corresponding to CCD observations generated with USNO-B1.0 reference star positions only are provided in Fig.4.12. The statistical information related to the residuals may be found in Table 4.2. The standard deviation of these residuals is  $0.18''$ . A significant offset in declination of about  $0.17''$  is seen.

Figure 4.13 shows the residuals  $\Delta\delta$  corresponding to observations, where only UCAC2 reference stars were used. The standard deviation is also about  $0.18''$ , but there is no offset in declination. The maximum declination for which only UCAC2 reference stars were used is about  $50^\circ$ , as the catalog coverage is restricted to  $\delta < 52^\circ$ . For higher declinations the USNO-B1.0 catalog is used exclusively. The large number of residuals in Fig. 4.12 between  $50^\circ$  and  $60^\circ$  is thus explained. Most of the observations occur in the declination area, where only the USNO-B1.0 catalog can be used. We may thus conclude that there is an offset in declination for CCD observations processed with USNO-B1.0 reference star positions.

In Fig. 4.13 (where only UCAC2 reference stars were used) only 10% of all CCD observations are included, which might limit the validity of our conclusions. Thus we include in Fig. 4.14 all observation, where 80 – 100% of UCAC2 reference stars were used, which corresponds to about 55% of all CCD observations. This figure does not reveal significant offsets, although a

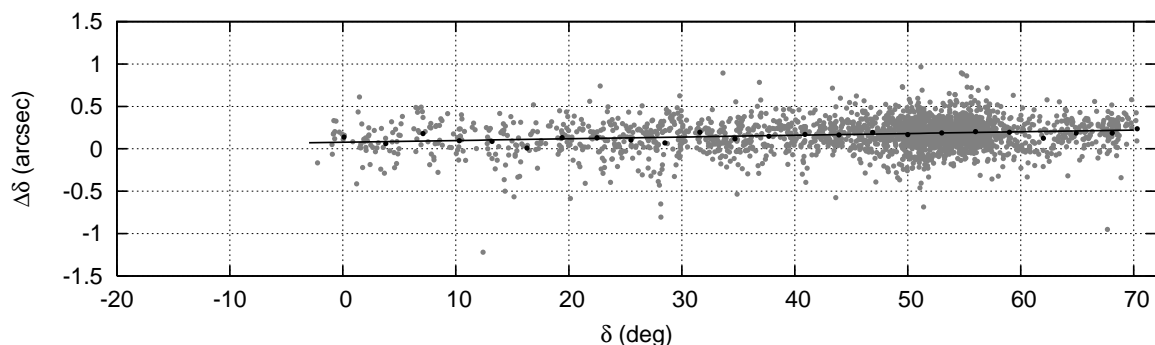


Figure 4.12: CCD residuals  $\Delta\delta$  for the GNSS satellites as a function of declination  $\delta$ ; all reference stars are from USNO-B1.0; mean values over  $3^\circ$  intervals (black dots); regression line (black line)

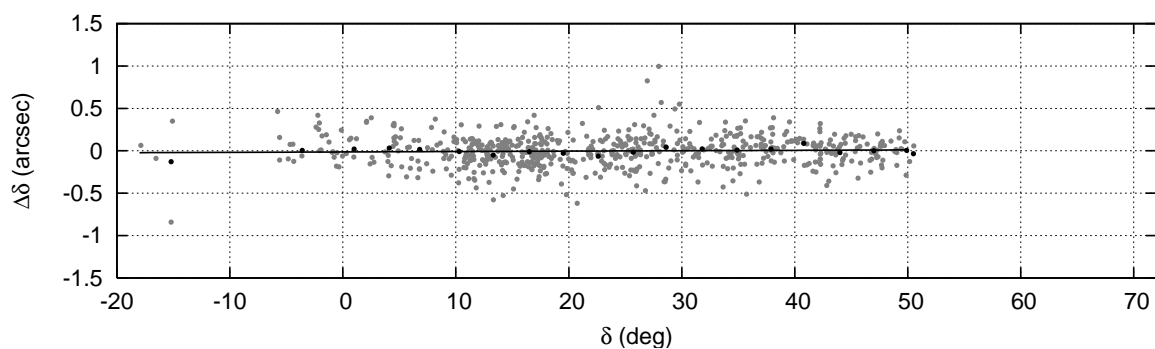


Figure 4.13: CCD residuals  $\Delta\delta$  for the GNSS satellites as a function of declination  $\delta$ ; all reference stars are from UCAC2; mean values over  $3^\circ$  intervals (black dots); regression line (black line)

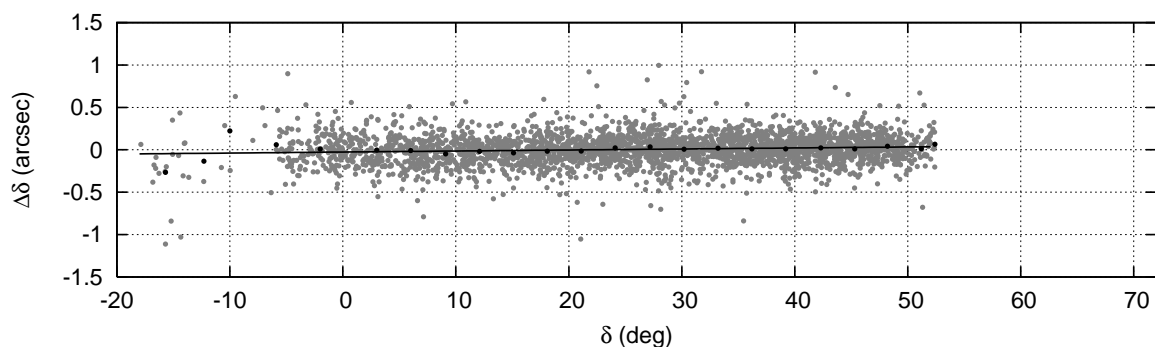


Figure 4.14: CCD residuals  $\Delta\delta$  for the GNSS satellites as a function of declination  $\delta$ ; more than 80% of the reference stars are from UCAC2 (from a total of USNO-B1.0 and UCAC2); mean values over  $3^\circ$  intervals (black dots); regression line (black line)

small systematic slope of the regression line is seen, which might be due to the up to 20% usage of USNO-B1.0 star positions.

In summary we conclude that there is an offset in declination of about  $0.17''$  related to USNO-B1.0 reference star positions. This offset was previously unknown. It is, however, within the specified position accuracy of  $0.2''$  given by Monet et al. (2003).

### 4.1.3 Validation Results for Astrometric Observations Using SLR-based Orbits

In order to validate the astrometric CCD observations, we may also use SLR orbits for the SLR satellites LAGEOS-1 and LAGEOS-2 and CCD observations of the two satellites. Seven-day SLR orbits produced by DGFI and CCD observations made by the ZIMLAT are used for this purpose. Due to the reduced height above the Earth surface and the larger orbital velocity (the apparent angular velocity is about  $30''/s$  for the GPS and about  $240''/s$  for the LAGEOS satellites) the apparent motion of the LAGEOS satellites is much larger than that of either GPS or GLONASS satellites. Therefore, LAGEOS-1 and LAGEOS-2 are well suited for the calibration of the epoch registration of the CCD observation system (time biases are expected to show larger values in the CCD residuals for LAGEOS compared to GNSS satellites). CCD observations of LAGEOS acquired with ZIMLAT are available for about 6 months in 2005. We expect to find the same time biases as those detected for the GNSS satellites.

Figure 4.15 shows the CCD residuals in right ascension  $\Delta\alpha^*$  and declination  $\Delta\delta$  for LAGEOS-1 (in gray) and LAGEOS-2 (in black) as a function of time. As expected both satellites show an offset in right ascension and a large scattering in declination indicating a time bias. The corresponding statistical information are summarized in Table 4.3. The standard deviation of the residuals is about  $1''$ . For LAGEOS-1 there is a positive mean value of about  $1''$ , and for LAGEOS-2 a negative mean value of about  $-1.4''$  in right ascension. The opposite signs result from the opposite crossing directions of the satellites with respect to the right ascension.

Figure 4.16 shows the distribution of the observations in right ascension and declination. In the observation period LAGEOS-1 moves from low to high right ascensions and declinations, whereas LAGEOS-2 moves from high to low right ascensions and declinations (indicated by

Residuals	$\sigma_{L1} (")$	$\bar{x}_{L1} (")$	$\sigma_{L2} (")$	$\bar{x}_{L2} (")$	Fig.
$\Delta\alpha^*(t)$ uncorrected	0.970	1.029	0.752	-1.400	4.15
$\Delta\delta(t)$ uncorrected	1.034	1.021	1.138	-0.329	4.15
$\Delta\alpha^*(t)$	0.271	0.010	0.263	0.023	4.17
$\Delta\delta(t)$	0.311	0.055	0.280	0.072	4.17

Table 4.3: Statistical information of the CCD residuals for LAGEOS-1 (L1) and LAGEOS-2 (L2): standard deviation  $\sigma$ , mean value  $\bar{x}$  with formal errors; the last column specifies the corresponding figures

#### 4 Mutual Validation of the Different Satellite-Geodetic Techniques

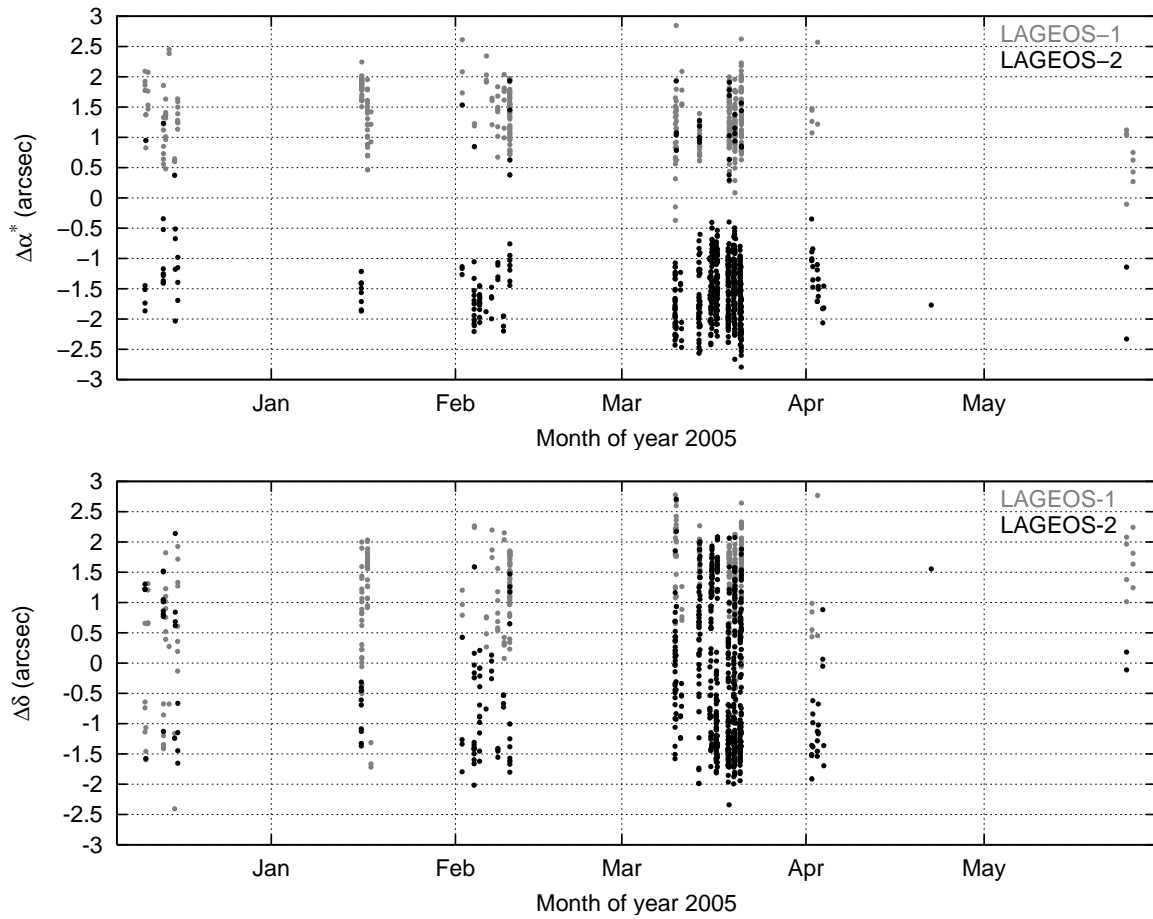


Figure 4.15: Raw CCD residuals  $\Delta\alpha^*$  and  $\Delta\delta$  for the LAGEOS satellites as a function of time

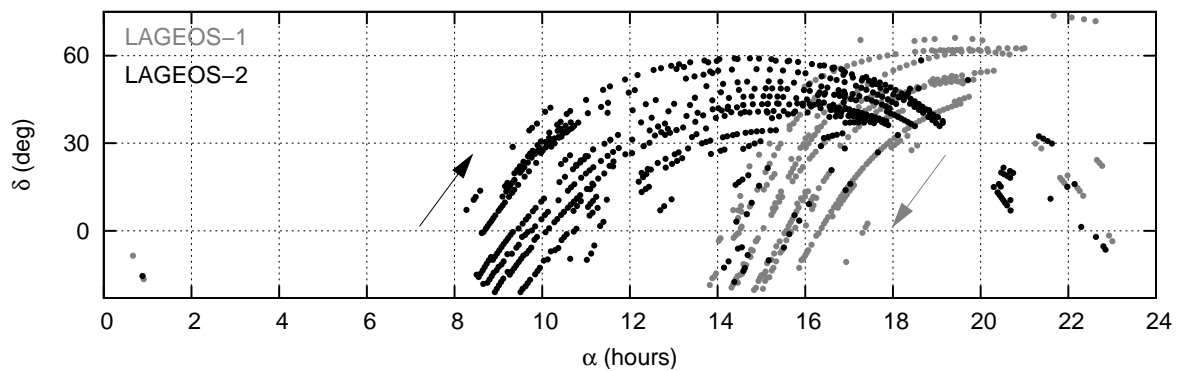


Figure 4.16: Distribution of the CCD observations for LAGEOS-1 and LAGEOS-2 satellites in  $\Delta\alpha^*$  and  $\Delta\delta$ ; the arrows indicate the direction of movement

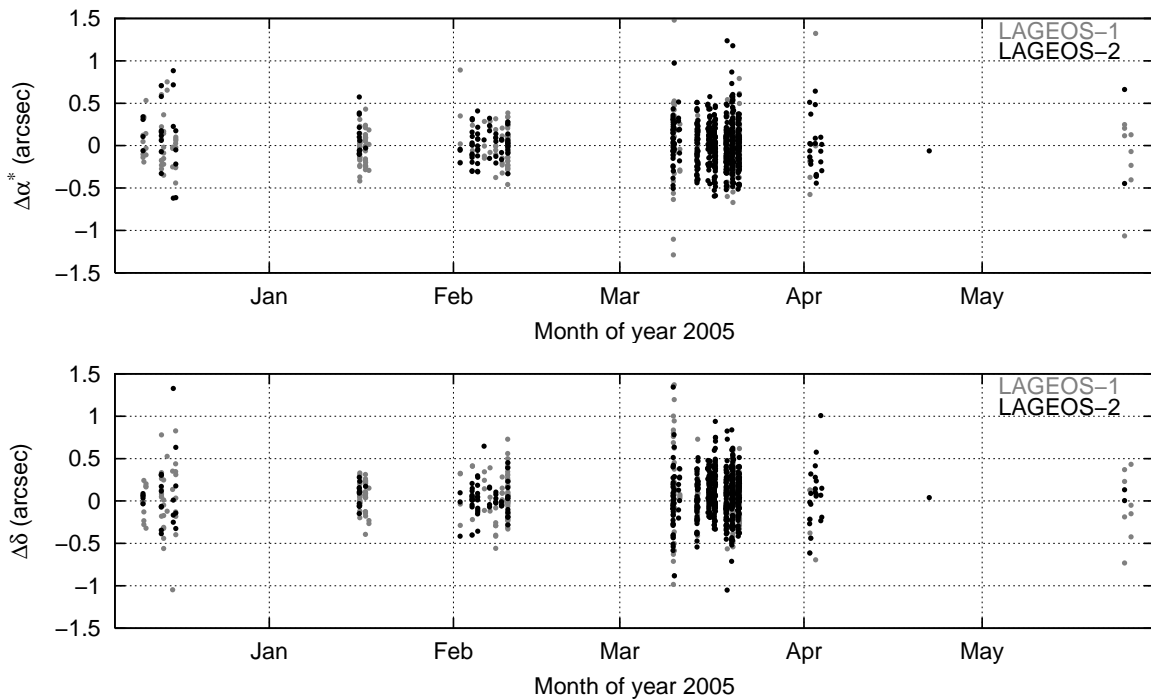


Figure 4.17: CCD residuals  $\Delta\alpha^*$  and  $\Delta\delta$  for the LAGEOS satellites as a function of time corrected for time bias due to camera change

the arrows in Fig. 4.16), due to the different inclination of the orbital planes. As only observations prior or after the culmination of the satellites are available, we also see a mean offset in declination. Introducing a time bias of about 0.01 seconds (which was already found in the previous section) removes the offsets in the residuals series and reduces the standard deviation of the residuals  $\Delta\alpha^*$  and  $\Delta\delta$  to  $0.03''$  (see Fig. 4.17 and Table 4.3). This formal error is slightly larger than for the GNSS satellites due to the higher velocity of the satellites. The reference stars are mapped on the exposure with longer streaks, which may weaken the estimation of the center of light.

## Conclusions

We validated about four years of astrometric CCD observations of GNSS satellites acquired with ZIMLAT using GNSS orbits based on microwave-phase observations. In addition CCD observations of the two LAGEOS satellites were validated using SLR-based orbits. The validation allows the estimation of the CCD observation accuracy and the identification of systematic errors. The RMS error of the CCD residuals with respect to the microwave orbits is of the order of  $0.2''$ , which reflects the accuracy of the CCD observations acquired with ZIMLAT. Systematic errors of the order of  $0.1''$  are not present neither for the astrometric observation technique itself nor for the data reduction procedure of the observation.

In addition, the validation of the astrometric observation technique using GNSS satellite has revealed the presence of two systematic effects. An epoch registration offset was detected with a value of 0.01 seconds. After correcting the CCD residuals for that time bias the formal errors of both time series of residuals in right ascension and declination have the same size of  $0.2''$ , indicating that there are no more systematic effects in the epoch registration. Further, we found a significant offset of about  $0.17''$  in the  $\Delta\delta$  residuals. This effect could very well be explained by a systematic catalog offset in declination of the USNO-B1.0 catalog.

We conclude that our validation technique is well suited for the calibration and monitoring of the critical epoch registration related to optical observations of fast moving objects. Low Earth Satellites (LEOs) as the LAGEOS satellites are particularly suitable for the calibration and monitoring of the epoch registration system. Thus we propose the continuous (once per observation-night, at least once per month) acquisition of a small number of optical LAGEOS observations, which can be compared with SLR-based orbits. Our proposed method consumes only very little observation time, and it can be executed in principle with any optical observation system. Thinking of future networks of optical observation systems (such as space surveillance) the development of a standardized procedure based on our method is highly recommended.

Further this validation technique allows the detection of other systematic effects that might be present in the data reduction process.

As reference stars from a given star catalog define a specific CRF, the optical observation of artificial Earth satellites allows also the validation of stellar reference frames. This idea is not new. In 1984, Baueršima (1984) proposed a project called the “Coupled Quasar, Satellite, and Star Positioning (CQSSP)”: Artificial satellites should be used to provide a direct link between the celestial reference frames (see also Schildknecht et al. (1991)). On the one hand, if the satellite is observed together with reference stars by optical telescopes, the satellite position is well defined in the stellar reference frame. On the other hand, the orbit of the satellite is well known in the terrestrial reference frame. The orientation of the terrestrial reference frame with respect to the quasar-based reference frame is given by the Earth orientation parameters (EOPs). Thus, optical astrometric observation of satellites would allow it to monitor the transformation between the quasar-based (using radio telescopes) and the stellar-based (using optical telescopes) reference frames.

Today the limiting factor still is the accuracy of the astrometric observations. To validate the EOPs the optical observation accuracy has to be improved by a factor of 100. The catalog offset found in declination at a size of about  $0.17''$  is, however, a good example for the capability to validate stellar reference frames with artificial Earth satellites. But the idea of CQSSP was not to detect such comparable large catalog errors. In principle a direct comparison of star positions from different catalogs would be a more appropriate (i.e., easier) way for the identification of catalog errors, unless the stars are not covered by both catalogs. In this case our validation method still allows catalog validation and moreover the assessment of the catalog accuracy, however, limited by the CCD observation accuracy.

## 4.2 Validating Microwave-based GNSS Orbits Using SLR Observations

In order to validate GNSS orbits based on microwave observations, the measured laser ranges are compared with the ranges derived from the orbital information (from GNSS analyses) and the SLR site position. This validation method is well known and several results have been published during the last 10 years. Degnan and Pavlis (1994) studied range residuals of the GPS satellite G05 for 100 days in 1993. Pavlis and Beard (1995) derived SLR orbits for the same satellite from 14 days measurements in November 1993. They compared the SLR orbits with GPS microwave orbits. Range residual analysis of both GPS satellites, G05 and G06, were carried out by Watkins et al. (1996) for SLR measurements from 1995, by Zhu et al. (1997) for measurements from November 1993 to January 1996, and by Springer (2000) for measurements from January 1995 to July 1999. Eanes et al. (1999) and Ineichen et al. (2000) studied range residuals for GLONASS satellites from 1998 and 1999. Appleby and Otsubo (2000) used data from January 1999 to May 2000 for range residuals analysis of both, GPS and GLONASS satellites.

Most of these studies revealed a bias of about  $-5.5$  cm for GPS satellites between the microwave-based orbits and the SLR measurements. The GPS orbit accuracy was estimated to about 5 cm. For the GLONASS satellites, there was also a negative offset found of about  $-4$  cm. The accuracy of the GLONASS orbits was at the 10 – 15 cm level.

The validation studies performed within the scope of this work are based on the analysis of range residuals for the two GPS satellites equipped with laser retroreflector arrays (LRA) G05 and G06, and for four GLONASS satellites using about four years of SLR data, starting in 2002 until early 2006. R07 is a new GLONASS-M type satellite and replaced the GLONASS satellite R24 in the SLR tracking scheme in August 2005. The final orbit products from three of the IGS analysis centers, namely from CODE, GFZ, JPL (see Table 4.4), as well as the combined IGS

Orbit	Institution	Software used	Model description
CODE	Center for Orbit Determination in Europe, Bern, Switzerland	Bernese GPS Software Version 5.0	(Hugentobler et al., in press)
GFZ	GeoForschungsZentrum Potsdam, Germany	EPOS.P.V2	(Ge et al., in press)
JPL	Caltech/NASA Jet Propulsion Laboratory, Pasadena, U.S.A.	GIPSY/ OASIS-II	(Vigue-Rodi et al., in press)
IGS	Combined orbit, generated by the IGS Analysis Center Coordinator (ACC)		(Gendt and Nischan, in press)

Table 4.4: Summary of the validated orbits

orbit product were validated. The final orbits are the central 24 hours of three-day arcs in the case of CODE and GFZ, and of 30-hours arcs in the case of JPL.

### 4.2.1 SLR Validation Procedure

To validate GNSS orbits using SLR, the ‘ranges’ or distances between the satellite and the observing site obtained from both, SLR range and microwave measurements, are compared. The difference between the observed SLR range and the range computed using the SLR site coordinates and the orbital information obtained from microwave phase data is known as range residual  $\Delta r$ , illustrated in Figure 4.18.

The range residuals are primarily an indicator for the radial accuracy of the microwave orbits, because the maximum angle of incidence of the laser pulse onto the satellite’s LRA is only about  $14^\circ$  due to the high altitude of the GNSS satellites.

As the orbits derived from microwave data refer to the satellite’s center of mass, the difference vector between the center of mass and the LRA center of reflection has to be added to the laser range measurement (see Sect. 2.4.2) in the validation procedure. This difference vector is commonly known as retroreflector offset. Table 4.5 lists the used satellites and the corresponding retroreflector offsets as provided by the ILRS (ILRS, 2008). They are expressed in the satellites’ body-fixed coordinate system (see Sect. 3.1.2). The GLONASS-M reflector offset differs from that of the other GLONASS type satellites. The LRA does no longer coincide with the z-axis as it was the case for the older GLONASS satellites. Furthermore, it is worth to note that a change

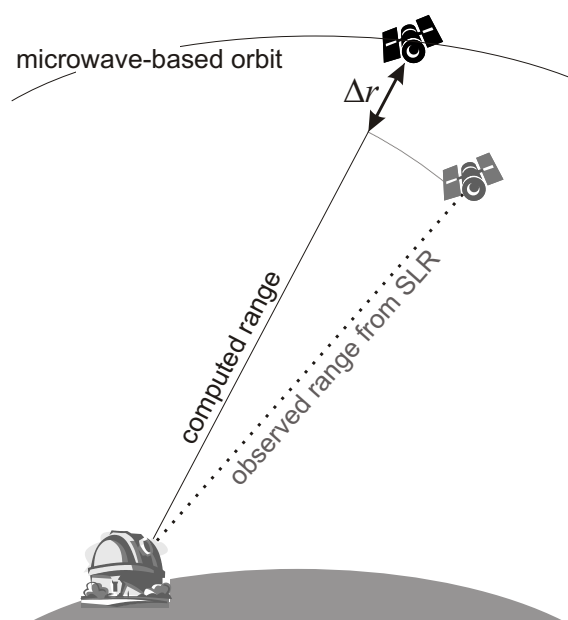


Figure 4.18: SLR validation method

Satellite type	PRN	COSPAR-ID	x (m)	y (m)	z (m)
GPS	G05	1993-054A	0.8626	-0.5245	0.6695
	G06	1994-016A	0.8626	-0.5245	0.6717
GLONASS	R03	2001-053B	0.0000	0.0000	1.5550
	R22	2002-060A	0.0000	0.0000	1.5550
	R24	2000-063B	0.0000	0.0000	1.5550
GLONASS-M	R07	2004-053B	0.1370	0.0030	1.8740

Table 4.5: Retroreflector offsets for the used GNSS satellites

in the z-offset for the two GPS satellites by about 1 cm is due to a tray segment between the LRA and the spacecraft, which was not considered before (Davis et al., 2005).

For the attitude modeling of GPS Block IIA satellites passing the Earth’s shadow, we apply yaw rotation rates provided by JPL (Bar-Sever, 1994). Disregarding the rotational behavior of GPS satellites during eclipse phase would lead to biased range measurements reaching values up to 40 cm. Figure 4.19 shows range residuals during an eclipse phase for the satellite G06 without (left) and with (right) applying JPL’s yaw rotation rates. Range residuals outside eclipses are marked in black, whereas residuals from observations during eclipse are marked in gray. The figure indicates that correct modeling of the satellite’s attitude within the Earth’s shadow decreases significantly the resulting SLR residuals.

The SLR site coordinates are given in the reference frame ITRF2000, whereas the orbit determination refers to the IGS00 reference frame, which is the IGS realization of the ITRF2000. The IGS00 is aligned to the ITRF2000, ensuring consistency between the two frames. The datum definition for the orbit determination is done with network constraints, i.e., a no-net-rotation condition is imposed for a set of well defined IGS core site. A translation of the network is allowed and accordingly estimated during the parameter adjustment. Hence, the orbits may be shifted with respect to the ITRF2000 reference frame. As this shift is not known to us for all of

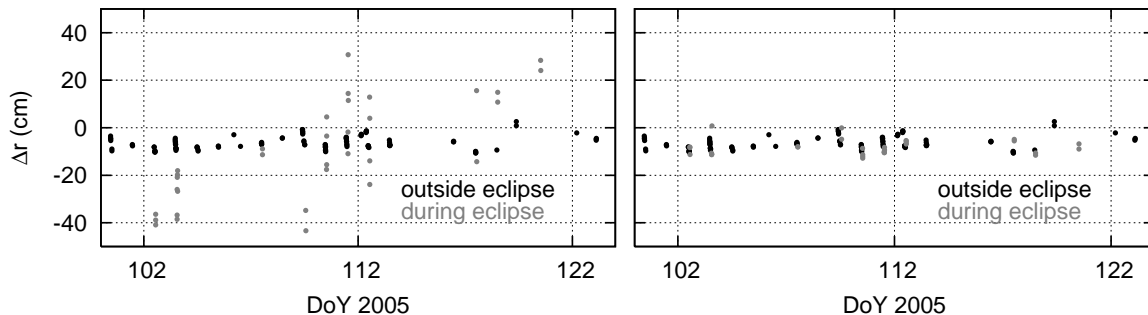


Figure 4.19: SLR residuals  $\Delta r$  derived from CODE final orbits for the GPS satellite G06 outside and during eclipse as a function of time; **left:** without applying yaw rotation rates; **right:** with applying yaw rotation rates

the used orbits, we have to neglect those network translations and thus accept small inconsistencies between orbits and SLR site coordinates.

SLR normal points causing residuals larger than 1 meter were excluded as outliers. In addition only normal points based on more than 12 data points were taken into account. In general about 100 single measurements contribute to one normal point, which is valid over time interval of 5 minutes.

### 4.2.2 SLR Validation Results

This section presents the validation results derived from the orbits of various analysis centers. The statistical information of the individual solutions are summarized in Table 4.6. It gives the standard deviation and the associated range biases in cm for all final orbit products considered. The last column gives the approximate number of used normal points.

In all solutions, the standard deviation (i.e., the root mean square deviation from the arithmetic mean) of the range residuals for the GPS orbits is about 2 – 3 cm. This value stands primarily for the radial accuracy of the three-day arcs. The mean bias (i.e., the arithmetic mean) for GPS satellites is between –3 cm and –4 cm. It differs by up to 1 cm between the orbit solutions, reflecting the orbital scale differences. The negative sign indicates that the distance to the satellite measured with SLR is shorter than the distance derived from the microwave-based orbits. For the GLONASS satellites the standard deviation of the range residuals is about 5 cm. The lower orbit quality compared to GPS is mainly due to the much sparser IGS tracking network for GLONASS satellites. The mean range bias for the GLONASS satellites does not differ significantly from zero.

Figure 4.20 shows the range residuals  $\Delta r$  derived from the CODE final orbits for the two GPS satellites G05 and G06, and Figure 4.21 for the GLONASS satellites R03, R22, R24, and the

PRN	$\sigma$ (cm)				$\bar{x}$ (cm)				# $\Delta r$
	CODE	GFZ	JPL	IGS	CODE	GFZ	JPL	IGS	
G05	2.2	2.3	2.2	1.9	–3.5	–3.6	–2.6	–3.1	11400
G06	2.7	2.7	2.5	2.5	–3.8	–3.9	–2.8	–2.8	10900
R03	4.9				–1.0				17600
R22	4.6				–0.4				21000
R24	5.1				–0.3				12600
R07	5.7				0.5				3200

Table 4.6: Statistical information of the SLR residuals derived from more than four years of microwave-based GNSS orbits (final orbits of CODE, GFZ, JPL, and combined IGS final orbits): standard deviation  $\sigma$ , mean value (range bias)  $\bar{x}$  with formal errors, and approximate number of SLR residuals (#  $\Delta r$ )

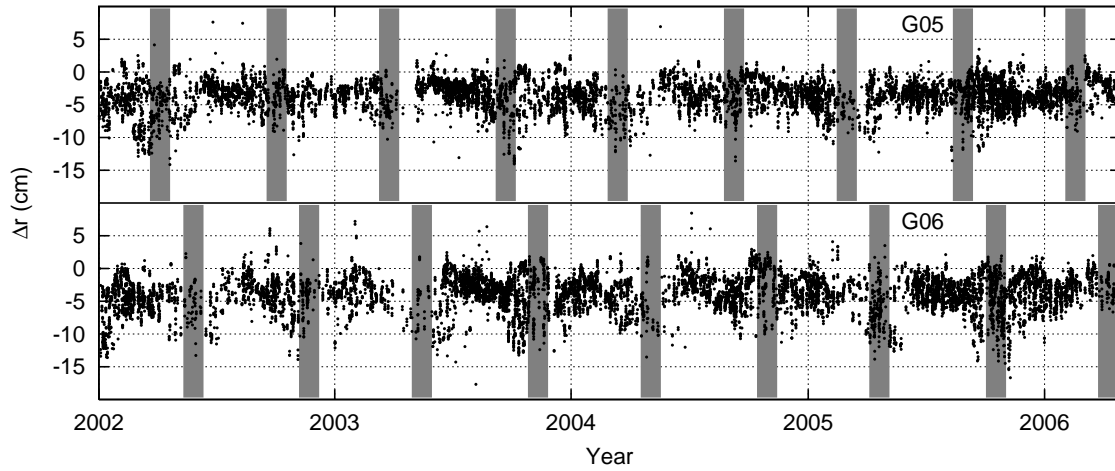


Figure 4.20: SLR residuals  $\Delta r$  derived from CODE final orbits for the GPS satellites G05 and G06 as a function of time; shaded areas indicate eclipse seasons

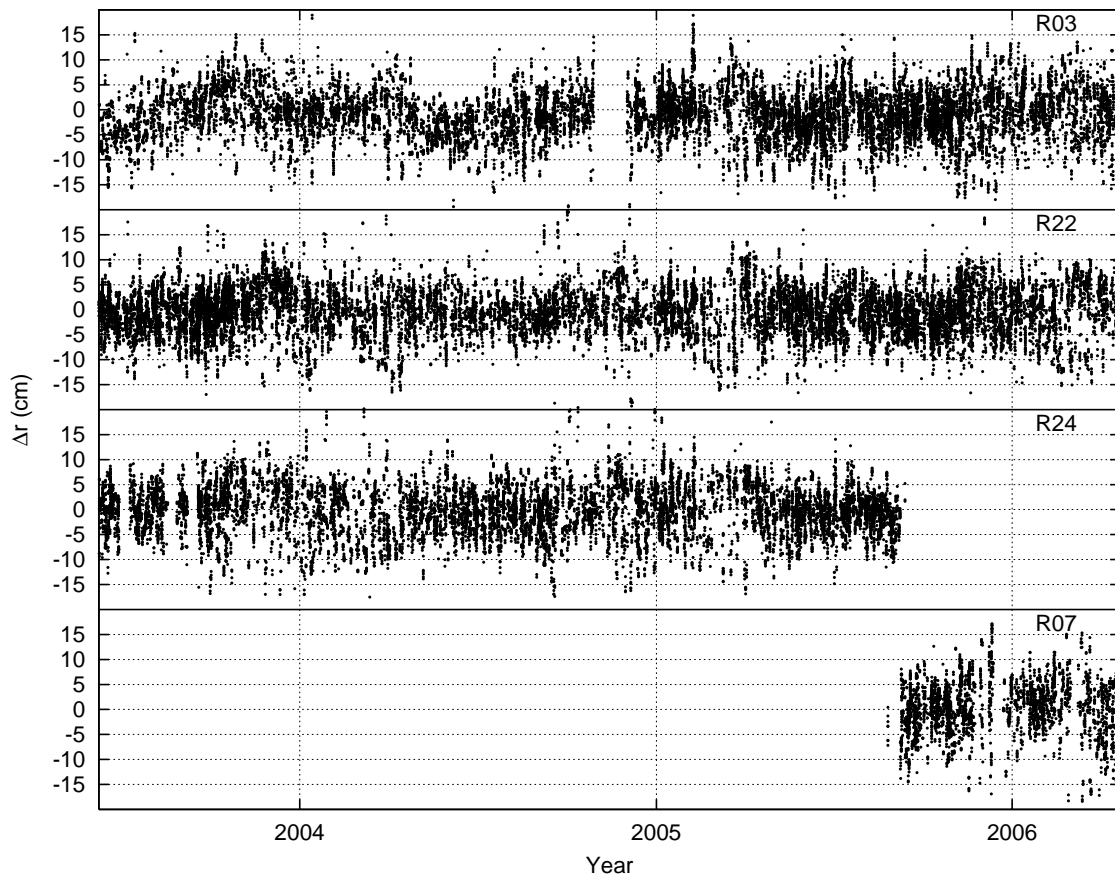


Figure 4.21: SLR residuals  $\Delta r$  derived from CODE final orbits for the GLONASS satellites R03, R22, R24, and R07 as a function of time

GLONASS-M satellite R07. The residuals are given as a function of time. For the GPS orbits, we observe a periodic pattern with residuals of up to 10 cm amplitude, systematically pointing into negative direction. The largest residuals occur when the satellite is observed within the Earth's shadow during eclipse seasons (indicated with shaded areas in Figure 4.20). But systematically large residuals are not restricted to shadow periods. The repeat period of this pattern is about 352 days, which corresponds to the draconitic GPS year (see Sect. 3.1.1). As both, observation geometry as well as the orbit-Sun geometry, repeat with this period, it is not easily possible to identify the source of the periodic pattern. It is not possible either to attach the effect to the SLR or to the microwave observation technique.

For further investigation of the periodic signature, the following experiment was performed. As the residuals for both GPS satellites show the same pattern, we analyze them together. We subtract the mean bias from the range residuals, and color the resulting residuals  $\Delta r^*$  according to their values as displayed in Figure 4.22.

These colored range residuals are now no longer displayed as a function of time, but rather in a system that takes into account the position of the Sun with respect to the satellite – the  $(\Delta u, \beta_0)$  coordinate system, where the angle  $\Delta u$  is the argument of latitude of the satellite with respect to the argument of latitude of the Sun and the angle  $\beta_0$  is the elevation of the Sun above the satellite's orbital plane (see Sect. 3.1.2). Figure 4.23 shows the color-coded range residuals  $\Delta r^*$  for both GPS satellites derived from the CODE final orbits in this system. Thus, the residuals are projected to the celestial sphere with the Earth's shadow at the center of the figure using a plate careé projection. The phase angle  $E$ , the angle Sun-satellite-Earth (geocenter), is indicated with circles spaced by  $15^\circ$ . Each circle represents a line of equal phase angle.  $E$  is  $0^\circ$  at the plot center ( $\Delta u = 180^\circ$  and  $\beta_0 = 0^\circ$ ), and  $180^\circ$  at ( $\Delta u = 0^\circ$  and  $\beta_0 = 0^\circ$ ).

During its orbital revolution a satellite crosses the figure on a horizontal line from left to right. If  $\beta_0 = 0^\circ$ , the Sun lies in the orbital plane and if, in addition,  $\Delta u = 180^\circ$ , the satellite is in the deepest shadow. At the opposite side of the orbital plane ( $\beta_0 = 0^\circ$ ,  $\Delta u = 0^\circ$ ) no SLR observations are available, as the satellite is too close to the Sun for laser observations. We observe a systematic pattern with the largest values for shadow passes, but large systematic effects are not restricted to the shadow passes.

Figure 4.23 (bottom) shows the projection of the residuals onto the  $\Delta u$ -axis, whereas the Fig. 4.23 (left) shows the projection onto the  $\beta_0$ -axis. The dependency of the residuals on the satellite's position within the orbital plane is clearly visible, and hence indicates problems in the microwave orbit modeling.

The same signature is observed when considering the range residuals stationwise. In Fig. 4.24, the range residuals are given for four SLR sites (Riyadh (7832), Herstmonceux (7840), Yarragadee (7090), and Zimmerwald (7810)). For each SLR site, although located at very different geographical locations, a similar pattern can be observed.

The SLR residuals derived from the IGS, GFZ as well as the JPL microwave-based orbits show a similar pattern, which is clearly not dependent on the SLR stations. The corresponding figures can be found in the Appendix B (Figs. B.1, B.2, B.3).

We conclude that the periodic pattern is not caused by the SLR observations, but must be due to deficiencies of the models used in the microwave data analysis.

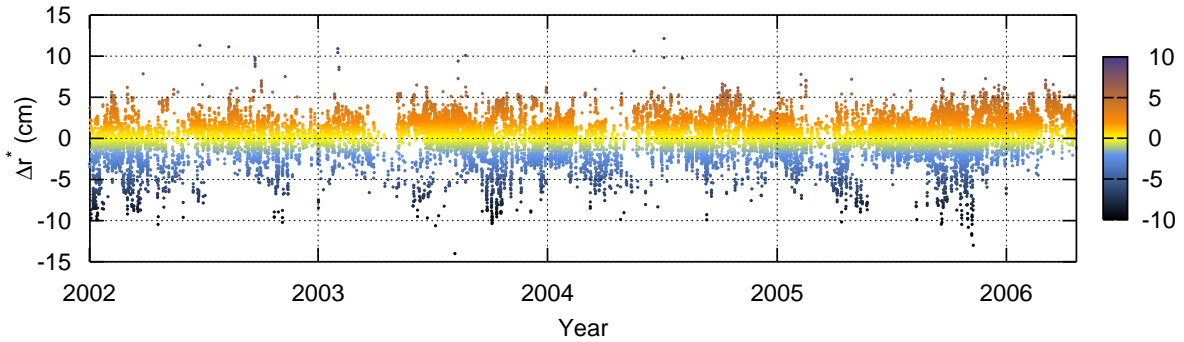


Figure 4.22: SLR residuals  $\Delta r^*$  derived from CODE final orbits for the GPS satellites G05 and G06 as a function of time

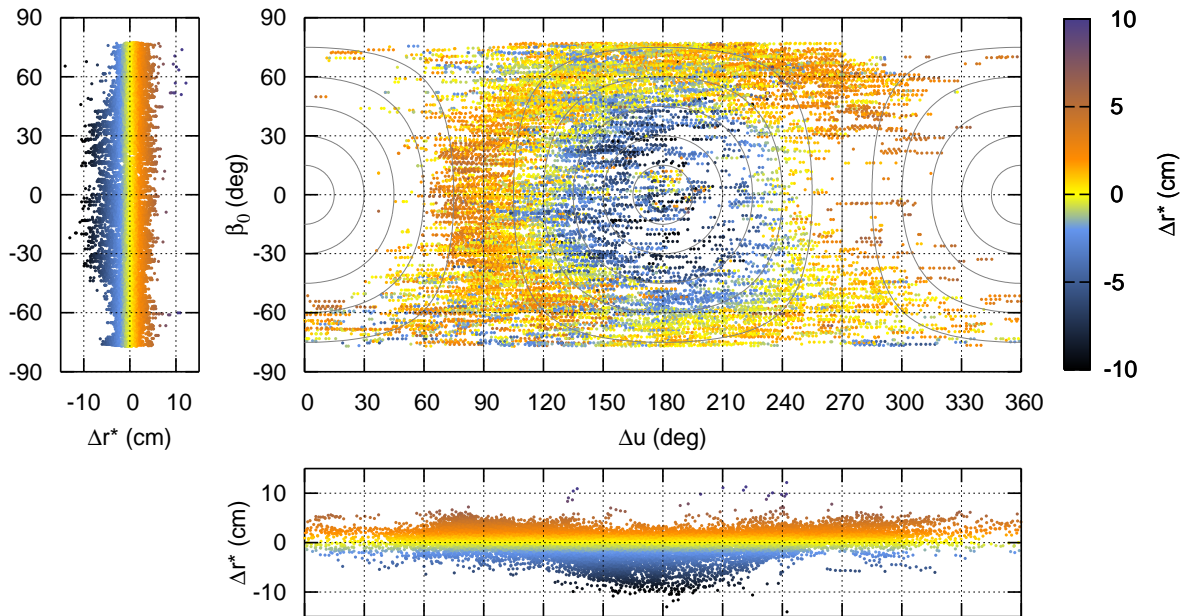


Figure 4.23: SLR residuals  $\Delta r^*$  derived from CODE final orbits for the GPS satellites G05 and G06 in the  $(\Delta u, \beta_0)$  coordinate system; **bottom:** projection onto  $\Delta u$ -axis; **left:** projection onto  $\beta_0$ -axis; circles represent the phase angle  $E$ ,  $15^\circ$  spacing,  $0^\circ$  at center ( $\Delta u = 180^\circ$  and  $\beta_0 = 0^\circ$ ),  $180^\circ$  at ( $\Delta u = 0^\circ$  and  $\beta_0 = 0^\circ$ )

The CODE final orbits were generated with the CODE orbit model ECOM (see Sect. 3.2.2). Six orbital elements and five dynamical parameter, namely three constant parameters ( $D0$ ,  $Y0$ ,  $B0$ ) and two once-per-revolution parameter ( $BS$ ,  $BC$ ), were estimated. For the validated CODE GPS orbits, the ROCK models T20 and T30 (see Sect. 3.1.3) were used as a priori solar radiation pressure (SRP) models until a model change to the CODE SRP model (see Sect. 3.1.3) in November 2005. The T20 and T30 models were also used for the GFZ orbits, but only two constant acceleration parameters,  $D0$  and  $Y0$ , were estimated. JPL uses the JPL empirical model (a ROCK-like model) for GPS Block II/IIA, and the Lockheed Martin SRP model (Bar-

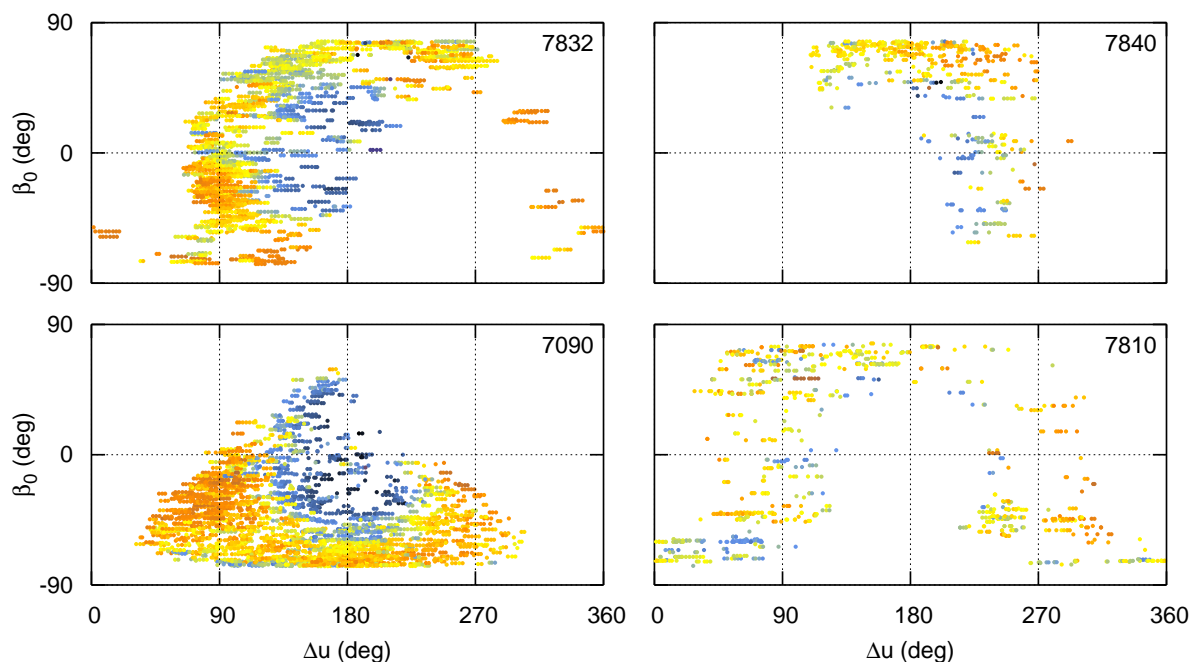


Figure 4.24: Station-specific SLR residuals  $\Delta r^*$  derived from CODE final orbits for the GPS satellite G05 in the  $(\Delta u, \beta_0)$  coordinate system

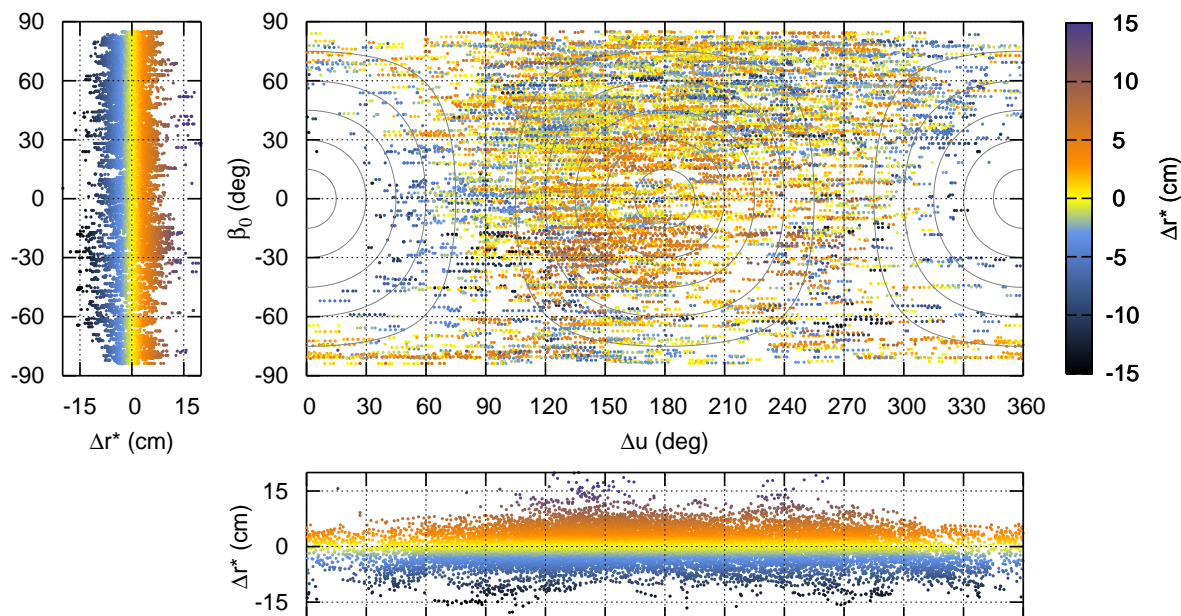


Figure 4.25: SLR residuals  $\Delta r^*$  derived from CODE final orbits for the GLONASS satellites R03, R22, R2, and R07 in the  $(\Delta u, \beta_0)$  coordinate system; **bottom:** projection onto  $\Delta u$ -axis; **left:** projection onto  $\beta_0$ -axis; circles represent the phase angle  $E$ ,  $15^\circ$  spacing,  $0^\circ$  at center ( $\Delta u = 180^\circ$  and  $\beta_0 = 0^\circ$ ),  $180^\circ$  at ( $\Delta u = 0^\circ$  and  $\beta_0 = 0^\circ$ )

Sever, 1998) for Block IIR satellites. Two SRP parameters,  $D0$  and  $Y0$ , and three stochastic parameters were estimated in addition.

Figure 4.25 shows the color-coded range residuals for one of the GLONASS satellites (R22) derived from the CODE final orbits. There is no systematic pattern observable for this satellite as well as for none of the other validated GLONASS satellites, but rather randomly distributed (although larger) residuals. It is interesting to note that for the GLONASS orbits no SRP a priori model was used.

### Conclusions

SLR range measurements are extremely useful for an independent validation of microwave-based GNSS orbits. Although the GPS orbits of the individual IGS analysis centers are consistent at the 2 cm level (see Sect. 3.2.3), we found two systematic effects for the GPS satellites at the few-cm level.

First, there is a constant bias of the order of  $-3$  to  $-4$  cm between the laser ranges and the orbits derived from microwave data. This bias is still as that reported in the previous studies, reduced by the recently found 1 cm LRA offset. Further studies are needed to understand the source of this inter-technique bias.

Second, the range residuals for the GPS satellites show significant systematic patterns with amplitudes between 5 cm and 10 cm and periods correlated to the eclipsing seasons. These periodic patterns have not been identified before. We have shown that the patterns are not caused by the SLR tracking data, but are due to the GNSS microwave analysis. The dependency of the residual pattern on the satellite's position with respect to the Sun most likely indicates deficiencies in the dynamic orbit model for GPS satellites.

An improved radiation pressure model, developed from the analysis of GPS orbits of the past ten years, might cure the problem. Deficiencies in the attitude model as, e.g., a satellite-specific misorientation of the z-axis may cause a similar periodic pattern in the range residuals. The well-known Y-bias (see Sect. 3.1.2) indicates already that attitude modeling problems exist (Fliegel et al., 1992).

Earth albedo radiation pressure (EAP) (see Sect. 2.1.3), which is not yet taken into account in the GNSS analysis at CODE, might have a non-negligible effect on the orbit, as well. A radial acceleration due to EAP (directed from the Earth to the satellite) of about  $10^{-9}\text{m/s}^2$  would lead to a radial error of about  $-2$  cm. The semi-major axis is expected to be slightly reduced using an EAP model. Ziebart et al. (2007) showed the impact of EAP on GPS orbit determination for five days. In these tests the range bias between the GPS orbits and the SLR measurements is reduced by 2.1 cm with the used EAP. Longer time spans should be used to confirm these results. As the force due to EAP is varying with the satellite's revolution, a periodic impact on the GNSS orbits is expected.

The impact of EAP on GNSS satellites should be of the same order of magnitude for GPS and GLONASS satellites. Differences in the satellites' revolution periods, altitudes, and sizes of the solar panels have to be considered. It is, however, interesting to note that we did not find

#### *4 Mutual Validation of the Different Satellite-Geodetic Techniques*

---

any systematic pattern in the SLR residuals of GLONASS satellites nor a significant range bias for GLONASS satellites. The differences in behavior for GPS and GLONASS satellites is an argument against EAP as an explanation for the modeling problems.

As only two of the GPS satellites are equipped with retroreflector arrays, both of type Block IIA, statements based on SLR validation can only be made for the Block IIA satellites. This means the assumed orbit model deficiencies are only valid for the GPS Block IIA satellites, so far.

## 5. Improvement of the GNSS Orbit Model

The validation studies of the GNSS orbits based on microwave-phase observations using SLR in Chapter 4 revealed deficiencies in the GNSS orbit model, at least for GPS Block IIA satellites. The question arises, whether it is possible to improve the GNSS orbit model by applying a solar radiation pressure (SRP) a priori model different from the ROCK model.

For this purpose three GNSS orbit time series are generated using three different SRP a priori models. The orbits are then validated with SLR measurements. This validation defines the absolute model accuracy. In addition we compare the three orbit types, in order to study dependencies on the orbital planes and on different Block-types.

Furthermore, we compute orbit predictions using the different SRP models. The differences analyzed for a particular orbit model and a particular satellite are  $|\vec{r}_p(t) - \vec{r}_t(t)|$ , where the index  $p$  stands for the predicted and  $t$  for the true orbit (as a matter of fact the orbit estimated with the observations of the particular day). These differences are also indicators for the SRP model accuracy.

We also analyze the orbit differences  $|\vec{r}_i(t) - \vec{r}_{i+1}(t)|$  for each satellite and each model type, where the index  $i$  characterizes the orbit generated with the observations of day  $i$ , and consequently  $i+1$  the orbit generated with the observations of day  $i+1$ . The difference  $|\vec{r}_i(t) - \vec{r}_{i+1}(t)|$  is evaluated at the day boundary between days  $i$  and  $i+1$ ; it is referred to as overlap error. Overlap errors of one-day and three-day arcs are analyzed with the goal to detect a systematic behavior, and if so, to clarify whether the use of different SRP models affects this behavior.

Moreover, we study the impact of the SRP models on the estimated station coordinates by analyzing the translation parameters (geocenter coordinates) estimated for the GNSS tracking network.

Last, but not least, we analyze the impact of different sets of dynamic orbit parameters and different argument angles (used for the periodic once-per-revolution parameters) on the estimated orbit.

We used a development version of the Bernese GPS Software (Dach et al., 2007) for all computations.

## 5.1 Different Solar Radiation Pressure Models

Studying the impact of different SRP a priori models on GNSS orbits requires a consistent time series of GNSS orbits. The orbits of each time series have to be generated using identical parameters and observation models (except, of course, SRP models). The time series of CODE final orbits, analyzed in Sect. 4.2, is inhomogeneous because of various model changes over the four years covered. We therefore reprocessed this time series three times using three different SRP a priori models. We did not, however, start reprocessing the raw data, but used the already preprocessed phase observations. These observations are single difference phase observations, which have been screened for outliers and cycle slips; the initial phase ambiguities on the double difference level are already resolved (to the extent possible). Differences in the preprocessing options as well as the impact of the SRP models on the preprocessing (assumed to be minor) are neglected.

The new orbit time series cover about four years of data starting from DoY 040/2003 until 365/2006. For each day, one-day arcs are computed and the corresponding normal equations are saved. Three consecutive normal equations are then stacked to generate the three-day arc solutions. The processing strategy including the observation model and the set up of parameters is the same as the processing scheme at CODE. The CODE final orbits of the validated time series in Sect. 4.2 have been determined in that way.

The Niell mapping functions (Niell, 1996) were used for modeling the tropospheric zenith path delay. Although absolute models for antenna phase center offsets and variations for receiver and satellite antennas are used today, we applied the relative antenna phase center models, only valid for receiver antennas, to stay consistent with the old orbit time series. For the same reason, we used the IGS00 reference frame (a realization of the ITRF2000) for the geodetic datum definition. The new ITRF2005 realization IGS05, available since October 2006, is used in today's GNSS analyses.

The following parameters are estimated: ambiguities, tropospheric zenith path delays, translation parameters for the set of IGS core sites, site coordinates for all sites, ERPs, and orbit parameters. The network translation parameters describe the difference between the origin of the reference frame IGS00 and the apparent geocenter (as determined by the GPS technique). Thus, these translation parameters may also be interpreted as geocenter coordinates.

The orbit parameters are the six osculating orbital elements and five dynamical parameters of the ECOM model (see Sect. 3.2.2), i.e., three constant accelerations ( $D0$ ,  $Y0$ ,  $B0$ ) and two once-per-revolution accelerations ( $BS$ ,  $BC$ ). In addition, stochastic pulses (small velocity changes) in radial, along-track and out-of-plane directions are estimated every 12 hours, at noon and at the day boundaries.

We generated the three orbit time series using the same observations, parameters, and models as described above, except for the SRP a priori model. The three SRP models used are listed below. The model name (in bold letters) will be used in this chapter to distinguish between the models.

1. **ROCK**: The ROCK SRP models T20 and T30 (see Sect. 3.1.3) for GPS Block II/IIA and Block IIR, respectively, were used.
2. **CODE**: The CODE SRP model (see Sect. 3.1.3), which was updated in 2006 and provides values for both, GPS and GLONASS satellites, was used.
3. **NONE**: No SRP a priori model was used.

Note that no a priori SRP model is used for the GLONASS satellites for the orbit solutions using the ROCK model, as the ROCK model is available for the GPS satellites. The impact of the GPS satellites, which are processed together with the GLONASS satellites, on GLONASS orbit determination is expected to be very small. There will be, however, small differences between the GLONASS orbit solutions using the ROCK and the NONE model. Therefore, we distinguish also for the GLONASS satellites between these two solutions.

Figure 5.1 shows the accelerations derived from the different SRP a priori models for the GPS Block IIA satellite G06. The accelerations are given in the directions D (top), Y (middle), and B (bottom). For the definition of the (D, Y, B) system see Sect. 3.1.2. Each subfigure contains five sections, covering 24 hours each, which correspond to different observation times with different elevation angles  $\beta_0$  of the Sun above the orbital plane. The five sections are arranged in such a way that the angle  $\beta_0$  decreases from the left hand side of the subfigure (maximum  $\beta_0$  value) to the right hand side of the subfigure ( $\beta_0 = 0$ ). The accelerations due to the ROCK model T20 are gray, those due to the CODE model are black. For obvious reasons “NONE” is missing in Fig. 5.1.

Although the ROCK model per se does not include any accelerations in Y-direction, constant a priori values for the D- and Y-directions are introduced in the Bernese GPS Software. For the satellite G06 this a priori acceleration in Y-direction is  $0.07 \cdot 10^{-8} \text{m/s}^2$ , and in D-direction about  $-0.35 \cdot 10^{-10} \text{m/s}^2$ .

Figure 5.1 shows a twice-per-revolution signal in D-direction and a once-per-revolution signal in B-direction (GPS satellites perform two revolutions in 24 hours). The amplitudes of these periodic signals increase with decreasing  $\beta_0$  angle. The D-accelerations are of the order of  $9 \cdot 10^{-8} \text{m/s}^2$ . The peak to peak variations of about  $0.7 \cdot 10^{-8} \text{m/s}^2$  are similar to the peak-to-peak variations for the B-accelerations. Note that the D- and B-accelerations of the ROCK and the CODE model are not in phase. Moreover the two accelerations are shifted in phase by  $90^\circ$ . This striking phase shift of precisely  $90^\circ$ , while a coherence in phase would be expected requires a detailed assessment of the implementation of the two models.

The acceleration  $\mathbf{a}_{srp}$  due to SRP estimated from the least squares adjustment is given in Fig. 5.2, with  $\mathbf{a}_{srp}$  being the sum of the SRP a priori values and the values estimated for the five parameters of the ECOM model ( $D0, Y0, B0, BS, BC$ ). In D-direction only a constant parameter  $D0$  was estimated. The resulting D-accelerations are shifted by constant values compared to the a priori value. Their mean values are similar for the ROCK and CODE model, in contrary to the values estimated when using no a priori model (i.e., the NONE model, indicated by the dashed lines in the figures). Actually, we expected the mean values of all solutions to be

the same as the estimated accelerations already include the a priori values. The difference between the estimated values using the NONE model and the other SRP models is not understood so far and has to be investigated.

In addition a constant acceleration in Y-direction  $Y_0$  (the so-called Y-bias) was estimated. The values of these Y-biases are almost the same for all three SRP models.

In B-direction a constant and two once-per-revolution parameters were estimated. As the CODE SRP model mainly contains an once-per-revolution signal in B, the estimated B-accelerations

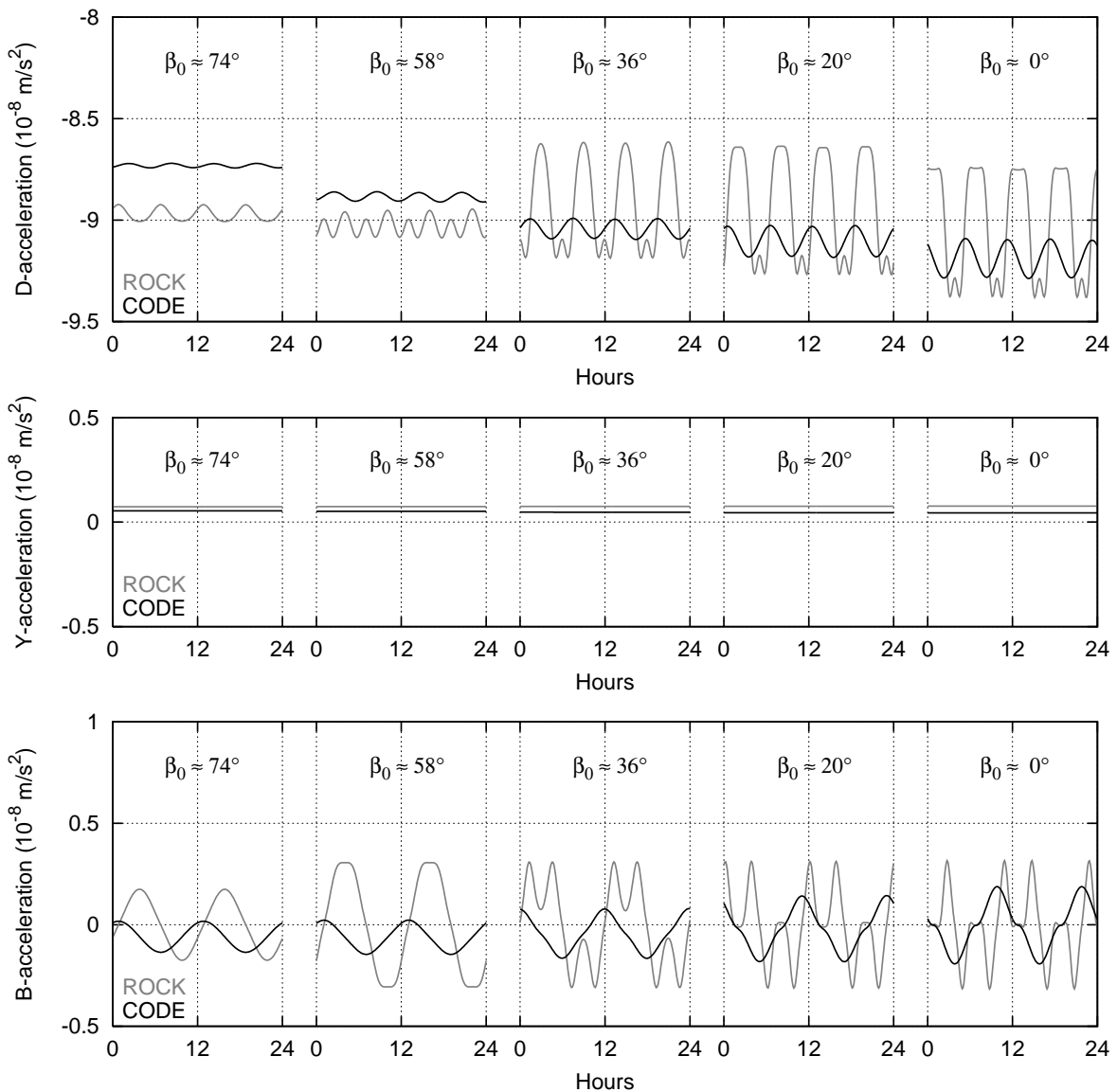


Figure 5.1: Accelerations due to SRP acting on the GPS satellite G06 (Block IIA), derived from the SRP a priori models ROCK (gray) and CODE (black)

are similar for the CODE and the NONE model. The major part of the CODE SRP model is reflected by the parameters of the ECOM model. The only differences of the CODE model compared to the parameters of the ECOM model are the periodic terms as a function of  $\beta_0$  (see Eqs. 3.10 and 3.11 in Sect. 3.1.3).

For large  $\beta_0$  angles (Sun high above the orbital plane) the B-accelerations using the ROCK model are similar to the that of the other models, i.e., the estimated parameters compensate for the  $90^\circ$  phase shift. For small angles of  $\beta_0$  the B-accelerations differ, however, for different

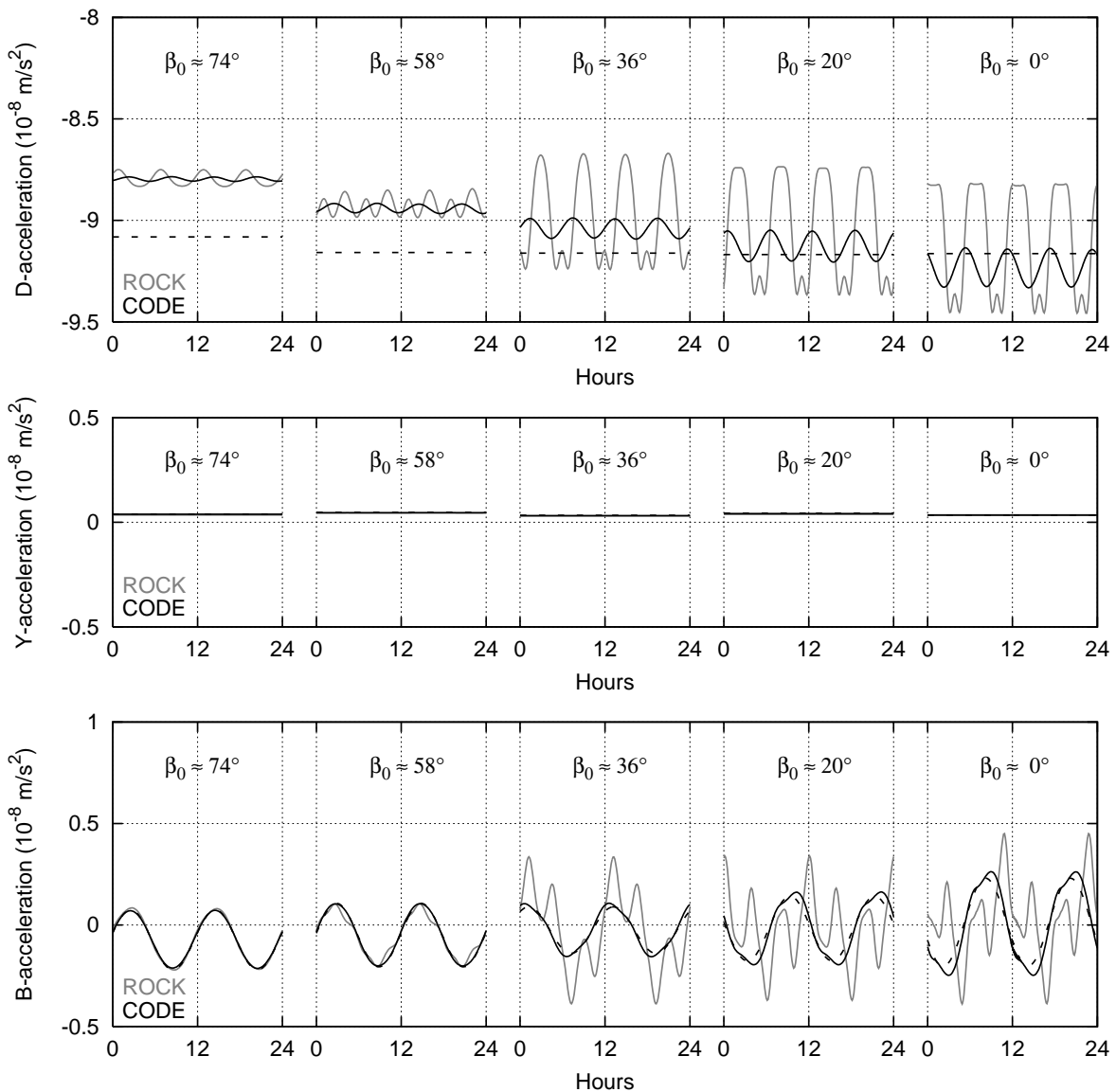


Figure 5.2: Estimated accelerations due to SRP acting on the GPS satellite G06 (Block IIA), derived from parameter adjustment using the SRP a priori models ROCK (gray), CODE (black), and NONE (dashed)

SRP models. This is due to the pronounced signal of the ROCK model at small  $\beta_0$  angles superimposing the once-per-revolution signal.

Figures C.1 and C.2, given in the Appendix C, show the a priori D-, Y-, and B-accelerations for a Block IIR satellite (G16) and the estimated accelerations, respectively. As the SRP models are block-specific, the accelerations differ in amplitude and size from that for the Block IIA satellite. The general characteristics described in this section remain the same, however.

## 5.2 Assessing the Quality of the Orbit Model

Let us now study the generated orbit time series in order to find out to what extent the a priori SRP model impacts the GNSS orbits, and, last but not least, which of the SRP model yields the best orbits.

### 5.2.1 ... by Analyzing SLR Residuals

An independent validation of the orbit time series using SLR measurements is possible only for the two Block IIA GPS satellites equipped with retroreflectors, G05 and G06, and the four GLONASS satellites R03, R07, R22, and R24, which were tracked by the ILRS during the considered time interval.

As a translation of the GNSS receiver network (i.e., geocenter coordinates) is estimated during the parameter adjustment process, the orbits may be shifted with respect to the ITRF2000 reference frame. For the orbit validation both, the SLR site coordinates, given in ITRF2000, and the orbits, have to refer to the same reference frame. Therefore, we apply the estimated geocenter coordinates to the SLR site coordinates (which is in essence a shift of the orbits, by translating the orbit positions with opposite sign). SLR site coordinates and orbit positions then both refer to the geocentric frame.

Table 5.1 summarizes the statistical information of the SLR residuals derived from the three time series of the reprocessed microwave-based GNSS orbits, using the SRP a priori models ROCK, CODE, and NONE.

The standard deviation of the range residuals for the GPS satellite orbits of the first solution (using the ROCK model) are 2.2 cm and 2.6 cm. These values are similar to the results derived from the validation of the CODE final orbits, presented in Sect. 4.2.2. This was expected, as for the CODE final orbits the ROCK SRP model was used, until a model change occurred to the CODE SRP model in November 2005. Figure 5.3 shows the SLR residuals  $\Delta r^*$ , which are color coded and reduced by their mean value of about  $-4$  cm, as a function of  $\Delta u$  and  $\beta_0$ . A comparison with Fig. 4.23 (in Sect. 4.2.2, page 85 ) shows a similar systematic pattern. The largest residuals, up to  $-10$  cm, occur close to the shadow region (center of figure), when the satellites pass the Earth's shadow.

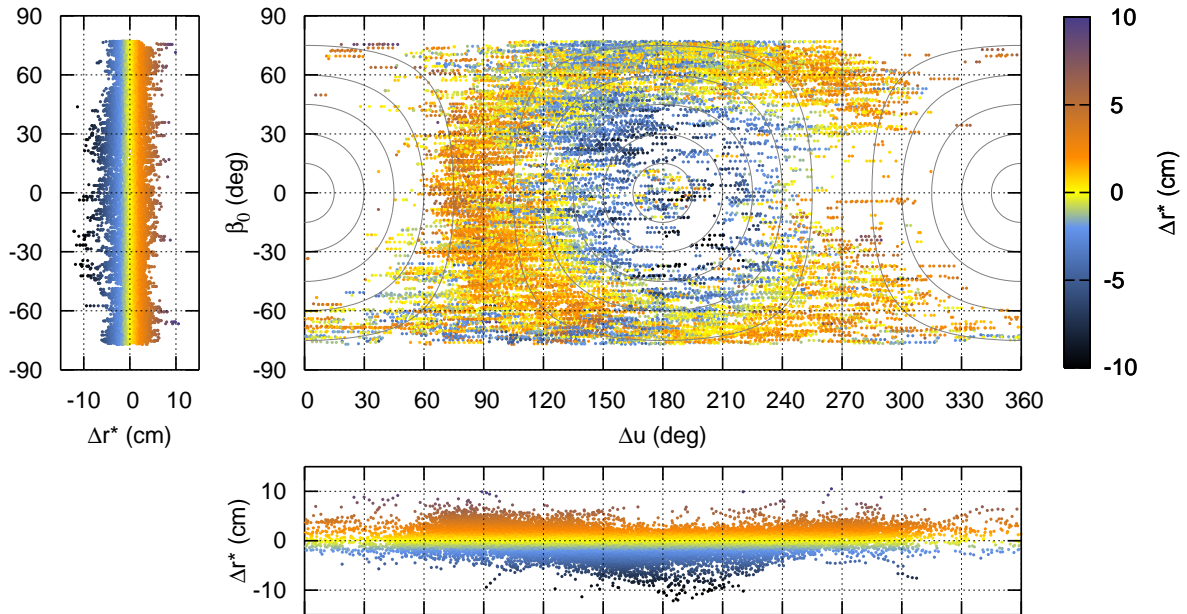


Figure 5.3: SLR residuals  $\Delta r^*$  derived from reprocessed orbits using the ROCK SRP model for the GPS satellites G05 and G06 in the  $(\Delta u, \beta_0)$  coordinate system; **bottom:** projection onto  $\Delta u$ -axis; **left:** projection onto  $\beta_0$ -axis; circles represent the phase angle  $E$ ,  $15^\circ$  spacing,  $0^\circ$  at center ( $\Delta u = 180^\circ$  and  $\beta_0 = 0^\circ$ ),  $180^\circ$  at ( $\Delta u = 0^\circ$  and  $\beta_0 = 0^\circ$ )

The range residuals derived from the orbit time series using the CODE and the NONE SRP model, show standard deviations of 1.9 cm and 2.1 cm for the satellites G05 and G06, respectively. These values are significantly smaller (by about 0.5 cm) than those for the orbit series using the ROCK SRP model. We find the explanation in Fig. 5.4, which shows the range

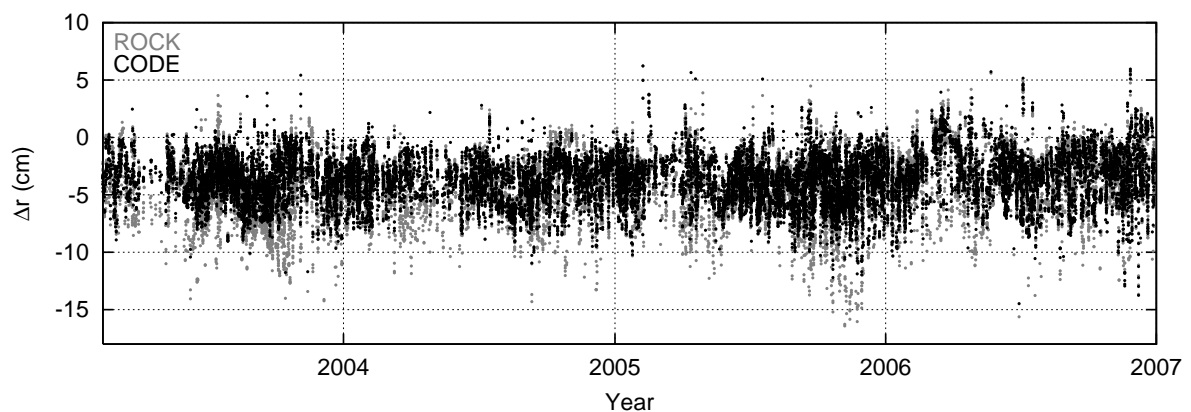


Figure 5.4: SLR residuals  $\Delta r$  derived from microwave-based orbits using the ROCK and the CODE SRP a priori model for the GPS satellites G05 and G06 as a function of time

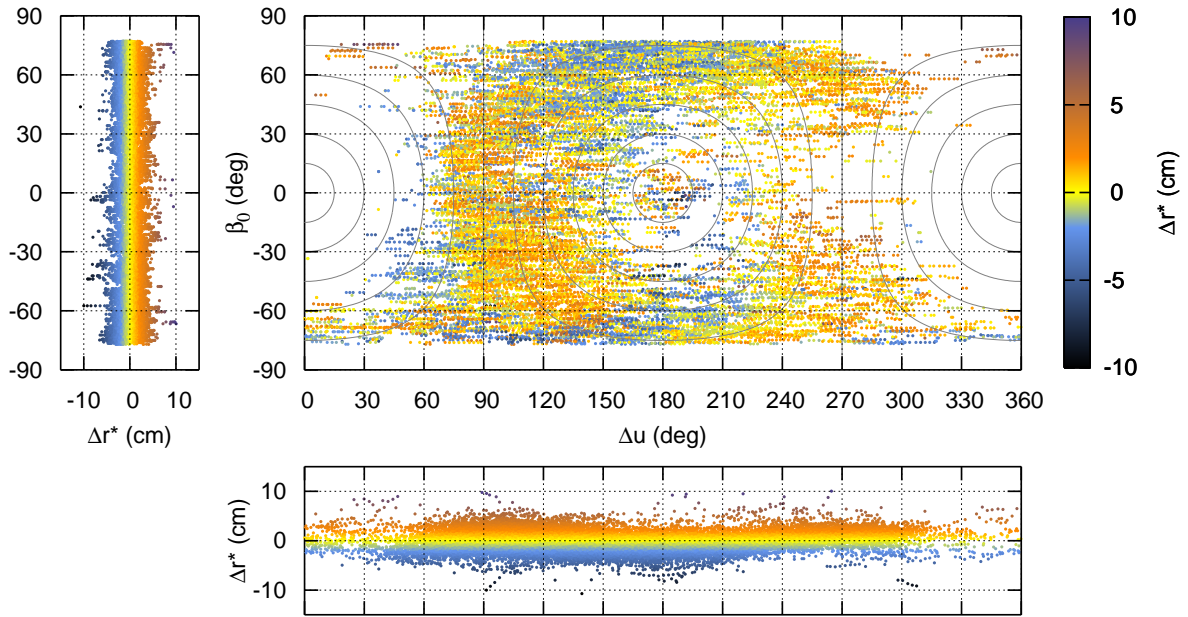


Figure 5.5: SLR residuals  $\Delta r^*$  derived from reprocessed orbits using the CODE SRP model for the GPS satellites G05 and G06 in the  $(\Delta u, \beta_0)$  coordinate system; **bottom:** projection onto  $\Delta u$ -axis; **left:** projection onto  $\beta_0$ -axis; circles represent the phase angle  $E$ ,  $15^\circ$  spacing,  $0^\circ$  at center ( $\Delta u = 180^\circ$  and  $\beta_0 = 0^\circ$ ),  $180^\circ$  at ( $\Delta u = 0^\circ$  and  $\beta_0 = 0^\circ$ )

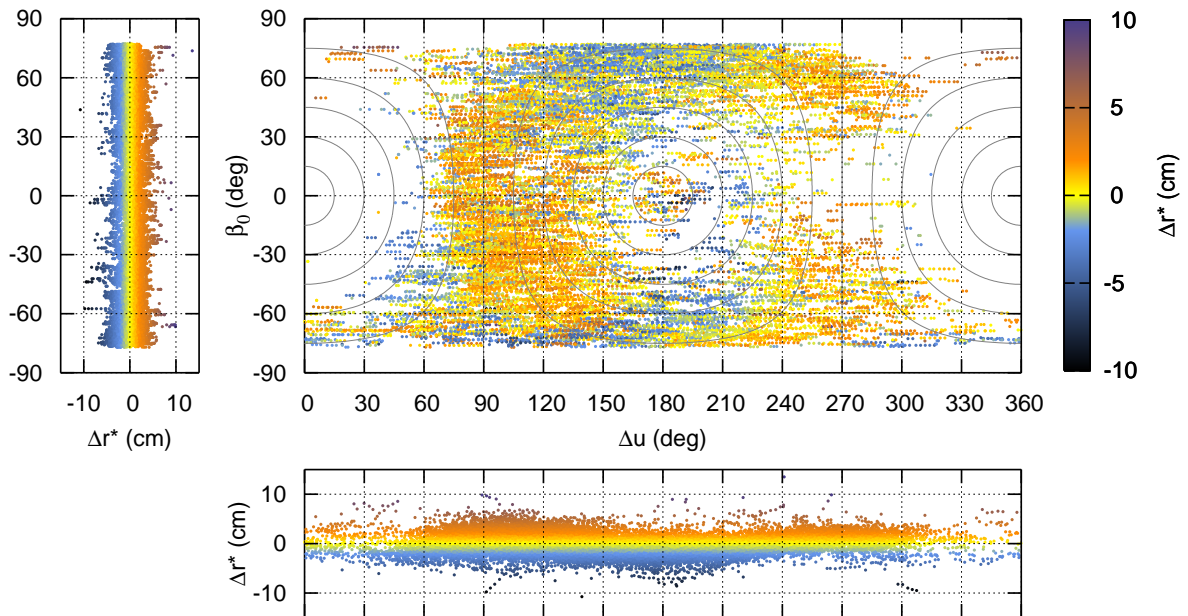


Figure 5.6: SLR residuals  $\Delta r^*$  derived from reprocessed orbits using the NONE SRP model for the GPS satellites G05 and G06 in the  $(\Delta u, \beta_0)$  coordinate system; **bottom:** projection onto  $\Delta u$ -axis; **left:** projection onto  $\beta_0$ -axis; circles represent the phase angle  $E$ ,  $15^\circ$  spacing,  $0^\circ$  at center ( $\Delta u = 180^\circ$  and  $\beta_0 = 0^\circ$ ),  $180^\circ$  at ( $\Delta u = 0^\circ$  and  $\beta_0 = 0^\circ$ )

PRN	$\sigma$ (cm)			$\bar{x}$ (cm)			# $\Delta r$
	ROCK	CODE	NONE	ROCK	CODE	NONE	
G05	2.2	1.9	1.9	-4.2	-3.9	-3.7	10700
G06	2.6	2.1	2.2	-4.4	-3.8	-3.6	10400
R03	4.9	5.0	4.9	-1.2	-1.2	-1.3	25000
R22	4.8	4.9	4.8	-0.8	-0.9	-0.8	24400
R24	5.1	5.0	5.0	-1.0	-0.8	-0.8	12100
R07	5.3	5.4	5.3	-0.0	-0.2	-0.2	6900

Table 5.1: Statistical information of the SLR residuals derived from more than four years of microwave-based GNSS orbits using different SRP a priori models (ROCK, CODE, NONE): standard deviation  $\sigma$ , mean value (range bias)  $\bar{x}$ , and approximated number of SLR residuals #  $\Delta r$

residuals  $\Delta r$  of the two GPS satellites as a function of time for the two orbit time series using the ROCK and the CODE model. The large negative residuals of  $-10$  to  $-15$  cm (including the range bias of about  $-4$  cm) that occur for the orbit series using the ROCK model are reduced for the orbits using the CODE model. This fact is also well illustrated by Fig. 5.5, showing the color-coded range residuals  $\Delta r^*$  in the  $(\Delta u, \beta_0)$  coordinate system for GPS orbits using the CODE SRP model. A range bias of about  $-4$  cm was subtracted from the residuals. Although there is still a systematic pattern, it is much reduced. Note that the largest residuals of  $-10$  cm in the center of the figure, and thus close to the shadow region, disappear. The same is true for orbits using the NONE model, i.e. using no SRP a priori model at all, see Fig. 5.6. Both, Figs. 5.5 and 5.6, and thus both series of range residual are very similar.

This means that both, the use of the CODE SRP a priori model and not using any SRP a priori model, reduce the SLR residuals and thus improve the GPS orbits, at least for the two GPS satellites G05 and G06. This result is supported by the validation results of the GFZ and the JPL final orbits presented in the previous chapter in Sect. 4.2.2. Both analysis centers, GFZ and JPL, use ROCK or ROCK-like SRP a priori models and show similar periodic patterns in the SLR residuals.

At the European Space Operations Centre (ESOC, Darmstadt, Germany) SLR validation of GPS final orbits was performed for 2006 using another software package, namely the Navigation Package for Earth Orbiting Satellites (NAPEOS). The validated orbit series have been the final orbits of CODE, JPL, MIT (Massachusetts Institute of Technology, Cambridge, U.S.A.), and SIO (Scripps Institution of Oceanography, San Diego, U.S.A.). The orbits of CODE and JPL have been generated using the ROCK or a ROCK-like model, whereas the orbits of MIT and SIO have been generated without using any SRP a priori model. For the CODE and JPL orbits the periodic pattern is clearly visible in the SLR residuals, for the MIT and SIO orbits there is no significant pattern observable (Springer, 2008). These results confirm our conclusion that the ROCK model causes the periodic signature in the SLR residuals and should thus not be used, at least not for the Block II/IIA satellites. Unfortunately, there is no independent validation

possible for Block IIR type satellites, as only two of the GPS satellites of type Block IIA are equipped with LRAs.

In principle, a SRP a priori model is applied to account for (existing) signals that cannot be reconstructed by the estimated parameters. An a priori model may, however, be destructive, if it includes non-existing signals, which might be the case for the ROCK model.

The mean biases of the SLR residuals are also given in Table 5.1. We found a negative range bias of about  $-4.3$  cm for the GPS satellite orbits using the ROCK model. This value is about  $0.5$  cm larger than the mean bias of the range residuals derived from the CODE final orbits in the previous chapter. As opposed to the validation of the CODE final orbits, we now applied the translations estimated for the GNSS network, in order to obtain orbit and SLR site coordinates in the same reference frame. This translation causes the increase of the range biases, because the SLR sites are not very well distributed and most of the sites are located in the Northern hemisphere.

The range biases for the orbits using the CODE or the NONE SRP model are between  $-3.6$  cm and  $-3.9$  cm, which is smaller by about  $0.5$  cm compared to the orbits using the ROCK model. This is due to the large negative residuals that are no longer present when using the CODE or the NONE model.

The standard deviations of the range residuals for the GLONASS satellites, given in Table 5.1, are about  $5$  cm, which is twice the value as for the GPS satellites. There is no significant difference in the standard deviations of the three orbit series using different SRP a priori models. The same holds for the GLONASS range biases. They are about  $-1$  cm for the GLONASS satellites and close to zero for the GLONASS-M satellite R07. The impact on GLONASS orbits of using the ROCK or the NONE model for GPS satellites is negligibly small as expected. No systematic pattern was found in the GLONASS range residuals for the three orbit series, which confirms the GLONASS orbit validation results in Sect. 4.2.2.

### 5.2.2 . . . by Analyzing Orbit Differences

In this section we study the orbit differences between the three orbit series generated for the GPS satellites using different SRP a priori models. As opposed to the SLR validation, the orbit differences are available for all GPS satellites. In addition, all ranges of  $\Delta u$  and  $\beta_0$  are covered when analyzing more than one year of orbit series. This analysis does not, however, provide absolute information on the orbit accuracy, but only relative information of one orbit with respect to the other.

The orbit differences in radial direction can be compared with the SLR residuals. Although the radial direction may differ slightly from the direction SLR site-satellite, only about 3% (at maximum) of the radial orbit differences do not map into the SLR residual for a satellite observed at low elevation.

For each day of the year 2005 the radial differences between the orbits estimated using the ROCK SRP model and those using the CODE SRP model are analyzed. Figure 5.7 shows

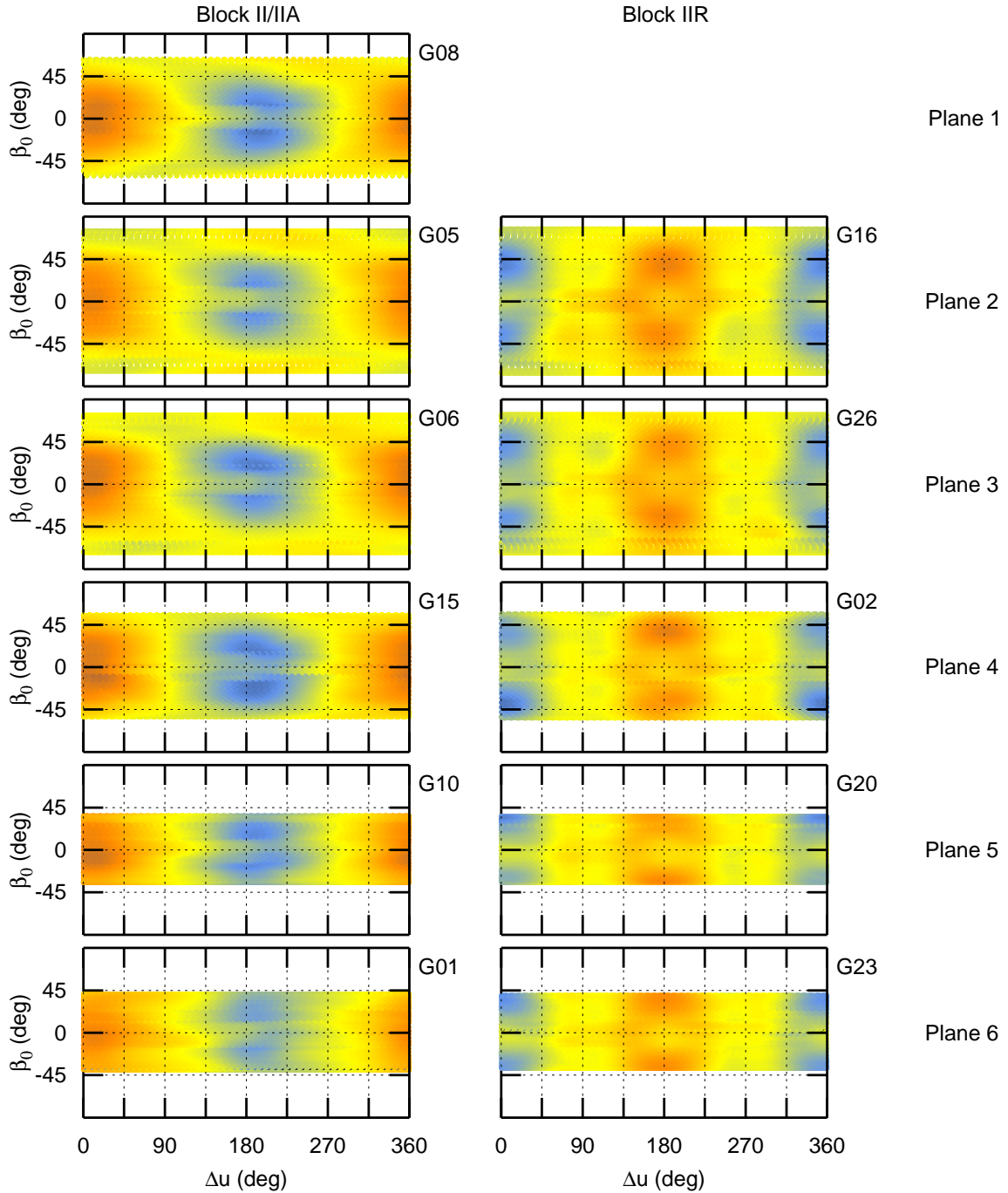


Figure 5.7: Radial orbit differences between orbits estimated using the ROCK and the CODE SRP a priori model for the GPS satellites in 2005; the color code is identical to Fig. 5.3, red corresponds to 6 cm, yellow corresponds to 0 cm, blue corresponds to -6 cm

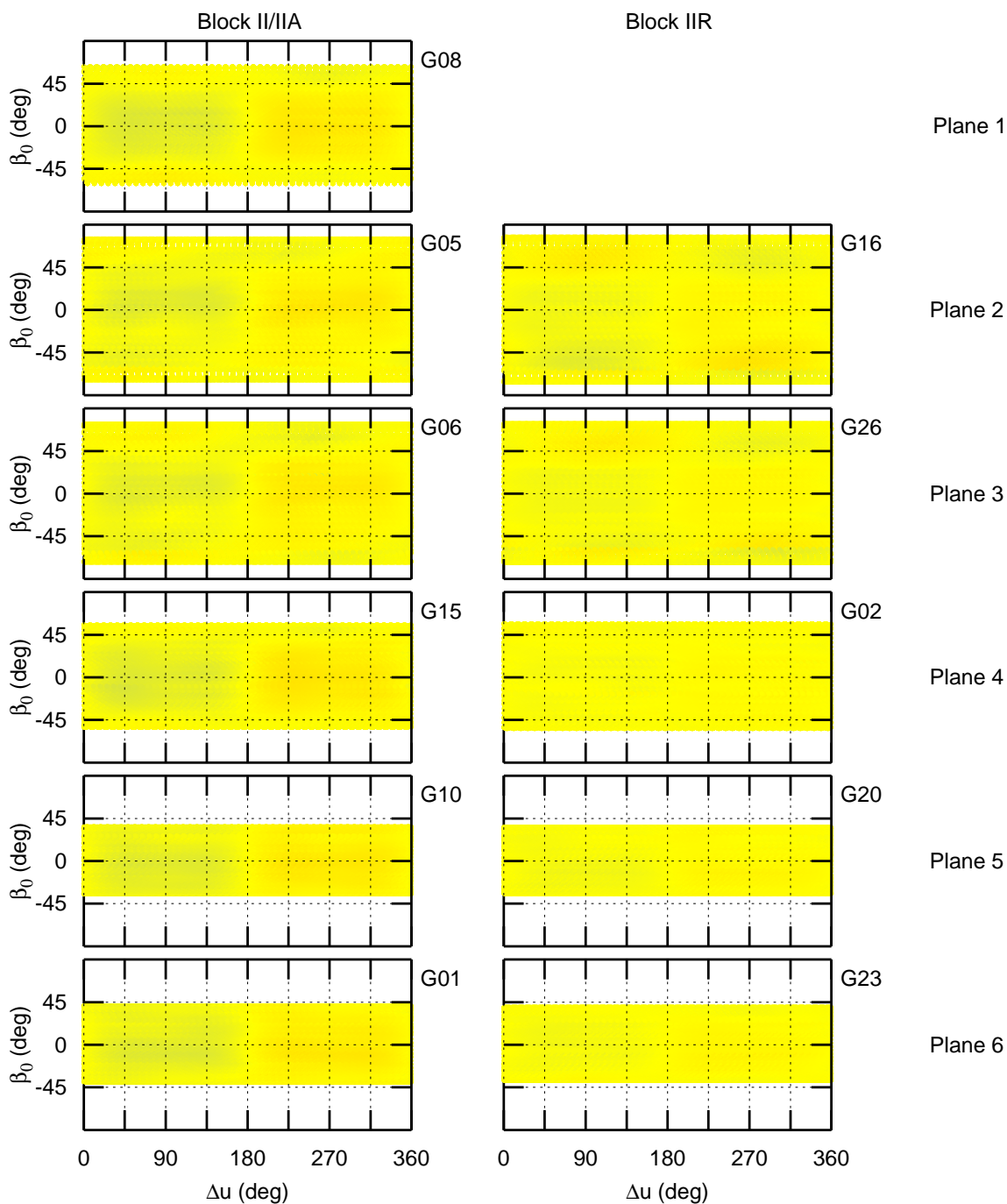


Figure 5.8: Radial orbit differences between orbits estimated using the CODE and the NONE SRP a priori model for the GPS satellites in 2005; the color code is identical to Fig. 5.3, red corresponds to 6 cm, yellow corresponds to 0 cm, blue corresponds to -6 cm

these differences as a function of  $\Delta u$  and  $\beta_0$  for two GPS satellites of each of the six orbital planes, except for plane 1 (there was no Block IIR satellite in this plane during the analyzed time interval). The orbit differences in the first column refer to Block II/IIA satellites whereas the second column shows orbit differences for Block IIR satellites. The range of  $\beta_0$  is given by the maximum elevation angle, which depends on the orbital plane, and changes slowly in time, i.e., with the regression rate of the ascending nodes of about  $14^\circ/\text{year}$  (see Sect. 3.1.1).

For comparison with the SLR residuals, the graphical presentation and the color code are the same as in the figures of Sect. 5.2.1, which show the SLR residuals as a function of  $\Delta u$  and  $\beta_0$ . We observe a pattern for the radial orbit differences of all Block II/IIA satellites that is similar to the SLR residuals of the satellites G05 and G06. In the center of the figure (around  $\Delta u = 180^\circ$ ) negative orbit differences up to  $-6$  cm (in blue) are present, whereas at the edges (around  $\Delta u = 0^\circ$ ) the differences are positive and reach up to  $+6$  cm (in red). Note that the orbit differences for the Block IIR satellites show the inverted pattern of the orbit differences for the Block II/IIA satellites.

We conclude that the orbit differences (using the ROCK and the CODE SRP model) are clearly block-specific. We already know from the SLR validation that for the satellites G05 and G06 the use of the CODE SRP model improves the orbits. We therefore assume that the CODE SRP model is superior to the ROCK model for all satellites of Block II/IIA, as the presented orbit differences are similar for all Block II/IIA satellites.

It was already pointed out that an independent validation of the orbits of Block IIR satellites using SLR is not possible. Therefore we cannot prove that the CODE model is superior to the ROCK model for all satellite types.

Figure 5.8 shows the orbit differences between orbits estimated using the CODE and the NONE model. Apart from small differences on the millimeter level both orbits are similar for Block II/IIA and Block IIR satellites, at least in the analyzed radial direction. The CODE SRP a priori model does not seem to be relevant, if in addition the dynamical parameters  $D0, Y0, B0, BS, BC$  are estimated. The values of the resulting accelerations due to SRP are similar when using the CODE or no SRP a priori model.

The difference between the accelerations derived from the ECOM model using the CODE and no SRP a priori model was illustrated in Fig. 5.2. Figure 5.2 shows the estimated accelerations for the GPS satellite G06 using the three different SRP a priori models ROCK, CODE, and NONE. The Y-accelerations are almost identical for all three models. In B-direction the accelerations of CODE and NONE are very similar. The accelerations of the ROCK model are similar to that of the other models only for high values of  $\beta_0 \geq 45^\circ$ . In D-direction, the accelerations derived with the CODE model show small variations with a twice-per-revolution period. Their mean values should correspond to the constant values of the NONE model (according to the theory of least squares, which they do not in Fig. 5.2 for unknown reasons). Thus the D-accelerations due to the CODE model are much closer to those derived with the NONE model than the D-accelerations derived with the ROCK model. The latter show large variations, especially for small angles of  $\beta_0$ , due to the a priori model. We conclude that the main accelerations due to the CODE SRP a priori model can be very well reproduced by the estimation of the five SRP parameters ( $D0, Y0, B0, BS,$  and  $BC$ ) (without using any SRP a priori model).

As both, the CODE and the NONE model, seem to lead to better orbits than the ROCK model (at least for the Block II/IIA satellites), the question arises whether an a priori SRP model is necessary at all. If dynamical orbit parameters, i.e., constant values in D-, Y-, and B-direction and periodic terms in B-direction, are estimated, GNSS orbit determination could be done without the use of an a priori SRP model (at least for Block II/IIA type satellites), unless a better model is found. For orbit prediction a good SRP a priori model is, however, indispensable, as there are no observations available that allow to estimate the dynamic orbit parameters.

### 5.2.3 . . . by Analyzing Orbit Predictions

In this section we show that good a priori models are necessary for orbit predictions. It is possible to assess the quality of the a priori models by analyzing orbit predictions. We will now compare orbit predictions that have been generated by using the three different a priori models ROCK, CODE, and NONE.

The orbits are predicted over 15 days by expanding the estimated three-day arc over the 15 days. This is done by numerical integration using the parameters of the three-day arc. These estimated orbits used for integration are exactly those introduced in Sect. 5.1, i.e., they correspond to the CODE final orbit product, but differ in the used SRP a priori model. The estimated orbit parameters are the six Keplerian elements and the two dynamical parameters  $D0$  and  $Y0$ , which are the direct SRP and the Y-bias, respectively. No other dynamical parameters are estimated. The orbit predictions are generated for 73 days in 2005.

For the SRP model verification we analyze for each day the difference  $|\vec{r}_p(t) - \vec{r}_t(t)|$  between the 15<sup>th</sup> day of prediction and the estimated orbit of the same day. Figure 5.9 shows the mean values of the orbit differences  $|\vec{r}_p(t) - \vec{r}_t(t)|$ , averaged over one day, as a function of time for six GPS satellites in six orbital planes. Each daily mean value is represented by a dot. The gray dots correspond to orbits based on the ROCK model, the black dots are based on the CODE model, and the empty dots on the NONE model. On the vertical axis (left), the scale of the orbit differences is given in meters. The gray line represents the elevation angle  $\beta_0$  of the Sun above the orbital plane. The corresponding scale is provided on the right-hand side.

The orbit differences are dominated by the along-track component. They are of the order of about 10 – 100 m. In fact, after 15 days of prediction, without any use of observation data, the predicted GPS orbit differ by about 100 m in maximum. In most cases the orbits using the CODE SRP model show smaller values than those using the ROCK or the NONE model.

Figure 5.9 tells that the orbit prediction is of excellent quality, if the satellites are never in the Earth's shadow (planes 1, 4, 6). Figure 5.10 repeats this figure with an extended scale of the ordinate. The superiority of the CODE model for orbit prediction is now obvious.

Figure 5.9 also tells that orbit prediction is problematic whenever a satellite is in the Earth's shadow (for  $|\beta_0| \leq 14^\circ$ ) at some time in the prediction interval (see planes 2, 3, and 5). This underlines that the behavior of the satellites during eclipse may not be predicted in a reliable way. In particular for the Block II/IIA type satellites the satellite's attitude is unknown for up to 30 min after the re-entry of the satellite into sunlight (see Sect. 3.1.2).

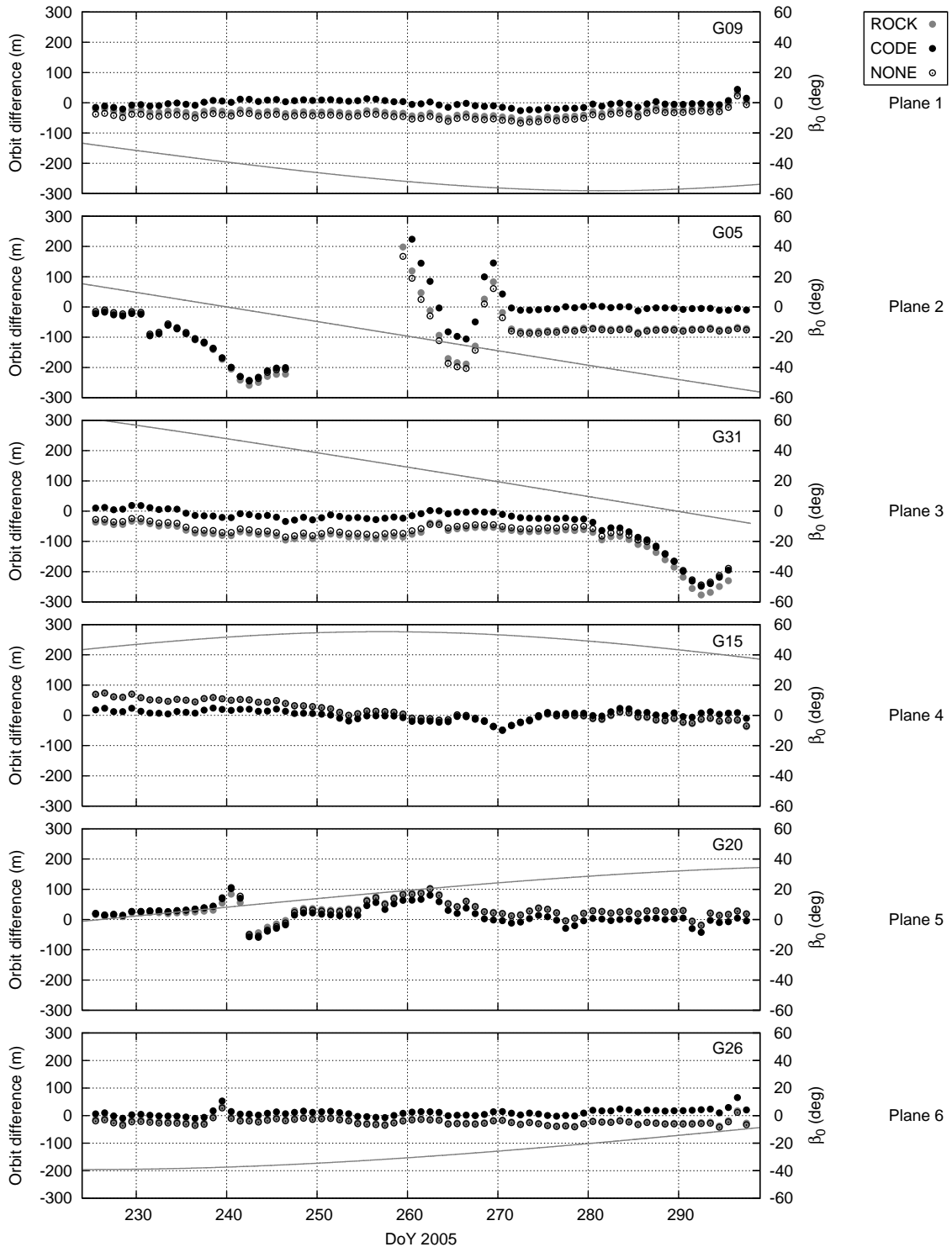


Figure 5.9: Orbit differences for the GPS satellites (one per orbital plane) between the 15<sup>th</sup> day of prediction and the corresponding estimated orbit for all three SRP models used: ROCK, CODE, and NONE; in addition the Sun elevation angle  $\beta_0$  is indicated by the grey line

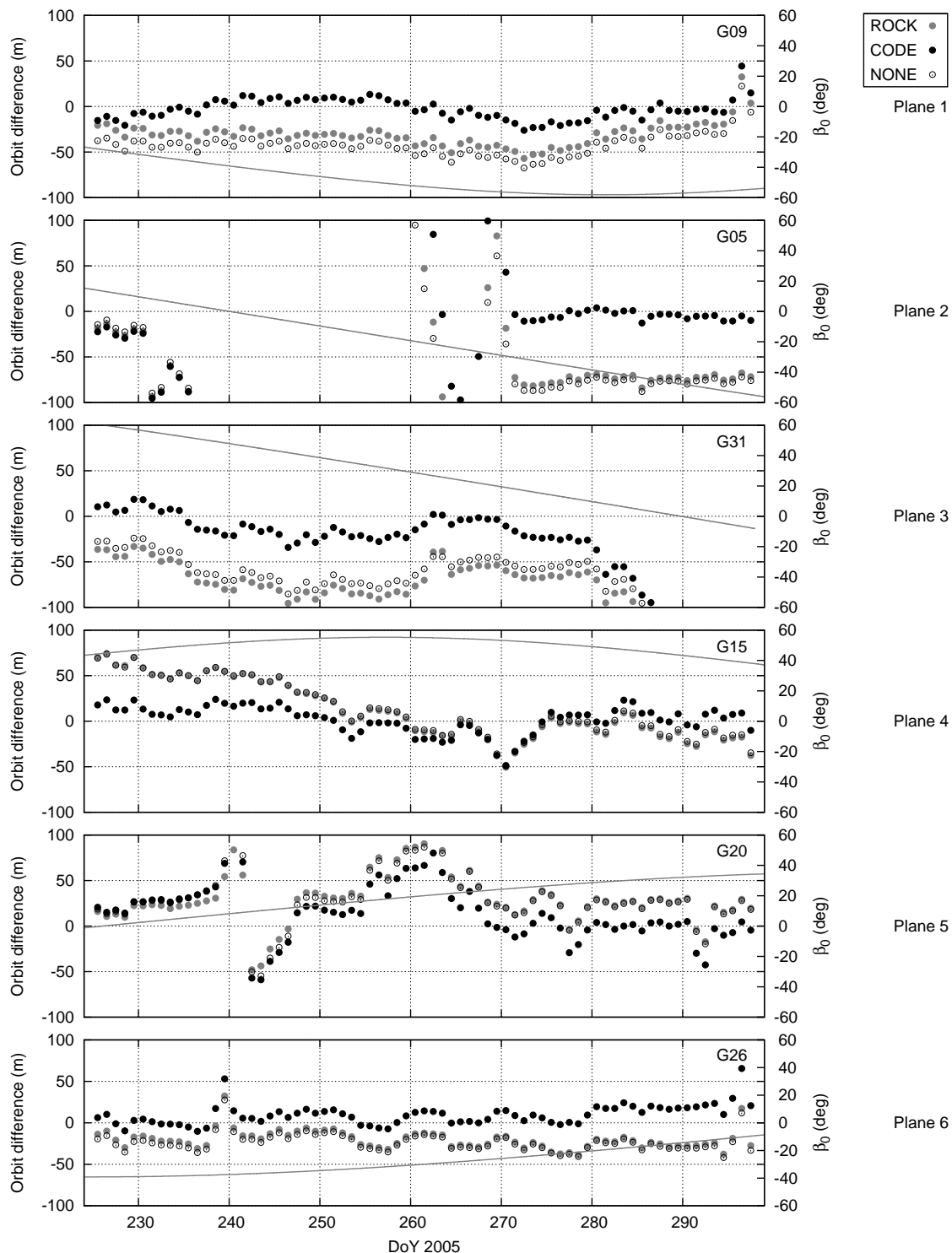


Figure 5.10: Orbit differences for the GPS satellites (one per orbital plane) between the 15<sup>th</sup> day of prediction and the corresponding estimated orbit for all three SRP models used: ROCK, CODE, and NONE; in addition the Sun elevation angle  $\beta_0$  is indicated by the gray line (the scale differs from Fig. 5.9)

Satellite G05 in orbital plane 2 (see Fig. 5.9, second subfigure) is a Block IIA satellite. Unfortunately, 12 days of estimated orbits (DoY 232-243) were missing for G05, which leads to the missing orbit predictions (DoY 247-258). From DoY 225 until 255 the satellite passes the Earth's shadow once per revolution; at DoY 240 the maximum duration of the shadow passing is reached, as  $\beta_0 = 0$ . These shadow passings affect the orbit predictions from DoY 240-270. In this time period there are (beside the missing days) easily recognizable large orbit differences (up to 250 m) for the Block IIA type satellite G05. At DoY 271 the orbit differences get small again, as the first day used for the generation of the orbit prediction of DoY 271 is the first day (DoY 256) after the eclipsing period, for which no further shadow passes occur.

A similar behavior of the orbit differences can be found for the satellite G31 in plane 3 (see third subfigure in Fig. 5.9). This satellite is also of type Block IIA and shows large orbit differences of up to 300 m when shadow passings occur. In contrary to the Block IIA satellites, the attitude of the Block IIR satellite is known. Thus the orbit predictions are much better, as we can see for the Block IIR satellite G20 in plane 5 (subfigure 5 in Fig. 5.9). The maximum orbit differences are about 100 m.

Figure 5.11 shows the daily mean values of the orbit differences for two GLONASS satellites in two different orbital planes. (The third plane was not occupied in 2005). For both planes satellite eclipses occur. For the predictions not affected by occultations, the orbit differences are at the order of a few 10 meters. There is no difference between ROCK and NONE observable for the GLONASS satellites, as the impact of the GPS satellites on GLONASS orbit determination is negligible small. Modeling problems during eclipse periods are obvious.

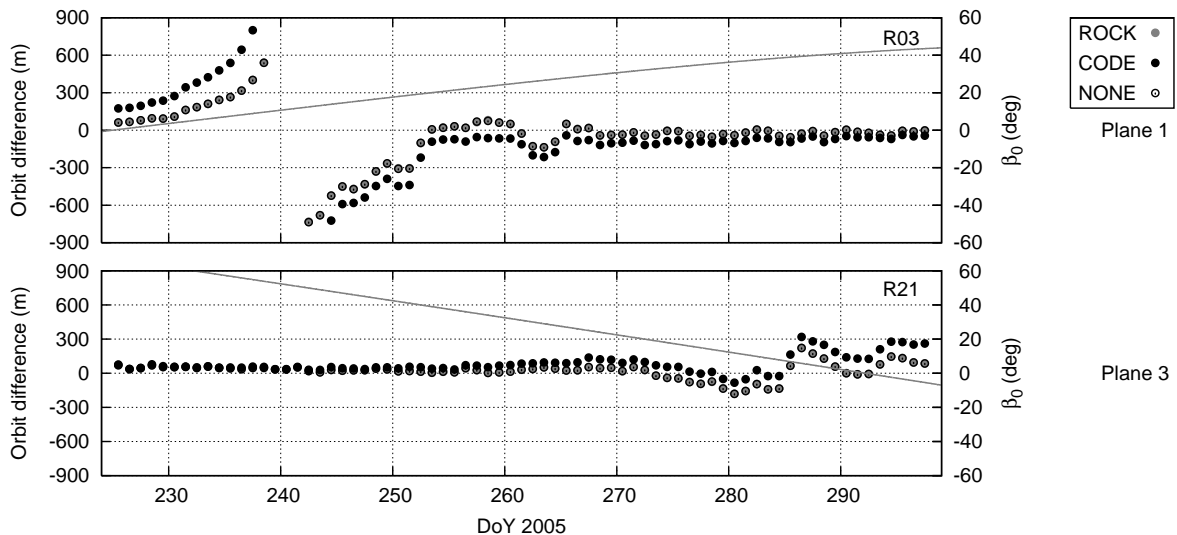


Figure 5.11: Orbit differences for the GLONASS satellites (one per orbital planes) between the 15<sup>th</sup> day of prediction and the corresponding estimated orbit for all three SRP models used: ROCK, CODE, and NONE; in addition the Sun elevation angle  $\beta_0$  is indicated by the gray line

## 5 Improvement of the GNSS Orbit Model

Figure 5.12 shows the root mean square (RMS) deviation of the daily mean values of the orbit differences from their arithmetic mean for all GPS satellites used, and Fig. 5.13 for all GLONASS satellites used. On the horizontal axis the satellite numbers are given ordered by orbital planes.

The daily mean values of the orbit differences for eclipsing orbits of Block IIA satellite have been excluded from the RMS computation, i.e. for the GPS satellites G05 and G30 in plane 2, for G03, G06, G07, and G31 in plane 3, and for G10 in plane 5. The orbit predictions generated with the CODE SRP model show much smaller RMS values than those generated with the

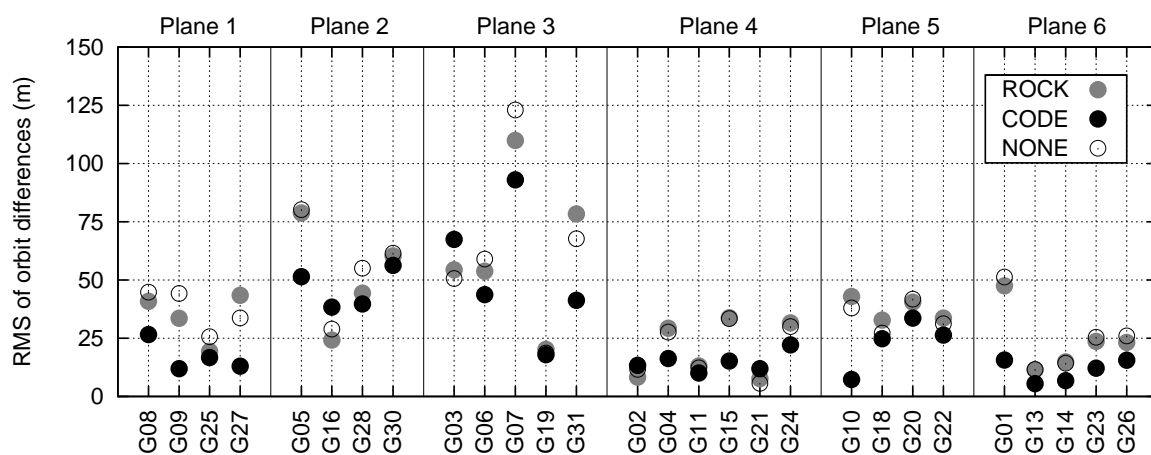


Figure 5.12: RMS of 73 orbit differences for the GPS satellites between the 15<sup>th</sup> day of prediction and the corresponding estimated orbit for the three SRP models used: ROCK, CODE, and NONE

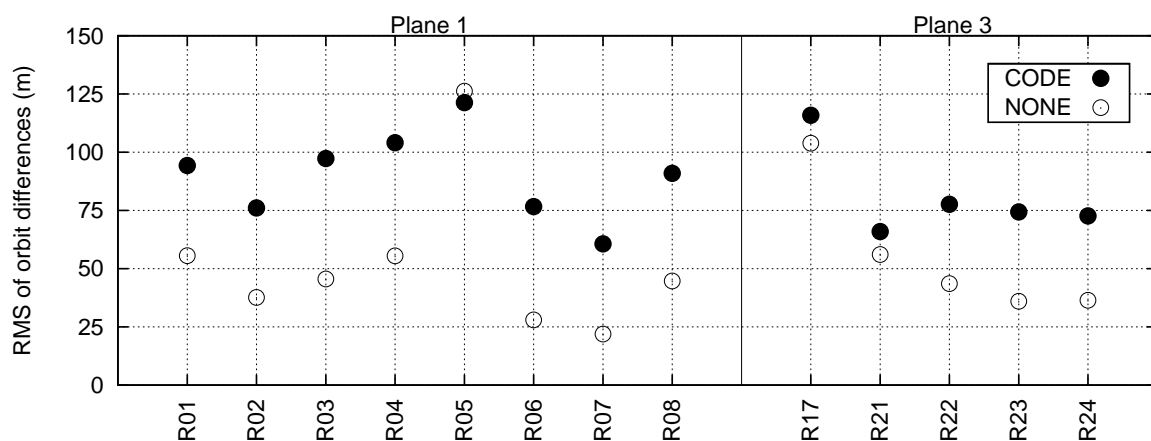


Figure 5.13: RMS of 73 orbit differences for the GLONASS satellites between the 15<sup>th</sup> day of prediction and the corresponding estimated orbit for the two SRP models used: CODE and NONE

ROCK or the NONE model. There is no significant difference observable between the ROCK and the NONE model.

In the case of GLONASS it makes only sense to compare the CODE and the NONE model, as the impact of the ROCK model (used for the GPS satellites) on the GLONASS orbits is negligible small. The orbit solutions using the ROCK and the NONE model are thus similar for the GLONASS satellites. As for the GPS Block IIA satellites, we excluded the daily mean values of the orbit differences for eclipsing GLONASS orbits for the RMS computation. The differences derived from orbits using the CODE model show much larger RMS values than those derived from orbits based on no SRP model at all. This is surprising, because it means that the CODE SRP model for GLONASS satellites degrades the orbit predictions and should thus not be used. A better and independent parameterization for the estimation of the CODE SRP model is necessary, as the current parameterization was adapted from the CODE SRP model used for the GPS satellites.

#### 5.2.4 ... by Analyzing Orbit Overlap Errors of One-day and Three-day Arcs

In this section we analyze orbit overlap errors at the day boundaries of the three GNSS orbit series generated using the ROCK, the CODE and the NONE SRP a priori models. Remember that these orbits have been generated by computing one-day arc solutions first, which were stacked to obtain the three-day arcs. We have therefore orbit series available with arc-lengths of one and of three days, respectively, for each of the three SRP models. The orbits resulting from the three-day arc solution are the central 24 hours of the three-day arcs. The orbit overlap errors are computed for each satellite as the difference  $|\vec{r}_i(t) - \vec{r}_{i+1}(t)|$  of two consecutive arcs evaluated at the day boundary of days  $i$  and  $i + 1$ . The overlap errors are then transformed into the radial, along-track and out-of-plane directions. Overlap time series covering about four years were analyzed for the one- and three-day arc orbit solutions listed in Table 5.2.

The analyses of these long time series of orbit overlap errors should answer the following questions: Are there systematic discontinuities at the day boundaries indicating errors in the GNSS orbits? If yes, what is the impact of using different SRP a priori models?

Orbit overlaps based on	one-day arc length			three-day arc length		
	ROCK	CODE	NONE	ROCK	CODE	NONE
GPS	✓	✓	✓	✓	-	✓
GLONASS	-	✓	✓	-	-	✓

Table 5.2: Overlap time series analyzed for one-day and three-day arc orbit solutions

### Overlap Errors of Daily One-day Arc Solutions for GPS Satellites

Figure 5.14 shows the orbit overlap errors in all three directions (radial, along-track, and out-of-plane) for one GPS Block IIA satellite (G05) derived from the one-day arc solutions using the ROCK model (in gray) and the CODE model (in black). We can clearly see a systematic behavior of the overlap errors in time in all three components. The systematic pattern repeats with a nearly annual period. The largest component is the along-track component, for which the overlap errors may reach values up to  $\pm 30$  cm. The standard deviations of the overlap errors are 3.6 cm, 9.5 cm, and 5.5 cm in radial, along-track, and out-of-plane direction, respectively. The mean values are about  $-0.4$  cm for the radial and about  $-1$  cm for the other two components.

There are only very small differences between the two orbit solutions using the ROCK and the CODE SRP model. The general characteristic of the overlap time series remains the same, independently of the used SRP a priori model. This result was not expected for the Block IIA satellite, as we have seen large differences between the Block IIA orbits using the ROCK and the CODE model (see Sect. 5.2.1). The overlap errors for the NONE model are not included in the figure, as they are almost identical with those of the CODE model.

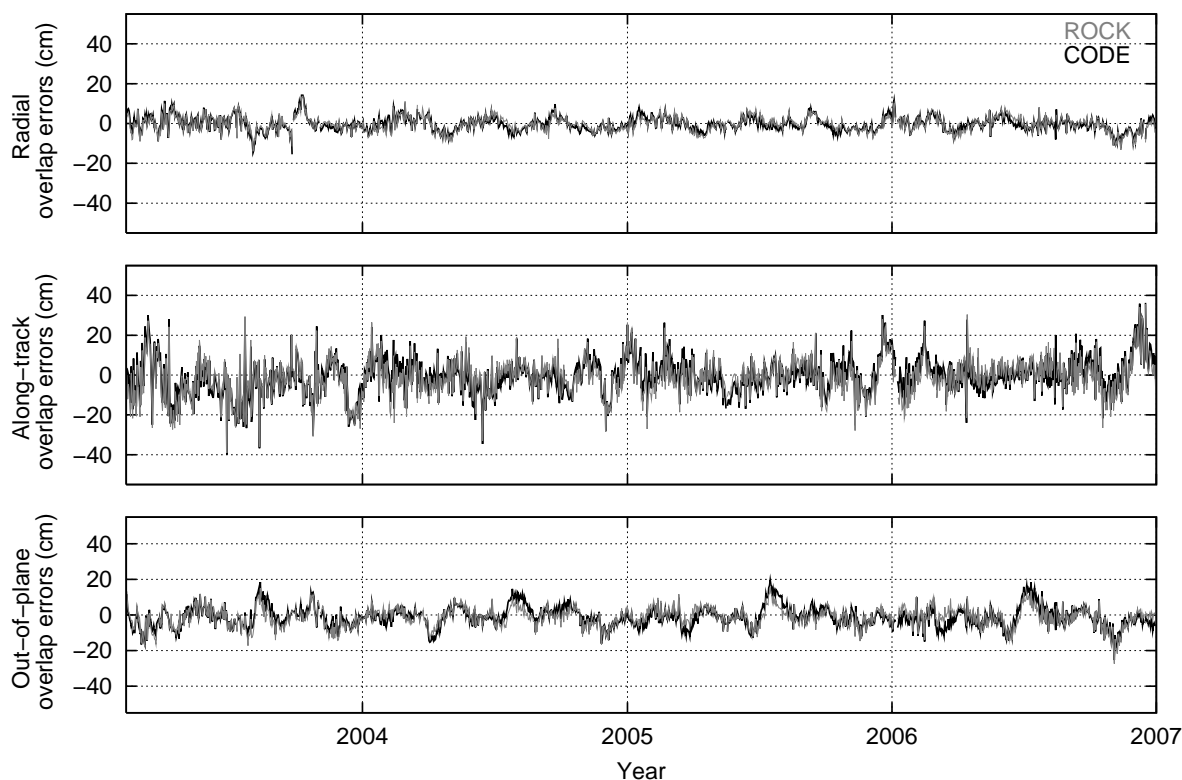


Figure 5.14: Orbit overlap errors of the GPS satellite G05 derived from one-day arcs using the ROCK and the CODE SRP a priori model

The along-track components of the overlap errors of 24 GPS satellites are shown in Fig. 5.15. Although 35 GPS satellites were observed during the considered time interval, 11 satellites were not available for the entire time span of our analysis. The orbits in Fig. 5.15 are one-day arcs using the CODE model. For most of the GPS satellites there is no obvious difference when using another SRP a priori model. We show the along-track component as it has the largest overlap values with a very systematic behavior. In the Appendix C also the corresponding figures for the radial (Fig. C.3) and the out-of-plane (Fig. C.5) components can be found.

The along-track overlap errors are shown separately for each satellite and the satellites are sorted according to their orbital plane. The overlap errors for the first satellite G05 were already shown in Fig. 5.14, from which the scale of the graphs can be derived. For the satellites in orbital plane 2 we observe a clear systematic pattern repeating nearly annually and similarly for all satellites. The same pattern can be observed for the satellites of planes 3 and 1, whereas the prominent amplitudes decrease from plane 2 over plane 3 to plane 1.

The maximum values of the Sun's elevation angle over the orbital plane decreases from about  $|\beta_0| \approx 78^\circ$  for plane 2 to  $|\beta_0| \approx 70^\circ$  for plane 1. The values of  $\beta_0$  are given by the gray lines. The overlap errors themselves are marked in gray for time spans during which  $|\beta_0| < 14^\circ$  when the satellites are passing the Earth's shadow during one orbital revolution. We could, however, not find a correlation between the periodic pattern of the overlap errors and the eclipsing periods. The main structure of the overlap pattern remains similar in time for the satellites of planes 1, 2, and 3, whereas the eclipsing periods for each orbital plane are shifted in time. The overlap errors of the satellites of the remaining planes 4, 5, and 6 also show a plane-specific behavior, but the pattern is not similar to the one of the other orbital planes.

Although the patterns of each orbital plane seem not to be correlated with the plane-specific eclipsing periods, we observe for planes 2 and 3 the most prominent peaks in the overlap pattern at maximum values of  $\beta_0$ . As the orbital planes are affecting each other within one parameter estimation process, it is imaginable that the pattern caused by one orbital plane (e.g., plane 2 or 3) impacts the other planes. To find out whether this is true, it would be interesting to see what happens to the overlap errors if the satellites of the (supposedly) causing orbital plane would be skipped in the parameter estimation (for future studies).

Table 5.3 summarizes the standard deviations and mean values of the overlap errors in the along-track direction for the GPS satellites (ordered in the same way as in Fig. 5.15). The first three columns give the standard deviations of the overlap errors derived from the one-day arc solutions  $\sigma_{1d}$  for the three orbit time series using the ROCK, the CODE, and the NONE SRP a priori model. The values of  $\sigma_{1d}$  are very similar for the three orbit series. They are also similar for all satellites corresponding to the same orbital plane. But the standard deviations decrease from plane 2 with the largest maximum value of angle  $|\beta_0| \approx 78^\circ$  to plane 5 with the smallest maximum value of  $|\beta_0| \approx 40^\circ$ , due to the plane-specific periodic pattern. Thus  $\sigma_{1d}$  is about 9–10 cm for plane 2, 8–9 cm for plane 3, 7–8 cm for plane 1, 6–7 cm for plane 4, 6 cm for plane 6, and 5–6 cm for plane 5. The mean values of the along-track overlap errors are mainly negative and assume values between –6 cm and +1 cm.

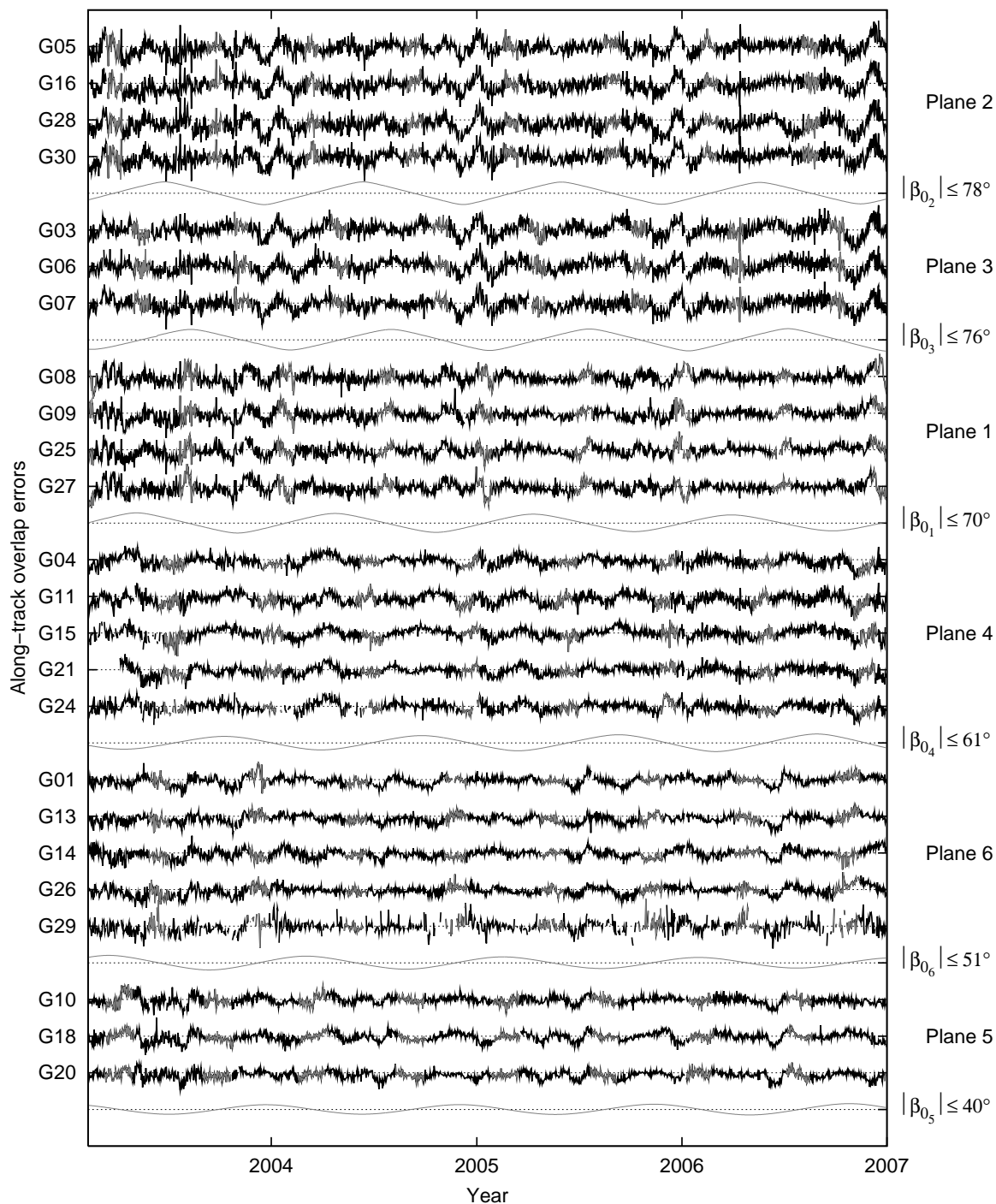


Figure 5.15: Orbit overlap errors in along-track direction of 24 GPS satellites derived from one-day arcs using the CODE SRP a priori model; the elevation angle  $\beta_0$  of the Sun above the orbital plane is given by the gray line; eclipsing periods are marked in gray; for the scale of the y-axis see Fig. 5.14

PRN	$\sigma_{1d}$ (cm)			$\sigma_{3d}$ (cm)		$\bar{x}_{1d}$ (cm)			$\bar{x}_{3d}$ (cm)	
	ROCK	CODE	NONE	ROCK	NONE	ROCK	CODE	NONE	ROCK	NONE
<i>Plane 2</i>										
G05	9.5	9.5	9.5	8.6	8.6	-0.7	-1.4	-1.4	-2.2	-2.2
G16	9.0	9.4	9.4	8.6	8.5	-2.4	-2.8	-2.8	-2.3	-2.4
G28	9.9	9.9	9.9	8.5	8.6	-5.3	-6.2	-6.2	-2.5	-2.6
G30	9.3	9.3	9.3	8.6	8.6	-0.6	-1.1	-1.1	-2.2	-2.1
<i>Plane 3</i>										
G03	9.2	9.3	9.3	7.8	7.7	0.7	0.7	0.7	-2.2	-2.2
G06	8.4	8.9	8.9	7.3	7.2	0.3	0.7	0.6	-1.9	-1.9
G07	8.4	8.7	8.7	7.7	7.5	-2.1	-2.0	-2.1	-2.0	-2.2
<i>Plane 1</i>										
G08	7.8	7.8	7.8	6.1	6.0	-0.4	-1.2	-1.2	-1.4	-1.4
G09	7.6	7.6	7.7	5.8	5.7	-0.8	-1.9	-1.8	-1.4	-1.3
G25	7.2	7.2	7.2	5.4	5.4	-0.3	-1.6	-1.6	-1.3	-1.3
G27	7.1	7.5	7.5	5.6	5.5	-1.0	-1.9	-1.9	-1.4	-1.5
<i>Plane 4</i>										
G04	6.1	6.5	6.4	2.7	2.7	-2.1	-2.3	-2.3	-0.8	-0.9
G11	7.1	7.1	7.1	3.5	3.4	-3.5	-4.2	-4.2	-1.1	-1.2
G15	6.4	6.7	6.7	2.8	2.8	-1.4	-0.8	-0.9	-0.7	-0.7
G21	6.0	6.1	6.1	2.8	2.7	-2.2	-1.6	-1.7	-0.6	-0.6
G24	6.0	6.3	6.3	3.4	3.4	-0.9	-0.8	-0.9	-0.8	-0.8
<i>Plane 6</i>										
G01	5.7	5.8	5.9	1.4	1.4	-0.6	-1.4	-1.4	-0.1	-0.1
G13	5.7	5.5	5.5	1.4	1.5	-2.5	-3.7	-3.8	-0.2	-0.3
G14	5.7	5.9	5.9	1.4	1.5	-1.2	-1.5	-1.5	-0.1	-0.1
G26	5.8	6.0	5.9	1.6	1.6	-0.6	-1.6	-1.5	-0.1	-0.1
G29	8.3	8.4	8.3	6.4	6.6	0.5	-0.4	-0.3	0.2	0.3
<i>Plane 5</i>										
G10	5.5	5.5	5.4	2.1	2.0	-0.7	-1.0	-0.9	0.3	0.3
G18	5.8	5.8	5.8	1.9	1.9	-1.4	-1.3	-1.3	0.3	0.3
G20	5.5	5.2	5.3	2.0	2.0	-2.4	-3.2	-3.2	0.1	0.0

Table 5.3: Statistical information for along-track orbit overlap errors of 24 GPS satellites derived from one-day and three-day arcs using the three SRP a priori models ROCK, CODE, and NONE: standard deviations  $\sigma_{1d}$  and  $\sigma_{3d}$ , and mean values  $\bar{x}_{1d}$  and  $\bar{x}_{3d}$  given in cm

The pattern for the satellite G29 of plane 6 differs significantly from the other satellites of the same orbital plane. This satellite is known to have attitude control problems making orbit modeling very challenging.

The standard deviation of the overlap errors in radial direction are given in Table C.1 in the Appendix C, as well as the corresponding Fig. C.3, which shows the overlap errors of the one-day arc solution using the CODE SRP a priori model. For the radial component we do not see a plane-specific behavior of the overlap errors, although there is still a significant systematic pattern visible in the overlap errors for each satellite. The standard deviation is about 3 – 5 cm, except for the satellite G29, for which it is 9 cm. The mean values of the radial overlap components range between –1 cm and +1 cm.

The statistical information for the out-of-plane component is also given in the Appendix C in Table C.2. Figure C.5 shows the corresponding overlap errors for the one-day arcs using the CODE SRP a priori model. The patterns are systematic, but they are not plane-specific, as for the radial component. The standard deviations of the out-of-plane overlap components seem, however, to be plane-specific. They increase from plane 2 with values of about 5 – 6 cm to about 7 – 8 cm for plane 5. This behavior is opposite to that of the along-track component.

Thus it is interesting to note that a Y-bias, i.e., an acceleration along the solar panel axis, corresponds to an acceleration in the along-track component if the Sun is perpendicular above the orbital plane with  $|\beta_0| = 90^\circ$ , and it corresponds to an acceleration in the out-of-plane component if the Sun is within the orbital plane with  $\beta_0 = 0^\circ$  (except for singularities at noon and midnight turns).

Figure 5.16 shows the estimated Y-biases (without the satellite-specific a priori values) for each of the GPS satellites as a function of time. For a better visibility the Y-biases are alternately marked in black and gray. As the a priori values (not considered in Figure 5.16) differ between the satellites (between about 0 and  $10^{-9}$  m/s<sup>2</sup>), we do not care about the different offsets of the Y-biases at the moment.

More interesting is the general structure of the Y-biases. We observe plane-specific periodic patterns, repeating nearly annually. The peak-to-peak variation of the Y-biases is of the order of  $10^{-9}$  m/s<sup>2</sup>. The largest values of the Y-biases seem to be correlated with extreme values of  $\beta_0$  (which is given in Fig. 5.16 by the gray line for each plane). Let us now display the Y-biases as a function of  $\beta_0$  (see Fig. 5.17), to figure out a possible correlation. The Y-biases show similar patterns for some satellites of one orbital plane, but not for all satellites of that plane; e.g., G05 and G16 show very similar Y-biases, whereas G28 and G30, which are in the same orbital plane, show Y-biases different from those of G05 and G16.

A clear indication for the nearly annual period of the Y-bias pattern is given by the fact that for each satellite the Y-biases repeat as a function of  $\beta_0$ . This means the satellite-specific Y-biases are repeating with the draconitic period. Further analyses are strongly needed to interpret the systematic behavior of the one-day overlaps for GPS satellites and the corresponding Y-biases, which show also a very significant pattern and a clear dependency on  $\beta_0$ .

For all three components of the overlap errors (radial, along-track, and out-of-plane) there are no significant differences for different SRP a priori models. Also we did not find any dependencies

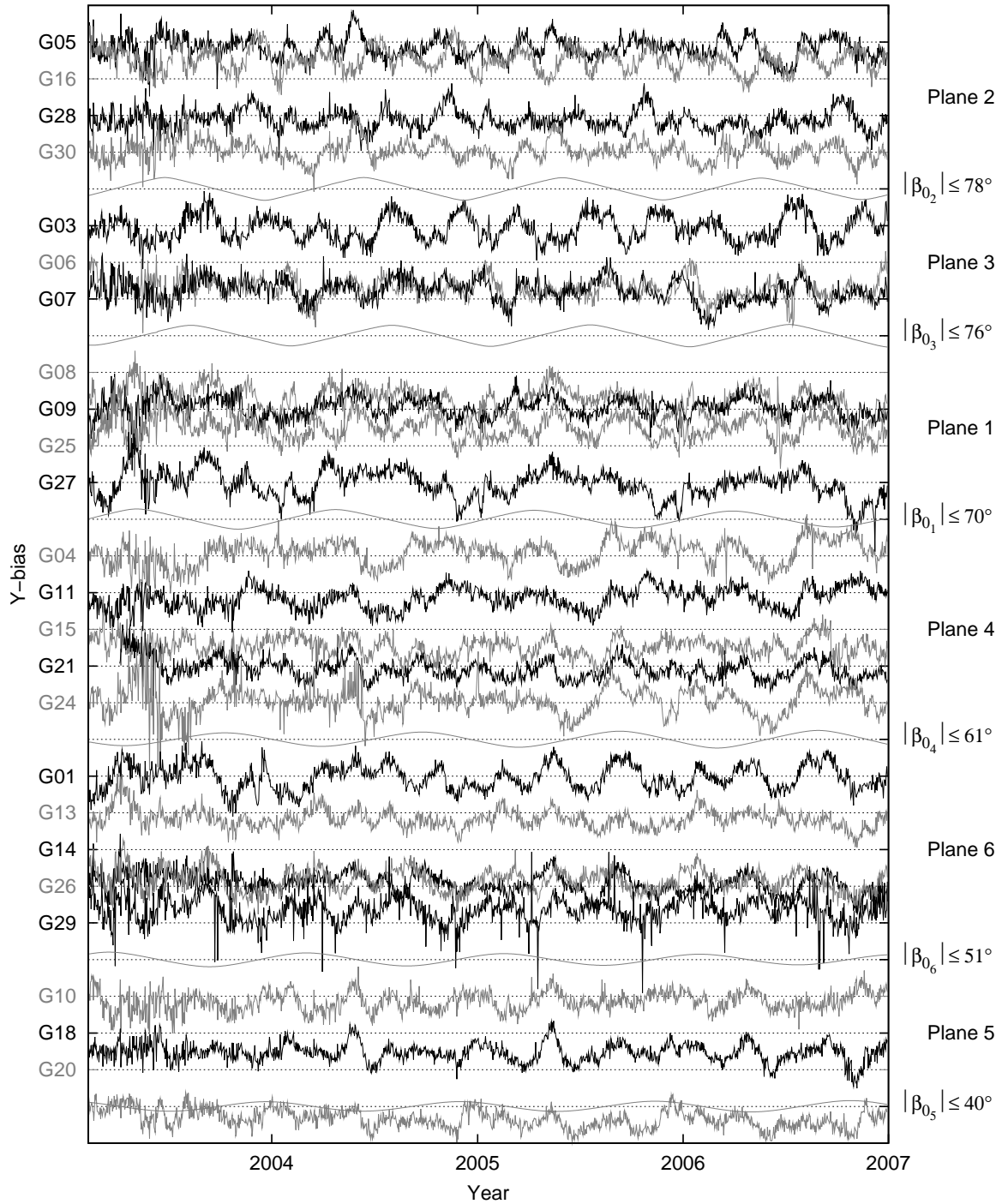


Figure 5.16: Y-bias of 24 GPS satellites derived from one-day arcs using the CODE SRP a priori model; the elevation angle  $\beta_0$  of the Sun above the orbital plane is given by the gray line

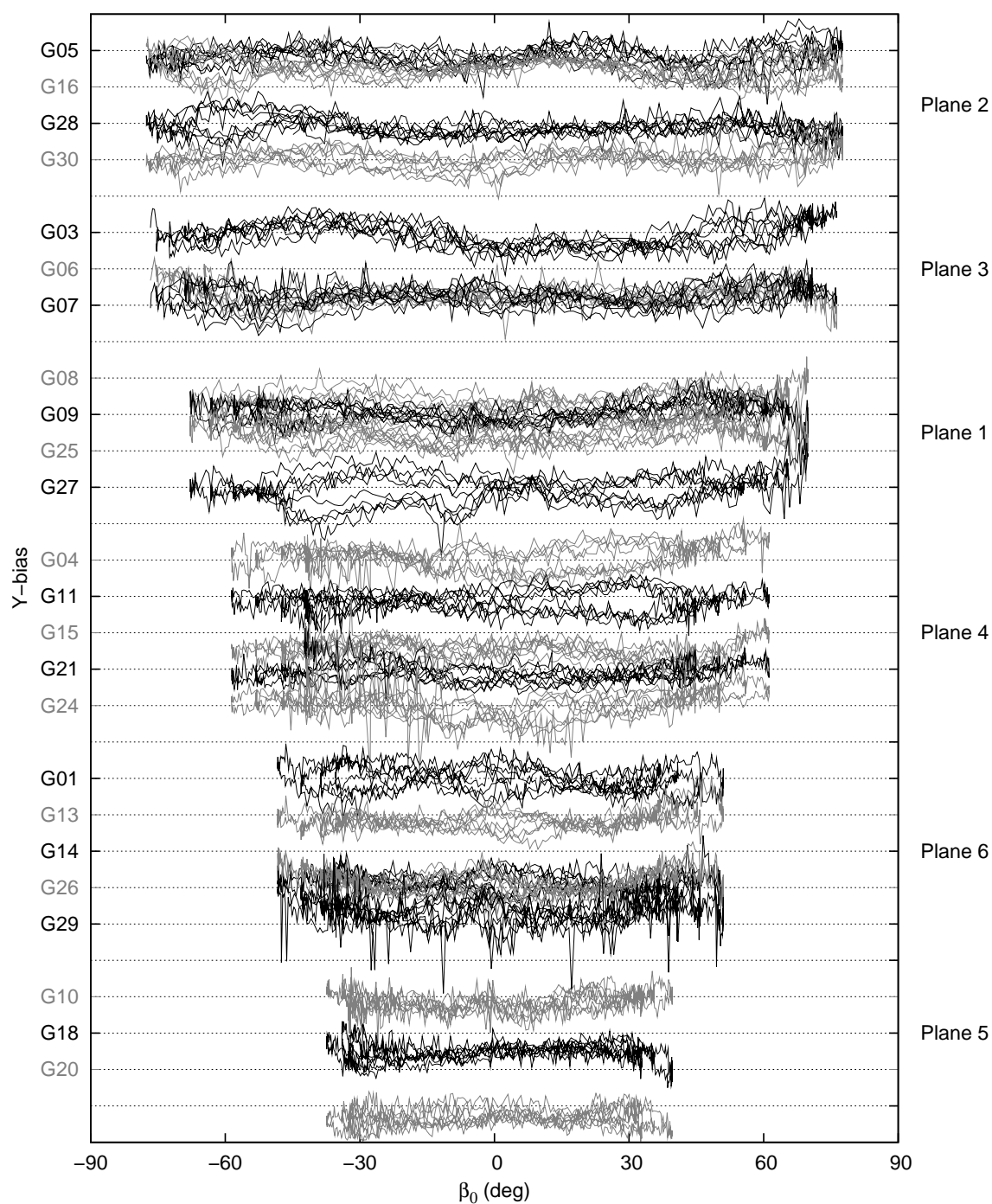


Figure 5.17: Y-bias of 24 GPS satellites derived from one-day arcs using the CODE SRP a priori model as a function of the elevation angle  $\beta_0$  of the Sun above the orbital plane

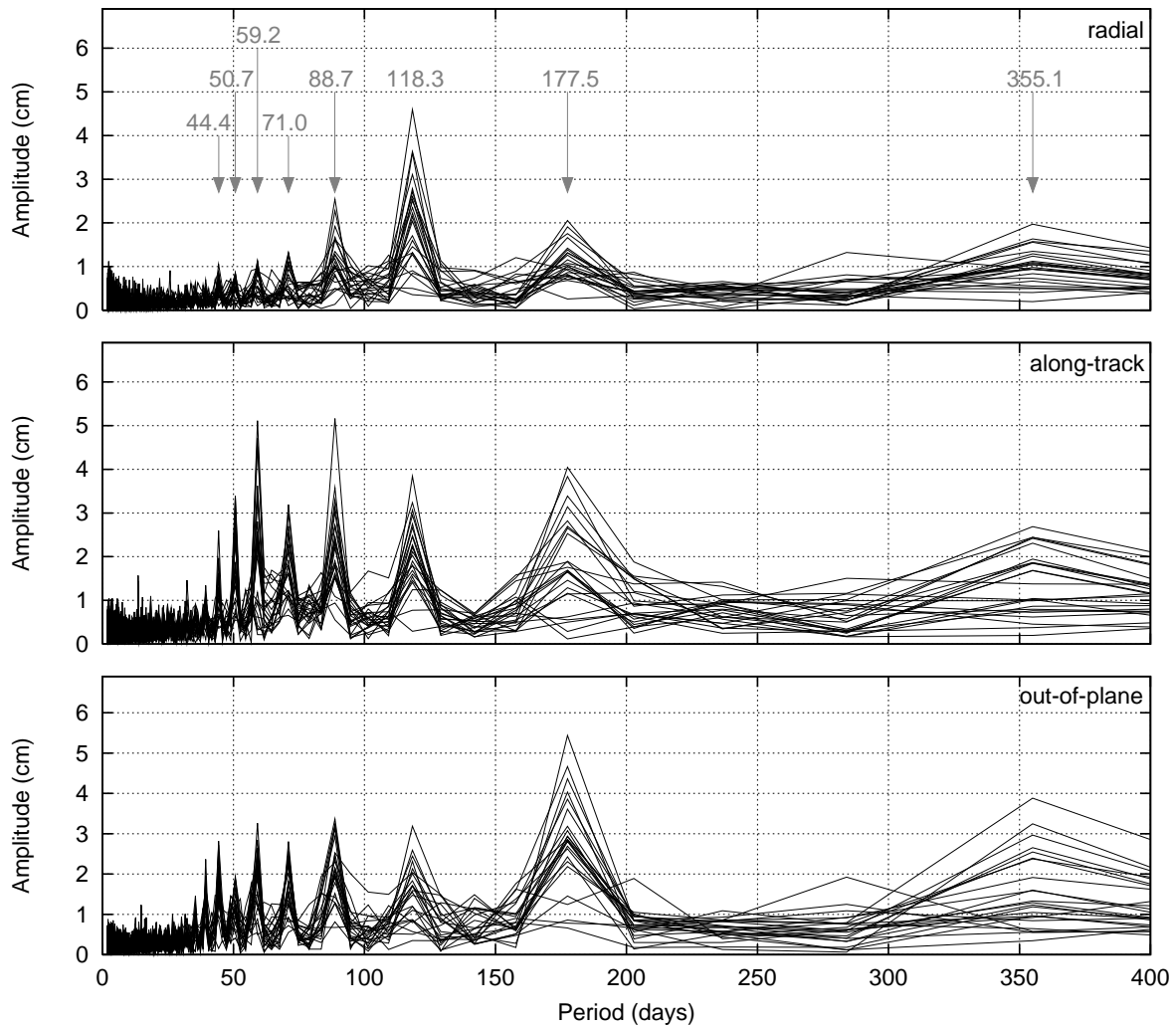


Figure 5.18: Amplitude spectra of GPS orbit overlap errors derived from one-day arcs using the CODE SRP model

on the specific Block types of the GPS satellites. The Block type of each satellite can be found in Table A.1 in the Appendix A.

In order to find the spectral behavior of the overlap errors, we performed a Fourier spectral analysis of the satellite-specific time series of the orbit overlap errors (derived from the one-day arc solution using the CODE SRP a priori model) for all 24 GPS satellites. The amplitude spectra are shown in Fig. 5.18. The amplitudes are given in millimeters as a function of the period for each of the three components. We see a main period of about 355 days with an amplitude of about 2 cm in all three overlap components. This period cannot be assessed accurately by the Fourier analysis, as the length of the time series is only four years. The basic period at 355 days as well as the higher harmonics at 44.4, 50.7, 59.2, 71.0, 88.7, and 118.3 days are integer divisors of the time series length of 1419 days.

In order to improve the spectral resolution for the basic period, the length of the time series was varied from 1360 to 1480 days in one-day steps. For lengths larger than 1419 days zero values were padded at the end. Thus the basic period of the Fourier spectra varied from 340 to 370 days. The period showing the largest amplitude may be assumed to correspond to the actual period. We expected the basic period to be similar for all satellites (at least for all satellites of one orbital plane) and to be close to the draconitic GPS year of 352 days. The basic periods estimated for the different GPS satellites did, however, differ significantly assuming between 340 and 370 days. We did not find a dependency of the period on the satellite type or on the satellites' orbital planes.

In this context, a spectral analysis of the Y-biases, which seem to repeat with the draconitic period, would be very interesting. After a draconitic GPS year the Sun-Earth-satellite constellation repeats. We conclude that the systematic pattern in the overlap errors of one-day arcs indicate orbit modeling errors. The use of different SRP a priori models does, however, not have a significant impact on the overlap patterns.

A more detailed analysis of the spectral behavior in a future work (e.g., studying the differences between the spectra of the three overlap components) might contribute to understanding the cause for the systematic patterns of the overlap errors.

### Overlap Errors of Daily Three-day Arc Solutions for GPS Satellites

After having studied the daily overlap errors of GPS orbits based on one-day arc solutions, we now inspect the daily overlap errors based on three-day arc solutions. Figure 5.19 shows the overlap errors for orbits of the GPS satellite G05 using the ROCK and the NONE model for SRP a priori modeling. The figure has the same scale as the one-day solutions (Fig. 5.14). We see a clear reduction of the standard deviations of all three overlap components compared to the one-day arc overlap errors - which is, by the way, a clear argument for using overlapping three-day arcs.

There are, however, noticeably large overlap values in along-track for 2004 for both orbit solutions, using the ROCK and the NONE SRP model. We believe that this large scatter may be caused by erroneously changing the processing options when generating the three-day arc solutions, which was done independently for each year. We were not able to resolve the problem, but we rule out orbit modeling errors causing the large scatter.

The problem is present for all GPS satellites, as can be seen in Fig. 5.20, showing the along-track overlap errors for the 24 GPS satellites. The corresponding statistical information is contained in Table 5.3, where the variables  $\sigma_{3d}$  and  $\bar{x}_{3d}$  are used for the standard deviations and the mean values of the overlap errors for the three-day arcs. The standard deviations decreased by about 1.5 cm for satellites of the orbital planes 1-3 and by about 3 cm for satellites of planes 4-6 compared to the overlap errors of the one-day solutions.

The mean values also changed. They show a plane-specific behavior decreasing from plane 2 to plane 5. Remember that the orbital planes are sorted in descending order of the maximum value of angle  $\beta_0$ , i.e.: planes 2, 3, 1, 4, 6, 5. Thus  $\bar{x}_{3d}$  is about  $-2.5$  cm for plane 2, about  $-2$  cm for

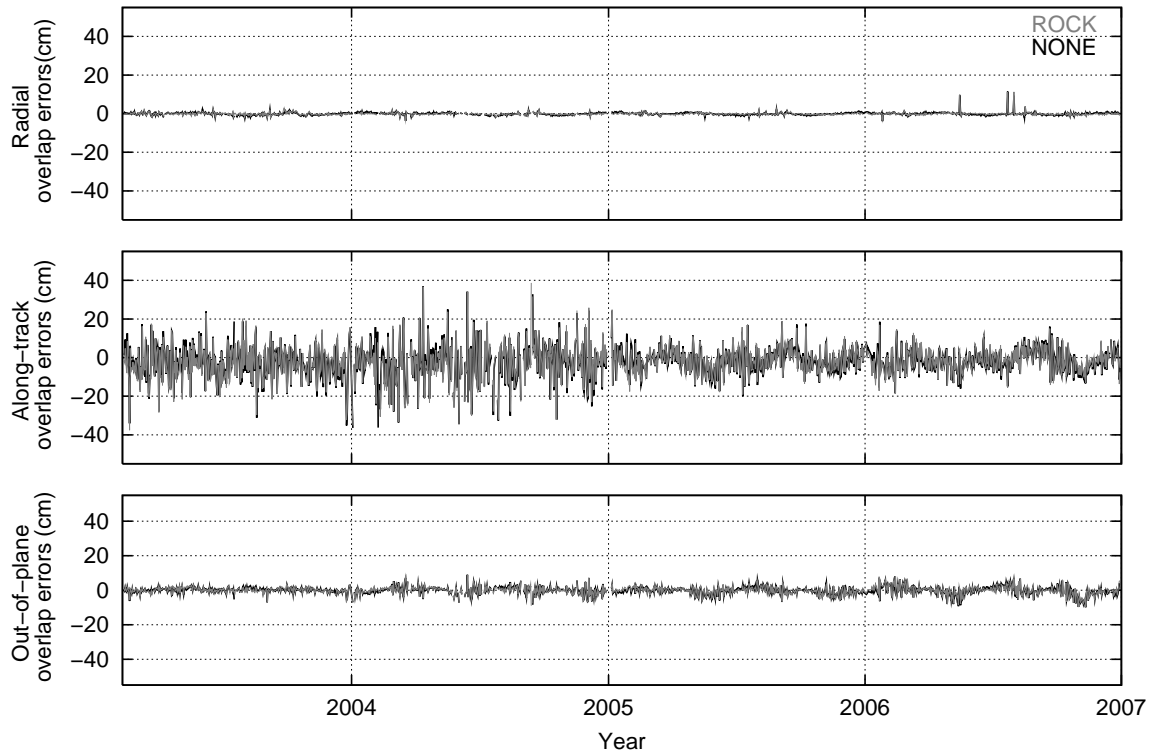


Figure 5.19: Orbit overlap errors of the GPS satellite G05 derived from three-day arcs using the ROCK and the NONE SRP a priori model

plane 3, about  $-1.5$  cm for plane 1, between  $-1.2$  cm and  $-0.6$  cm for plane 4, about  $-0.2$  cm for plane 6, and about  $0.3$  cm for plane 5. Satellite G29 shows a different behavior from that of the other satellites in the same orbital plane. Note that the mean values of the first two orbital planes, planes 2 and 3 (which show the largest pattern), were very different for the satellites of the one-day arc solution, but they are now very similar for all satellites of the three-day arc solution with about  $-2$  cm to  $-2.5$  cm.

In radial direction the standard deviations of the overlap errors are about 1 cm, which is smaller compared to those of the one-day solution. The mean values of the radial overlap errors are close to zero. We see again a plane-specific behavior for the out-of-plane overlap errors for which the standard deviations increase from 2 cm for plane 2 up to 6 – 7 cm for plane 5.

The figures and statistical information for the radial and out-of-plane overlap components are provided in the Appendix C (Figs. C.4 and C.6, and Tables C.1 and C.2). There is no significant difference between orbits generated with the ROCK or the NONE SRP a priori model.

Overlap errors of the three-day arc orbit solution using the CODE model were not generated. For the one-day orbit solutions we have already noticed that there were no significant differences between the orbits based on the ROCK, CODE, and NONE model. There is also no difference between the three-day arc solutions using the ROCK and the NONE model. Thus, we did not expect any new insights from overlaps of the three-day arcs based on the CODE model. We

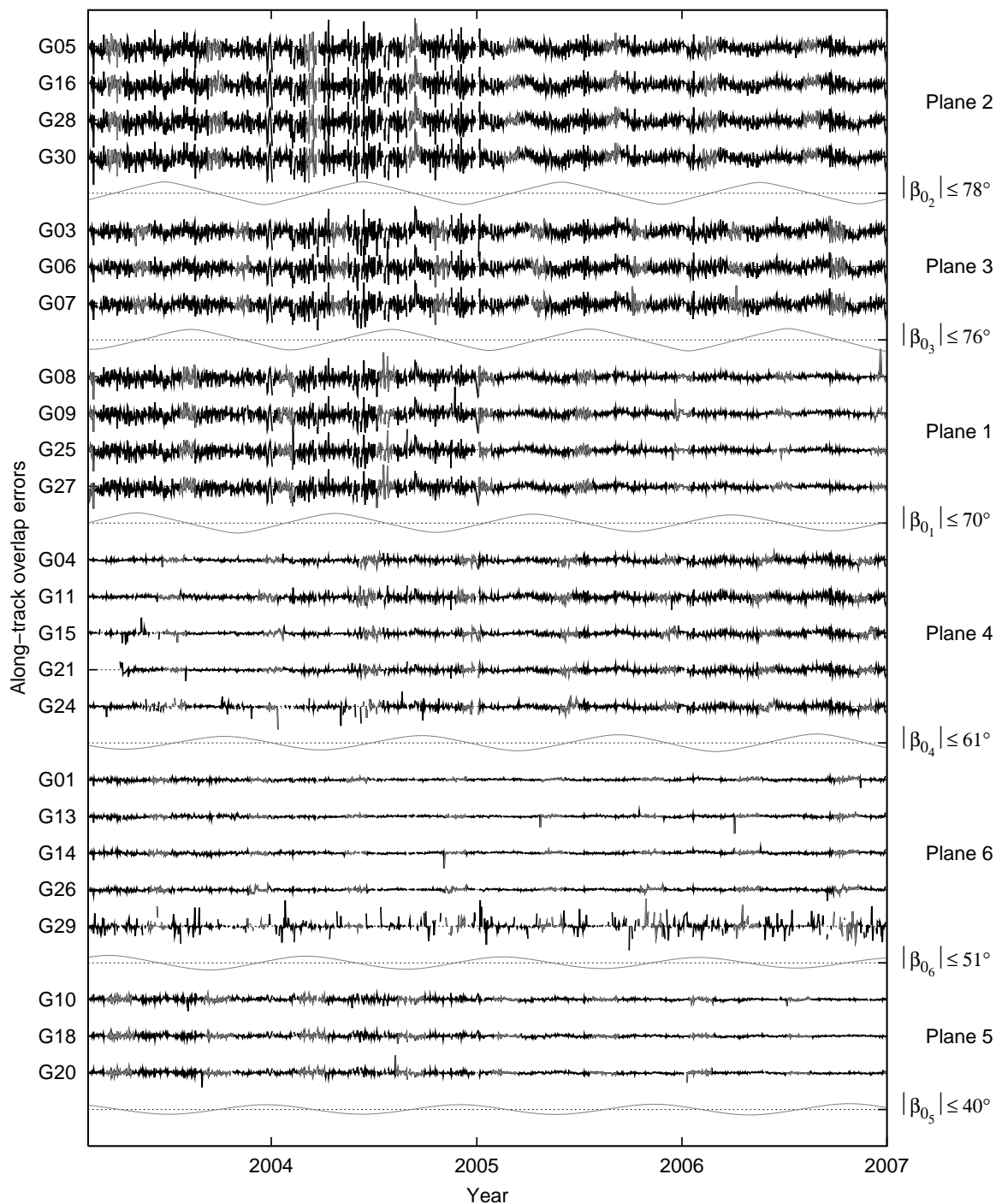


Figure 5.20: Orbit overlap errors in along-track direction of 24 GPS satellites derived from three-day arcs using the NONE SRP a priori model; the elevation angle  $\beta_0$  of the Sun above the orbital plane is given by the gray line; eclipsing periods are marked in gray; for the scale of the y-axis see Fig. 5.19

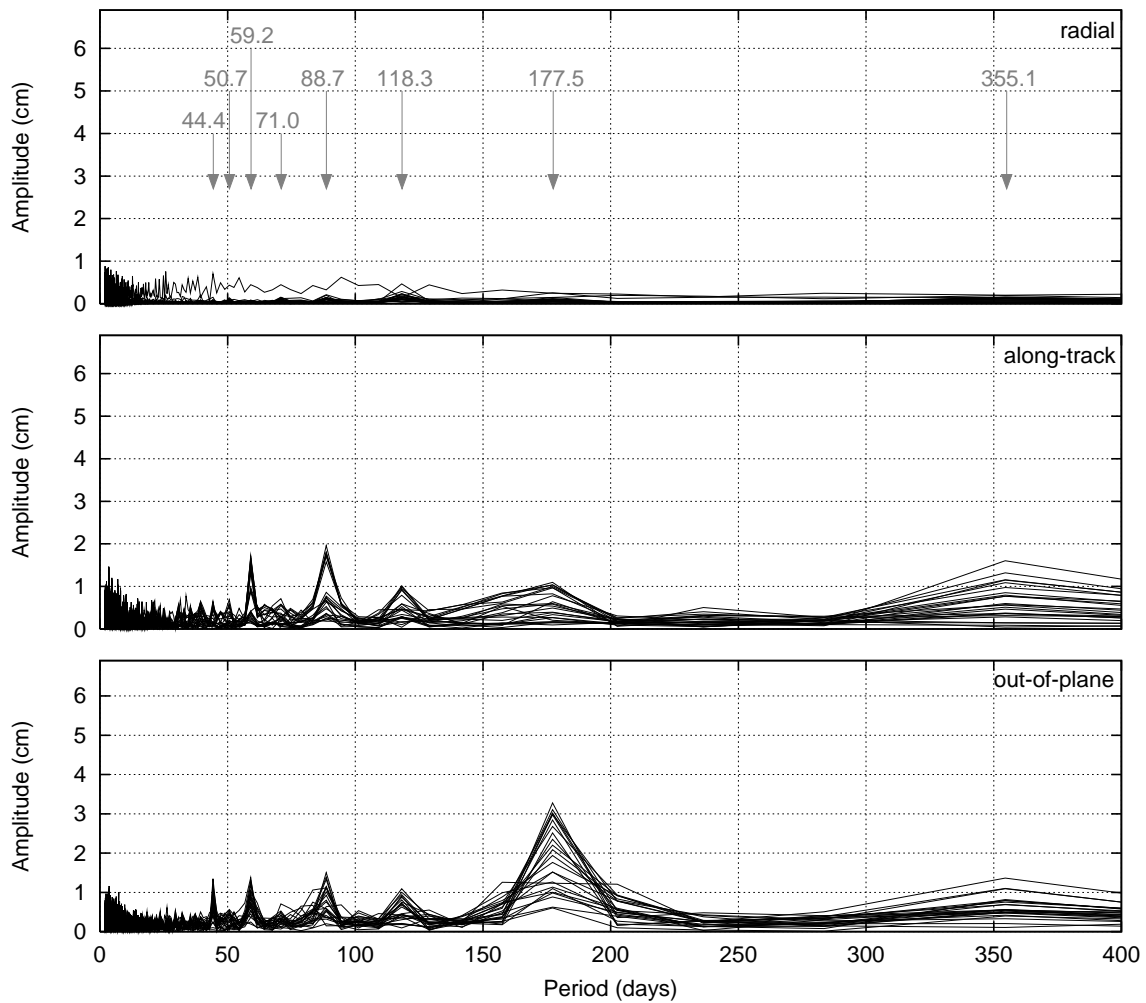


Figure 5.21: Amplitude spectra of GPS orbit overlap errors derived from three-day arcs using the NONE SRP model

assume that the overlap errors of the CODE solution will not differ from the ROCK and the NONE solutions. Therefore, we skipped the computation of orbit overlaps for three-day arcs generated with the CODE SRP model.

The amplitude spectra of the orbit overlap errors derived from the three-day arc solutions are shown in Fig. 5.21. The gray arrows indicate the periods found for the overlap errors of the one-day arcs. There are no spectral lines visible for the radial component. In the along-track and out-of-plane directions the amplitudes decreased significantly for most of the 24 GPS satellites. The most prominent remaining period is at 177.5 days for the out-of-plane component with an amplitude of about 3 cm, which is half of the amplitude for the one-day arc solutions. In the along-track and out-of-plane directions the period at about 355 days is visible for some of the GPS satellites, but with a much smaller amplitude (about 1 cm) than for the one-day arc overlaps.

### Overlap Errors of Daily One-day Arc Solutions for GLONASS Satellites

We now perform the same analysis as for the GPS satellites for 10 satellites of the GLONASS constellation, namely for those with a long observation time span to generate good solutions during the entire or at least large parts of the 3.5 year time interval.

Figure 5.22 shows the orbit overlap errors for one GLONASS satellite R22 in all three components, namely in the radial, along-track, and out-of-plane components. Observe the difference in scale compared to the corresponding figures for the GPS satellites. In general, the GLONASS overlap errors are larger than the GPS overlap errors. This is due to the much sparser network of GLONASS receivers. The comparatively small number of observations leads to less well defined satellite orbits.

The figure shows both solutions, i.e., the overlap errors derived from one-day arcs using the CODE and the NONE SRP a priori model. There is no significant difference between them, as for the GPS satellites. The radial overlap errors show a slightly systematic behavior, whereas no systematic behavior is observed in the out-of-plane component. The standard deviations are about 15 cm in the radial and about 16 cm in the out-of-plane component.

The standard deviation of the overlap errors in along-track direction is about 30 cm. The mean value of the along-track component is also noticeably larger (33 cm). We found similar mean values for the other GLONASS satellites ranging between 32 cm and 38 cm. Deficiencies of

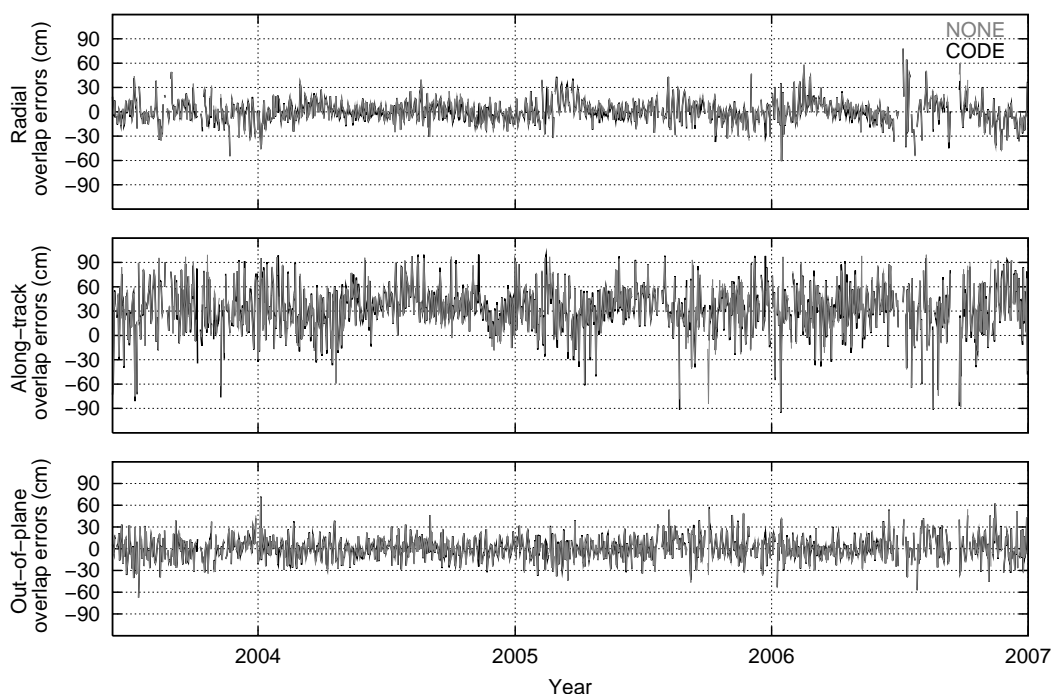


Figure 5.22: Orbit overlap errors of the GLONASS satellite R22 derived from one-day arcs using the CODE and the NONE SRP a priori model

the relative antenna phase center correction (PCC) model used (i.e., antenna phase center offset (PCO) and phase center variation (PCV)) may explain an error in the semi-major axis (causing along-track errors). Therefore we generated a new orbit series using the CODE SRP model and the absolute antenna PCC model, which provides antenna phase center offsets and variations for the receivers and the satellites. The resulting overlap errors are shown in Fig. 5.23.

The solution using the relative PCC model (named CODE) is given in black, whereas the new solution using the absolute PCC model (named CODE-A) is given in gray. Note that the mean offset of the along-track overlap errors is now about  $-3$  cm for the CODE-A orbit solution. This indicates wrong values in the relative PCC model for the GLONASS satellites. For most of the GLONASS satellites the antenna phase center offsets are unknown. To build the absolute PCC model the phase center offsets and variations have been estimated from the observations. The absolute antenna phase center offsets in Z-direction for the GLONASS satellites are about 2 m. According to Zhu et al. (2003), about 95% of the Z-offset is absorbed by the satellite clock corrections. The remaining 5% correspond to a change of the semi-major axis of about 2 cm, which could produce an along-track error of about 35 cm after one day. This value corresponds nicely to the mean values found for the overlap along-track components (ranging between 32 cm and 38 cm) of the orbit solution using the relative PCC model. The change of the semi-major axis of about 2 cm is reflected by the radial overlap component of the CODE solution (see Table C.3), which is between 1–3 cm for all GLONASS satellites (except for R05).

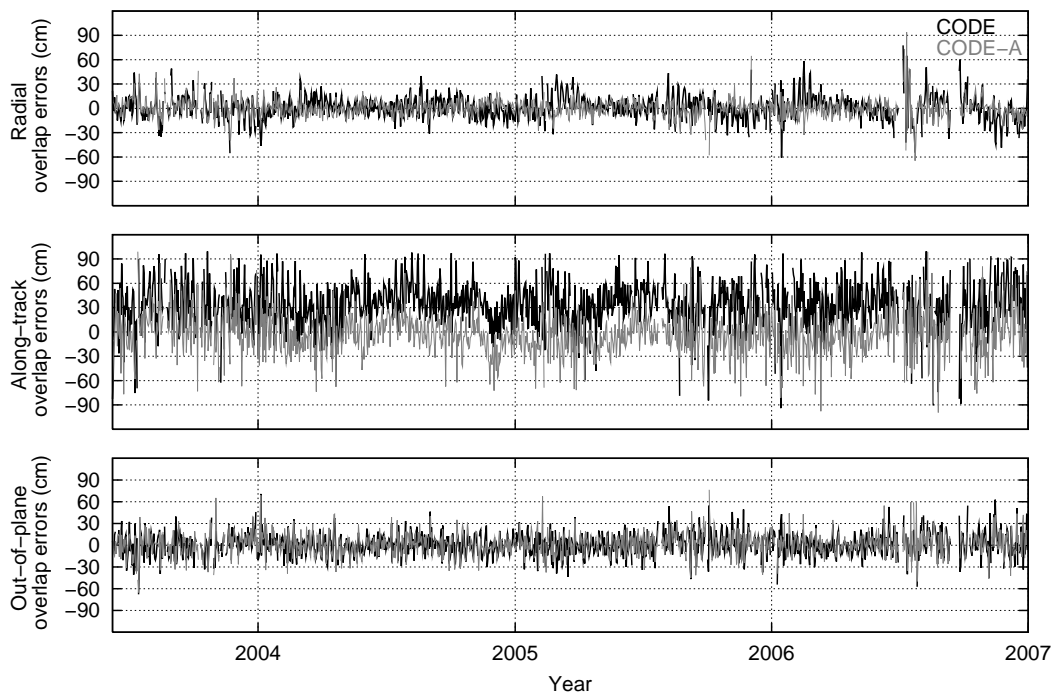


Figure 5.23: Orbit overlap errors of the GLONASS satellite R22 derived from one-day arcs using the CODE SRP a priori model using the relative (CODE) and the absolute (CODE-A) antenna PCC model

The systematic behavior observed in the radial component for the CODE solution is no longer visible in the CODE-A solution. Consequently the standard deviation of the radial component decreases and is about 12 cm for CODE-A. In the along-track direction the standard deviation is then about 27 cm.

Figure 5.24 shows the along-track overlap errors of the one-day arc solution using the CODE SRP a priori model and the absolute PCC model for the 10 GLONASS satellites. They are sorted according to the orbital planes. Only two planes (of three), plane 1 and 3, were occupied during the time interval analyzed. The elevation angle  $\beta_0$  of the Sun above the orbital plane is given by the gray line. The eclipsing periods are marked in gray. Table 5.4 contains the corresponding statistical information in columns 3 ( $\sigma_{1d}$ ) and 7 ( $\bar{x}_{1d}$ ). The statistical information for the CODE and the NONE solution are provided, as well. Both series of overlap errors are similar. Only the CODE-A solution differs due to the absolute antenna PCC model and the corresponding correction of the mean value of the overlap errors. The standard deviations of the CODE-A overlap errors range between 24 cm and 28 cm, the mean values between  $-2$  cm and  $-4$  cm (except for satellite R05, for which it is  $+4.3$  cm).

The along-track components of the satellites in the orbital plane 3 all show a similar systematic behavior repeating nearly annually. The radial components (see Fig. C.7 and Table C.3 in the Appendix C) and the out-of-plane components (see Fig. C.9 and Table C.4 in the Appendix C) also reveal slight plane-specific systematic patterns.

PRN	$\sigma_{1d}$ (cm)			$\sigma_{3d}$ (cm)	$\bar{x}_{1d}$ (cm)			$\bar{x}_{3d}$ (cm)
	CODE	CODE-A	NONE	NONE	CODE	CODE-A	NONE	NONE
<i>Plane 1</i>								
R02	25.2	22.7	25.3	4.9	35.9	-2.0	35.8	1.4
R03	29.7	26.5	29.0	6.5	34.5	-3.2	34.1	1.9
R04	28.8	24.1	29.1	5.7	33.8	-3.7	34.2	1.3
R05	32.1	29.4	32.0	7.0	36.2	4.3	36.0	2.2
<i>Plane 3</i>								
R17	30.2	28.4	30.1	10.3	34.1	-2.9	34.1	-0.5
R18	28.3	27.6	28.3	13.3	32.3	-2.8	32.3	-0.3
R21	28.8	28.7	28.7	10.4	32.1	-2.0	32.4	-0.5
R22	29.6	26.6	29.7	10.2	33.2	-3.2	33.1	-0.6
R23	28.3	27.3	28.4	11.3	34.7	-4.3	34.6	-0.6
R24	30.1	28.9	30.1	11.0	37.8	-2.3	37.6	-0.2

Table 5.4: Statistical information for along-track orbit overlap errors of 10 GLONASS satellites derived from one-day and three-day arcs using the two SRP a priori models CODE and NONE; for the CODE-A solution the CODE SRP a priori model and the absolute antenna PCC model were used: standard deviations  $\sigma_{1d}$  and  $\sigma_{3d}$ , and mean values  $\bar{x}_{1d}$  and  $\bar{x}_{3d}$  given in cm

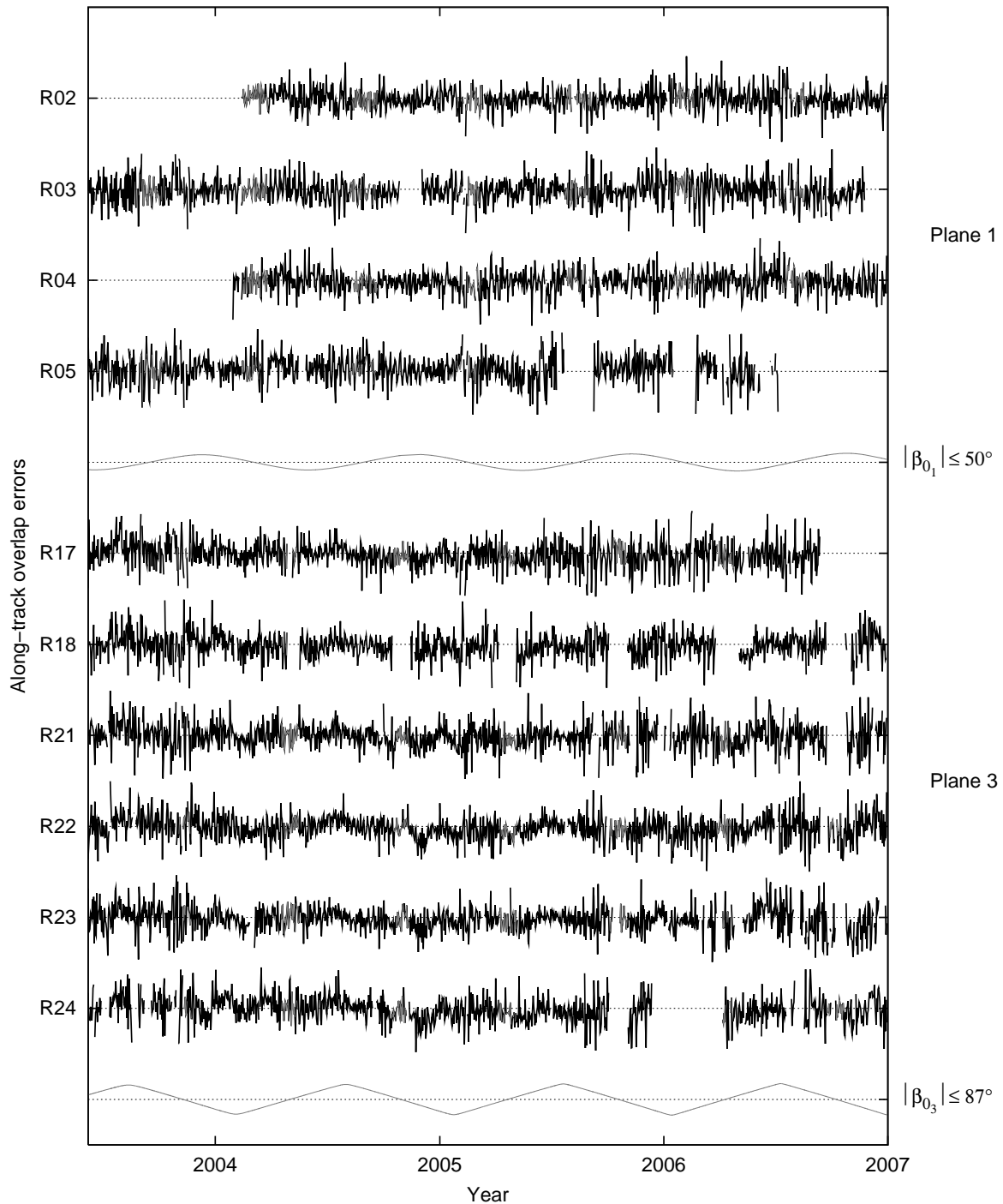


Figure 5.24: Orbit overlap errors in along-track direction of 10 GLONASS satellites derived from one-day arcs using the CODE SRP a priori model and the absolute antenna PCC model; the elevation angle  $\beta_0$  of the Sun above the orbital plane is given by the gray line; eclipsing periods are marked in gray; for the scale of the y-axis see Fig. 5.23

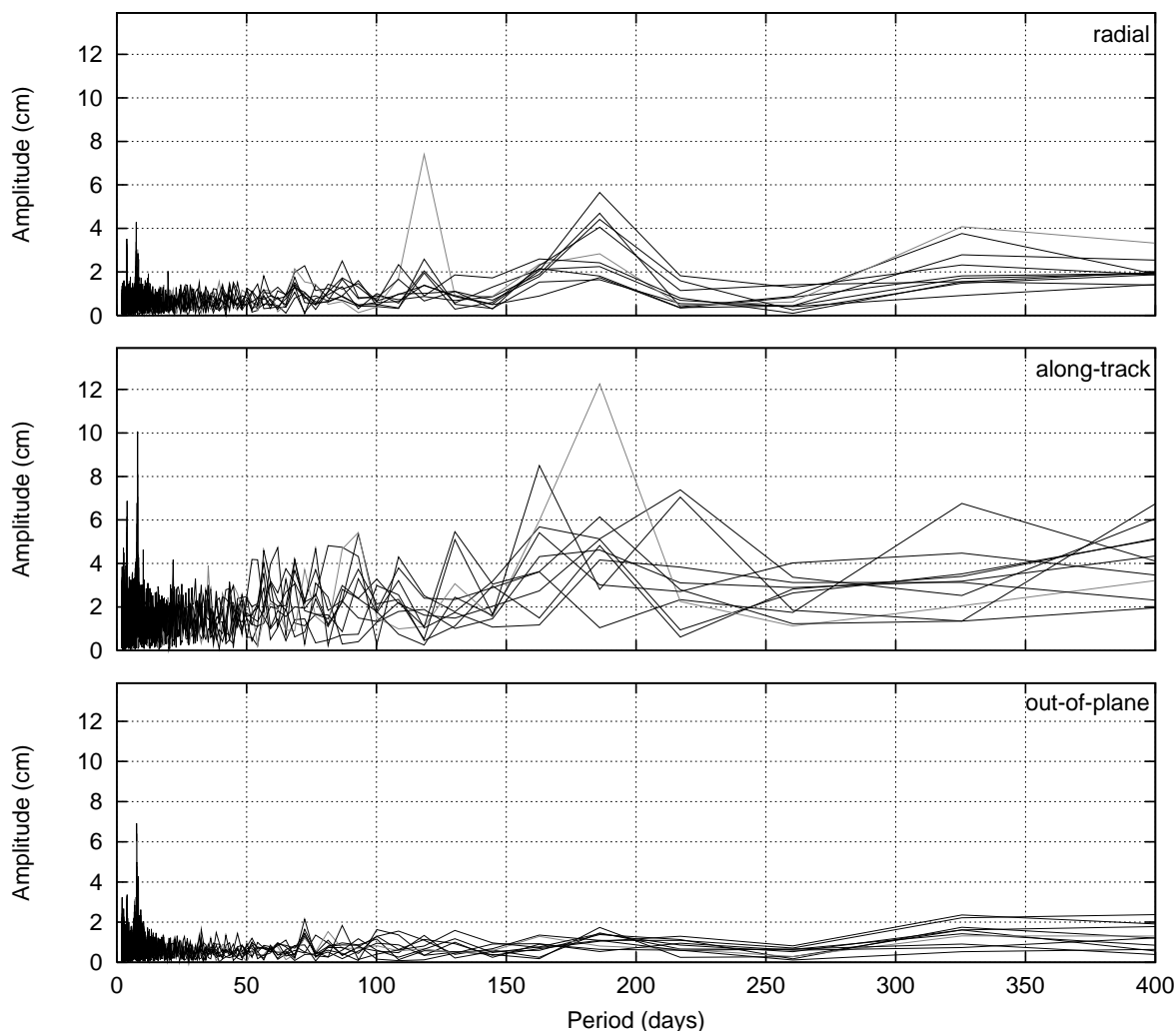


Figure 5.25: Amplitude spectra of GLONASS orbit overlap errors derived from one-day arcs using the NONE SRP model

Figure 5.25 gives the amplitude spectra of the orbit overlap errors derived from the one-day arc solutions using the NONE SRP model for each of the 10 GLONASS satellites. The mean offsets were subtracted from the satellite-specific overlap series before performing the Fourier analysis. In radial direction there is a significant peak around 186 days, the largest amplitudes of 4 – 6 cm are associated with the satellites in plane 3. The peak around 120 days is associated with satellite R18. This satellite repeatedly has data gaps (due to a “switch off” during eclipsing periods probably due to battery problems) which may cause the unexpected period. The spectral lines of this satellite therefore are marked in gray.

There are no significant periods in the along-track and out-of-plane direction common to all satellites at first sight. But there are noticeably large peaks around 8 days with amplitudes up to 10 cm in the along-track direction. Figure 5.26 shows the interval between 2 and 10 days

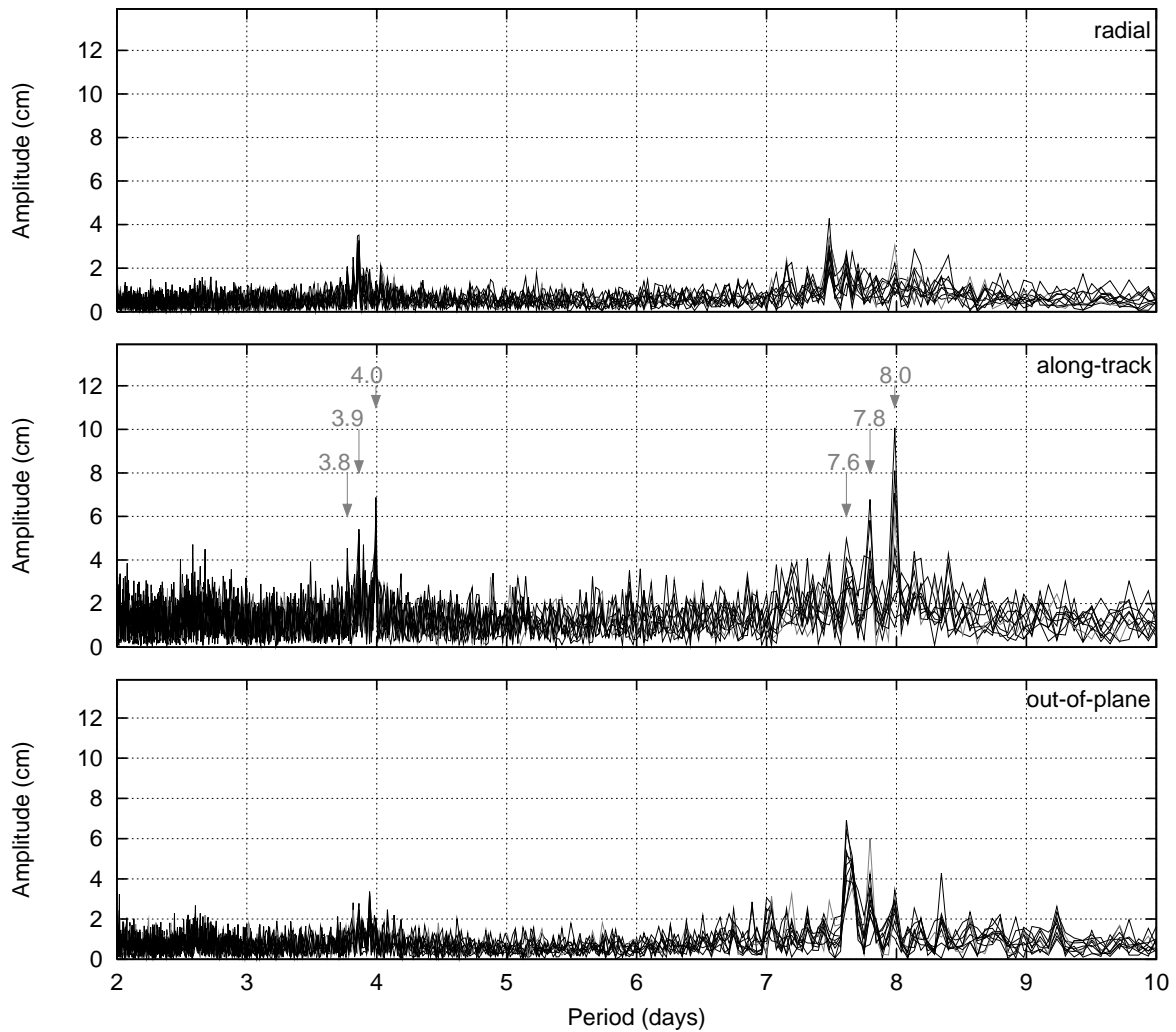


Figure 5.26: Amplitude spectra of GLONASS orbit overlap errors derived from one-day arcs using the NONE SRP model (zoomed)

of Fig. 5.25. We find three peaks mainly in the along-track component at about 7.6, 7.8, and 8.0 days and their second harmonics at about 3.8, 3.9, and 4.0 days.

The period of 8 days corresponds to the repeat period of the GLONASS satellites (which is 7.98 days). The remaining two periods may be caused by a superposition of periods. The sidereal revolution period of GLONASS satellites ( $11^{\text{h}}15^{\text{m}}48^{\text{s}}$ ) sampled at 24 hour intervals leads to a beat period of 7.6 days, whereas the synodic period ( $11^{\text{h}}16^{\text{m}}47^{\text{s}}$ ) sampled at 24 hour intervals would lead to a 7.8 day beat period. We conclude that there are systematic once-per-revolution errors in the GLONASS orbits, which might be caused by the use of the relative PCC model. Unfortunately, a spectral analysis of the CODE-A solution, which would give the answer to this speculation, was not performed at the time of our analysis.

### Overlap Errors of Daily Three-day Arc Solutions for GLONASS Satellites

Figure 5.27 shows the three overlap components for the GLONASS satellite R22 (using no SRP a priori model). We see that the overlap errors are reduced significantly compared to the one-day arc overlaps. The overlap errors for the year 2004 show larger values, as it was the case for GPS. The standard deviations of the overlap errors in the three components are 1.5 cm, 10 cm, and 7 cm, for radial, along-track, and out-of-plane, respectively.

Figure 5.28 shows the along-track overlap errors for the 10 GLONASS satellites for the three-day arc solutions using the NONE SRP a priori model. The corresponding statistical information is summarized in Table 5.4. The standard deviations of the overlap errors range between 5 cm and 7 cm for satellites of plane 1, whereas they are larger for the satellites of plane 3 with about 10 – 11 cm. Only satellite R18 shows a significantly different standard deviation of about 13 cm, which is due to the systematic pattern in the along-track time series. There is a prominent linear trend with alternating sign at semi-annual intervals, probably due to attitude problems.

The mean values of the along-track overlap errors are also plane-specific with about 2 cm for plane 1 satellites, and about  $-0.5$  cm for plane 3 satellites. It is interesting to note that the bias of about 30 cm disappeared (as it did for the one-day arc solutions when using the absolute

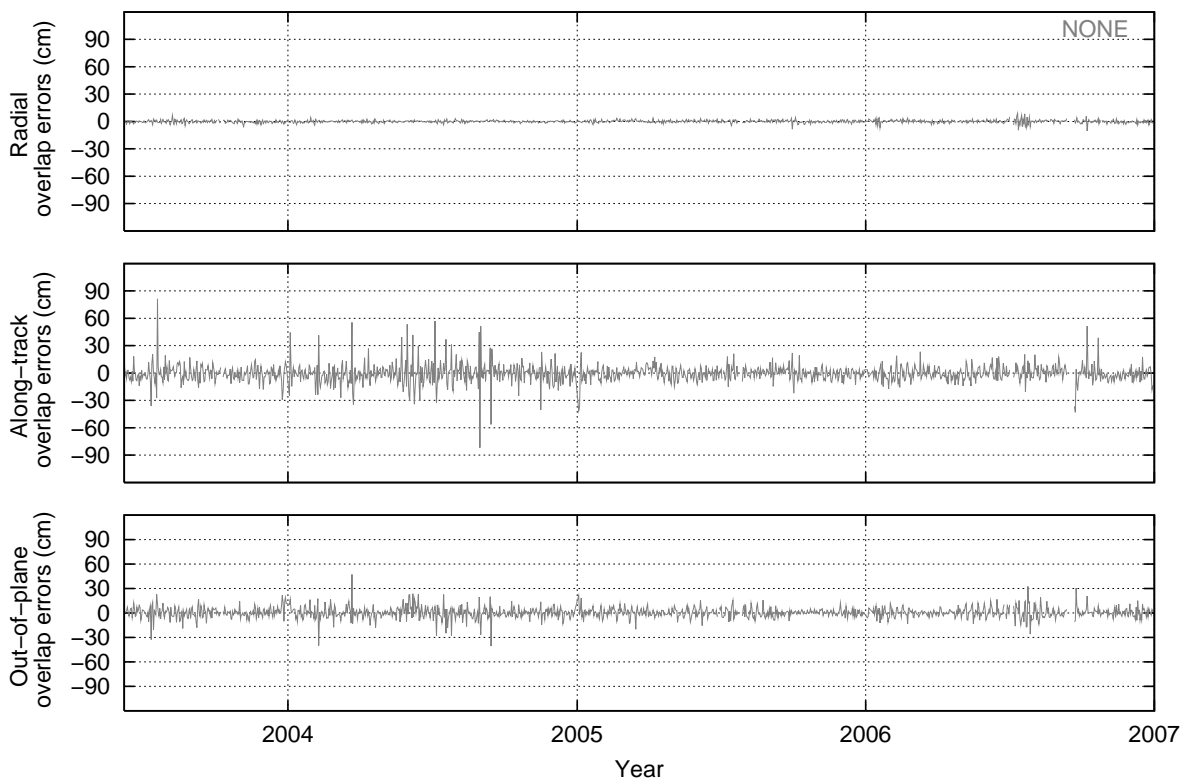


Figure 5.27: Orbit overlap errors of the GLONASS satellite R22 derived from three-day arcs using the CODE and the NONE SRP a priori model

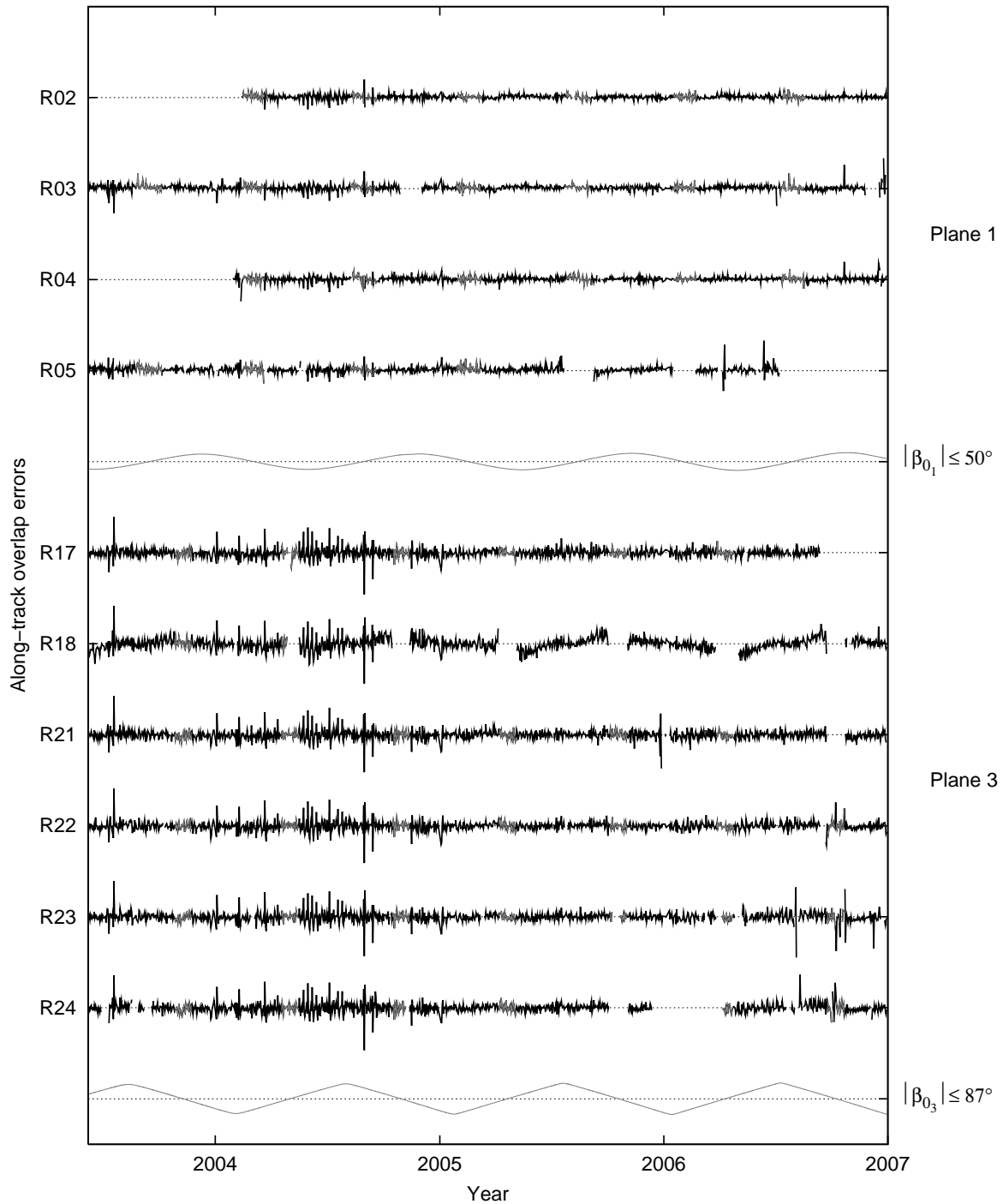


Figure 5.28: Orbit overlap errors in along-track direction of 10 GLONASS satellites derived from three-day arcs using the NONE SRP a priori model; the elevation angle  $\beta_0$  of the Sun above the orbital plane is given by the gray line; eclipsing periods are marked in gray; for the scale of the y-axis see Fig. 5.27

antenna PCC model), despite using the relative antenna PCC model. In this case the semi-major axis, which determines the mean motion of the satellite, is better determined by the orbit dynamics for the longer arc-length of three days. Other parameters, as the satellite clocks, are then implicitly compensating for wrong values of the relative PCC model. The remaining 2 cm and  $-0.5$  cm for plane 1 and 3 might still be the result of the used relative PCC model. An overlap analysis of the CODE-A solution for three-day arcs, which was not performed in this work, would thus be very valuable.

More information concerning the radial and out-of-plane component are provided in the Appendix C (see Figs. C.8 and C.10, and Tables C.3 and C.4). In radial direction the standard deviation of the overlap errors is between 1.3 cm and 3.5 cm. The mean values of the radial overlap errors are close to zero. The standard deviations for the 10 GLONASS satellites vary between 7 cm

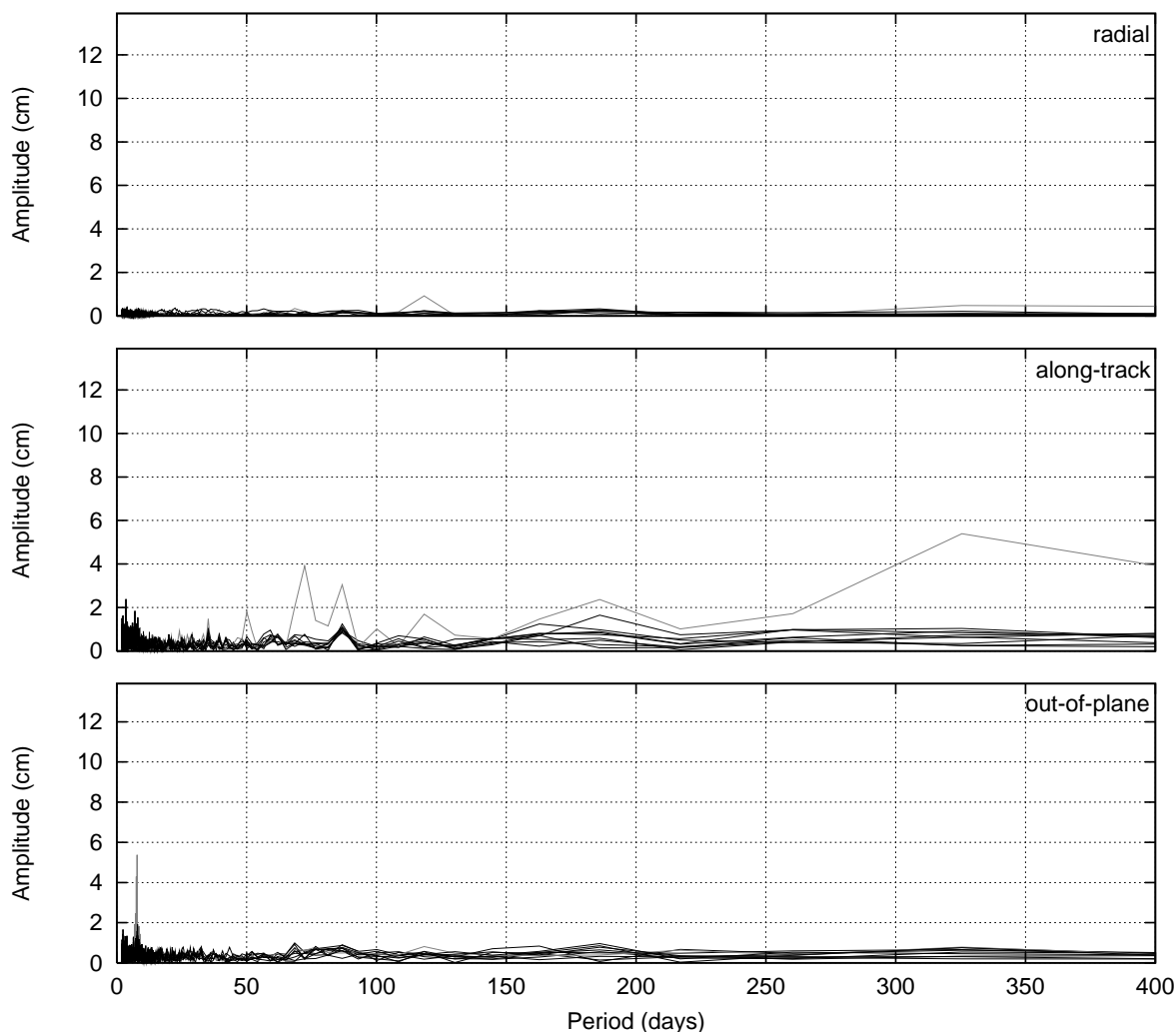


Figure 5.29: Amplitude spectra of GLONASS orbit overlap errors derived from three-day arcs using the NONE SRP model

and 10 cm in the out-of-plane component. The overlap mean values in out-of-plane direction show a plane-specific behavior with about  $-0.3$  cm for plane 1 satellites and about  $0.3$  cm for plane 3 satellites.

Figure 5.29 shows the spectra for the overlap components derived from the three-day arc solutions using the NONE SRP model. There are no significant spectral lines except for the satellite R18. We conclude that the arc-length of three days improves (as expected) the GNSS orbit quality, compared to an arc-length of only one day. Contrary to our expectation, the overlap errors do not depend on the specific SRP model used.

### 5.2.5 . . . by Analyzing the Geocenter Coordinates

Up to now we analyzed the orbits in order to assess the quality of the underlying model. It is also possible (and makes sense) to study the impact of the orbit model on other parameters of the daily analyses at CODE. Here we study in particular the impact on the geocenter coordinates. The position of the Earth's center of mass (which is determined by the satellite orbits) with respect to the ITRF-origin is referred to as the geocenter coordinates. These coordinates are estimated in the least squares adjustment as translation parameters of the set of IGS core sites with respect to the ITRF-origin.

Daily values for the geocenter coordinates were estimated for a time span of about four years (040/2003 until 365/2006) for each of the three-day solutions, using the ROCK, the CODE, and the NONE SRP a priori model. The amplitude spectra of the three geocenter time series for the Z-component may be inspected in Fig. 5.30.

The largest spectral line, with an amplitude of about 9 mm, resides at a period of 352.3 days. This spectral line belongs to the ROCK model time series (indicated in gray). The period is that of the draconitic GPS year. As our time series of about four years is too short for precisely estimating this period we reconstruct it from the harmonics at 175.1, 117.4, 70.5, and

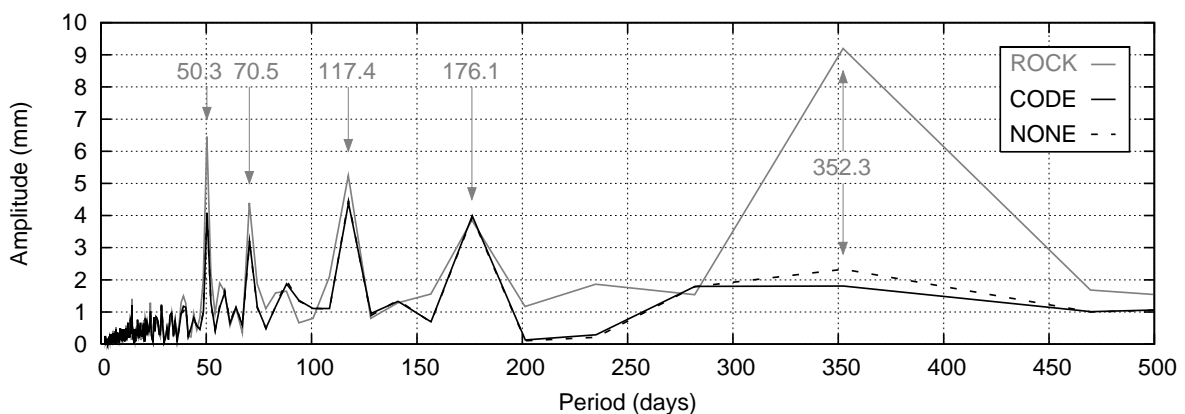


Figure 5.30: Amplitude spectra of the geocenter Z-coordinate derived from daily orbit solutions using three different SRP a priori models: ROCK, CODE, and NONE

50.3 days. The prominent spectral lines indicate orbit modeling problems. The amplitude decreases significantly to about 2 mm for the CODE (in black) and the NONE (dashed) model. This confirms the previous results, namely that the use of the CODE SRP a priori model or of “no SRP” a priori model leads to improved GNSS orbits, provided that the five SRP parameters ( $D0, Y0, B0, BS, BC$ ) are estimated in addition to the six orbit parameters.

Also interesting is the fact that the peaks at 50.3, 70.5, and 117.4 days are odd factors ( $\frac{1}{7}, \frac{1}{5}, \frac{1}{3}$ ) of the main period of about 352 days. The factors  $\frac{1}{4}$  and  $\frac{1}{6}$  are missing. Is there a signal divisible by seven causing the very significant peak at 50.3 days, which is about 6.5 mm for the solution using the ROCK model, and about 4 mm for the CODE and the NONE model? In this context it is interesting to note that the intersection of the six orbital planes with the equatorial plane yields equally spaced nodal lines, whereas the intersection of the orbital planes with the ecliptic plane do not yield to equally spaced nodal lines. Moreover the smallest distance between the nodal lines occurs for the two orbital planes, for which  $\beta_0$  is largest. Surprisingly this distance is about 50 days. There might be a correlation between these 50 days and the similar spectral line in the geocenter Z-coordinate.

According to Steigenberger (2007), the geocenter Z-coordinates derived from a reprocessing of a global GPS network over 11 years (Steigenberger et al., 2006) show a similar prominent spectral line at about 50 days. The ROCK model was used as SRP a priori model for the reprocessing. Steigenberger found the same spectral line for the geocenter Z-component derived from a reprocessing of the GPS data of TIGA (GPS Tide Gauge Benchmark Monitoring) stations by GFZ using another software package “EPOS Potsdam-7”. Thus, we can rule out any software problems causing the 50 day period. The period is “real” and has to be understood. Further analysis are necessary to find the cause for the spectral line in the geocenter time series.

### 5.3 Estimating Different Sets of Dynamic Orbit Parameters

So far, the five dynamic orbit parameters  $D0, Y0, B0, BS$ , and  $BC$  were estimated according to Eq. (3.22) for the generation of GNSS orbits. The argument for the periodic terms is  $u$ , that is the argument of latitude of the satellite. We already know from analyzing the SLR residuals that the range residuals show a systematic pattern in the  $(\Delta u, \beta_0)$ -space, where  $\Delta u$  is the argument of latitude of the satellite with respect to the argument of latitude of the Sun. We believe that the angle  $\Delta u = u - u_0$  (corresponding to the synodic period) is better suited to describe the impact of SRP on the satellite than the angle  $u$  (corresponding to the draconitic period). The difference between the synodic and the draconitic period is about one minute, which might be important for SRP parameter estimation. Therefore we modified the orbit model by replacing the argument angle  $u$  of the periodic orbit parameters by  $\Delta u$ . The resulting acceleration of a satellite due to SRP is thus written as

$$\mathbf{a}_{srp} = \mathbf{a}_{srp0} + D(\Delta u)\mathbf{e}_D + Y(\Delta u)\mathbf{e}_Y + B(\Delta u)\mathbf{e}_B \quad (5.1)$$

with the coefficients

$$\begin{aligned} D(\Delta u) &= D0 + DC \cos(\Delta u) + DS \sin(\Delta u) \\ Y(\Delta u) &= Y0 + YC \cos(\Delta u) + YS \sin(\Delta u) \\ B(\Delta u) &= B0 + BC \cos(\Delta u) + BS \sin(\Delta u) \end{aligned} \quad (5.2)$$

where  $\mathbf{a}_{srp}$  ... Acceleration due to the SRP  
 $\mathbf{a}_{srp0}$  ... Acceleration derived from the a priori SRP model  
 $\Delta u = u - u_0$  ... Argument of latitude of the satellite relative to the argument of latitude of the Sun .

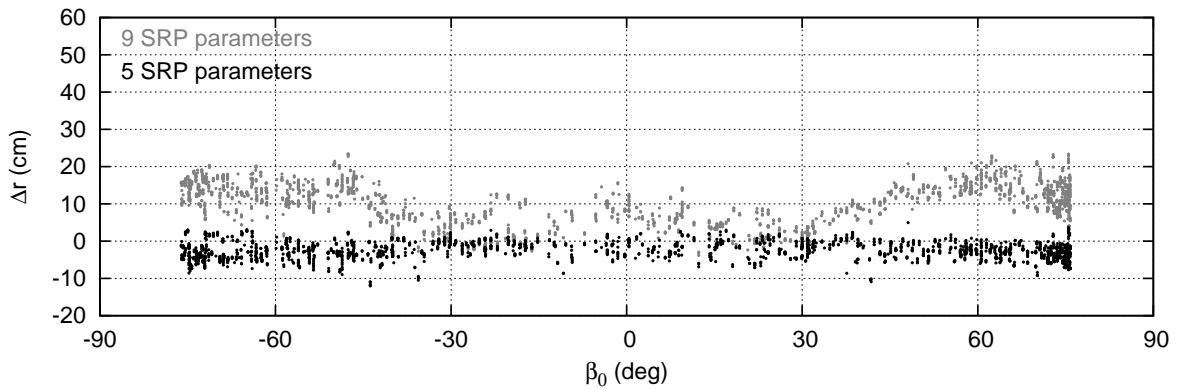
We repeated the orbit determination using the five dynamic parameters ( $D0, Y0, B0, BS, BC$ ) as before, but with the angle  $\Delta u$  as independent argument, to find out whether a change in the argument angle changes the resulting orbits. Three-day solutions were generated for each day of 2006. We did not use any SRP a priori model, which corresponds to the NONE model solution. The resulting orbits were then validated using SLR observations.

The SLR validation results are compared with the validation results of Sect. 5.2.1 for the three-day arcs using the NONE model and the argument angle  $u$ . The range residuals of the two orbit solutions using either  $u$  or  $\Delta u$  differ at the sub-mm level only. This result may be due to the fact that the argument angle is only relevant for the  $BS$  and  $BC$  terms in our parameter estimation.

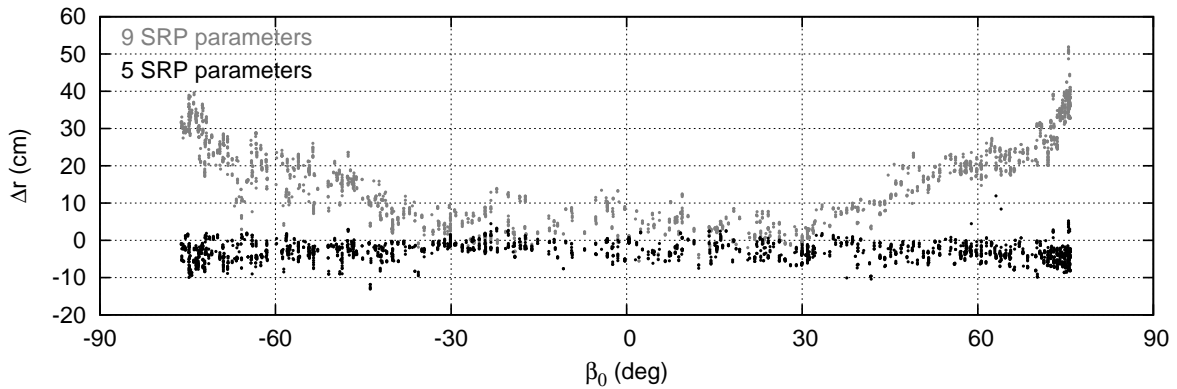
This is why we generated a new orbit time series by estimating the full set of nine dynamic parameters, i.e., three constant terms ( $D0, Y0, B0$ ) and six once-per-revolution terms in all three directions ( $DS, DC, YS, YC, BS, BC$ ) using the argument  $\Delta u$ . For comparison we also generated the corresponding orbit time series estimating the nine SRP parameters and using the argument angle  $u$ .

Figures 5.31(a) and 5.31(b) show the SLR residuals  $\Delta r$  derived from the microwave-based orbits of the GPS satellite G06, estimated by using different argument angles for the once-per-revolution orbit parameters. In Fig. 5.31(a) angle  $u$  was used, whereas in Fig. 5.31(b) angle  $\Delta u$  was used. The range residuals are shown as a function of the elevation angle  $\beta_0$  of the Sun above the orbital plane. Residuals corresponding to the nominal setup of the five dynamic parameters for orbit determination are indicated with black dots. Those corresponding to the full set of nine dynamic parameters are given in gray.

Figures 5.32(a) and 5.32(b) show the corresponding range residuals for the GLONASS satellite R22. We observe residuals of a comparable size for the orbits generated with five SRP parameters and the different argument angles  $u$  and  $\Delta u$  for both satellites, G05 and R22. The orbits generated with the full set of nine SRP parameters differ significantly from those generated using five SRP parameters, mainly in radial direction as indicated by the range residuals. A dependency on the angle  $\beta_0$  is also apparent. The range residuals grow rapidly for angles  $|\beta_0| > 30^\circ$ . For the maximum  $\beta_0$  angle the residuals for the GPS satellite reach values up to 40 cm, and up to 100 cm for the GLONASS satellite. The resulting orbits derived by estimating nine SRP parameters are therefore not realistic. This may be caused by correlations between certain orbit parameters with other parameters estimated in the adjustment process. According



(a) Argument angle  $u$



(b) Argument angle  $\Delta u$

Figure 5.31: SLR residuals  $\Delta r$  for the GPS satellite G06 derived from microwave-based orbits generated by estimating five (black) and nine (gray) SRP parameters, and by using the angles  $u$  and  $\Delta u$ , respectively, as independent arguments; the residuals are given as a function of  $\beta_0$

to Springer et al. (1999) the optimized orbit parameterization consists of five parameters of the ECOM model, namely the three constant accelerations in D-, Y-, and B-direction and two periodic terms (sine and cosine) in B-direction. Springer et al. (1999) have shown that the estimation of additional periodic terms in D- and Y-direction significantly increases the formal errors of the LOD estimates. Therefore the use of the five parameters  $D0$ ,  $Y0$ ,  $B0$ ,  $BS$ , and  $BC$  is recommended. The use of additional SLR observations in a combined analysis of microwave and SLR data for orbit determination may contribute to a reduction of the correlations between the orbit parameters, and thus allow the experimental use of more orbit parameters in future analyses.

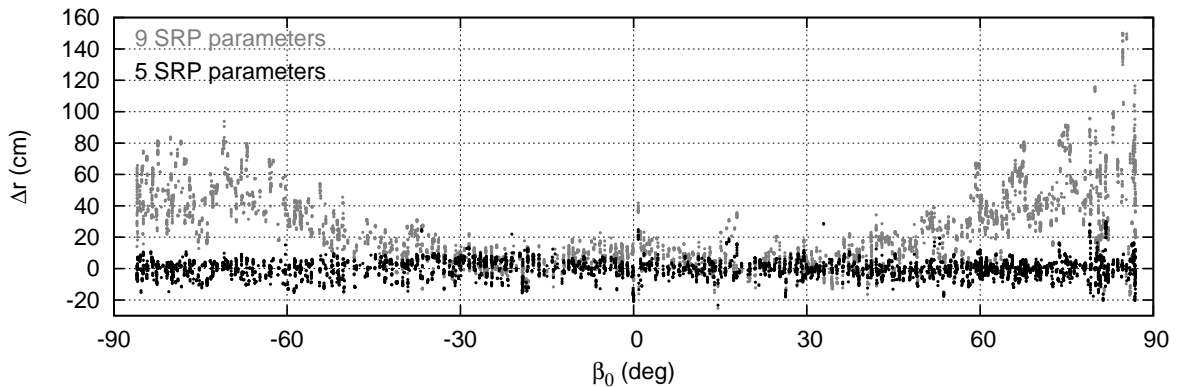
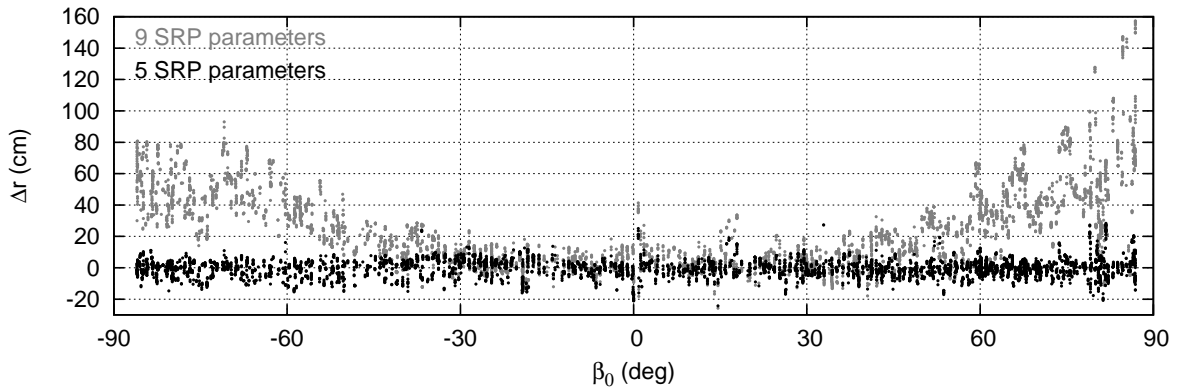
(a) Argument angle  $u$ (b) Argument angle  $\Delta u$ 

Figure 5.32: SLR residuals  $\Delta r$  for the GLONASS satellite R22 derived from microwave-based orbits generated by estimating five (black) and nine (gray) SRP parameters, and by using the angles  $u$  and  $\Delta u$ , respectively, as independent arguments; the residuals are given as a function of  $\beta_0$

## 5.4 Conclusions

The analysis of SLR residuals derived from GNSS microwave-based orbits has revealed deficiencies in GNSS orbit modeling on the 5 – 10 cm level. As SRP is the most important non-gravitational force acting on GNSS satellites, we used different SRP a priori models and checked their impact on GNSS orbits.

The SLR validation results of Sect. 5.2.1 allow it to draw the following conclusions. The orbits for the two Block IIA GPS satellites (equipped with LRAs) improve when using the CODE or no SRP a priori model instead of the ROCK model. The use of the ROCK model leads to a

systematic pattern of the SLR residuals with a once-per-revolution period. The SLR residuals show maximum values close to the shadow region, when the satellite passes through the Earth's shadow. If the CODE model or no SRP a priori model is used instead this pattern decreases significantly. A range bias of about  $-4$  cm is still present and not explained. For GLONASS satellites there is no significant pattern in the SLR residuals, independently of using the CODE model or not using any a priori model. A range bias of about  $-1$  cm was estimated for the GLONASS satellites, but with a value close to zero for the GLONASS-M satellite.

SLR observations are only available for the two Block IIA satellite. In order to check the orbits of the other Block IIA and Block IIR GPS satellite we compared the GPS orbits based on the different SRP models in Sect. 5.2.2. The comparison was carried out in radial direction to make the orbit differences comparable with the SLR residuals. We found a clear block-specific behavior of the orbit differences. For the two satellites G05 and G06, which have been already validated with SLR, the orbit differences between the orbits using the ROCK and the CODE model show a pattern similar to that of the SLR residuals derived from the orbits based on the ROCK model. From this result we conclude that the CODE model or no SRP model at all is superior to the ROCK model for all Block IIA satellites. For the Block IIR satellites we cannot decide which SRP model is better suited, due to the absence of absolute validation methods. Furthermore, there is no significant difference between the orbits based on the CODE and the NONE model. Orbits of comparable quality can thus be obtained by determining GNSS orbits without any SRP a priori model, if in addition the five SRP parameters of the ECOM model ( $D0, Y0, B0, BS, BC$ ) are estimated, as these parameters reflect the major part of the CODE SRP model.

A good SRP a priori model is, however, required for orbit predictions. This result was obtained in Sect. 5.2.3. Orbit predictions based on the three SRP models are compared with estimated orbits (at the time of the prediction) to assess the quality of the models. The CODE SRP model yields better orbits for most of the GPS satellites, independently of the Block type, except for the orbits, which are partially eclipsed. The satellite's attitude is unknown for Block IIA satellites during eclipse (up to 30 min after re-entry into the sunlight), whereas the attitude is known for Block IIR satellites. Therefore orbit predictions for Block IIA satellites during eclipse periods show much larger differences with respect to the estimated orbit than the predictions for Block IIR satellites.

Orbit predictions for the GLONASS satellites based on the CODE model reveal larger differences with respect to the orbits estimated (using the observations at the time of the predictions) than orbit predictions generated without an a priori model. Therefore, the CODE model should not be used for the GLONASS satellites. At CODE the model is no longer in use for GLONASS since November 2007.

In Sect. 5.2.4 we analyzed the orbit overlap errors of one-day and three-day arcs of GPS and GLONASS satellites to search for systematic discontinuities at the day boundaries. In fact, the overlap components show strong systematic patterns, but no dependencies on the used SRP model were found, which was not expected. The patterns are similar for the three solutions using the three SRP a priori models.

We see a plane-specific pattern for the GPS one-day arcs, in particular for the along-track component repeating after about 355 days. As the length of the analyzed time series is only approximately four years, it cannot be estimated accurately using Fourier analysis. The pattern is larger for planes for which the elevation angle  $\beta_0$  of the Sun above the orbital plane reaches large values. The pattern decreases with decreasing maximum  $\beta_0$ . We did not find a clear correlation between the pattern and the eclipsing periods. It might well be that a specific problem exists for one particular orbital plane, which affects the other planes.

The overlap errors are much larger for one-day than for three-day arcs. We observe significant mean values in along-track direction for the three-day arcs of about  $-2$  cm for all satellites of the orbital planes 2 and 3 (with the largest values of  $\beta_0$ ), which still have to be explained. Further studies are necessary to explain the systematic patterns in the overlap errors.

For GLONASS, we also found systematic patterns in the orbit overlaps errors. A spectral analysis of the one-day arcs revealed spectral lines at the beat periods 7.6 days and 7.8 days (the sidereal and synodic revolution period sampled at 24 hour intervals) and the repeat period of 8 days, indicating systematic once-per-revolution orbit errors. These might be caused by the used relative antenna PCC model, which does not provide any values for the GLONASS satellites. The PCO values of the absolute PCC model are about 2 m for most of the GLONASS satellites in Z-direction, which may cause along-track errors of about 30 cm. Along-track errors of this size were found in the one-day arc overlap studies, whereas they disappeared when using the absolute antenna PCC model. The analysis of three-day arcs was done only with the NONE model. The spectral lines at about 8 days are no longer present. But there are still significant mean values of 2 cm for plane 1 and of  $-0.5$  cm for plane 3, which might disappear when using the absolute PCC model. Therefore, we recommend to analyze the overlap errors for three-day arcs based on the absolute antenna PCC model.

A spectral analysis of the geocenter Z-coordinate was performed to assess the impact of the different SRP a priori models on the geocenter (defined by the GNSS satellite orbits). The ROCK model shows the largest peak at a spectral line of 352 days, indicating once more orbit modeling problems. Using the CODE a priori SRP model or not using any SRP a priori model reduces this peak significantly, which confirms the results of the previous analyses that the ROCK model shows model deficiencies and should thus not be used. In addition, a period of about 50 days was found, which is  $\frac{1}{7}$  of 352 days, and which is still unexplained. This period is also present in time series of other analysis centers using other software packages. Further investigations are needed to understand this effect.

Last but not least, we estimated different sets of dynamical orbit parameters, namely five and nine parameters of the ECOM model ( $D0, Y0, B0, BS, BC$  and  $D0, Y0, B0, DS, DC, YS, YC, BS, BC$ ). We used the angle  $\Delta u$  as independent argument (instead of  $u$ ) for the five parameter solution, but did not find significant differences. Solutions using the set of nine dynamical parameters could not be used for further studies, as the parameters are not well determined due to the correlations between the parameters. Using in addition SLR observations might improve the GNSS orbit determination.

Our results confirm that we are facing deficiencies of the GNSS orbit model. Using the CODE SRP models improves the GPS orbits (compared to the use of the ROCK model). There are,

however, small systematic patterns visible in the SLR residuals and more prominently in the overlap errors for the orbits based on the CODE model, which need to be explained. Independent studies, e.g., Ray et al. (2008), indicate effects due to GNSS orbit mismodeling, who found a period of about 350 days (close to the draconitic period) in time series of GPS coordinates.

Ostini (2007) analyzed time series of GPS coordinates using GNSS orbits that were generated using three SRP a priori models (ROCK, CODE, and NONE). The results of a spectral analysis of the site coordinates confirm the period of about 350 days independently of the SRP model used, as there is no significant difference in the spectra of the three different solutions using the ROCK, the CODE, or no SRP model.

## 6. Improving GNSS Orbits with SLR

In the scope of this work studies on combination were carried out to verify whether and (if yes) to what extent the combined analysis of microwave and SLR measurements improves the GNSS orbits.

Section 6.1 presents the combined analysis of microwave and SLR tracking data and is based on the publications Urschl et al. (2005) and Urschl et al. (2007).

Section 6.2 presents first orbit determination results for the Galileo test-bed satellite GIOVE-A based on SLR data only. This study was already presented in Urschl et al. (2006).

### 6.1 GNSS Orbit Determination Based on Combined Microwave and SLR Data Analysis

The combination of space-geodetic techniques is considered as an important tool for improving the accuracy and consistency of the resulting geodetic products. For GNSS satellites, tracking data are regularly collected by both, the microwave and the SLR observation technique.

In Sect. 6.1.2 we study the impact of a combined analysis of microwave and SLR observations on precise orbit determination of GNSS satellites. Combined orbits are generated for the two GPS satellites equipped with laser retroreflector arrays (LRAs) and for three GLONASS satellites, which were observed by the ILRS network at the time of the analysis. The combination is done at the observation level, implying that all parameters common to both techniques are derived from both observation types. Several experimental orbits are determined using different observation weights. As the bias between SLR measurements and GPS microwave orbits is unexplained (see Sect. 4.2.2), range biases as well as satellite retroreflector offsets are estimated in addition to the orbit parameters. The different orbit solutions are then compared in order to determine whether and to what extent the SLR measurements influence a microwave orbit primarily derived from microwave observations.

Note, that the offsets of the LRAs onboard of the GPS satellites of about 1 cm (Davis et al., 2005) have not been known at the time when the following analyses were carried out. Hence, the mean value of the range bias between SLR measurements and the microwave orbits is always reported to be about  $-5$  cm. The correct value considering the corrected LRA offset would have been about  $-4$  cm.

In Sect. 6.1.3 variance-covariance analyses are performed in order to study the impact of a combined analysis of microwave and SLR data on GNSS orbit determination independently of (existing) inter-technique modeling problems (as a correct modeling can be assumed). This kind of analysis allows to check easily (without using actual observations) whether a specific observation scenario (specified only by the observation epochs) is well suited for orbit improvement.

We simulated regularly collected SLR data for GPS and GLONASS satellites and show the contribution of these SLR data on GNSS orbit determination. In addition, we show for the first Galileo test-bed satellite GIOVE-A (see Sect. 3.1.1) the possible positive impact of SLR data on orbit determination. GIOVE-A orbit determination based on microwave data relied initially on a very limited number of observations. Therefore, the additional use of SLR data in a combined analysis gives an important contribution to precise orbit determination. As no microwave data were available at the time our analysis was performed, we simulated the microwave data of GIOVE-A and made a variance-covariance analysis using real SLR data and simulated microwave data.

### 6.1.1 Combination Strategy

We combine the measurements of different types on the observation level (using microwave double difference phase observations in ionosphere-free linear combinations and SLR range observations). Technically, the technique-specific normal equation contributions are stacked. Parameters common to both observation types are derived from the normal equations of both techniques. Common parameters are orbit parameters, EOPs, geocenter coordinates, and coordinates of collocated sites constrained with local ties. As our analysis focuses on the estimation of orbit parameters only, we constrain all other parameters to highly accurate a priori values. The geocenter is constrained to the origin of the ITRF2000. EOPs are constrained to the weekly EOPs, derived from the CODE final orbit solution. For the datum definition, the coordinates of the laser tracking sites and the sites with microwave receivers are constrained to their ITRF2000 estimates.

### 6.1.2 Combined Analysis of Microwave and SLR Observations

Two types of combined orbits using microwave and SLR data were generated, namely one-day and three-day arcs. For the three-day arcs the orbit dynamics is a stronger constraint than for the one-day arcs, which reduces the impact of the SLR observations on the resulting orbit. The CODE orbit model (see Sect. 3.2.2) was used. The six orbital elements, nine dynamical orbit parameters and one stochastic pulse at noon and, for the three-day arcs, at the day boundaries were estimated. Combined orbits were computed for the two GPS satellites (G05 and G06) equipped with laser retroreflectors and three of the GLONASS satellites (R03, R22, R24), which were tracked by the ILRS network at the time of this analysis.

## Data Set

The microwave phase measurements from 157 GNSS sites as well as the laser ranging measurements from 13 SLR sites were used to generate a time series of 41 days in 2004 (DoY 305-345). Figure 6.1 shows the global distribution of the used SLR (triangle) and GNSS (circles) sites. Most of the sparsely distributed SLR sites tracking GNSS satellites are located on the Northern hemisphere. Only 27 of the 157 sites with microwave receivers tracked both, GPS and GLONASS satellites, whereas the majority of stations (i.e. 130) tracked only GPS satellites.

The number of observations available for the parameter estimation process differs greatly between the two techniques and the two satellite systems, GPS and GLONASS. About 20 000 microwave measurements for each GPS satellite and about 3 000 for each GLONASS satellite were used to generate a combined orbit (one-day arc), considering a sampling rate of 180 seconds. On a daily average, SLR measurements of only 5 to 20 normal points for each GPS satellite and about 10 to 40 normal points for each GLONASS satellite are available from the selected sites during the considered time interval. Figure 6.2 shows the varying number of normal points for each satellite over the analyzed time interval.

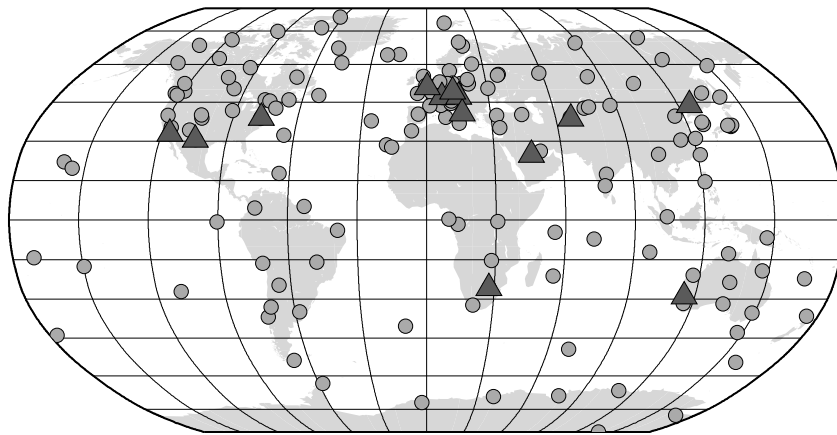


Figure 6.1: SLR and GNSS sites (triangle, SLR; circle, GNSS)

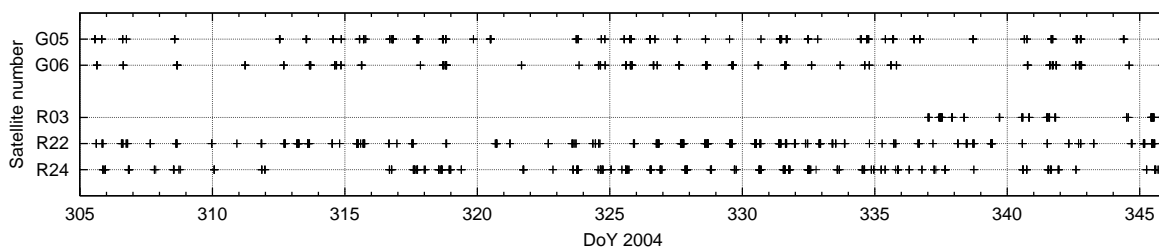


Figure 6.2: SLR normal points of the GNSS satellites over the considered time interval

## Combination Experiments

We performed three combination experiments:

**Experiment 1** is a “quick-look” experiment to study the impact of SLR observations on the combined orbits without making the attempt to model the range bias between SLR and microwave observations. We address the question whether the microwave observation model is able to absorb this bias by, e.g., adapting phase ambiguities or receiver clocks, or whether the orbit dynamics is strong enough not to absorb the bias. The former effect would result in a scaling of the orbit, while the latter would more and more deform the orbit, when increasing the weight of the SLR observations.

**Experiment 2** Daily range biases for each station and each satellite are estimated in addition to the orbit parameters. Due to these range biases the SLR contribution is strongly reduced in this experiment. Only the pass-specific SLR information contributes to the combined orbit. The question remains: what is the impact of the pass-specific SLR contribution on the orbit?

**Experiment 3** The mean range biases are modeled by estimating two satellite reflector offsets in the radial direction (pointing to the geocenter), one for the two GPS satellites and one for the three GLONASS satellites. These offsets absorb the mean bias of all SLR observations to GPS and GLONASS satellites, each over the considered time interval. Compared to the second experiment, the SLR observations to GPS satellites have more influence on the resulting orbit, because the day to day variations of the laser ranges contribute to the orbit determination. Therefore, the third experiment is the most interesting one to study the impact of additional laser measurements on the microwave measurements-dominated orbit.

Several orbits are determined for each experiment. We characterize the orbits with a scheme of “solution IDs” that is used throughout this section. Table 6.1 lists the solution IDs and the corresponding characteristics. The table contains three parts, corresponding to the three experiments.

The initial character of the solution ID characterizes the observation weighting, the second character corresponds to the experiment number. We use four different weight scenarios, *A*, *B*, *C* and *D*. The a priori sigma of the microwave observations (double difference phase, ionosphere-free linear combination)  $\sigma_{MW}$  is 1 cm in all cases, whereas the a priori sigma of the range measurements changes in such a way that the weight of the SLR observations increases with consecutive solution IDs.

In case *A* the a priori sigma of the SLR measurements  $\sigma_A$  is set to infinity, which corresponds to a weight of zero, implying that the SLR measurements do not contribute to the orbit determination (i.e., orbit *A1* is a microwave-only orbit). The a priori sigma  $\sigma_B$  corresponds in order of magnitude to the actual measurement accuracy of the range measurements as well as to  $\sigma_{MW}$ . Both measurement types have approximately the same weight. Cases *C* and *D* increase the weight of the range measurements with respect to the microwave measurements.

Orbit ID	SLR weighting	Additional parameters
<i>Experiment 1</i>		
<i>A1</i>	$\sigma_A = \infty$	
<i>B1</i>	$\sigma_B = 10 \text{ mm}$ ( $\equiv \sigma_{MW}$ )	
<i>C1</i>	$\sigma_C = 1 \text{ mm}$	
<i>D1</i>	$\sigma_D = 0.1 \text{ mm}$	
<i>Experiment 2</i>		
<i>B2</i>	$\sigma_B = 10 \text{ mm}$	range bias
<i>C2</i>	$\sigma_C = 1 \text{ mm}$	range bias
<i>Experiment 3</i>		
<i>B3</i>	$\sigma_B = 10 \text{ mm}$	satellite reflector offset
<i>C3</i>	$\sigma_C = 1 \text{ mm}$	satellite reflector offset

Table 6.1: Listing of orbit solution IDs

In the first experiment, we compute four different orbit solutions with the four different weighting cases. In the second and third experiment only weight types *B* and *C* are considered.

## Results

When increasing the weight of the range observations we expect the SLR residuals to have smaller mean values and standard deviations. The residuals indicate whether the small amount of SLR observations is able to “influence” an orbit determined by microwave observations. They do not allow it, however, to draw conclusions on the orbit accuracy.

In order to assess the “deformation” of the orbits, we compare the orbits directly (in radial, along-track, and out-of plane direction). The parameters of a Helmert transformation will reveal in addition possible translation, rotation and scaling effects.

Orbit quality is assessed by the orbit overlap errors, i.e., the position differences of consecutive orbital arcs evaluated at the day boundaries. If the orbits are well defined, consecutive arcs should fit together well and the overlap error should be small.

**Discussion of Experiment 1** For the first experiment, we compute one-day arcs of the orbit types *A1*, *B1*, *C1*, and *D1* (see Table 6.1) for each of the 41 days in the considered time interval.

Figure 6.3 shows the SLR residuals for one of the GPS satellites (G05). Table 6.2 lists the mean values and standard deviations of the SLR residuals for all GNSS satellites. For the microwave-only solution *A1* the standard deviation of the SLR residuals is about 2 cm for the GPS satellites and about 5 cm for the GLONASS satellites, which corresponds to the microwave

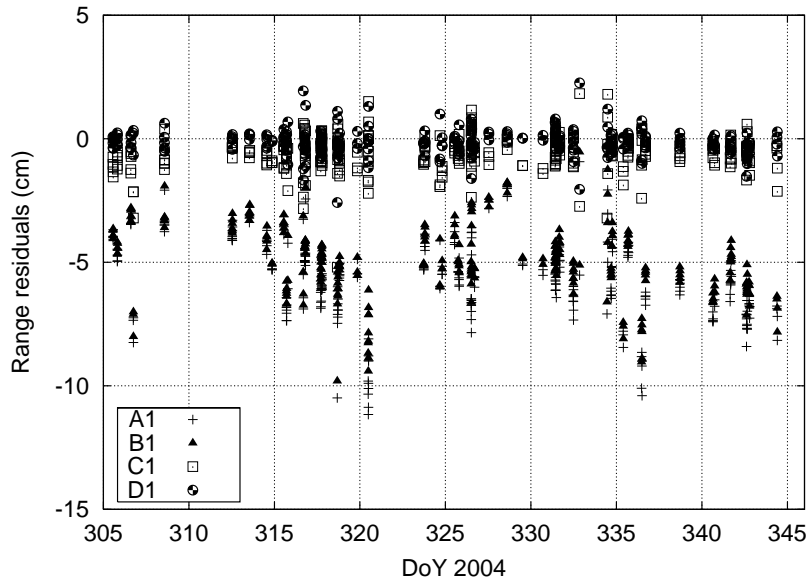


Figure 6.3: SLR residuals derived from one-day arc orbit solutions *A1*, *B1*, *C1*, and *D1* for the GPS satellite G05

orbit accuracy of one-day arc solutions. The mean values of the residual are similar for the two GPS satellites with  $-5.7$  cm and  $-5.8$  cm, whereas they differ for the three GLONASS satellites with  $-3$  cm,  $0$  cm and  $1$  cm, respectively.

As expected, the SLR residuals become smaller with increasing weight of the SLR observations. For solution *B1*, significant changes in the SLR residuals can be noticed already, particularly for the GLONASS satellites. The mean value of the range residuals for the GLONASS satellites approaches zero when increasing the weight of the SLR observations. The mean offset for the GPS satellites, however, remains at the  $-5$  cm to  $-6$  cm level for orbit solution *B1*, but decreases to  $0.1$  cm for solution *D1*.

Satellite	<i>A1</i>		<i>B1</i>		<i>C1</i>		<i>D1</i>	
	$\bar{x}$	$\sigma$	$\bar{x}$	$\sigma$	$\bar{x}$	$\sigma$	$\bar{x}$	$\sigma$
G05	$-5.7$	1.7	$-5.0$	1.4	$-0.6$	0.8	$-0.1$	0.5
G06	$-5.8$	3.5	$-5.5$	3.3	$-1.2$	1.3	$-0.1$	0.6
R03	$-3.1$	5.6	$-0.5$	2.3	0.0	1.5	0.0	1.3
R22	0.0	5.0	$-0.3$	2.3	0.0	1.0	0.0	0.9
R24	1.1	6.3	0.0	2.4	0.0	0.7	0.0	0.6

Table 6.2: Mean values and standard deviations (cm) of the SLR residuals derived from the solutions *A1*, *B1*, *C1*, and *D1*

Let us now compare the microwave-only orbit  $A1$  with the combined orbits  $B1$ ,  $C1$ , and  $D1$ . Helmert transformation parameters for each one-day arc are estimated for the solutions pairs  $A1 - B1$ ,  $A1 - C1$ , and  $A1 - D1$ . There are no significant rotations. Table 6.3 displays the mean values and standard deviations of the translation parameters and the scale difference averaged over the considered 41 days. The mean values of the Helmert parameters of the pair  $A1 - B1$  are zero for the GPS orbits. For GLONASS, we see variations of up to 4 cm. Both, translation parameters and scale difference, increase with the weight of the SLR observa-

Satellite	$A1 - B1$		$A1 - C1$		$A1 - D1$	
	$\bar{x}$	$\sigma$	$\bar{x}$	$\sigma$	$\bar{x}$	$\sigma$
<i>x-translation (cm)</i>						
G05	0.0	0.2	-0.4	1.0	-0.4	1.2
G06	0.0	0.1	-0.6	0.9	-1.4	1.9
R03	0.0	2.6	-0.3	3.5	-0.9	6.4
R22	0.2	1.0	0.7	3.1	1.6	8.5
R24	-0.1	1.0	0.2	2.1	3.7	12.2
<i>y-translation (cm)</i>						
G05	0.0	0.1	-0.7	1.1	-0.7	1.3
G06	-0.1	0.1	-1.2	1.4	-1.7	1.9
R03	2.0	4.0	3.7	7.3	-1.1	22.9
R22	0.9	1.5	2.3	3.4	1.4	7.7
R24	1.2	1.8	2.8	4.0	4.9	12.7
<i>z-translation (cm)</i>						
G05	0.0	0.2	-0.3	1.1	-0.6	1.5
G06	-0.1	0.2	-1.0	1.5	-1.0	2.8
R03	-2.0	3.5	-4.7	9.7	-2.7	5.4
R22	1.3	1.7	2.7	3.3	4.0	7.7
R24	1.6	3.0	2.4	5.9	3.5	14.1
<i>scale difference (ppb)</i>						
G05	-0.1	0.1	-0.7	0.6	-0.9	0.8
G06	0.0	0.0	-0.3	0.4	-0.4	0.6
R03	-0.4	0.6	-0.7	1.0	-0.6	1.3
R22	-0.1	0.3	-0.2	0.6	-0.4	1.6
R24	-0.1	0.2	-0.1	0.6	-0.2	2.3

Table 6.3: Mean values and standard deviations of the Helmert transformation parameters averaged over 41 days between the solutions  $A1 - B1$ ,  $A1 - C1$ , and  $A1 - D1$

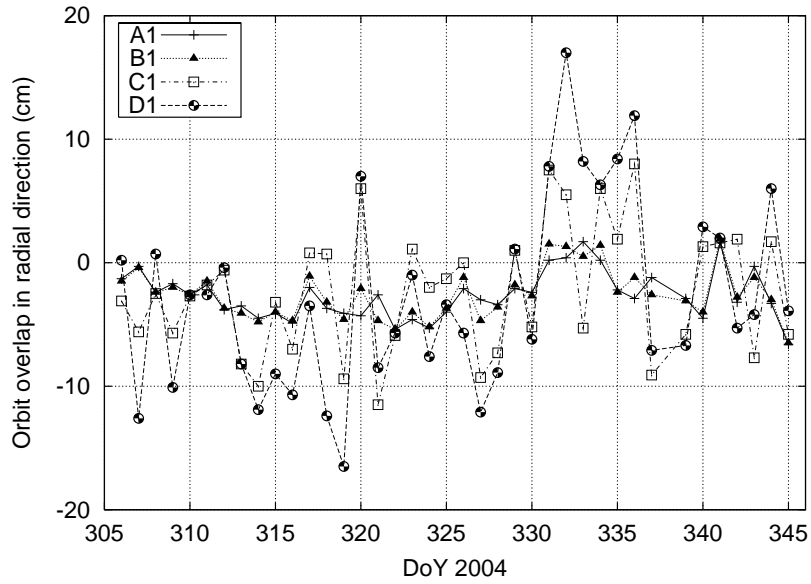
tions. For  $A1 - D1$  the translation parameters for GLONASS orbits vary by up to 23 cm about a mean value of up to 5 cm. For GPS the mean value is at  $-1$  cm with a variation of up to 3 cm. The influence of SLR measurements on GLONASS satellites is larger due to the larger number of normal points and the smaller number of microwave measurements when compared to GPS satellites. The scale difference is about 0.6 ppb (1.3 cm in radial direction) on the average, but may reach values up to 1 ppb for some orbit solutions.

Table 6.4 gives the standard deviations of the daily orbit differences over the 41 days for each GNSS satellite after the Helmert transformation. These standard deviations increase with increasing SLR weight. The along-track component shows the largest values. For the pair  $A1 - D1$  the standard deviations of the orbit differences reach values up to 5 cm for the GPS and up to 40 cm for the GLONASS satellites.

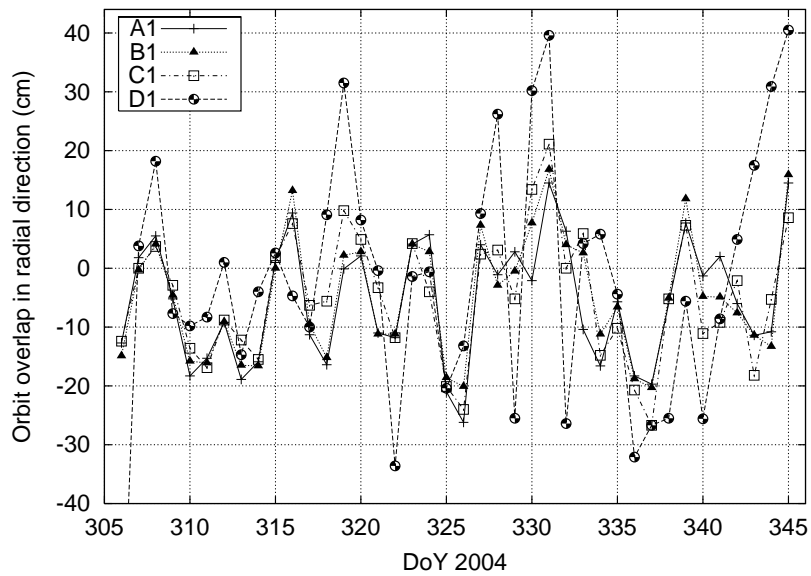
Figures 6.4(a) and 6.4(b) display the radial overlap components for the satellites G05 and R22. The overlap error for solution  $A1$  is about 5 cm for the GPS orbits. This value is much larger for the GLONASS orbits, due to the low number of GLONASS tracking sites. The overlap errors in the along-track and out-of-plane directions are of the same order of magnitude. We found

Satellite	$A1 - B1$	$A1 - C1$	$A1 - D1$
<i>radial (cm)</i>			
G05	0.2	1.2	1.6
G06	0.1	1.9	3.3
R03	2.8	5.2	13.4
R22	1.4	2.8	6.7
R24	1.7	3.8	15.1
<i>along-track (cm)</i>			
G05	0.2	1.6	2.6
G06	0.2	2.8	4.8
R03	8.5	15.1	38.5
R22	3.6	7.8	20.7
R24	4.1	10.4	41.6
<i>out-of-plane (cm)</i>			
G05	0.2	2.2	3.5
G06	0.1	1.5	2.2
R03	2.3	4.2	8.7
R22	1.4	3.2	10.1
R24	1.7	3.4	15.3

Table 6.4: Standard deviations of orbit differences of 41 days between the solutions  $A1 - B1$ ,  $A1 - C1$ , and  $A1 - D1$ , after Helmert transformation



(a) G05



(b) R22

Figure 6.4: Orbit overlap errors in radial direction of the one-day arc orbit solutions  $A1$ ,  $B1$ ,  $C1$ , and  $D1$  for the GPS satellite G05 and the GLONASS satellite R22

that the orbit overlap errors become larger for the combined orbits with increasing weight of the SLR observations. The overlap error of the combined orbit  $B1$  does not change significantly compared to the microwave orbit  $A1$ , while it gets larger in cases  $C1$  and  $D1$ .

**Discussion of Experiment 2** We estimate daily range biases for each station and satellite when generating the combined orbit in order to absorb the mean offsets (solution IDs  $B2$  and  $C2$ ). As a result, the impact of the SLR observations on the orbit is greatly reduced.

The SLR residuals derived from the combined orbits  $B2$  and  $C2$  have a zero mean value with a standard deviation of about 1 – 2 cm (see Table 6.5).

The mean values of the Helmert parameters between the one-day arc orbits  $A1$  and  $B2$  are about zero (no table included). For GLONASS orbits the translation parameters show variations of about 1 cm. With increasing weight of the SLR observations (solution  $C2$ ) the mean translation parameters of the GLONASS orbits have values of about 2 cm. The variations of the translation parameters increase to 3 cm for GLONASS and to 0.5 cm for GPS orbits. The scale change is negligible. The GLONASS orbits show a slight scale variation with zero mean values for the difference  $A1 - C2$ .

Comparing the combined orbits with the microwave orbits we see no significant changes for the GPS satellites, neither for  $A1 - B2$  nor for  $A1 - C2$  comparisons. The standard deviation of the daily GPS orbit comparisons is below the one cm level, see Table 6.6. But for the GLONASS satellites we observe orbit differences of up to 5 – 10 cm, which are due to the fact that pass-specific patterns in the range measurements are much larger for the GLONASS than for the GPS satellites. Figure 6.5 demonstrates the improvement of the range residual pattern for one pass of the GLONASS satellite R24 observed by the SLR site 7090 (Yarragadee) when increasing the weight of the range measurements.

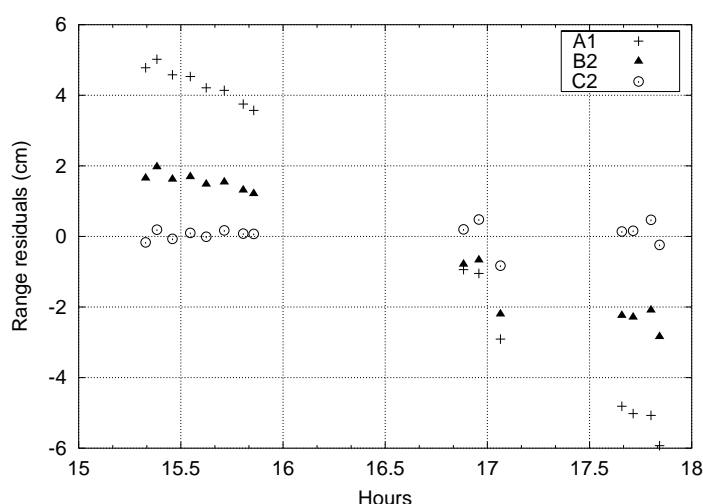


Figure 6.5: Pass-specific range residuals of the GLONASS satellite R24 observed by the SLR site 7090 for the orbit solutions  $A1$ ,  $B2$ , and  $C2$

## 6.1 GNSS Orbit Determination Based on Combined Microwave and SLR Data Analysis

---

The size of the orbit overlap errors does not change significantly when increasing the SLR weight, neither for the *B2* nor for the *C2* solutions (no figures included).

Satellite	<i>B2</i>		<i>C2</i>	
	$\bar{x}$	$\sigma$	$\bar{x}$	$\sigma$
G05	0.0	0.6	0.0	0.5
G06	0.0	1.6	0.0	0.8
R03	0.0	1.8	0.0	1.4
R22	0.0	1.4	0.0	0.9
R24	0.0	1.6	0.0	0.7

Table 6.5: Mean values and standard deviations (cm) of the SLR residuals derived from the solutions *B2* and *C2*

Satellite	<i>A1 – B2</i>	<i>A1 – C2</i>
<i>radial (cm)</i>		
G05	0.0	0.2
G06	0.0	0.4
R03	1.7	3.2
R22	0.5	1.9
R24	1.1	2.6
<i>along-track (cm)</i>		
G05	0.0	0.2
G06	0.0	0.7
R03	5.3	10.0
R22	1.4	4.7
R24	2.6	5.6
<i>out-of-plane (cm)</i>		
G05	0.0	0.1
G06	0.0	0.4
R03	0.6	3.6
R22	0.6	1.9
R24	0.9	2.5

Table 6.6: Standard deviations of orbit differences of 41 days between the solutions *A1 – B2* and *A1 – C2*, after Helmert transformation

**Discussion of Experiment 3** For the third set of combined orbit solutions we estimate retroreflector offsets together with the orbit parameters instead of constraining the reflector offsets to their a priori values. Two offsets (satellite-type-specific) in radial direction are determined, one offset for the GPS satellites and one for the GLONASS satellites. Thus, we allow for an additional constant offset for each satellite-type, but not for each satellite and not for each station (as in Experiment 2).

Table 6.7 shows the estimated retroreflector offsets with respect to the a priori values for the GPS and GLONASS satellites and the one-day arc solutions  $B3$ ,  $C3$ . The a priori retroreflector offsets in radial direction are 0.6584 m for the GPS and 1.5416 m for the GLONASS satellites. The estimated reflector offset correction is about 5 cm for the GPS satellites and close to zero for the GLONASS satellites. As expected, these values correspond to the range biases estimated in the first experiment.

As for the second experiment, the SLR residuals derived from the combined orbits  $B3$  and  $C3$  vary around zero but with a slightly larger standard deviation of about 1 – 3 cm (see Table 6.8), as expected from the significantly smaller number of estimated parameters.

The Helmert parameters for the solution pairs  $A1 - B3$  and  $A1 - C3$  are slightly larger than for the pairs  $A1 - B2$  and  $A1 - C2$  from the second experiment. The mean values of the translation parameters between solution  $A1$  and  $B3$  are zero for the GPS orbits. The GLONASS orbits show mean translations of about 1 cm for  $A1 - B3$  (no table included). When increasing the weight of the SLR observations ( $C3$ ) the mean translations increase up to 3 cm for GLONASS

Satellite	$B3$	$C3$
GPS	$5.56 \pm 0.06$ cm	$5.55 \pm 0.02$ cm
GLONASS	$0.50 \pm 0.08$ cm	$1.44 \pm 0.05$ cm

Table 6.7: Estimated satellite retroreflector offset correction in radial direction (in cm) and formal RMS for GPS and GLONASS satellites from solutions  $B3$  and  $C3$

Satellite	$B3$		$C3$	
	$\bar{x}$	$\sigma$	$\bar{x}$	$\sigma$
G05	-0.1	1.6	0.0	0.6
G06	-0.3	3.3	-0.1	1.1
R03	-0.5	2.2	0.0	1.4
R22	-0.1	2.2	0.0	1.0
R24	0.2	2.4	0.0	0.7

Table 6.8: Mean values and standard deviations (cm) of the SLR residuals derived from the solutions  $B3$  and  $C3$

with variations of up to 5 cm. The scale differences of the GPS orbits is at the zero level. For the GLONASS orbits the scale differences between the solutions  $A1$  and  $C3$  is about 0.5 ppb.

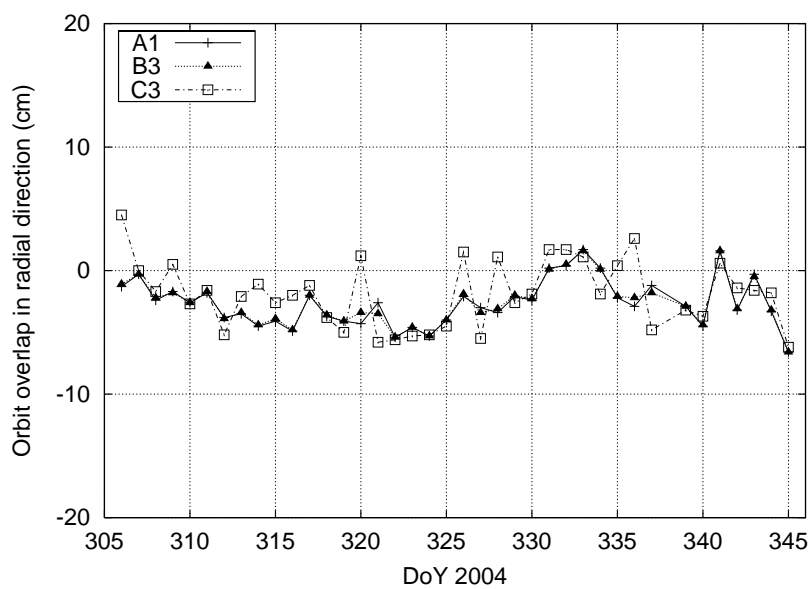
Table 6.9 shows the standard deviations of the daily orbit differences. Only small differences are encountered between the microwave orbit  $A1$  and the combined orbits  $B3$  and  $C3$  for the GPS satellites.

For solution  $B3$  the orbit overlap errors are similar to that of solution  $A1$ , whereas they are larger for solution  $C3$ . Figures 6.6(a) and 6.6(b) show the overlap errors in radial direction for G05 and R22.

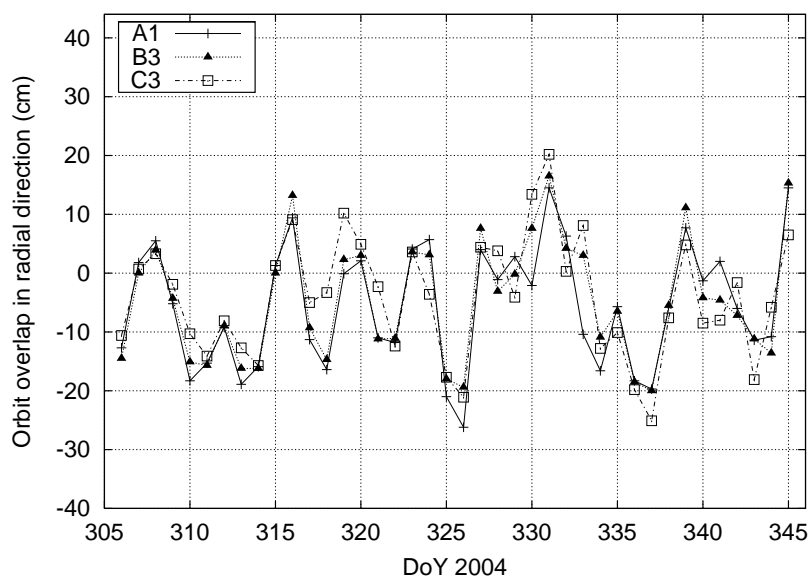
Three-day arcs were analyzed in an analogous manner as the one-day arcs for all three experiments. As observations from the adjacent days are included for orbit determination, the orbit overlaps of the three-day arcs are always better defined than the same overlaps of the corresponding one-day arcs. The overlap errors of the combined orbits are, however, not decreased compared to those of the microwave orbits. The resulting SLR residuals and orbit parameters for the three-day arc solutions do not show any significant differences to the analysis results of the one-day arc solutions.

Satellite	$A1 - B3$	$A1 - C3$
<i>radial (cm)</i>		
G05	0.1	0.4
G06	0.1	1.2
R03	2.6	4.8
R22	1.4	2.7
R24	1.7	3.1
<i>along-track (cm)</i>		
G05	0.1	0.5
G06	0.1	1.4
R03	7.9	12.8
R22	3.5	7.4
R24	4.1	8.1
<i>out-of-plane (cm)</i>		
G05	0.1	0.5
G06	0.0	0.7
R03	2.2	3.8
R22	1.3	2.9
R24	1.8	3.1

Table 6.9: Standard deviations of orbit differences of 41 days between the solutions  $A1 - B3$  and  $A1 - C3$ , after Helmert transformation



(a) G05



(b) R22

Figure 6.6: Orbit overlap errors in radial direction of the one-day arc orbit solutions  $A1$ ,  $B3$ , and  $C3$  for the GPS satellite G05 and the GLONASS satellite R22

## Conclusions

From the first experiment we conclude that the generated combined orbits are sensitive to introducing additional range measurements. Depending on the SLR weighting (with respect to the microwave observations), SLR observations have an impact on an orbit dominated by microwave observations, even if the number of SLR measurements is about three orders of magnitude smaller than the number of microwave measurements. A range observation is the geometric distance of an observatory to a satellite and is, therefore, much “stronger” than a microwave phase measurement, which corresponds to a range biased by ambiguity and clock corrections.

Table 6.2 shows that the mean values and standard deviations of the resulting SLR residuals decrease with increasing SLR weight. Even for solution *B1*, with the smallest SLR weight, improvements of the standard deviation especially for the GLONASS satellites are observed.

The radial bias between microwave- and SLR-derived GPS orbits of about  $-5$  cm does not disappear without “damaging” the combined orbit. By “overweighting” the SLR measurements, the bias decreases to zero, but the resulting orbit is deformed rather than scaled. The observed scale change (Table 6.3) and the change of the along-track component (Table 6.4) correspond radially to about 1 cm, only. This indicates that the microwave observations determine the satellite orbit and scale rather well, and that the orbit dynamics is strong enough not to absorb the 5 cm-bias.

In the second experiment we changed the observation model. Daily range biases were estimated in addition to the orbit parameters already set up in Experiment 1. These range biases were found to absorb the main range information. When solving for such parameters, the impact of SLR observations on the combined orbits becomes very small. However, for the GLONASS satellites orbit differences between the microwave orbit *A1* and the combined orbits *B2* and *C2* of up to 10 cm are seen (see Table 6.6) due to the pass-specific residual patterns that are much larger for the GLONASS than for the GPS satellites (see, e.g., Fig. 6.5).

The values of the overlap errors do not change significantly with increasing weight of the SLR observations. But the SLR residuals show clear improvements in the pass-specific patterns (see Fig. 6.5) when including SLR observations into the orbit determination process.

The 5 cm-bias for GPS satellites between microwave- and SLR-determined orbits might be attributed to unidentified errors in the location of the retroreflector arrays with respect to the satellite’s center of mass (Appleby and Otsubo, 2004). Thus, we adapted the observation model in the third experiment and estimated only two additional parameters, one constant retroreflector offset for all GPS and one for all GLONASS satellites in radial direction. The estimated offset for the GPS satellites correspond with about  $-5$  cm to the mean range bias derived from the microwave-only orbit (Table 6.7). The average of the resulting range residuals decreases to zero. But there are still significant differences of several centimeters in the orbit positions between the microwave-only orbit solution *A1* and the combined solutions *B3* and *C3* for the GLONASS satellites (Table 6.9), showing the impact of SLR observations. The overlap errors of the combined orbits do not change significantly when compared to the microwave orbit.

We have shown that from the technical point of view a combined orbit determination analysis of microwave and SLR tracking data is no problem. Range measurements have an impact

on a combined microwave-SLR orbit, where the impact depends on the observation weight. Significant biases between the two observation techniques do not allow a rigorous combination for GNSS orbit determination without modifying the observation model. The estimation of additional satellite retroreflector offsets absorbs the bias between the microwave orbits and the SLR measurements. The pass-specific patterns of the SLR residuals improve with increasing weight of the SLR observations.

We have seen that the impact of SLR on GLONASS orbits is much larger than on GPS orbits due to the small number of GLONASS microwave tracking sites. A similar situation can be expected for the new Galileo system in its startup phase. Therefore, the use of SLR measurements to the Galileo satellites should considerably improve the orbits (as compared to pure microwave orbits).

### **6.1.3 Variance-Covariance Studies for the Combined Analysis of Microwave and SLR Observations of GPS and GLONASS Satellites**

In the previous section we showed that SLR tracking data can be used in a combined analysis together with microwave data for GNSS orbit determination. The combination of two different techniques is only reasonable, however, if inter-technique modeling problems are solved before.

Therefore, variance-covariance studies are most appropriate (before the mentioned modeling problems have been solved) to assess the impact of SLR data on GNSS orbit determination. The variance-covariance studies are based on a user defined observation scenario, characterized by the observation epochs, the observing sites, the satellites involved, and the observation types. Furthermore, the error models for the observations of all types have to be specified, e.g. observation errors with expectation values “zero” and a user-defined variance. The individual observations are assumed to be uncorrelated. With this information it is possible to calculate the resulting variance-covariance matrix of all parameters (without using actual observations), which usually is fully populated. The variance-covariance matrix of the resulting parameters may then be used to calculate, e.g., the standard deviations of satellite positions at any time.

The variance-covariance matrix associated with the orbit parameters, as derived from microwave and SLR data, will now be established for different observation scenarios. Our analysis should answer the question whether a combined analysis of microwave and SLR data makes sense for GNSS orbit determination under the assumption that the existing modeling problems can be solved.

#### **Realistic Scenario**

For our study we used microwave observations (double difference phase, ionosphere-free linear combination) at epochs separated by 180 seconds from over 150 IGS sites and SLR observations from 13 ILRS sites. The mean errors of the microwave observations were assumed to be 1 cm.

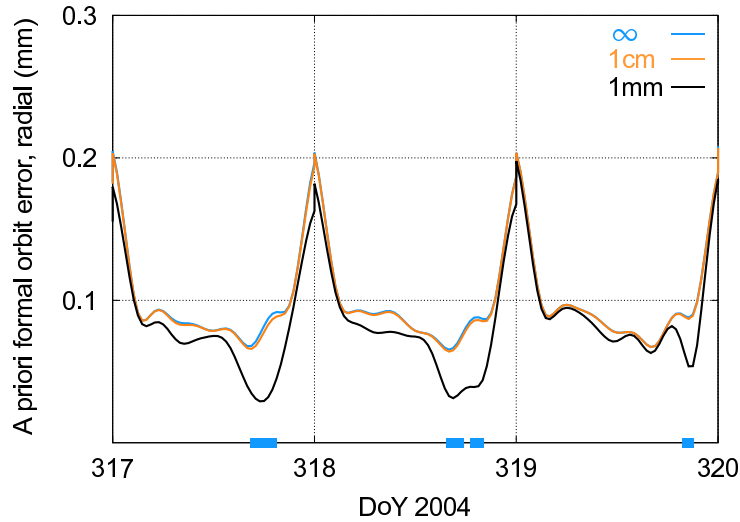


Figure 6.7: Formal errors of the radial orbit component for the GPS satellite G05, derived from real data; observation epochs are indicated on the abscissa

For the SLR observations, three different observation weights were used. In the first case, the a priori sigma  $\sigma_{SLR}$  was set to infinity, corresponding to a weight of zero, implying that the SLR observations do not contribute to the orbit determination. In the second case,  $\sigma_{SLR}$  was set to 1 cm, and in the third case to 1 mm. The covariance study was done for 41 one-day arcs (DoY 255 - 295, 2005). For each arc, the six osculating elements and five dynamical orbit parameters of the ECOM model (see Sect. 3.2.2) were set up. The dynamical parameters represent solar radiation pressure (SRP) parameters, i.e. constant acceleration in D-, Y-, and B-direction and an once-per-revolution accelerations in direction B. For the definition of the (D, Y, B) system see Sect. 3.1.2.

Figure 6.7 shows the formal errors of the radial orbit component derived from the covariance matrices for three consecutive one-day arcs of the GPS satellite G05. The three lines refer to the different SLR observation weights, where the upper line corresponds to  $\sigma_{SLR} = \infty$ , the middle line to  $\sigma_{SLR} = 1$  cm, and the lower line to  $\sigma_{SLR} = 1$  mm. The SLR observation epochs are indicated on the abscissa. No significant improvements can be found when using SLR observations with 1 cm measurement noise. An improvement of the formal errors occurs only when using heavy SLR weights, and only around epochs where SLR data were available. The same is true for the along-track and the out-of-plane directions (not shown here). This result was expected, as the SLR tracking data are very sparse and not very well distributed (as opposed to the microwave observations).

### Idealized Scenario

How does the situation change, if SLR observations cover the complete satellite arc? To answer this question, we simulated evenly distributed SLR observations, i.e., observation epochs. Those observation epochs were assumed to be equally spaced at 15 min intervals for altogether

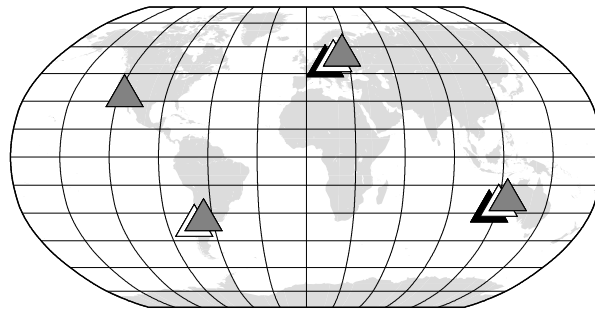


Figure 6.8: SLR site distribution for SLR data simulation

four globally distributed SLR sites, in North and South America, Europe, and Australia respectively (see Figure 6.8). Three different computations were performed, using either two, three, or four sites, indicated in Figure 6.8 with black, white, and gray triangles. The data of two SLR sites cover about 50% of a GNSS orbit (one-day arc), the data of three sites cover almost 75% and that of four sites cover as much as 90%.

Figure 6.9 shows the formal orbit errors in radial direction for the satellite G05 assuming evenly distributed observations of four SLR sites in addition. Shaded areas on the abscissa denote the 90% data coverage. As opposed to Figure 6.7 (derived from real SLR data), the formal error does significantly improve if SLR observations of 1 cm noise (line in the middle) were used. The errors are even more reduced when the SLR weight increases by a factor of 100.

In order to study the results for several arcs we focus on the formal error of the semi-major axis. Figure 6.10 shows the formal errors of the semi-major axis of the satellite G06 for the 41 consecutive one-day arcs. The four line types indicate the number of SLR sites from which

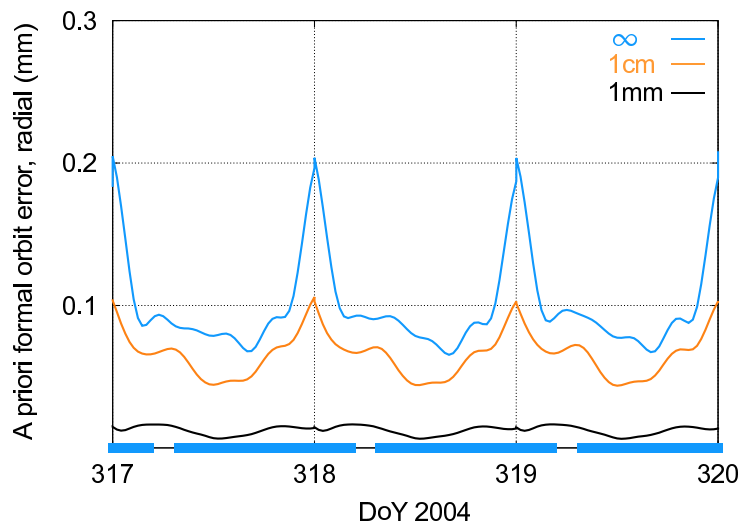


Figure 6.9: Formal errors of the radial orbit component for the GPS satellite G05, derived from simulated data; observation epochs are indicated on the abscissa

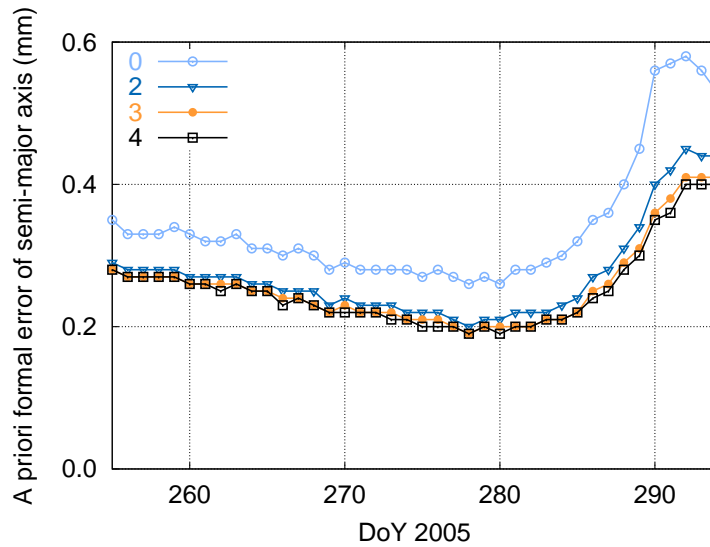


Figure 6.10: Formal errors of the semi-major axis for the GPS satellite G06, derived from simulated data for a different number of SLR sites

simulated observations were used for the combined solution. The first line flagged with “0” corresponds to the microwave-only solution. The remaining three are derived from the combined solutions, using simulated SLR observations of either two, three, or four SLR sites. The general variation of the orbit error within one solution is due to the high correlation of the orbit parameters with the elevation of the Sun above the orbital plane. The formal errors are in the range of 2 – 6 mm. This order of magnitude is too optimistic, as model errors, formal errors of

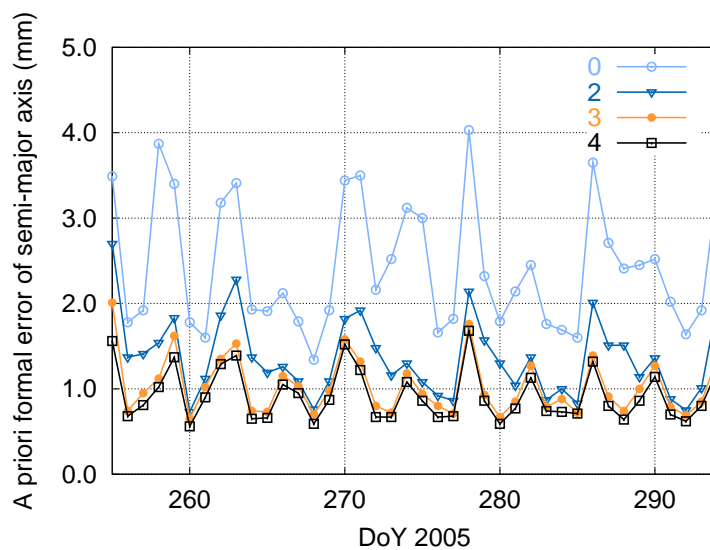


Figure 6.11: Formal errors of the semi-major axis for the GLONASS satellite R03, derived from simulated data for a different number of SLR sites

introduced parameters, as well as correlations in time between consecutive microwave observations are not considered in this variance-covariance study. Using SLR observations of two sites (corresponding to a 50% coverage of the arc) the formal error of the semi-major axis decreases by about 20%. With three sites the formal error decreases even more. The inclusion of the observations of the fourth site does not further improve the solution.

The formal errors of the semi-major axis for the GLONASS satellite R03 are shown in Fig. 6.11. The formal errors are one order of magnitude larger compared to the GPS satellites, as the number of microwave observations for GLONASS ( $\sim 3\,000$ ) is much lower than for GPS ( $\sim 20\,000$ ). Therefore the impact of additional SLR data on the quality of GLONASS orbits is larger than for GPS. Figure 6.11 indicates an improvement of about 50%.

### Conclusions

The combined analysis of microwave phase and SLR range measurements for GNSS orbit determination would improve the orbit, compared to a pure microwave-based solution under the following assumptions: Inter-technique biases have to be understood and modeled, and the orbit modeling has to be improved.

The currently available small number of SLR measurements (in general not well distributed over the day) represents a challenge when trying to improve GNSS orbits by using SLR data. A good distribution of SLR data over the entire orbital arc is important. A small network of three “globally distributed” SLR sites, tracking GNSS satellites continuously, is sufficient to cover a great portion of the orbital arc. From the variance-covariance analysis we conclude that the semi-major axis improves by about 20% for GPS and about 50% for GLONASS satellites, if three SLR sites are continuously tracking the satellites.

The contribution of SLR data to GNSS orbits is even more important if the microwave tracking network is sparse, as it is the case for the GLONASS satellites.

#### 6.1.4 Variance-Covariance Studies for the Combined Analysis of Microwave and SLR Observations of the GIOVE-A Satellite

We have seen that the impact of SLR on GLONASS orbits is much larger than on GPS orbits due to the small number of GLONASS microwave tracking sites. A similar situation can be expected for the new Galileo system in its startup phase. The microwave-based GIOVE-A orbits as well as the first Galileo orbits in the In Orbit Validation (IOV) phase initially will rely on microwave tracking data of a very limited number of microwave tracking receivers. SLR is therefore expected to contribute significantly to precise orbit determination.

This section demonstrates the possible contribution of SLR to GIOVE-A orbit determination through a combined analysis of microwave and SLR data. As no microwave tracking data of GIOVE-A were available at the time of our analysis, we performed a variance-covariance analysis using SLR data from the tracking campaigns and simulated microwave data of GIOVE-A.

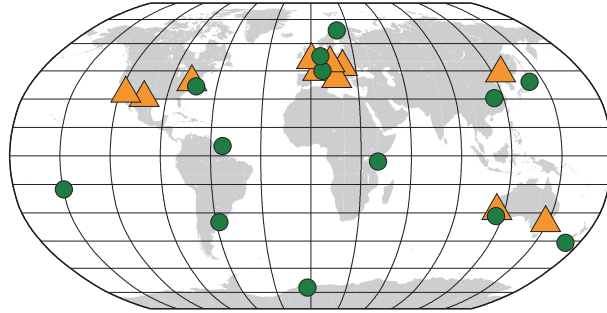


Figure 6.12: GIOVE-A microwave tracking sites (circles) and SLR tracking sites (triangles)

Microwave phase observations were simulated for 13 GIOVE-A tracking sites, selected at proposed sites of the first Galileo tracking network. Their distribution is indicated by circles in Fig. 6.12. In addition we used the true SLR observations of the SLR sites (represented with triangles).

The microwave phase observations are spaced by 30 seconds with an assumed accuracy of 1 mm. Observation equations were set up for microwave phase zero difference observations and SLR normal points. Satellite clocks, ambiguities, and orbit parameters were included in the parameter estimation process. Other parameters, such as station coordinates, receiver clocks, tropospheric zenith path delays, and EOPs are assumed to be known, e.g., from a global analysis of GPS and GLONASS data.

The variance-covariance matrix is derived from the normal equation system. The formal errors of the orbit parameters are then computed from the variance-covariance matrix. We solved for six osculating elements and nine SRP parameters for GIOVE-A, i.e., for constant and once-per-revolution accelerations in D-, Y-, and B-direction. In summary 57 overlapping three-day arcs were determined.

Three analyses with different SLR observation weight scenarios were performed to assess the impact of additional SLR observation on GIOVE-A orbit determination. The first solution corresponds to a pure microwave solution. The SLR observation weight is set to zero by  $\sigma_{SLR} = \infty$ . In the second case,  $\sigma_{SLR} = 1$  cm, in the third case, the SLR observation weight is increased (with  $\sigma_{SLR} = 1$  mm), and corresponds to the microwave observation weight.

We calculate the formal errors of the satellite position in the inertial system from the variance-covariance matrix associated with the orbit parameters. Figure 6.13 shows the formal errors of the satellite position in radial, along-track, and out-of plane components for the three different solutions of a GIOVE-A three-day arc, where the upper line corresponds to  $\sigma_{SLR} = \infty$ , the middle line to  $\sigma_{SLR} = 1$  cm, and the lower line to  $\sigma_{SLR} = 1$  mm.

The resulting errors are too optimistic, as the error scales with the number of observations. We used microwave observation sampled at 30 seconds intervals, but did neglect any temporal correlations between consecutive observations. Observation sampled at 180 seconds intervals should rather be used for further studies.

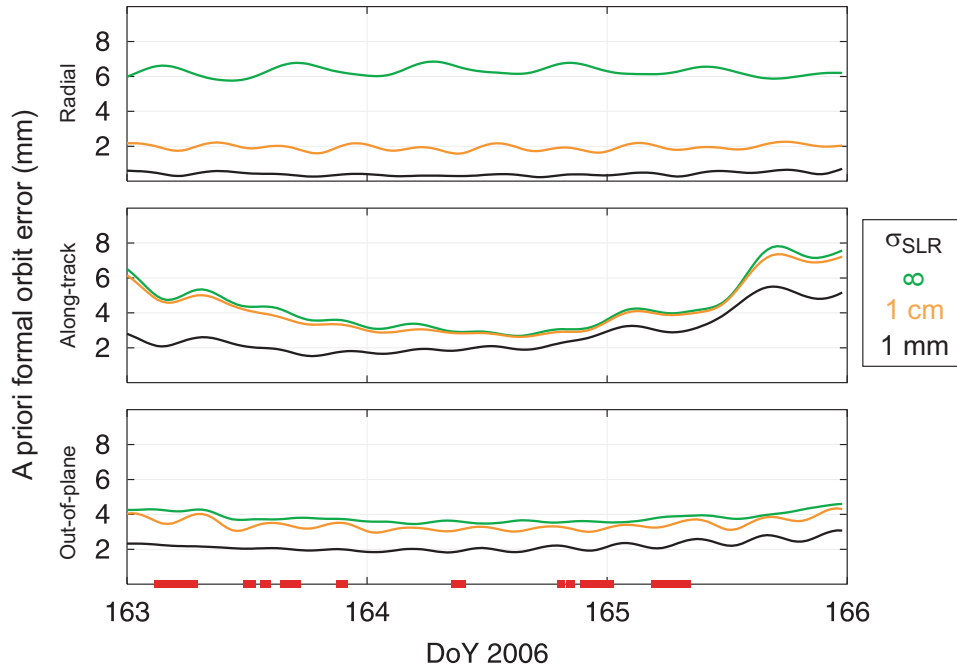


Figure 6.13: Formal orbit errors for a GIOVE-A three-day arc; the three lines indicate the different orbit solutions using different a priori sigmas  $\sigma_{SLR}$  for the SLR observations; the bars on the horizontal axis indicate the SLR observation epochs

The parameters (e.g., station coordinates, troposphere parameters), which are assumed to be known from the GPS/GLONASS analysis, are not error-free. Neglecting the formal errors of these parameters, and of temporal correlations between observations, is responsible for too optimistic formal errors.

In this analysis we are not interested in the absolute errors, but rather in the difference of these errors for the three solutions. These differences may be used to assess the impact of SLR observations on GIOVE-A (or Galileo) orbits. The major impact of SLR data on the resulting orbit accuracy is given in the radial orbit component. The radial orbit accuracy may be improved by about 60-80%, depending on the SLR weight and the number and distribution of SLR observations. The orbit error in along-track and out-of-plane components decreases only when using heavy SLR weights. A good distribution of the SLR observations over the entire arc is always necessary.

We conclude that SLR data provide an important contribution to GIOVE-A orbits. A significant orbit improvement (mainly in radial direction) was demonstrated, if well distributed SLR observations are (would be) available. For the upcoming Galileo system we assume a similar beneficial impact of SLR data as the number of Galileo microwave tracking sites initially will be very small.

## 6.2 GIOVE-A Orbit Determination Based on SLR Observations

GIOVE-A, the first test-bed satellite of the European navigation system Galileo, carries a retro-reflector array and therefore may be observed by SLR. For evaluating the performance of the on-board atomic clocks a first SLR tracking campaign of GIOVE-A was initiated, which lasted for nine weeks. Between 22 May and 24 July 2006, 14 globally well-distributed SLR stations participated in the campaign. These SLR data are publicly available for GIOVE-A orbit determination (as opposed to the microwave data).

We present orbit determination results for GIOVE-A based on SLR data only. Different solutions with varying arc-lengths were generated. In order to assess the orbit quality, differences of orbit overlaps were analyzed. In addition, the orbits were predicted and the quality of the predictions was assessed by comparing the predicted orbits with the orbits derived from real tracking data.

SLR data of the first GIOVE-A SLR tracking campaign, made available by the ILRS, was used. The triangles in Fig. 6.14 indicate the geographical locations of the 11 SLR sites included in our analysis. The numbering of the triangles allows the identification of the SLR sites by using Table A.3 in the Appendix A. We did not use the SLR measurements of San Juan (located in South America), as no reliable coordinates were available at the time of analysis. The distribution of the SLR tracking data in time is given in Fig. 6.15. SLR observation epochs are indicated with a bar. The varying data coverage is clearly visible. Therefore, the quality of the orbits derived from these data will vary as well, depending on the availability of SLR data.

In each orbit determination process six osculating elements and nine dynamical orbit parameters of the ECOM model were estimated. The nine dynamical parameters are three constant acceleration (in D-, Y-, and B-direction) as well as six once-per-revolution sinusoidal accelerations (sine and cosine in D-, Y-, and B-direction). Different solutions were generated using arc-lengths of n-days ( $n = 5, 7, 9, 11, 14$ ) in order to find out the optimal arc-length leading to the best orbit quality.

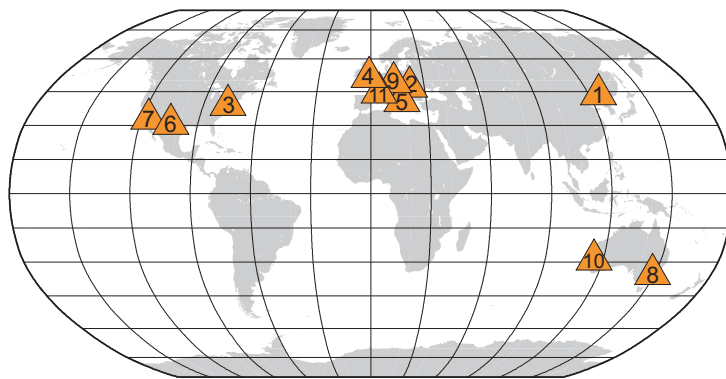


Figure 6.14: Geographical location of the 11 SLR sites used for GIOVE-A orbit determination

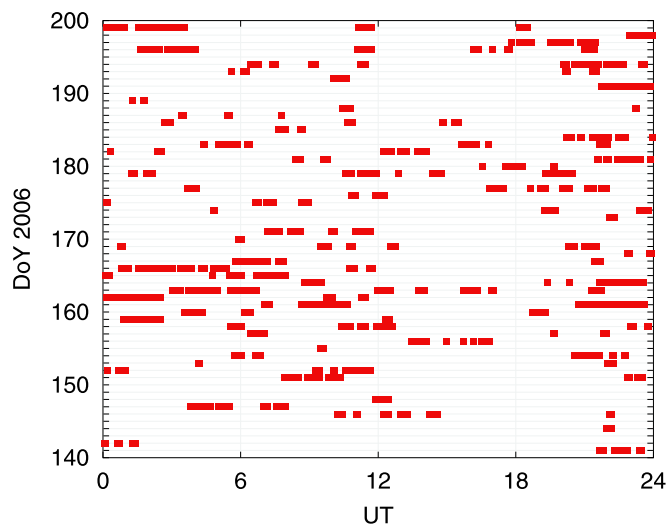


Figure 6.15: SLR data coverage of the GIOVE-A SLR tracking campaign

For each solution type we generated between 32 and 50 n-day arcs within the 60 days of the SLR tracking campaign of GIOVE-A. Consecutive n-day arcs are shifted by one day each, which is why we have overlapping arcs. The differences of the orbit overlaps are an indication of the orbit quality. Small differences indicate a good quality, whereas large ones indicate a bad quality of the determined orbit. We expect that the central part of an arc is best defined and that the boundary parts of an arc are of inferior quality.

The overlap analysis compares the central day of an arc “i” with the corresponding last day of arc “i+k” of the same arc-length, as illustrated in Fig. 6.16, where each line represents a 9-day arc (k=4) with tic marks as day boundaries. The arrows indicate the orbital parts that are compared. Figure 6.17 shows the overlap differences of the GIOVE-A 9-day arcs. This arc length of 9 days has turned out to be the best one.

The orbit overlap differences vary significantly, as the orbit quality is highly correlated with the number and (temporal) distribution of the SLR observations. Arcs with few observations

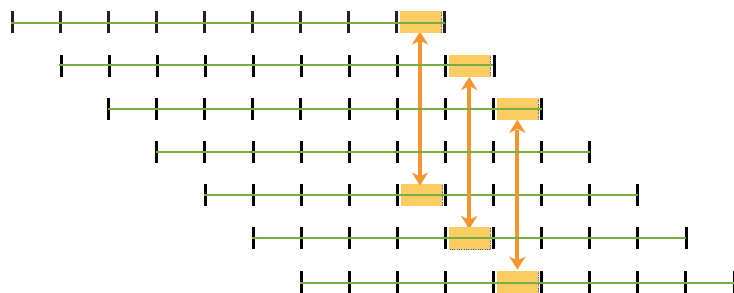


Figure 6.16: Overlapping 9-day arcs; center day of arc “i” is compared to end day of arc “i+4” for overlap studies

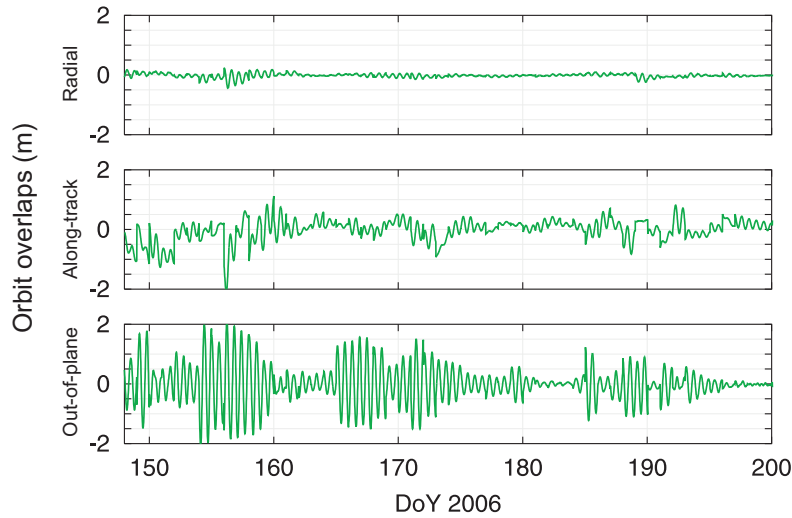


Figure 6.17: Orbit overlap differences of SLR-based 9-day arcs of GIOVE-A

are not well determined. Satellite maneuvers also cause problems, if they are not known. The radial overlap differences show values of up to 10 cm. The radial component is best defined, as SLR observes mainly the radial component. Orbit overlap differences in the along-track and out-of-plane components reach values up to 1 m and 2 m, respectively. For arcs with a good distribution of SLR data the overlap differences are smaller with values up to 0.5 m in the along-track and 1 m in the out-of-plane components.

Figure 6.18 displays the range residuals derived from the 9-day arcs. The standard deviation of the residuals is about 2 cm, which is within the accuracy of the SLR observations. SLR observations are assumed to be accurate at the 1 – 2 cm level.

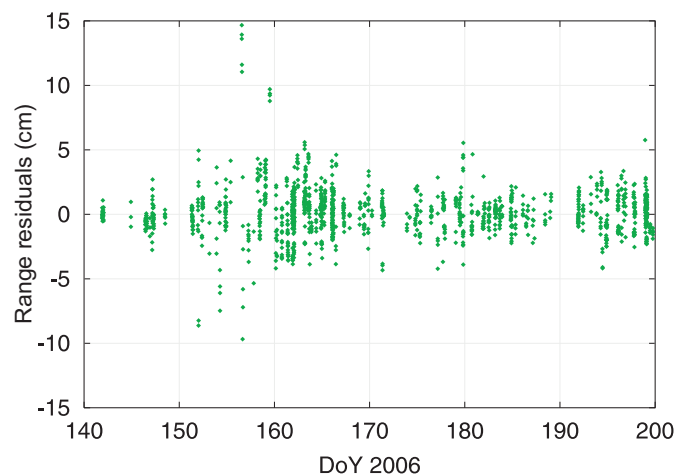


Figure 6.18: Range residuals derived from SLR-based 9-day arcs of GIOVE-A

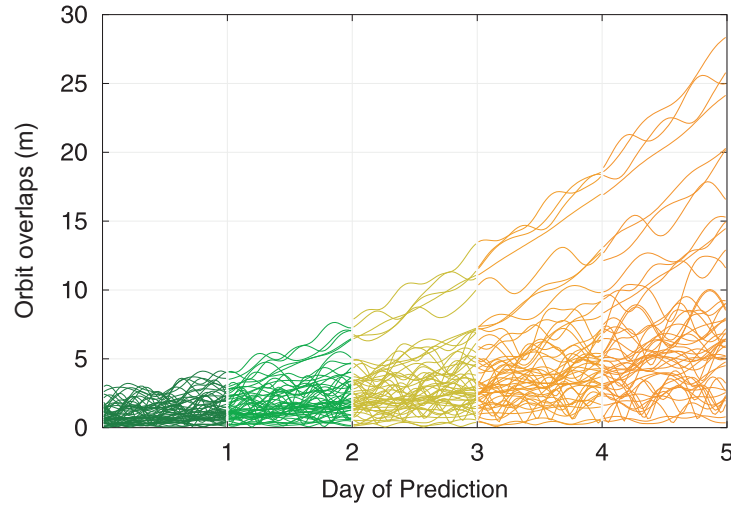


Figure 6.19: Orbit overlap differences of 5-day predictions based on GIOVE-A 9-day arcs

In addition to the SLR-based 9-day arcs, we computed consecutive 5-day orbit predictions. For the computation of the overlap differences, each predicted day is compared with the corresponding central day of the orbit part covered by SLR observations. Thus, for each 9-day arc overlap differences of the five prediction days are generated.

Figure 6.19 shows the orbit overlap differences for all prediction days of all orbital arcs. The predictions are getting worse in time due to a slightly erroneous semi-major axis (and therefore mean motion). The overlap differences are dominated by the along-track error of the orbital arc.

Figure 6.19 shows the orbit overlap differences as a function of the prediction time. The quality of the predictions is on one hand dictated by the correctness of the underlying orbit model and on the other hand by the actual errors of the estimated orbit parameters. A small error in the semi-major axis is translated into a small error of the mean motion, which in turn results in an error in along-track direction growing linearly with time. This is why the errors of Fig. 6.19 are mainly along-track (not documented here). After five days of prediction the accuracy of the predicted orbits is of about 20 – 30 m.

## Conclusions

We presented GIOVE-A orbit determination results based on SLR observations of the first GIOVE-A SLR tracking campaign. Orbits with varying arc-lengths were determined and compared. Nine-day arcs proved to provide the best orbits. No a priori SRP model was introduced in the orbit determination, but constant accelerations and once-per-orbit-revolution accelerations were estimated. The orbit accuracy of a 9-day arc is about 10 cm, 0.5 m, and 1 m in the radial, along-track, and out-of-plane components, except if the observation coverage is poor. Orbit predictions are at the 20 – 30 m accuracy level after five days.

## 7. Conclusions and Recommendations

The main objective of this work was the mutual validation of the three satellite-geodetic techniques: GNSS, SLR, and optical astrometry. Based on the validation results we checked the GNSS orbit model and discussed model improvements.

In the first part of our analysis we validated the astrometric observation technique by using GNSS and LAGEOS satellites. The CCD observations are compared with the positions derived from microwave-based or SLR-based orbits. We used astrometric observations of 53 GNSS and the two LAGEOS satellites acquired for this purpose by the ZIMLAT telescope at the Zimmerwald Observatory during four years (2003-2006). Optical observations of GNSS satellites acquired from a single observing system covering a time span of several years are unique so far.

The validation method allows the calibration of the optical observation system and the assessment of the accuracy of astrometric CCD observations. The RMS error of the CCD observations with respect to the positions derived from microwave-based orbits is of the order of  $0.2''$ , reflecting the accuracy of the CCD observations acquired with ZIMLAT. This determined observation accuracy corresponds well with the already known accuracy of CCD observations of stars and minor planets using ZIMLAT.

Furthermore, our validation has revealed the existence of two systematic effects. First, an epoch registration offset of 0.01 seconds was detected. Second, a significant offset of about  $0.2''$  was found in the CCD residuals in declination. This offset could be attributed to a systematic catalog offset in declination of the USNO-B1.0 star catalog.

Our method is well suited for calibrating and monitoring the epoch registration procedure related to optical observations of fast moving objects. Low Earth satellites as the LAGEOS satellites are particularly well suited for this purpose. We therefore recommend the continuous (preferably once per observation-night, but at least once per month) acquisition of a small number of optical LAGEOS observations, which can be compared with SLR-based orbits, and the development of a standardized procedure based on our method. Such a procedure consumes only little observation time, and it can be performed with any optical observation system. It is therefore of interest for tracking networks of telescopes. The ILRS may consider providing LAGEOS orbits as official product to the scientific community.

The optical observation of artificial Earth satellites allows also the validation of stellar reference frames, as reference stars from a given star catalog define a specific reference frame. The

CQSSP project (Baueršima, 1984) proposed the use of artificial satellites to provide a direct link between the celestial reference frames and, in particular, to monitor the transformation between the quasar-based (using radio telescopes) and the stellar-based (using optical telescopes) reference frames. The limiting factor for CQSSP still is the accuracy of the astrometric observations. The identification of a systematic catalog offset is, however, a good example for the suitability of validating stellar reference frames using artificial Earth satellites.

In the second part of the validation analysis we validated GNSS orbits, based on microwave observations, by using SLR measurements. The measured laser ranges are compared with the ranges derived from SLR site coordinates and GNSS orbits. Previous studies, carried out by different authors (between 1993 and 1999) revealed a range bias of about  $-5.5$  cm for the GPS satellites, and of about  $-4$  cm for the GLONASS satellites. The accuracy of the GPS orbits was estimated to be 5 cm, that of the GLONASS orbits 10 – 15 cm. For the validation studies performed in this work, we used about four years of SLR data, from 2002 until early 2006. We validated the final orbit products from different IGS analysis centers for the two GPS satellites equipped with retroreflector arrays and for four of the GLONASS satellites.

The accuracy of the GNSS orbits improved significantly within the last years. The validation revealed an accuracy for the GPS orbits of 2 – 3 cm, and for the GLONASS orbits of about 5 cm (both in radial direction). Range biases of  $-3$  cm to  $-4$  cm were estimated for the GPS satellites, confirming the bias reported in previous studies, reduced by the 1 cm offset of the laser retroreflector array (LRA), which was not considered before (Davis et al., 2005). Further studies are needed to understand the source of this inter-technique bias. One possible explanation might be an unidentified error in the location of the LRA with respect to the satellite's center of mass. The range biases estimated for the GLONASS satellites are small with about  $-1$  cm. No significant range bias was found for the GLONASS-M satellite R07.

In addition, our validation revealed a periodic signature in the SLR residuals for the GPS satellites, which was not identified before and clearly indicates GNSS orbit modeling problems. The periodic signature becomes obvious when displaying the SLR residuals as a function of the angles  $\Delta u$  (argument of latitude of the satellite with respect to the argument of latitude of the Sun) and  $\beta_0$  (elevation angle of the Sun above the orbital plane). Therewith the dependency of the residual pattern on the satellite's position with respect to the Sun is described. This dependency indicates deficiencies in the dynamic orbit model.

We generated three orbit time series using the ROCK model, the CODE model, and no solar radiation pressure (SRP) a priori model at all. The analysis of these orbits showed that the periodic pattern of the residuals is mainly caused by the ROCK SRP model. But this conclusion can only be drawn for the GPS satellites of type Block IIA, as SLR observations (which allow for an independent validation) are only available for the two Block IIA satellites. The analysis of orbit predictions revealed, however, that the CODE model is superior to the ROCK model for most of the GPS satellites, independently from the Block type. The ROCK model may include signals without corresponding physical source (in particular for small Sun elevation angles  $\beta_0$ ) that cannot be compensated by the estimated SRP parameters. In conclusion, we recommend the use of the CODE SRP model for GPS orbit determination. The analysis of orbit predictions for the GLONASS satellites revealed better orbits if no SRP model instead of the CODE model

---

is used. Therefore, we recommend not to use an a priori SRP model for GLONASS orbit determination.

The analysis of the one-day and three-day arcs for GPS and GLONASS satellites using different SRP models raises questions and provides some answers. Follow-on studies will have to be performed to answer the following questions:

- What causes the systematic discontinuities at the day boundaries, in particular for GPS one-day arcs? The spectral analysis of the overlap errors revealed signals with a period of about 355 days (see Sect. 5.2.4). Due to the limited length of the time series of about four years, this period cannot be assessed accurately using Fourier analysis. One may nevertheless ask the question what the reason of this period is? The estimated Y-biases show a systematic pattern. Does this pattern repeat with the period of the draconitic GPS year of 352 days? A spectral analysis of the Y-bias should answer this question. Moreover, an overlap analysis of a reprocessed orbit time series, considering the advances in observation models (e.g., absolute antenna phase center models) and IERS conventions, is recommended.
- What causes the period of about 50 days for the geocenter Z-coordinate (see Sect. 5.2.5)? This period corresponds well to  $\frac{352}{7}$  days, but does this allow to conclude that it is a harmonic of 352 days (draconitic GPS year)? The intersection of the six orbital planes with the ecliptic plane yields not evenly distributed nodal lines. The smallest distance between two nodal lines appears for the orbital planes with the largest elevation of the Sun above the orbital plane, and this distance is about 50 days.
- Should the estimation of the selected set of five dynamic orbit parameters ( $D0, Y0, B0, BS, BC$ ) be reconsidered (see Sect. 5.3)? A combined analysis with SLR data might improve the orbit determination.

For future studies we recommend the use of a simple boxwing model for SRP modeling. The boxwing model may be used not only as a priori model but also to estimate the model parameters describing the surface properties of the satellite. In addition, Earth albedo parameters may be estimated. A study of the adjusted parameters may contribute to a better understanding of the impact of SRP on GNSS orbits.

Finally, we demonstrated that the combination of microwave phase and SLR observations for GNSS orbit determination would result in better orbits, compared to a pure microwave-based solution, provided that inter-technique biases have been understood and modeled, and that well-distributed SLR data covering the entire orbital arc are available. Already a small network of three “globally distributed” SLR sites, tracking GNSS satellites continuously, would be sufficient. The contribution of SLR data to GNSS orbits is even more important if the microwave tracking network is sparse, as it is the case for the GLONASS satellites or as it will be the case for the upcoming Galileo system (at least initially).

The observed inconsistencies between different observation techniques underline the need for co-location of measurement types not only at sites on the Earth surface, but also on the satellites.

## *7 Conclusions and Recommendations*

---

SLR retroreflector arrays should not be considered as a luxury for new GNSS satellites. At least one reflector array for each satellite type and orbital plane is a necessity.

# A. Observing GNSS Satellites

## A.1 GNSS Satellite Information

Table A.1 provides a list of all GPS satellites (as per January 29, 2008) including the following satellite-specific information: PRN number, SVN, Block type, COSPAR-ID, launch and end date, satellite mass, and number of the orbital plane. The PRN numbers are preceded by a one-character system identifier (G for GPS, R for GLONASS), as used in the RINEX (Receiver Independent Exchange Format) observation files. This notation is also used throughout this work for the identification of the satellites. Note that the PRN numbers are only valid for the corresponding time window. The satellites are sorted by their COSPAR-IDs, and thus in chronological order. The two satellites equipped with LRAs, G05 and G06, are marked in gray.

Table A.2 provides a list of all GLONASS satellites launched since 1992 (as per January 29, 2008) including the following satellite-specific information: PRN number, SVN, GLONASS type, COSPAR-ID, launch and end date (or status), satellite mass, number of the orbital plane, and slot number. Decommissioning phases are indicated by “decomm. phase”. The slot number together with the system identifier “R” is used in the RINEX format for the satellite identification. In this work, this number is referred to as “PRN number” to be consistent with the notation of the GPS satellites. The satellites are sorted by their COSPAR-IDs, and thus in chronological order. The four satellites used in this work for SLR validation, R03, R07, R22, and R24, are marked in gray.

## A Observing GNSS Satellites

PRN	SVN	Block	COSPAR-ID	Launch date yyyy mm dd	Date withdrawn yyyy mm dd	Mass (kg)	Plane	Change of PRN code
G04	01	I	1978-020A	1978 02 22	1985 07 17	521.8		
G07	02	I	1978-047A	1978 05 13	1981 07 16	453.8		
G06	03	I	1978-093A	1978 10 06	1992 05 18	453.8		
G08	04	I	1978-112A	1978 12 10	1989 10 14	440.9		
G05	05	I	1980-011A	1980 02 09	1983 11 28	521.8		
G09	06	I	1980-032A	1980 04 26	1991 03 06	462.6		
G11	08	I	1983-072A	1983 07 14	1993 05 04	519.8	3	
G13	09	I	1984-059A	1984 06 13	1994 06 20	520.4	3	
G12	10	I	1984-097A	1984 09 08	1995 11 18	519.8	1	
G03	11	I	1985-093A	1985 10 09	1994 04 13	521.8	3	
G14	14	II	1989-013A	1989 02 14	2000 04 14	880.0	5	
G02	13	II	1989-044A	1989 06 10	2004 05 12	880.0	2	
G16	16	II	1989-064A	1989 08 18	2000 10 13	880.0	5	
G19	19	II	1989-085A	1989 10 21	2001 09 11	880.0	1	
G17	17	II	1989-097A	1989 12 11	2005 02 22	880.0	4	
G18	18	II	1990-008A	1990 01 24	2000 08 18	880.0	6	
G20	20	II	1990-025A	1990 03 26	1996 05 10	880.0	2	
G21	21	II	1990-068A	1990 08 02	2003 01 27	880.0	5	
G15	15	II	1990-088A	1990 10 01	2007 03 14	880.0	4	
G23/32	23	IIA	1990-103A	1990 11 26		975.0	5	23 →32 (12/06)
G24	24	IIA	1991-047A	1991 07 04		975.0	4	
G25	25	IIA	1992-009A	1992 02 23		975.0	1	
G28	28	IIA	1992-019A	1992 04 10	1997 08 16	975.0	3	
G26	26	IIA	1992-039A	1992 07 07		975.0	6	
G27	27	IIA	1992-058A	1992 09 09		975.0	1	
G01	32	IIA	1992-079A	1992 11 22		975.0	6	
G29	29	IIA	1992-089A	1992 12 18	2007 10 23	975.0	6	
G22	22	IIA	1993-007A	1993 02 03	2003 08 06	975.0	2	
G31	31	IIA	1993-017A	1993 03 30	2005 10 24	975.0	3	
G07	37	IIA	1993-032A	1993 05 13	2007 12 20	975.0	3	
G09	39	IIA	1993-042A	1993 06 26		975.0	1	
G05	35	IIA	1993-054A	1993 08 30		975.0	2	
G04	34	IIA	1993-068A	1993 10 26		975.0	4	
G06	36	IIA	1994-016A	1994 03 10		975.0	3	
G03	33	IIA	1996-019A	1996 03 28		975.0	3	
G10	40	IIA	1996-041A	1996 07 16		975.0	5	
G30	30	IIA	1996-056A	1996 09 12		975.0	2	
G08	38	IIA	1997-067A	1997 11 06		975.0	1	
G13	43	IIR-A	1997-035A	1997 07 23		1100.0	6	
⋮								

A.1 GNSS Satellite Information

PRN	SVN	Block	COSPAR-ID	Launch date yyyy mm dd	Date withdrawn yyyy mm dd	Mass (kg)	Plane	Change of PRN code
⋮								
G11	46	IIR-A	1999-055A	1999 10 07		1100.0	4	
G20	51	IIR-A	2000-025A	2000 05 11		1100.0	5	
G28	44	IIR-A	2000-040A	2000 07 16		1100.0	2	
G14	41	IIR-A	2000-071A	2000 11 10		1100.0	6	
G18	54	IIR-A	2001-004A	2001 01 30		1100.0	5	
G16	56	IIR-A	2003-005A	2003 01 29		1100.0	2	
G21	45	IIR-A	2003-010A	2003 03 31		1100.0	4	
G22	47	IIR-B	2003-058A	2003 12 21		1100.0	5	
G19	59	IIR-B	2004-009A	2004 03 20		1100.0	3	
G23	60	IIR-B	2004-023A	2004 06 23		1100.0	6	
G02	61	IIR-B	2004-045A	2004 11 06		1100.0	4	
G17	53	IIR-M	2005-038A	2005 09 26		1100.0	3	
G31	52	IIR-M	2006-042A	2006 09 25		1100.0	1	
G12	58	IIR-M	2006-052A	2006 11 17		1100.0	2	
G15	55	IIR-M	2007-047A	2007 10 17		1100.0	6	
G29	57	IIR-M	2007-062A	2007 12 20		1100.0	6	

Table A.1: List of GPS satellites, providing satellite-specific information as per January 29, 2008

## A Observing GNSS Satellites

PRN	GLONASS No. Type	COSPAR-ID	Launch date yyyy mm dd	Date withdrawn yyyy mm dd	Mass (kg)	Plane	Slot	Slot change
R03	768	1992-005A	1992 01 29	1993 06 29	900.0	1	3	
R08	769	1992-005B	1992 01 29	1997 06 24	900.0	1	8	
R01	771	1992-005C	1992 01 29	1996 12 21	900.0	1	1	
R24	774	1992-047A	1992 07 30	1996 08 26	900.0	3	24	
R18/21	756	1992-047B	1992 07 30	1997 08 05	900.0	3	18 → 21	
R21	772	1992-047C	1992 07 30	1994 08 27	900.0	3	21	
R02	773	1993-010A	1993 02 17	1994 08 17	900.0	1	2	
R03	757	1993-010B	1993 02 17	1997 08 23	900.0	1	3	
R06/07	759	1993-010C	1993 02 17	1997 08 05	900.0	1	6 → 7	(12/94)
R17	760	1994-021A	1994 04 11	1999 09 09	900.0	3	17	
R23	761	1994-021B	1994 04 11	1997 08 29	900.0	3	23	
R18	758	1994-021C	1994 04 11	2000 01 15	900.0	3	18	
R12	767	1994-050A	1994 08 11	1999 02 03	900.0	2	12	
R16	775	1994-050B	1994 08 11	2000 09 28	900.0	2	16	
R14	770	1994-050C	1994 08 11	2000 01 15	900.0	2	14	
R03	763	1994-076A	1994 11 20	1999 10 05	900.0	1	3	
R06	764	1994-076B	1994 11 20	1999 11 30	900.0	1	6	
R04	762	1994-076C	1994 11 20	1999 11 19	900.0	1	4	
R20	765	1995-009A	1995 03 07	1999 11 19	900.0	3	20	
R22	766	1995-009B	1995 03 07	2001 02 05	900.0	3	22	
R19	777	1995-009C	1995 03 07	1997 12 26	900.0	3	19	
R15	780	1995-037A	1995 07 24	1999 04 06	900.0	2	15	
R10	781	1995-037B	1995 07 24	2001 10 15	900.0	2	10	
R11	785	1995-037C	1995 07 24	2001 04 06	900.0	2	11	
R13	782	1995-068A	1995 12 14	2001 10 15	900.0	2	13	
R09/15	778	1995-068B	1995 12 14	2001 12 30	900.0	2	9 → 15	(04/99)
R09	776	1995-068C	1995 12 14	2000 09 28	900.0	2	9	
R01	779	1998-077A	1998 12 30	2002 07 08	900.0	1	1	
R08	784	1998-077B	1998 12 30	2003 12 19	900.0	1	8	
R07	786	1998-077C	1998 12 30	2003 10 20	900.0	1	7	
R17	787	2000-063A	2000 10 13	2007 04 16	900.0	3	17	
R24	788	2000-063B	2000 10 13	2006 03 29	900.0	3	24	
R18	783	2000-063C	2000 10 13	2007 11 23	900.0	3	18	
R05	711	2001-053A	2001 12 01	decomm. phase	900.0	1	5	
R03	789	2001-053B	2001 12 01	decomm. phase	1415.0	1	3	
R06	790	2001-053C	2001 12 01	2003 12 19	1415.0	1	6	
R22	791	2002-060A	2002 12 25	2007 11 30	1480.0	3	22	
R23/20	793	2002-060B	2002 12 25	2007 04 16	1480.0	3	23 → 20	(02/06)
R21	792	2002-060C	2002 12 25	decomm. phase	1480.0	3	21	
⋮								

A.1 GNSS Satellite Information

PRN	GLONASS No.	Type	COSPAR-ID	Launch date yyyy mm dd	Date withdrawn yyyy mm dd	Mass (kg)	Plane	Slot	Slot change
⋮									
R06	701	M	2003-056A	2003 12 10		1415.0	1	6	
R02	794		2003-056B	2003 12 10	decomm. phase	900.0	1	2	
R04	795		2003-056C	2003 12 10		900.0	1	4	
R01	796		2004-053A	2004 12 26		900.0	1	1	
R07	712	M	2004-053B	2004 12 26		1415.0	1	7	
R08	797		2004-053C	2004 12 26		900.0	1	8	
R23	714	M	2005-050A	2005 12 25		1415.0	3	23	
R24	713	M	2005-050B	2005 12 25		1415.0	3	24	
R19/22	798		2005-050C	2005 12 25	decomm. phase	900.0	3	19 → 22	(10/07)
R15	716	M	2006-062A	2006 12 25		1415.0	2	15	
R10	717	M	2006-062B	2006 12 25		1415.0	2	10	
R14	715	M	2006-062C	2006 12 25		1415.0	2	14	
R19	720	M	2007-052A	2007 10 26		1415.0	3	19	
R20	719	M	2007-052B	2007 10 26		1415.0	3	20	
R17	718	M	2007-052C	2007 10 26		1415.0	3	17	
R13	721	M	2007-065A	2007 12 25		1415.0	2	13	
R09	722	M	2007-065B	2007 12 25		1415.0	2	9	
R11	723	M	2007-065C	2007 12 25		1415.0	2	11	

Table A.2: List of GLONASS satellites, providing satellite-specific information as per January 29, 2008

## A.2 SLR Sites

Table A.3 provides a list of the SLR sites that observed GNSS satellites between 2003 and 2006. The station ID is the so-called Crustal Dynamics Project (CDP) number, a 4-digit code. Further the location and country of the SLR sites are given, as well as the corresponding IERS DOMES numbers. DOMES (Directory Of MERIT Sites) is a numbering system for the space geodetic sites. It was designed at the start of the MERIT (Monitoring of Earth Rotation and Intercomparison of the Techniques of Observation and Analysis) campaign in early 80s in order to give an unambiguous identifier to all instrument reference points and markers involved in this MERIT campaign. The numbers in the last column correspond to the numbers used in Fig. 6.14 in Sect. 6.2 that shows the geographical distribution of the SLR sites used for GIOVE-A orbit determination.

SLR station ID	Location name	Country	IERS DOMES number
1864	Maidanak 1	Uzbekistan	12340S002
7080	McDonald Observatory	Texas, U.S.A.	40442M006 (6)
7090	Yarragadee	Australia	50107M001 (10)
7105	Greenbelt	Maryland, U.S.A.	40451M105 (3)
7110	Monument Peak	California, U.S.A.	40497M001 (7)
7210	Haleakala	Hawaii	40445M001
7237	Changchun	China	21611S001 (1)
7501	Hartebeesthoek	South Africa	30302M003
7810	Zimmerwald	Switzerland	14001S007 (11)
7825	Mt Stromlo	Australia	50119S003 (8)
7832	Riyadh	Saudi Arabia	20101S001
7839	Graz	Austria	11001S002 (2)
7840	Herstmonceux	United Kingdom	13212S001 (4)
7845	Grasse	France	10002S002
7941	Matera	Italy	12734S008 (5)
8834	Wetzell	Germany	14201S018 (9)

Table A.3: Listing of SLR sites, including the 4-digit station ID, the SLR site location and country, and the IERS DOMES number

# B. Mutual Validation of the Different Satellite-Geodetic Techniques

## B.1 SLR Residuals

Figures B.1, B.2, and B.3 show the color-coded SLR residuals  $\Delta r^*$  for the two GPS satellite G05 and G06 as a function of the angle  $\Delta u$  (argument of latitude of the satellite with respect to the argument of latitude of the Sun) and the angle  $\beta_0$  (elevation of the Sun above the satellite's orbital plane). The residuals are derived from the GFZ, JPL, and IGS final orbits, respectively. Further details are given in Sect. 4.2.2.

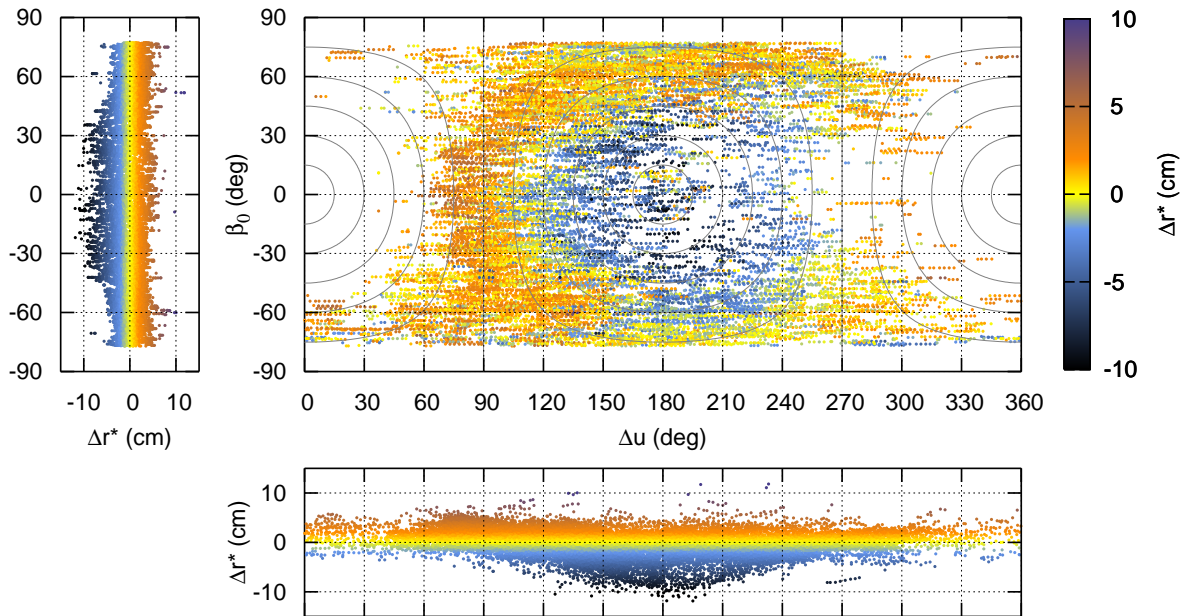


Figure B.1: SLR residuals  $\Delta r^*$  derived from GFZ final orbits for the GPS satellites G05 and G06 in the  $(\Delta u, \beta_0)$  coordinate system; **bottom:** projection onto  $\Delta u$ -axis; **left:** projection onto  $\beta_0$ -axis; circles represent the phase angle  $E$ ,  $15^\circ$  spacing,  $0^\circ$  at center ( $\Delta u = 180^\circ$  and  $\beta_0 = 0^\circ$ ),  $180^\circ$  at ( $\Delta u = 0^\circ$  and  $\beta_0 = 0^\circ$ )

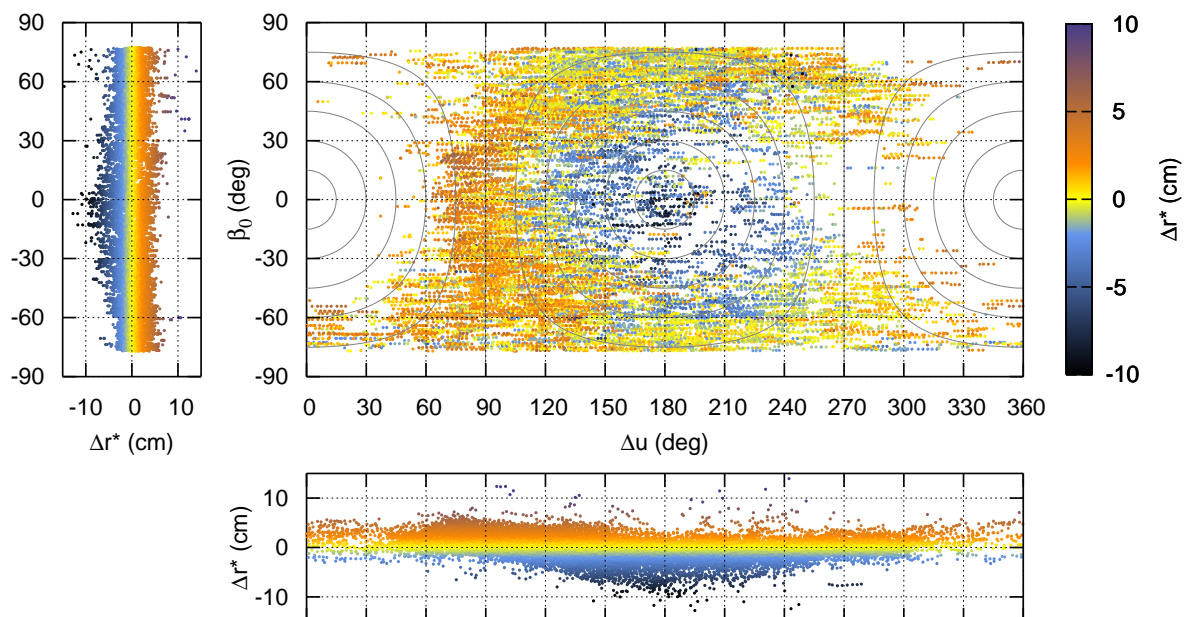


Figure B.2: SLR residuals  $\Delta r^*$  derived from JPL final orbits for the GPS satellites G05 and G06 in the  $(\Delta u, \beta_0)$  coordinate system; **bottom:** projection onto  $\Delta u$ -axis; **left:** projection onto  $\beta_0$ -axis; circles represent the phase angle  $E$ ,  $15^\circ$  spacing,  $0^\circ$  at center ( $\Delta u = 180^\circ$  and  $\beta_0 = 0^\circ$ ),  $180^\circ$  at ( $\Delta u = 0^\circ$  and  $\beta_0 = 0^\circ$ )

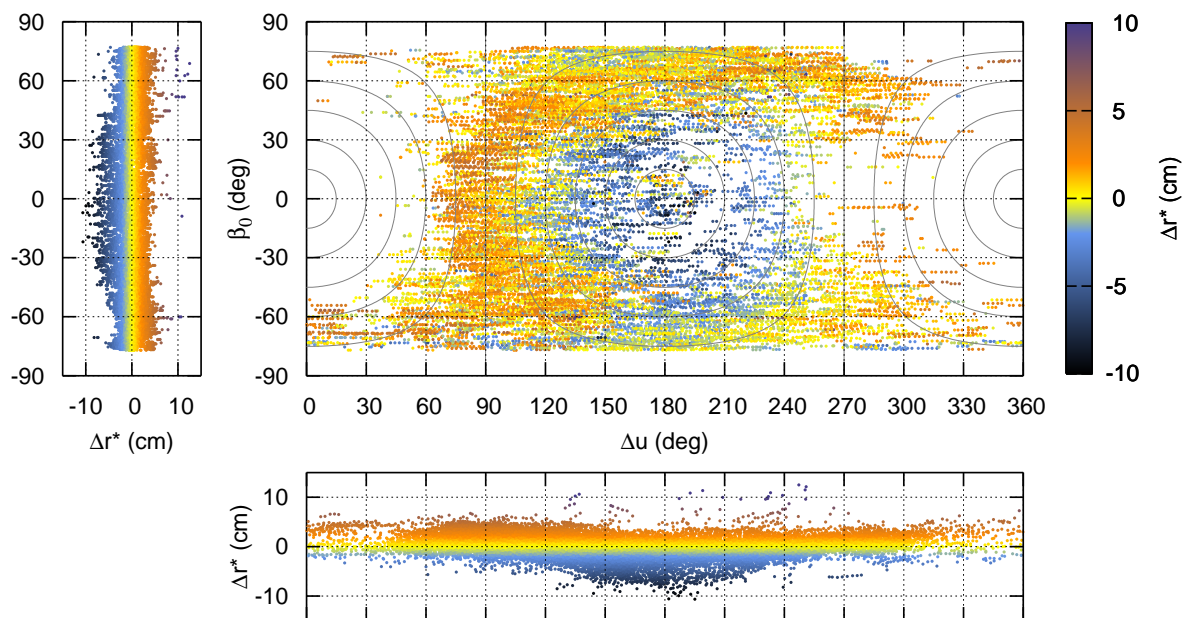


Figure B.3: SLR residuals  $\Delta r^*$  derived from IGS final orbits for the GPS satellites G05 and G06 in the  $(\Delta u, \beta_0)$  coordinate system; **bottom:** projection onto  $\Delta u$ -axis; **left:** projection onto  $\beta_0$ -axis; circles represent the phase angle  $E$ ,  $15^\circ$  spacing,  $0^\circ$  at center ( $\Delta u = 180^\circ$  and  $\beta_0 = 0^\circ$ ),  $180^\circ$  at ( $\Delta u = 0^\circ$  and  $\beta_0 = 0^\circ$ )

## **C. Improvement of the GNSS Orbit Model**

### **C.1 Accelerations Due to Different Solar Radiation Pressure Models**

Figures C.1 and C.2 show the a priori and the estimated accelerations in D-, Y-, and B-direction due to different SRP a priori models for a Block IIR satellite (G16). The accelerations estimated when using no a priori model (i.e., the NONE model) are indicated by the dashed lines. Further details are given in Sect. 5.1.

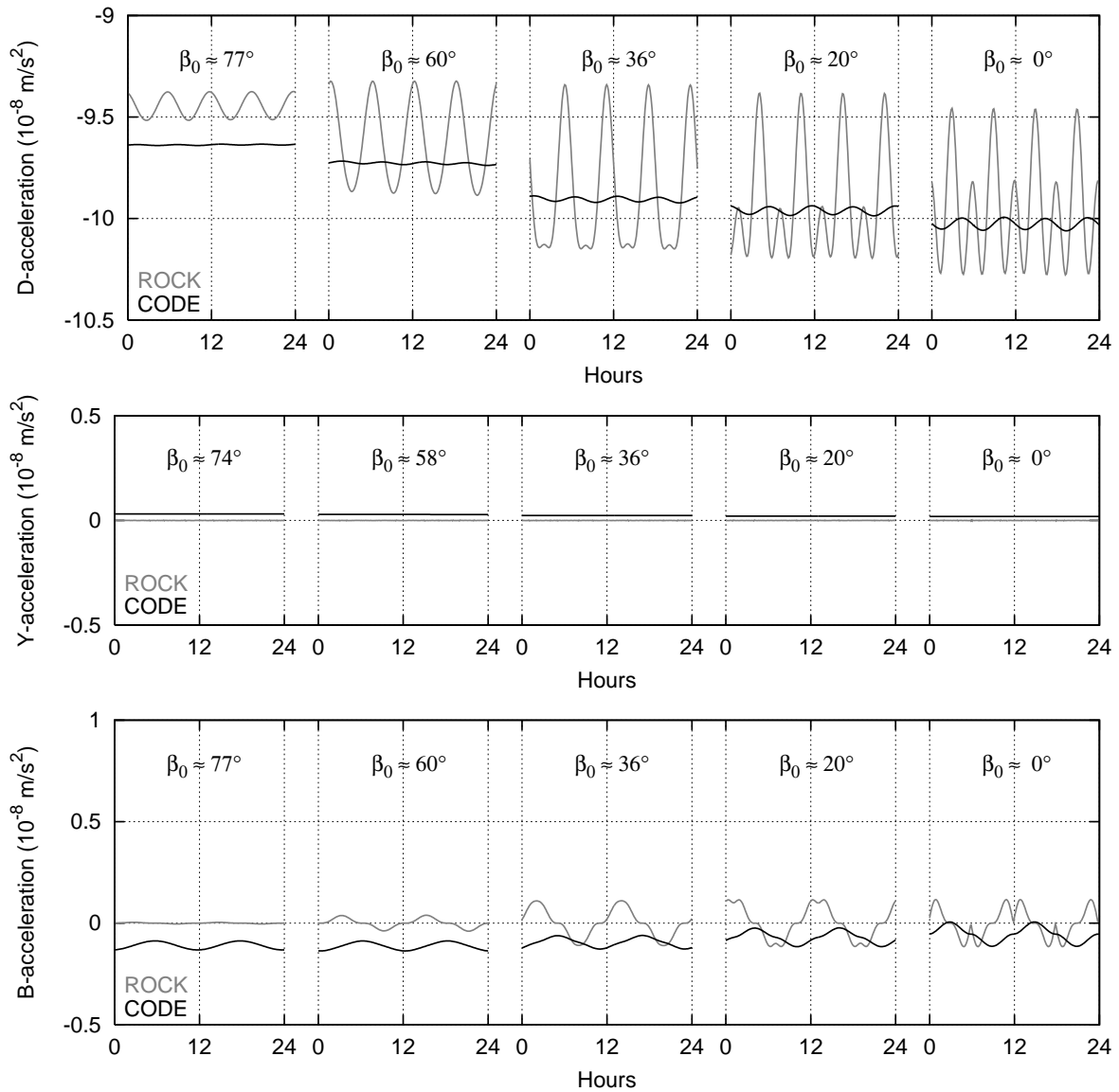


Figure C.1: Accelerations due to SRP acting on the GPS satellite G16 (Block IIR), derived from the SRP a priori models ROCK (gray) and CODE (black)

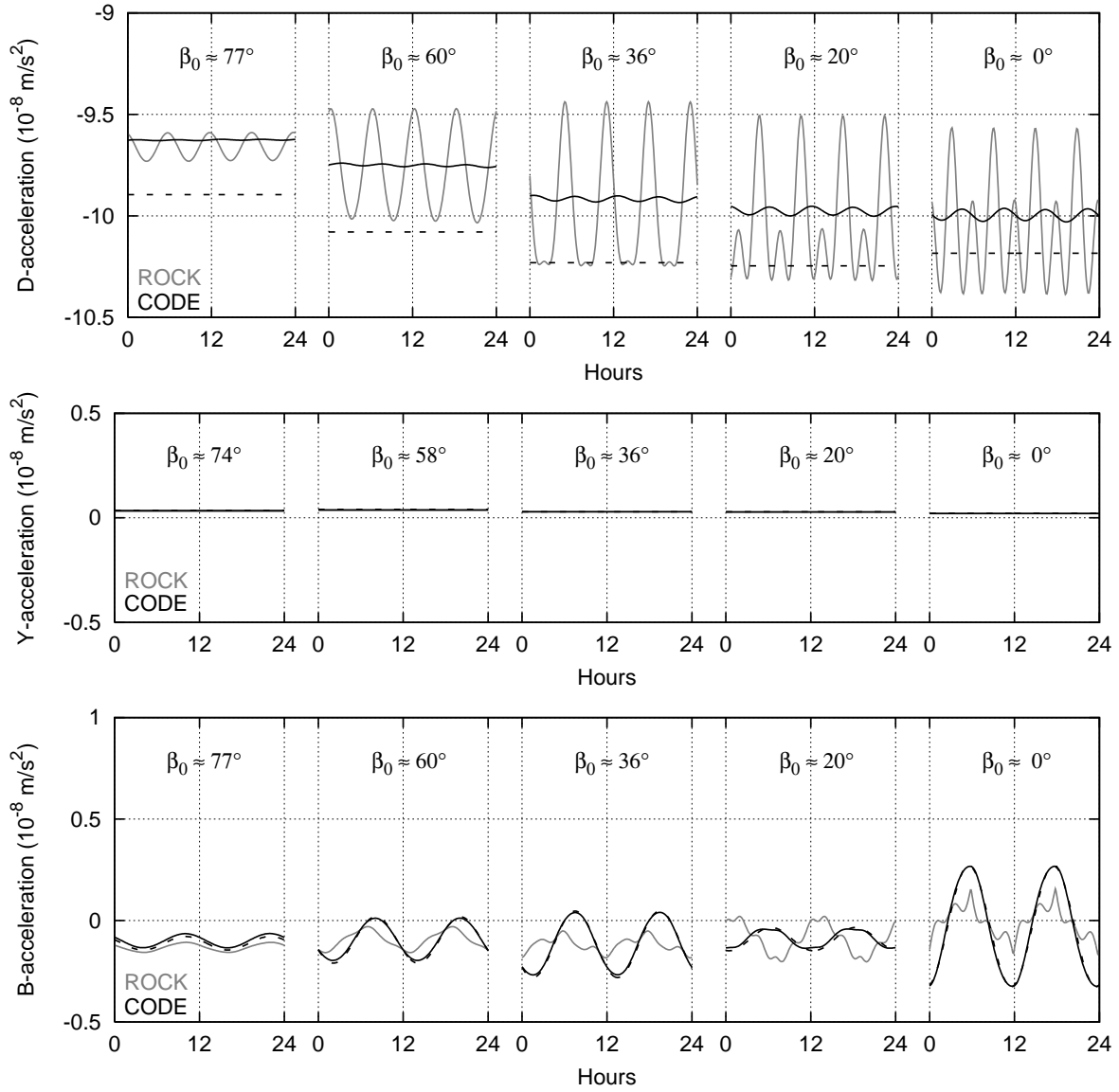


Figure C.2: Estimated accelerations due to SRP acting on the GPS satellite G16 (Block IIR), derived from parameter adjustment using the SRP a priori models ROCK (gray), CODE (black), and NONE (dashed)

## **C.2 Overlap Errors of One-day and Three-day Arcs**

The following figures show the radial and the out-of-plane components of the overlap errors analyzed in Sect. 5.2.4. In that section only the along-track components are shown, but a discussion of the figures and of the statistical information is done for all three components.

Figures C.3 and C.4 show the radial components of the overlap errors of 24 GPS satellites derived from the one-day and three-day arc solutions, respectively. The overlap errors of the one-day arc solutions are based on the CODE SRP a priori model, whereas the overlap errors of the three-day arc solution are based on the NONE model. Table C.1 provides the corresponding statistical information.

Figures C.5 and C.6 show the out-of-plane components of the overlap errors of the one-day and three-day solutions, respectively. The statistical information of the out-of-plane components is summarized in Table C.2.

The corresponding figures of the along-track components of the one-day and three-day solutions can be found on page 110 (Fig. 5.15) and page 118 (Fig. 5.20), respectively.

Figures C.7 and C.8 show the radial components of the overlap errors of 10 GLONASS satellites derived from the one-day and three-day arc solutions, respectively. The overlap errors of the one-day arc solutions are based on the CODE SRP a priori model and the absolute antenna PCC model. The overlap errors of the three-day arc solution are based on the NONE model. Table C.3 provides the corresponding statistical information.

Figures C.9 and C.10 show the out-of-plane components of the overlap errors of the one-day and three-day solutions, respectively, for the GLONASS satellites. The statistical information of the out-of-plane components is summarized in Table C.4.

The corresponding figures of the along-track components of the one-day and three-day solutions for the GLONASS satellites can be found on page 123 (Fig. 5.24) and page 127 (Fig. 5.28), respectively.

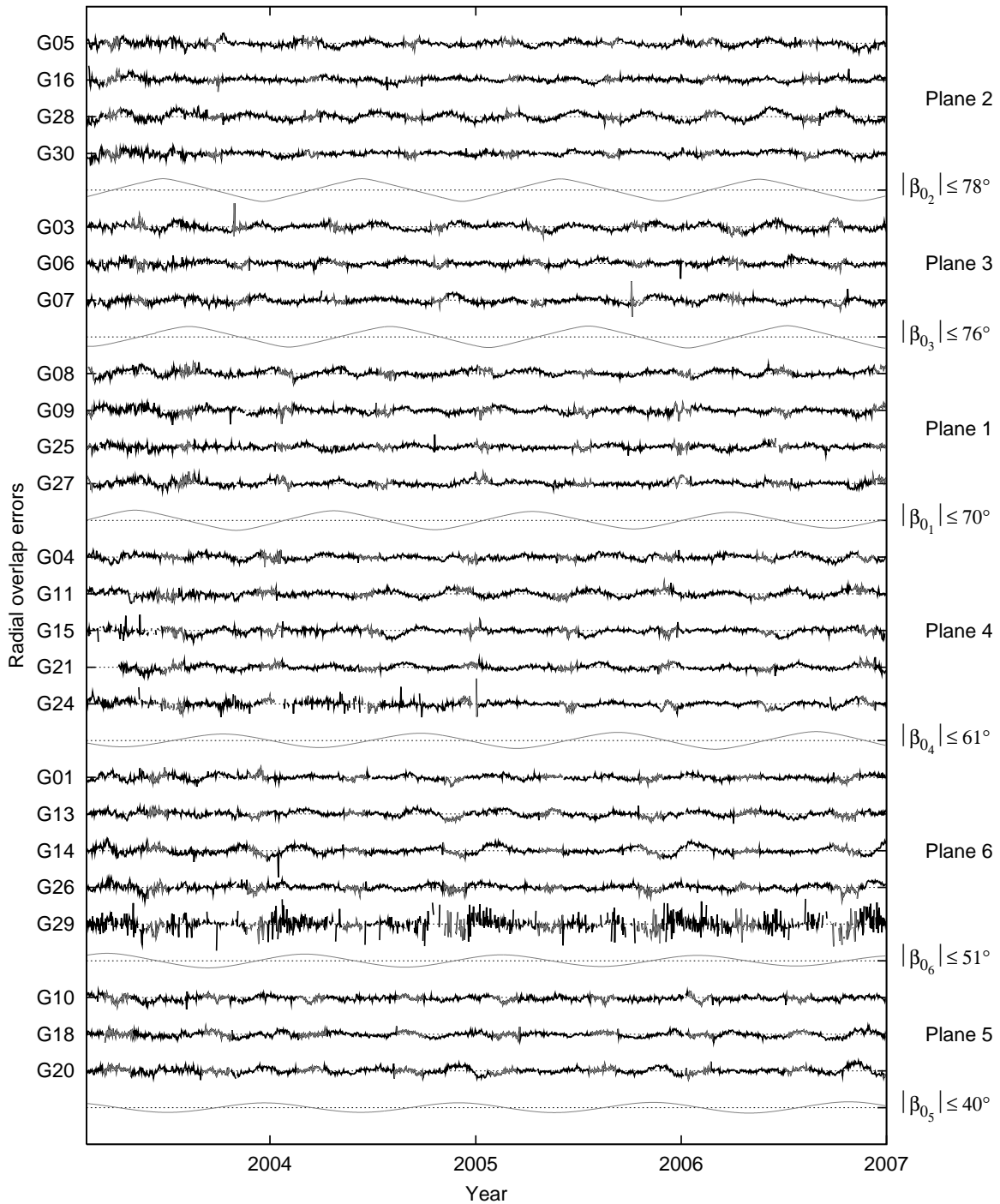


Figure C.3: Orbit overlap errors in radial direction of 24 GPS satellites derived from one-day arcs using the CODE SRP a priori model; the elevation angle  $\beta_0$  of the Sun above the orbital plane is given by the gray line; eclipsing periods are marked in gray; for the scale of the y-axis see Fig. 5.14

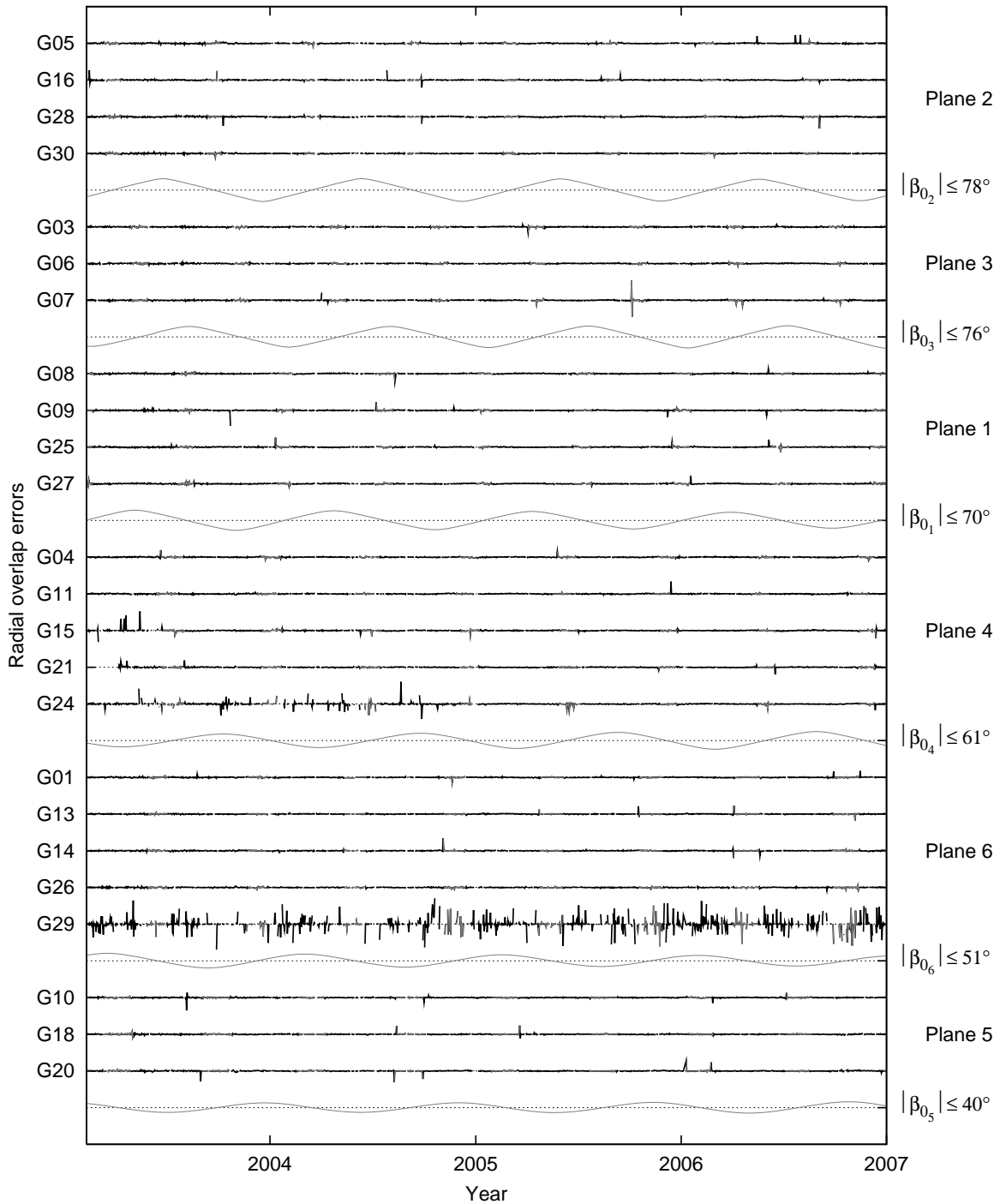


Figure C.4: Orbit overlap errors in radial direction of 24 GPS satellites derived from three-day arcs using the NONE SRP a priori model; the elevation angle  $\beta_0$  of the Sun above the orbital plane is given by the gray line; eclipsing periods are marked in gray; for the scale of the y-axis see Fig. 5.19

C.2 Overlap Errors of One-day and Three-day Arcs

PRN	$\sigma_{1d}$ (cm)			$\sigma_{3d}$ (cm)		$\bar{x}_{1d}$ (cm)			$\bar{x}_{3d}$ (cm)	
	ROCK	CODE	NONE	ROCK	NONE	ROCK	CODE	NONE	ROCK	NONE
<i>Plane 2</i>										
G05	3.6	3.7	3.7	0.8	0.7	-0.4	-0.4	-0.4	-0.1	-0.1
G16	3.0	3.0	3.1	0.8	0.8	-0.6	0.6	0.6	-0.1	-0.1
G28	4.4	4.7	5.0	0.7	0.8	-0.1	0.1	0.1	-0.1	-0.1
G30	3.0	3.1	3.0	0.7	0.5	-0.6	-0.4	-0.4	-0.1	-0.1
<i>Plane 3</i>										
G03	4.4	4.1	4.2	0.7	0.6	-0.2	-0.1	-0.1	-0.2	-0.2
G06	3.4	3.4	3.4	0.6	0.5	0.4	0.1	0.1	-0.1	-0.1
G07	3.9	3.8	3.8	1.2	1.1	-0.7	-0.6	-0.6	-0.2	-0.2
<i>Plane 1</i>										
G08	3.9	3.9	4.0	0.6	0.6	0.9	1.0	1.1	-0.1	-0.1
G09	3.8	3.7	3.6	0.9	0.9	-0.5	-0.5	-0.6	-0.1	-0.1
G25	3.0	3.0	3.0	0.7	0.7	-0.3	-0.0	-0.1	-0.1	-0.1
G27	3.6	3.5	3.7	0.6	0.6	0.4	0.6	0.7	-0.1	-0.1
<i>Plane 4</i>										
G04	3.4	3.4	3.4	0.6	0.6	0.0	-0.2	-0.3	-0.1	-0.1
G11	4.4	4.1	4.1	0.7	0.6	-0.4	-0.1	-0.1	-0.1	-0.1
G15	4.1	3.9	4.0	1.4	1.4	-0.2	-0.8	-0.8	-0.1	-0.1
G21	2.9	3.3	3.3	0.9	0.7	-0.3	-0.3	-0.3	-0.1	-0.1
G24	4.2	4.2	4.1	2.0	2.0	0.2	-0.1	-0.1	-0.1	-0.1
<i>Plane 6</i>										
G01	3.3	3.2	3.2	0.6	0.6	0.1	-0.2	-0.1	-0.1	-0.1
G13	4.0	3.5	3.5	0.7	0.7	-0.7	0.2	0.2	-0.1	-0.1
G14	3.8	4.5	4.3	0.7	0.7	1.0	0.1	0.2	-0.0	-0.1
G26	3.8	3.8	3.7	0.5	0.5	0.3	0.1	0.0	-0.1	-0.1
G29	8.8	9.0	9.0	7.5	7.6	-0.1	-0.3	-0.3	-0.2	-0.2
<i>Plane 5</i>										
G10	3.2	3.1	3.0	0.7	0.7	-0.9	-1.3	-1.3	-0.2	-0.2
G18	2.9	3.3	3.2	0.7	0.6	0.1	-0.4	-0.4	-0.1	-0.1
G20	4.2	3.8	3.8	0.9	0.9	0.1	0.2	0.2	-0.1	-0.1

Table C.1: Statistical information for radial orbit overlap errors of 24 GPS satellites derived from one-day and three-day arcs using the three SRP a priori models ROCK, CODE, and NONE: standard deviations  $\sigma_{1d}$  and  $\sigma_{3d}$ , and mean values  $\bar{x}_{1d}$  and  $\bar{x}_{3d}$

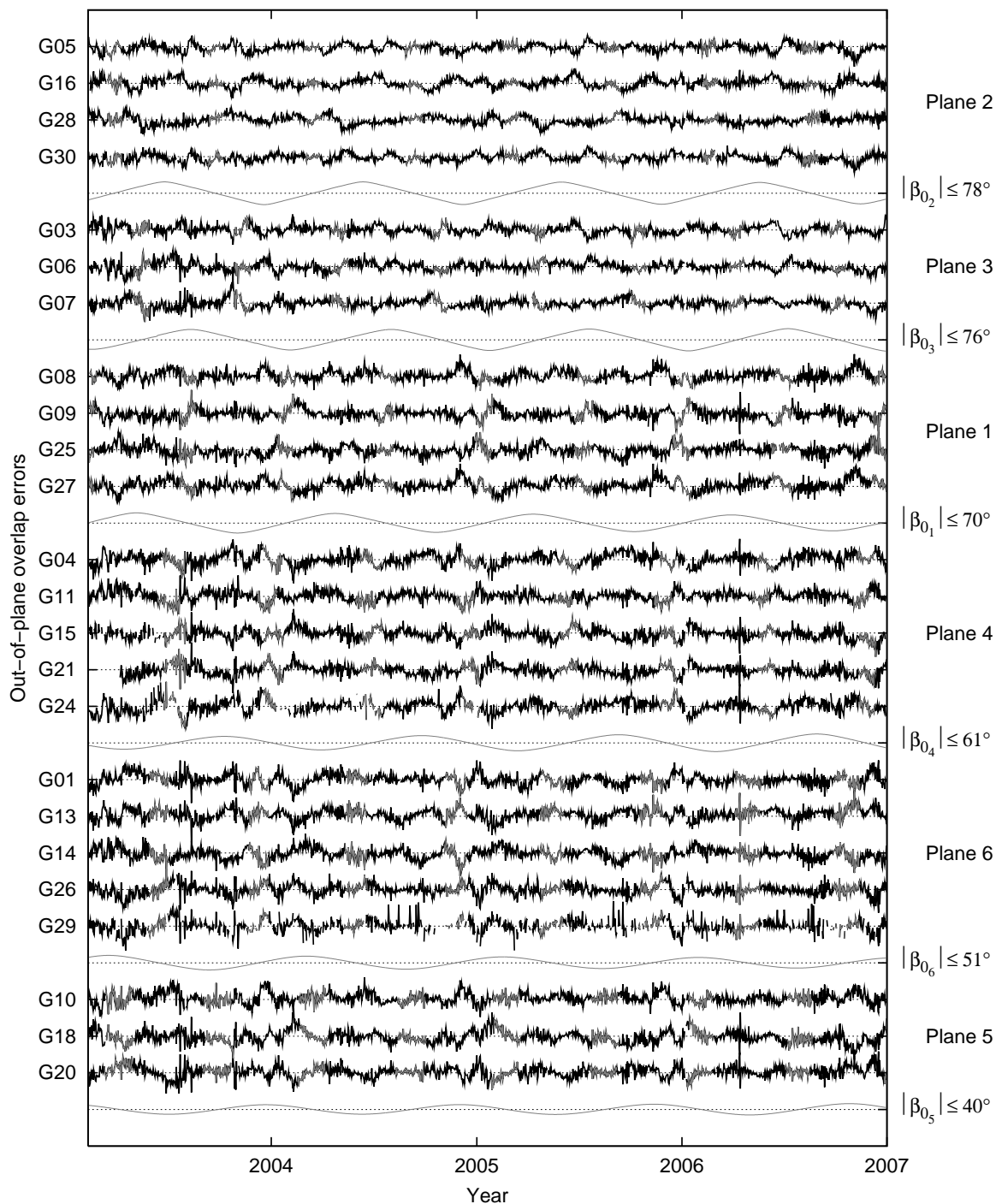


Figure C.5: Orbit overlap errors in out-of-plane direction of 24 GPS satellites derived from one-day arcs using the CODE SRP a priori model; the elevation angle  $\beta_0$  of the Sun above the orbital plane is given by the gray line; eclipsing periods are marked in gray; for the scale of the y-axis see Fig. 5.14

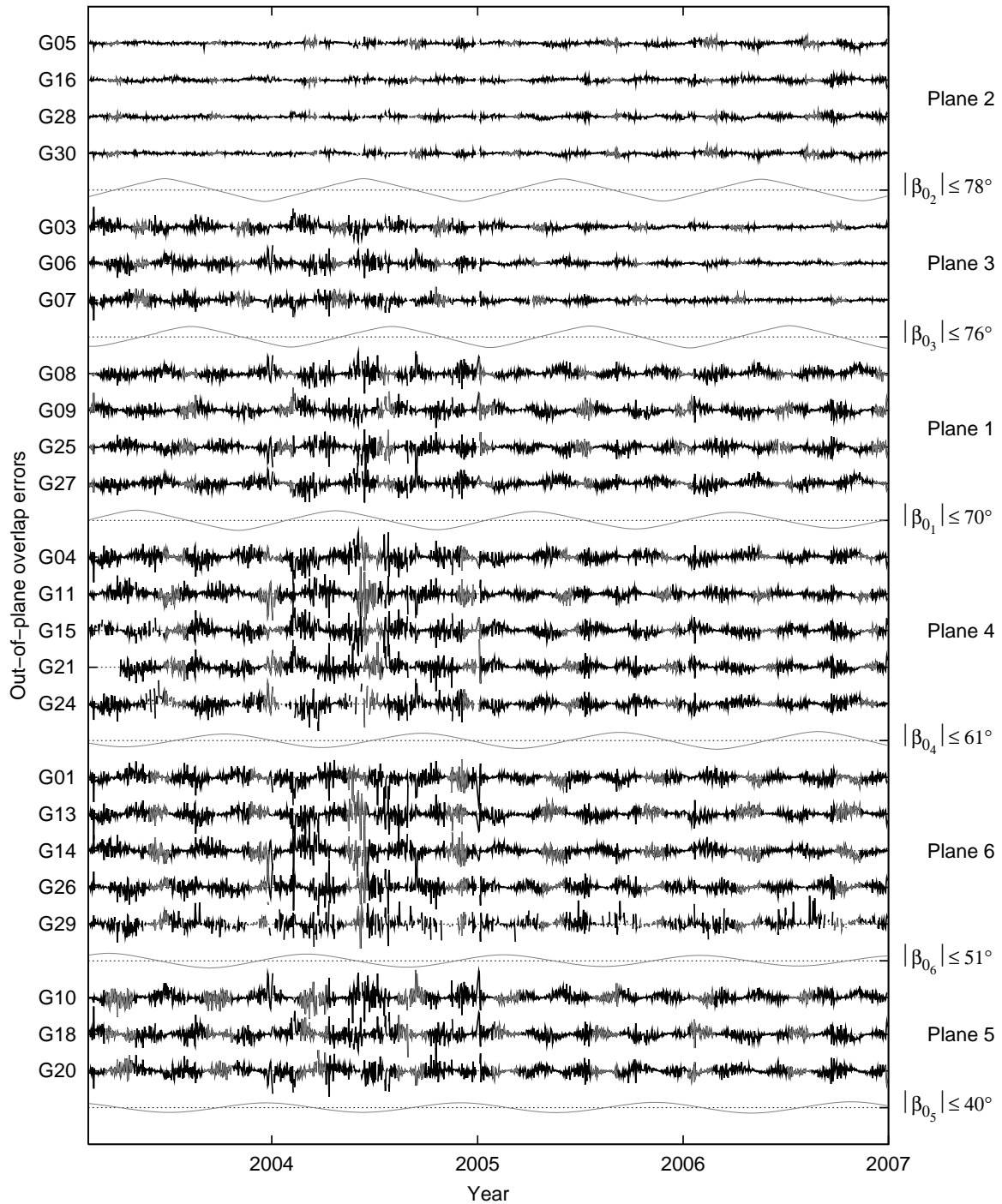


Figure C.6: Orbit overlap errors in out-of-plane direction of 24 GPS satellites derived from three-day arcs using the NONE SRP a priori model; the elevation angle  $\beta_0$  of the Sun above the orbital plane is given by the gray line; eclipsing periods are marked in gray; for the scale of the y-axis see Fig. 5.19

PRN	$\sigma_{1d}$ (cm)			$\sigma_{3d}$ (cm)		$\bar{x}_{1d}$ (cm)			$\bar{x}_{3d}$ (cm)	
	ROCK	CODE	NONE	ROCK	NONE	ROCK	CODE	NONE	ROCK	NONE
<i>Plane 2</i>										
G05	5.8	5.3	5.4	2.3	2.2	-1.1	-1.3	-1.3	-0.1	-0.1
G16	5.2	5.9	6.0	2.2	2.2	-0.1	0.3	0.2	0.1	0.1
G28	4.7	5.5	5.6	2.0	2.0	0.1	-0.2	-0.1	-0.0	-0.0
G30	5.3	5.2	5.0	2.1	2.1	-1.3	-1.4	-1.5	-0.2	-0.2
<i>Plane 3</i>										
G03	5.4	5.9	5.8	3.9	3.9	0.2	0.3	0.2	0.1	0.0
G06	6.1	6.1	6.1	4.0	4.0	-0.1	-0.1	-0.1	0.5	0.4
G07	5.8	6.0	6.0	3.7	3.8	-0.3	-0.3	-0.3	-0.2	-0.1
<i>Plane 1</i>										
G08	7.1	6.8	6.8	5.6	5.5	1.6	1.1	1.2	0.6	0.5
G09	6.7	7.0	7.1	5.5	5.5	-0.8	-1.2	-1.2	0.2	0.2
G25	6.8	6.9	6.8	5.5	5.5	-1.2	-0.7	-0.7	-0.7	-0.6
G27	7.7	7.4	7.4	5.8	5.7	2.4	1.9	2.0	0.5	0.4
<i>Plane 4</i>										
G04	7.8	8.1	8.1	6.7	6.7	0.5	0.6	0.7	0.1	0.1
G11	7.3	7.0	7.0	6.4	6.4	-0.6	0.1	0.1	-0.7	-0.5
G15	8.0	7.4	7.5	6.7	6.7	-2.0	-1.4	-1.3	-0.0	0.0
G21	7.2	7.2	7.3	6.4	6.3	-0.8	-0.9	-0.9	0.4	0.2
G24	8.2	8.4	8.4	6.8	6.8	0.3	-0.1	-0.0	0.1	-0.0
<i>Plane 6</i>										
G01	7.3	7.6	7.6	6.6	6.5	-0.8	0.0	-0.0	-0.9	-0.8
G13	7.8	7.7	7.8	7.0	7.0	2.0	2.6	2.6	0.1	0.2
G14	7.3	7.7	7.6	7.0	6.9	-2.4	-1.4	-1.5	-0.6	-0.4
G26	7.4	7.6	7.6	6.6	6.6	0.2	-0.3	-0.3	0.4	0.3
G29	8.9	8.7	8.8	7.8	7.8	0.9	0.4	0.5	1.0	1.0
<i>Plane 5</i>										
G10	7.6	7.5	7.5	6.9	6.9	1.9	1.6	1.7	0.6	0.5
G18	7.4	8.3	8.3	6.6	6.5	-1.7	-1.5	-1.5	0.1	0.0
G20	7.0	7.7	7.7	6.2	6.3	0.3	1.1	1.1	-0.4	-0.2

Table C.2: Statistical information for out-of-plane orbit overlap errors of 24 GPS satellites derived from one-day and three-day arcs using the three SRP a priori models ROCK, CODE, and NONE: standard deviations  $\sigma_{1d}$  and  $\sigma_{3d}$ , and mean values  $\bar{x}_{1d}$  and  $\bar{x}_{3d}$

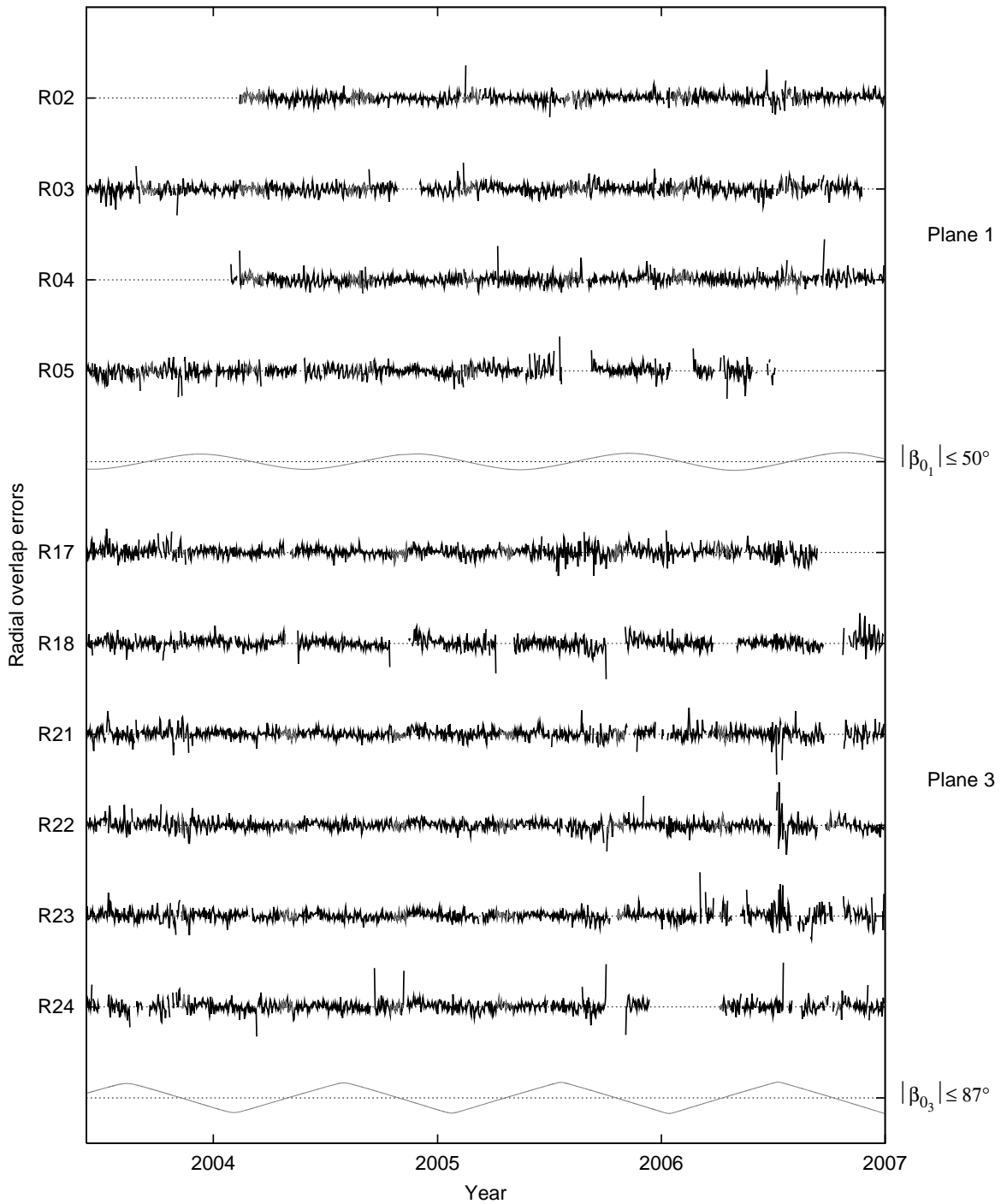


Figure C.7: Orbit overlap errors in radial direction of 10 GLONASS satellites derived from one-day arcs using the CODE SRP a priori model and the absolute antenna PCC model; the elevation angle  $\beta_0$  of the Sun above the orbital plane is given by the gray line below each orbital plane; eclipsing periods are marked in gray; for the scale of the y-axis see Fig. 5.23

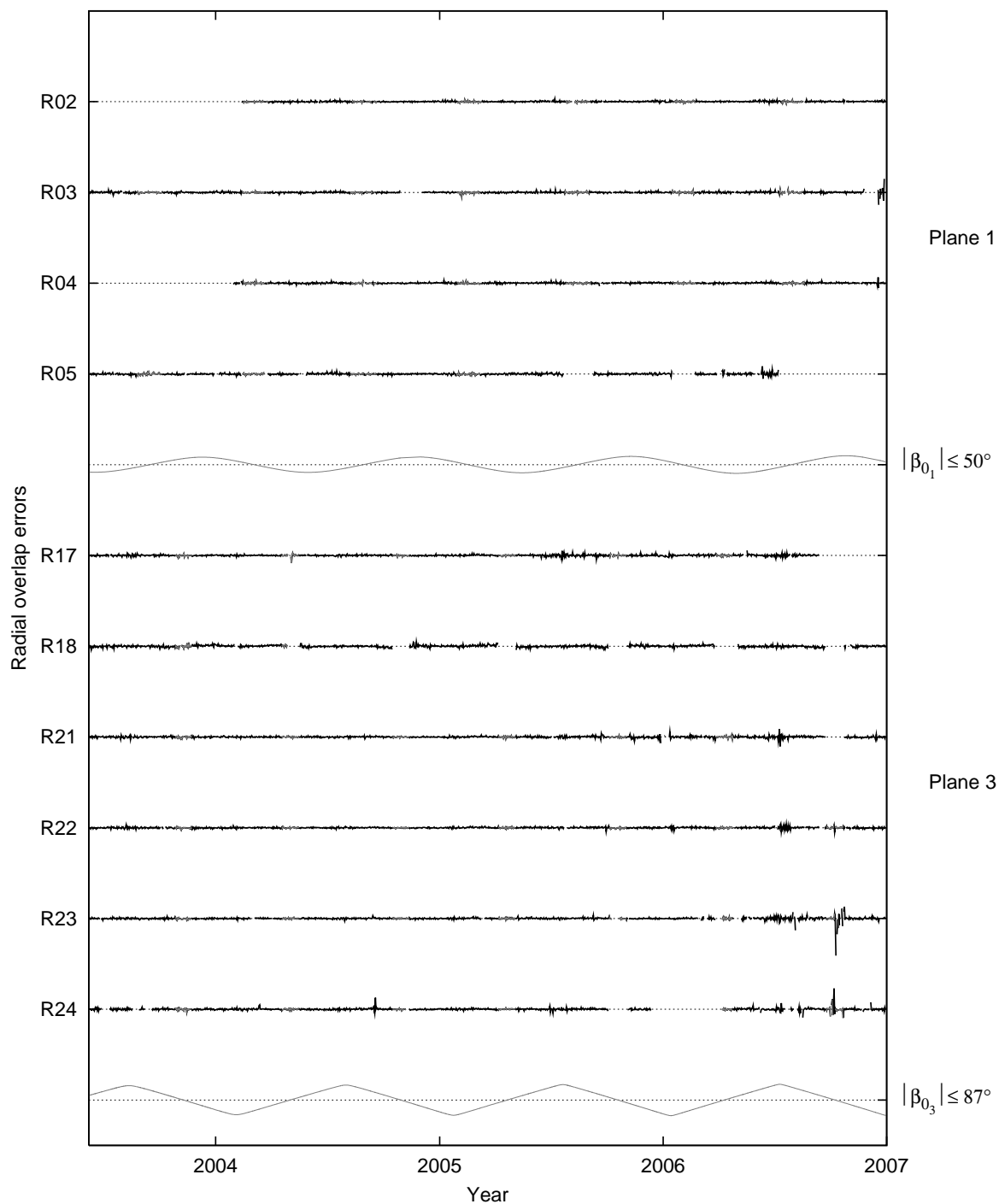


Figure C.8: Orbit overlap errors in radial direction of 10 GLONASS satellites derived from three-day arcs using the NONE SRP a priori model; the elevation angle  $\beta_0$  of the Sun above the orbital plane is given by the gray line; eclipsing periods are marked in gray; for the scale of the y-axis see Fig. 5.27

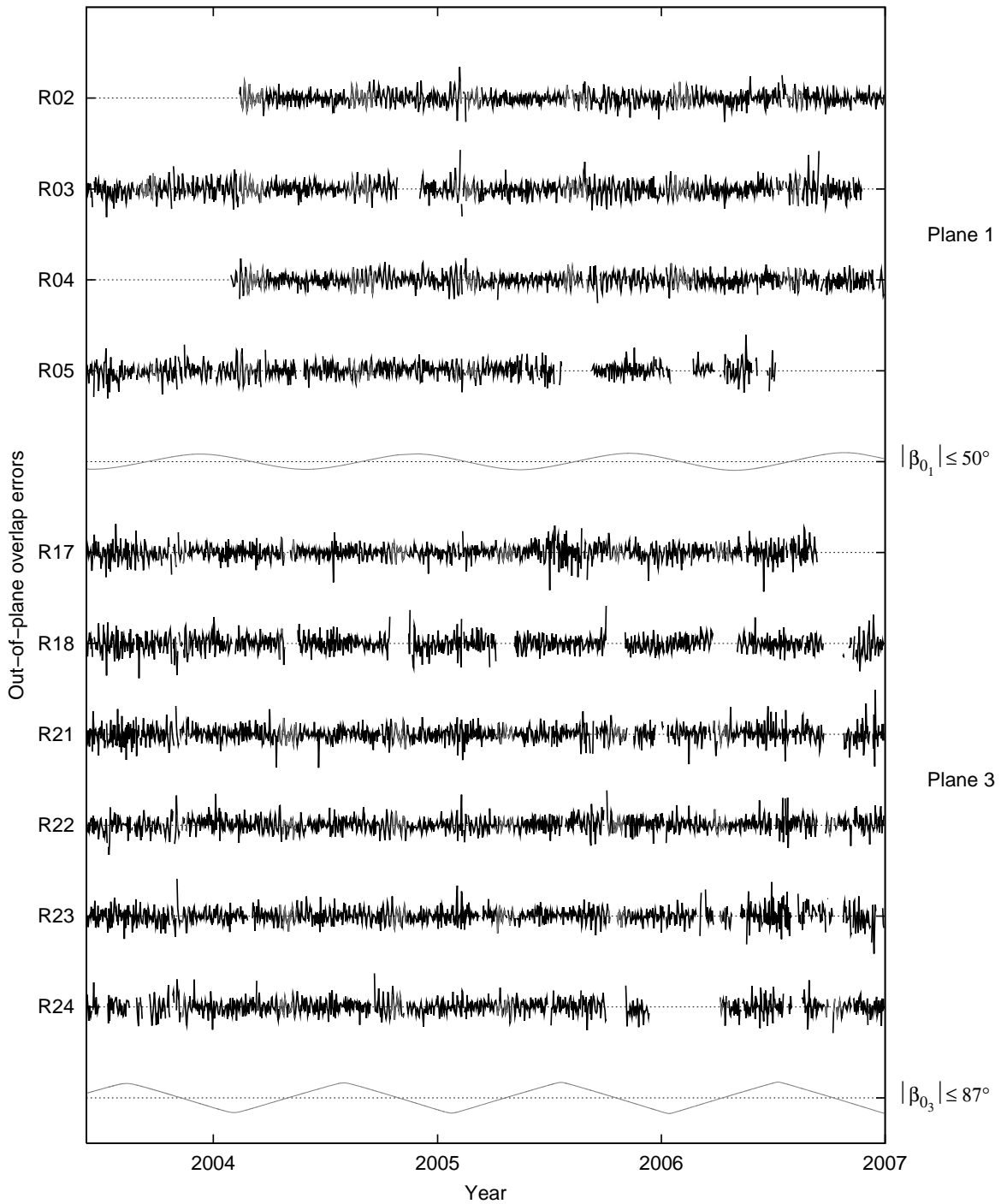


Figure C.9: Orbit overlap errors in out-of-plane direction of 10 GLONASS satellites derived from one-day arcs using the CODE SRP a priori model and the absolute antenna PCC model; the elevation angle  $\beta_0$  of the Sun above the orbital plane is given by the gray line; eclipsing periods are marked in gray; for the scale of the y-axis see Fig. 5.23

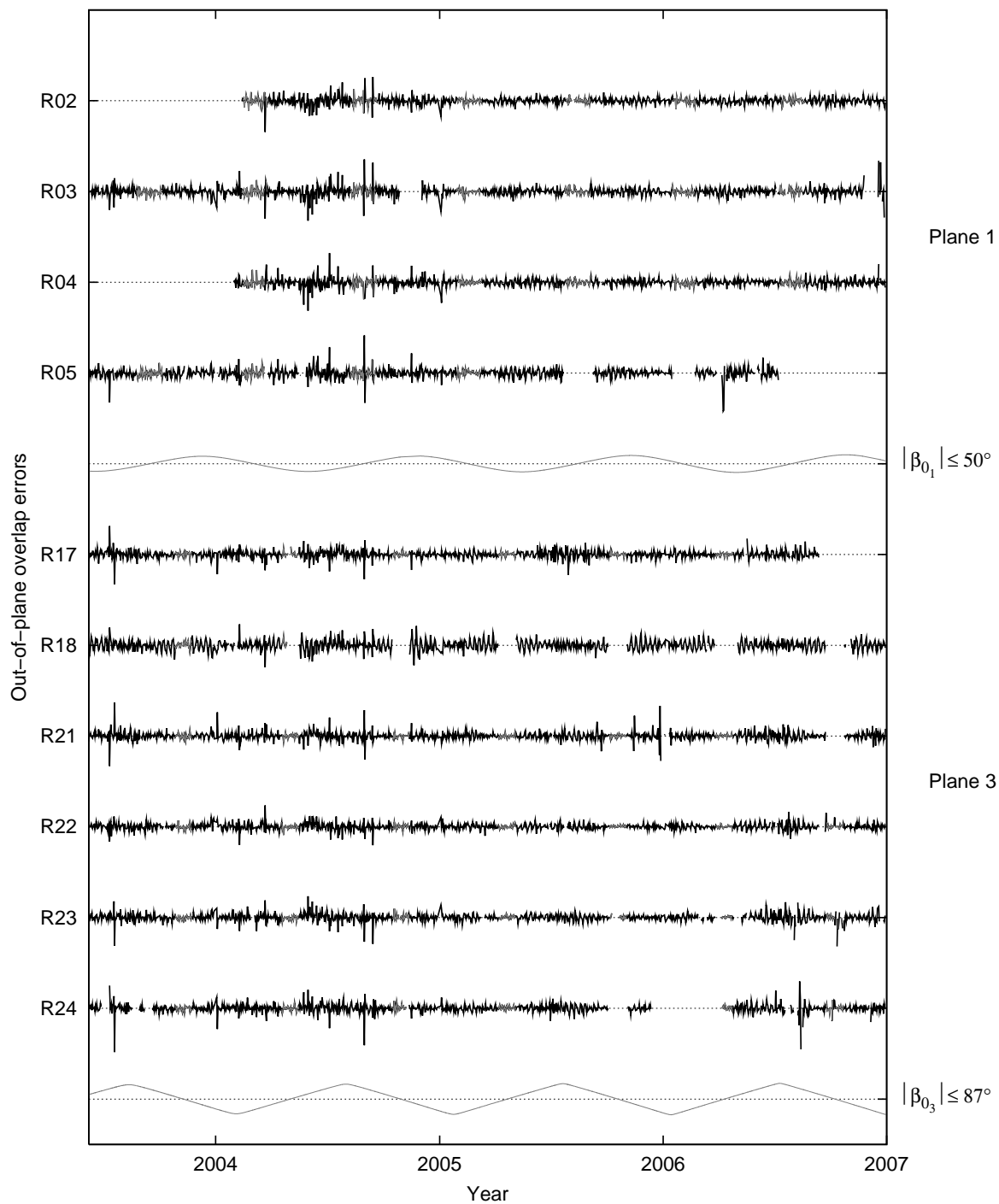


Figure C.10: Orbit overlap errors in out-of-plane direction of 10 GLONASS satellites derived from three-day arcs using the NONE SRP a priori model; the elevation angle  $\beta_0$  of the Sun above the orbital plane is given by the gray line; eclipsing periods are marked in gray; for the scale of the y-axis see Fig. 5.27

C.2 Overlap Errors of One-day and Three-day Arcs

PRN	$\sigma_{1d}$ (cm)			$\sigma_{3d}$ (cm)	$\bar{x}_{1d}$ (cm)			$\bar{x}_{3d}$ (cm)
	CODE	CODE-A	NONE	NONE	CODE	CODE-A	NONE	NONE
<i>Plane 1</i>								
R02	11.6	9.3	11.2	1.3	2.4	1.1	1.5	0.2
R03	12.8	10.6	12.3	2.0	1.2	0.2	0.3	0.0
R04	12.8	10.3	12.5	1.4	3.4	1.5	2.6	0.2
R05	15.7	12.8	15.3	1.8	-0.9	-0.5	-1.9	-0.1
<i>Plane 3</i>								
R17	14.8	11.4	14.6	1.8	2.4	1.3	1.6	0.2
R18	15.9	11.9	15.8	2.1	0.7	0.7	0.7	0.0
R21	14.4	11.3	14.6	1.9	2.5	1.0	1.8	0.0
R22	14.9	11.6	14.7	1.5	1.0	0.1	0.3	0.0
R23	14.5	12.5	14.8	3.5	2.4	1.2	1.8	0.0
R24	15.0	12.3	15.0	2.8	0.6	1.1	0.1	0.1

Table C.3: Statistical information for radial orbit overlap errors of 10 GLONASS satellites derived from one-day and three-day arcs using the two SRP a priori models CODE and NONE; for the CODE-A solution the CODE SRP a priori model and the absolute antenna PCC model were used: standard deviations  $\sigma_{1d}$  and  $\sigma_{3d}$ , and mean values  $\bar{x}_{1d}$  and  $\bar{x}_{3d}$

PRN	$\sigma_{1d}$ (cm)			$\sigma_{3d}$ (cm)	$\bar{x}_{1d}$ (cm)			$\bar{x}_{3d}$ (cm)
	CODE	CODE-A	NONE	NONE	CODE	CODE-A	NONE	NONE
<i>Plane 1</i>								
R02	15.1	13.7	15.0	7.8	-1.0	-0.7	-0.9	-0.3
R03	16.8	16.1	16.7	9.6	-1.5	-0.8	-1.6	-0.3
R04	14.9	13.8	14.8	8.3	-0.7	-0.7	-0.6	-0.4
R05	17.4	16.1	17.4	10.0	0.4	0.6	0.3	-0.4
<i>Plane 3</i>								
R17	18.9	16.2	18.8	8.1	-0.7	0.4	-0.5	0.3
R18	18.9	17.7	18.9	10.3	-1.2	-0.5	-1.2	0.0
R21	18.4	17.3	18.4	8.6	-0.1	0.6	-0.2	0.3
R22	16.4	15.6	16.3	6.8	0.7	1.6	0.8	0.4
R23	17.4	16.7	17.4	8.3	0.1	0.4	0.1	0.2
R24	18.2	16.5	18.4	9.4	-0.3	-0.0	-0.2	0.1

Table C.4: Statistical information for out-of-plane orbit overlap errors of 10 GLONASS satellites derived from one-day and three-day arcs using the two SRP a priori models CODE and NONE; for the CODE-A solution the CODE SRP a priori model and the absolute antenna PCC model were used: standard deviations  $\sigma_{1d}$  and  $\sigma_{3d}$ , and mean values  $\bar{x}_{1d}$  and  $\bar{x}_{3d}$



# Bibliography

- Appleby, G., and T. Otsubo (2000), Comparison of SLR measurements and orbits with GLONASS and GPS microwave orbits, in *Proc. of 12th International Workshop on Laser Ranging*, Matera, Italy, November 13–17 2000.
- Appleby, G., and T. Otsubo (2004), Laser ranging as a precise tool to evaluate GNSS orbital solutions, in *Proc. of 14th International Workshop on Laser Ranging*, San Fernando, Spain, June 7–11 2004.
- Baker, T. F., D. J. Curtis, and A. H. Dodson (1995), Ocean tide loading an GPS, *GPS World*, 6(3), pp. 54–59.
- Bar-Sever, Y. E. (1994), Improvement to the GPS attitude control subsystem enables predictable attitude during eclipse seasons, IGSMail #0591, May 1994.
- Bar-Sever, Y. E. (1996), A new model for GPS yaw attitude, *Journal of Geodesy*, 70, pp. 714–723.
- Bar-Sever, Y. E. (1997), Information regarding Block IIR modeling, IGSMail #1653, July 1997.
- Bar-Sever, Y. E. (1998), A new model for GPS Block IIR solar radiation pressure, IGSMail #1833, March 1998.
- Baueršima, I. (1984), Coupled Quasar, Satellite and Star Positioning (CQSSP), *Mitteilungen der Satelliten-Beobachtungsstation Zimmerwald*, 13.
- Beutler, G. (1998), GPS satellite orbits, in *GPS for Geodesy*, edited by P. J. G. Teunissen and A. Kleusberg, pp. 37–99, Springer, ISBN 3-540-63661-7.
- Beutler, G. (2005), *Methods of Celestial Mechanics*, Springer, ISBN 3-211-82364-6.
- Beutler, G., E. Brockmann, W. Gurtner, U. Hugentobler, L. Mervart, and M. Rothacher (1994), Extended orbit modeling techniques at the CODE processing center of the International GPS Service for Geodynamics (IGS): theory and initial results, *Manuscripta Geodaetica*, 19, pp. 367–386.
- Boucher, C., and Z. Altamimi (1996), International Terrestrial Reference Frame, *GPS World*, 7(9), pp. 71–74.

## Bibliography

---

- Boucher, C., Z. Altamimi, P. Sillard, and M. Feissel-Vernier (2004), The ITRF2000, *IERS Technical Note 31*, Verlag des Bundesamts für Kartographie und Geodäsie, Frankfurt am Main.
- Brockmann, E. (1997), *Combination of Solutions for Geodetic and Geodynamic Applications of the Global Positioning System (GPS)*, Vol. 55 of *Geodätisch-geophysikalische Arbeiten in der Schweiz*, Schweizerische Geodätische Kommission, Institut für Geodäsie und Photogrammetrie, Eidg. Technische Hochschule Zürich, Zürich.
- Dach, R., U. Hugentobler, S. Schaer, and P. Fridez (2007), *Bernese GPS Software Version 5.0*, Druckerei der Universität Bern, Switzerland.
- Davis, M., A. Trask, J. Middour, A. Hope, C. Moore, W. Scharpf, R. Smith, M. Suite, H. Burris, and M. Stella (2005), NGA GPS navigation accuracy assessment using SLR techniques, Unpublished manuscript, March 2005.
- Degnan, J. J. (1993), *Millimeter accuracy satellite laser ranging: a review*, Vol. 25 of *Contributions of Space Geodesy to Geodynamics: Technology*, pp. 133–162, D.E. Smith and D.L. Turcotte, AGU Geodynamics Series edition.
- Degnan, J. J., and E. C. Pavlis (1994), Laser ranging to GPS satellites with centimeter accuracy, *GPS World*, 5(9), pp. 62–70.
- Dick, W., and B. Richter (2001), IERS Annual Report 2000, Bundesamt für Kartographie und Geodäsie, Frankfurt am Main, Germany.
- Donath, T., T. Schildknecht, P. Brousse, J. Laycock, T. Michal, P. Ameline, and L. Leushacke (2005), Proposal for a European Space Surveillance System, in *Proc. of the 4th European Conference on Space Debris*, Vol. ESA SP-587, edited by D. Danesy, pp. 31–37, ESA Publications Division, The Netherlands, September 10–14 2005.
- Eanes, R. J., and S. Bettadpur (1992), The CSR 3.0 global ocean tide model, *Technical memorandum, CSR-TM-95-06*, Center for Space Research, University of Texas, Austin, Texas, U.S.A.
- Eanes, R. J., R. S. Nerem, P. A. M. Abusali, W. Bamfort, K. Key, J. C. Ries, and B. E. Schutz (1999), GLONASS orbit determination at the center for space research, in *Proc. of Int. GLONASS Experiment (IGEX-98) Workshop*, IGS, Nashville, Tennessee, U.S.A., September 13–14 1999.
- Fliegel, H. F., and T. E. Gallini (1989), Radiation pressure models for Block II GPS satellites, in *Proc. of the Fifth International Symposium on Precise Positioning with the Global Positioning System*, pp. 789–798, National Geodetic Survey, NOAA, Rockville, Maryland, U.S.A., April 1989.
- Fliegel, H. F., and T. E. Gallini (1996), Solar force modeling of Block IIR Global Positioning System satellites, *Journal of Spacecraft and Rockets*, 33(6), pp. 863–866.

- Fliegel, H. F., W. A. Feess, W. C. Layton, and N. W. Rhodus (1985), The GPS radiation force model, in *Proc. of the First International Symposium on Precise Positioning with the Global Positioning System*, edited by Clyde Goad, pp. 113–119, National Geodetic Survey, NOAA, Rockville, Maryland, U.S.A., March 1985.
- Fliegel, H. F., T. E. Gallini, and E. R. Swift (1992), Global positioning system radiation force model for geodetic applications, *Journal of Geophysical Research*, 97(B1), pp. 559–568.
- Flohrer, T., T. Schildknecht, C. Früh, R. Musci, and M. Ploner (2007), Optical observations at the Zimmerwald Observatory, in *Proc. of the 58th International Astronautical Congress*, Hyderabad, India, September 24–28 2007.
- Flury, W., A. Massart, T. Schildknecht, U. Hugentobler, J. Kuusela, and Z. Sodnik (2000), Searching for small debris in the geostationary ring, *ESA bulletin*, 104, pp. 92–100.
- Fricke, W., H. Schwan, and T. Lederle (1988), Fifth fundamental catalogue (FK5), 32, Astronomisches Rechen-Institut Heidelberg, Verlag G. Braun, Karlsruhe.
- Gaposchkin, E. M., C. v. Braun, and J. Sharma (2000), Space-based space surveillance with the Space-Based Visible, *Journal of Guidance, Control, and Dynamics*, 23(1), pp. 148–152.
- Ge, M., G. Gendt, and F. Zhang (in press), GFZ Analysis Center of IGS - Annual report for 2003-2004, in *International GPS Service 2003-2004 Technical Report*, IGS Central Bureau, Jet Propulsion Laboratory, Pasadena, California, U.S.A.
- Gendt, G., and T. Nischan (in press), 2003/2004 Analysis coordinator report, in *International GPS Service 2003-2004 Technical Report*, IGS Central Bureau, Jet Propulsion Laboratory, Pasadena, California, U.S.A.
- Gurtner, W., R. Noomen, and M. R. Pearlman (2004), The International Laser Ranging Service: current status and future developments, *Advances in Space Research*, 36, pp. 327–332.
- Hofmann-Wellenhof, B., H. Lichtenegger, and J. Collins (1992), *GPS: Theory and Practice*, Springer, ISBN 3-211-82364-6.
- Hugentobler, U. (1998), *Astrometry and Satellite Orbits: Theoretical Considerations and Typical Applications*, Vol. 57 of *Geodätisch-geophysikalische Arbeiten in der Schweiz*, Institut für Geodäsie und Photogrammetrie, Eidg. Technische Hochschule Zürich, Zürich, Switzerland.
- Hugentobler, U., S. Schaer, G. Weber, C. Boucher, M. Meindl, G. Beutler, H. Bock, R. Dach, A. Jäggi, C. Urschl, L. Mervart, M. Rothacher, E. Brockmann, D. Ineichen, A. Wiget, U. Wild, and H. Habricht (in press), CODE IGS analysis center technical report 2003/2004, in *International GPS Service 2003-2004 Technical Report*, IGS Central Bureau, Jet Propulsion Laboratory, Pasadena, California, U.S.A.

## Bibliography

---

- ILRS (2008), SLR Satellite Center-of-Mass Offset Information, available at [http://ilrs.gsfc.nasa.gov/satellite\\_missions/center\\_of\\_mass/index.html](http://ilrs.gsfc.nasa.gov/satellite_missions/center_of_mass/index.html), March 2008.
- Ineichen, D., T. A. Springer, and G. Beutler (2000), Combined processing of the IGS and the IGEX network, *Journal of Geodesy*, 75, pp. 575–586.
- Johnson, N. L. (1993), U.S. Space Surveillance, *Advances in Space Research*, 13(8), pp. (8)5–(8)20.
- Marini, J. W., and C. W. Murray (1973), Correction of Laser range tracking data for atmospheric refraction at elevations above 10 degrees, X-591-73-351, NASA GSFC.
- McCarthy, D. D. (1996), IERS Conventions (1996), *IERS Technical Note 21*, Observatoire de Paris, Paris, July 1996.
- McCarthy, D. D., and G. Petit (2004), IERS Conventions (2003), *IERS Technical Note 32*, Bundesamt für Kartographie und Geodäsie, Frankfurt am Main.
- Mendes, V. B., G. Prates, E. C. Pavlis, D. E. Pavlis, and R. B. Langley (2002), Improved mapping functions for atmospheric refraction correction in SLR, *Geophysical Research Letters*, 29(10), pp. 1414.
- Monet, D. G., S. E. Levine, B. Canzian, H. D. Ables, A. R. Bird, C. C. Dahn, H. H. Guetter, H. C. Harris, A. A. Henden, S. K. Leggett, H. F. Levison, C. B. Luginbuhl, J. Martini, A. K. B. Monet, J. A. Munn, J. R. Pier, A. R. Rhodes, B. Riepe, S. Sell, R. C. Stone, F. J. Vrba, R. L. Walker, G. Westerhout, R. J. Brucato, I. N. Reid, W. Schoening, M. Hartley, M. A. Read, and S. B. Tritton (2003), The USNO-B catalog, *The Astronomical Journal*, 125, pp. 984–993.
- Montenbruck, O., and E. Gill (2000), *Satellite Orbits*, Springer, ISBN 3-540-67280-X.
- Niell, A. E. (1996), Global mapping functions for the atmosphere delay at radio wavelengths, *Journal of Geophysical Research*, 101(B2), pp. 3227–3246.
- Ostini, L. (2007), Analysis of GNSS Station Coordinate Time Series, Diploma thesis, Astronomisches Institut, Universität Bern.
- Otsubo, T., G. Appleby, and P. Gibbs (2001), GLONASS laser ranging accuracy with satellite signature effect, *Surveys in Geophysics*, 22, pp. 506–516.
- Pavlis, E. C., and Ronald L. Beard (1995), The laser retroreflector experiment on GPS-35 and 36, in *GPS Trends in Precise Terrestrial, Airborne, and Spaceborne Applications*, edited by Beutler *et al.*, pp. 154–158, Springer.
- Pearlman, M. R. (1984), Laser system characterization, in *Proc. of 5th International Workshop on Laser Ranging Instrumentation*, Vol. 1, edited by J. Gaignebet, pp. 66–83, Groupe de Recherches de Geodesie Spatiale, Herstmonceux Castle, U.K., September 10–14 1984.

- Perryman, M. A. C., and ESA (eds.) (1997), *The HIPPARCOS and TYCHO catalogues. Astrometric and photometric star catalogues derived from the ESA HIPPARCOS Space Astrometry Mission*, Vol. 1200 of *ESA Special Publication*.
- Ray, J., Z. Altamimi, X. Collilieux, and T. van Dam (2008), Anomalous harmonics in the spectra of GPS position estimates, *GPS Solutions*, 12(1), pp. 55–64.
- Ries, J. C., R. J. Eanes, C. Huang, B. E. Schutz, C. K. Shum, B. D. Tapley, M. M. Watkins, and D. N. Yuan (1989), Determination of the gravitational coefficient of the Earth from near-Earth satellites, *Geophysical Research Letters*, 16(4), pp. 271–274.
- Roscosmos (2004), Access to space, *Special Roscosmos series*, 16.
- Rothacher, M. (1992), *Orbits of Satellite Systems in Space Geodesy*, Vol. 46 of *Geodätisch-geophysikalische Arbeiten in der Schweiz*, Schweizerische Geodätische Kommission, Institut für Geodäsie und Photogrammetrie, Eidg. Technische Hochschule Zürich, Zürich.
- Schildknecht, T. (1994), *Optical Astrometry of Fast Moving Objects Using CCD Detectors*, Vol. 49 of *Geodätisch-geophysikalische Arbeiten in der Schweiz*, Institut für Geodäsie und Photogrammetrie, Eidg. Technische Hochschule Zürich, Zürich, Switzerland.
- Schildknecht, T. (2007), Optical surveys for space debris, *Astronomy and Astrophysics Review*, 14, pp. 41–111.
- Schildknecht, T., I. Baueršima, U. Hugentobler, A. Verdun, and G. Beutler (1991), CQSSP: a new technique for establishing the tie between the stellar and quasar celestial reference frames, in *IAU Colloq. 127: Reference Systems*, edited by J. A. Hughes *et al.*, p. 341.
- Schildknecht, T., U. Hugentobler, and M. Ploner (1999), Optical surveys of space debris in GEO, *Advances in Space Research*, 23(1), pp. 45–54.
- Seidelmann, P. K. (1992), *Explanatory Supplement to the Astronomical Almanac*, University Science Books, ISBN 0-935702-68-7.
- Slabinski, V. J. (2006), IGS rapid orbits: systematic error at day boundaries, in *Proc. of IGS Workshop 2006*, Darmstadt, Germany, May 8–12 2006.
- Springer, T. A. (2000), *Modeling and Validating Orbits and Clocks Using the Global Positioning System*, Vol. 60 of *Geodätisch-geophysikalische Arbeiten in der Schweiz*, Schweizerische Geodätische Kommission, Institut für Geodäsie und Photogrammetrie, Eidg. Technische Hochschule Zürich, Zürich, Switzerland.
- Springer, T. A. (2008), Personal communication, January 2008.
- Springer, T. A., G. Beutler, and M. Rothacher (1999), Improving the orbit estimates of GPS satellites, *Journal of Geodesy*, 73(3), pp. 147–157.

## Bibliography

---

- Standish, E. M. (1990), The observational basis for JPL's DE200, the planetary ephemerides of the *Astronomical Almanac*, *Astronomy and Astrophysics*, 233, pp. 252–271.
- Standish, E. M. (1998), JPL Planetary and Lunar Ephemerides, DE405/LE405, *JPL Interoffice Memorandum IOM 312.F-98-048*.
- Steigenberger, P. (2007), Personal communication, August 2007.
- Steigenberger, P., M. Rothacher, R. Dietrich, M. Fritsche, A. Rülke, and S. Vey (2006), Re-processing of a global GPS network, *Journal of Geophysical Research*, 111(B05402).
- Tapley, B. D., M. M. Watkins, J. C. Ries, G. W. Davis, R. J. Eanes, S. R. Poole, H. J. Rim, B. E. Schutz, C. K. Shum, R. S. Nerem, F. J. Lerch, J. A. Marshall, S. M. Klosko, N. K. Pavlis, and R. G. Williamson (1996), The Joint Gravity Model 3, *Journal of Geophysical Research*, 101, pp. 28029–28049.
- Teunissen, P. J. G., and A. Kleusberg (eds.) (1998), *GPS for Geodesy*, Springer, ISBN 3-540-63661-7.
- Urschl, C., G. Beutler, W. Gurtner, U. Hugentobler, and S. Schaer (2005), GPS/GLONASS orbit determination based on combined microwave and SLR data analysis, in *Proc. of IAG, IAPSO, IABO Joint Conference, Dynamic Planet 2005: Frontiers in the analysis of space geodetic measurements*, pp. 115–122, Cairns, Australia, August 22–26 2005.
- Urschl, C., G. Beutler, W. Gurtner, U. Hugentobler, and M. Ploner (2006), Orbit determination of GIOVE-A using SLR tracking data, in *Proc. of the 15th International Workshop on Laser Ranging*, pp. 40–46, Canberra, Australia, October 15–20 2006.
- Urschl, C., G. Beutler, W. Gurtner, U. Hugentobler, and S. Schaer (2007), Contribution of SLR tracking data to GNSS orbit determination, *Advances in Space Research*, 39(10), pp. 1515–1523.
- Van Dam, T. M., and J. M. Wahr (1987), Displacements of the Earth's surface due to atmospheric loading: effects on gravity and baseline measurements, *Journal of Geophysical Research*, 92(B2), pp. 1281–1286.
- Verdun, A. (1993), *Objekterkennung und Zentroidbestimmung bei CCD-Richtungsbeobachtungen*, Master's thesis, Universität Bern, Astronomisches Institut, Druckerei der Universität Bern.
- Vigue-Rodi, Y., Y. E. Bar-Sever, B. Newport, F. H. Webb, and J. F. Zumberge (in press), JPL IGS analysis center report, 2003-2004, in *International GPS Service 2003-2004 Technical Report*, IGS Central Bureau, Jet Propulsion Laboratory, Pasadena, California, U.S.A.
- Violet, M., J. Crum, J. Carberry, R. Smetek, M. O'Brine, S. Hutsell, and F. Mueller (1999), Navigation accuracy or satellite health? Controlling momentum on aging GPS satellites, in *Proc.*

- of the 12th International Technical Meeting of the Satellite Division of the Institute of Navigation ION GPS-99, pp. 2269–2280, Nashville Convention Center, Nashville, Tennessee, U.S.A., September 1999.
- Watkins, M. M., Y. E. Bar-Sever, and D. N. Yuan (1996), Evaluation of IGS GPS orbits with satellite laser ranging, in *IGS analysis center workshop*, edited by R E et. al Neilan, pp. 9–12, Central Bureau, Jet Propulsion Laboratory, Pasadena, California, U.S.A., 19–21 March 1996.
- Wu, J. T., C. Wu, G. A. Hajj, W. I. Bertiger, and S. M. Lichten (1993), Effects of antenna orientation on GPS carrier phase, *Manuscripta Geodaetica*, 18, pp. 91–98.
- Zacharias, N., S. E. Urban, M. I. Zacharias, G. L. Wycoff, D. M. Hall, D.G. Monet, and T.J. Rafferty (2004), The second US Naval Observatory CCD Astrograph Catalog (UCAC2), *The Astronomical Journal*, (127), pp. 3043–3059.
- Zhu, S. Y., C. Reigber, and Z. Kang (1997), Apropos laser tracking to GPS satellites, *Journal of Geodesy*, 71, pp. 423–431.
- Zhu, S. Y., F.-H. Massmann, and C. Reigber (2003), Satellite antenna phase center offsets and scale errors in GPS solutions, *Journal of Geodesy*, 76, pp. 668–672.
- Ziebart, M., S. Adhya, A. Sibthorpe, S. Edwards, and P. Cross (2005), Combined radiation pressure and thermal modelling of complex satellites: Algorithms and on-orbit tests, *Advances in Space Research*, 36, pp. 424–430.
- Ziebart, M., Y. Bar-Sever, A. Sibthorpe, P. Cross, and B. Haines (2007), Cracking the GPS-SLR orbit anomaly, ION GNSS 2007 conference, Fort Worth, Texas, U.S.A., September 2007.

*Bibliography*

---

## **“Geodätisch-geophysikalische Arbeiten in der Schweiz”**

**(Fortsetzung der Publikationsreihe ”Astronomisch-geodätische Arbeiten in der Schweiz”)  
der Schweizerischen Geodätischen Kommission (ab Bd. 51):**

- 51** 1995 Dreidimensionales Testnetz Turtmann 1985-1993, Teil II (GPS-Netz).  
F. Jeanrichard (Hrsg.) Autoren: G. Beutler, A. Geiger, M. Rothacher, Stefan Schaer, D. Schneider, A. Wiget, 173 Seiten.
- 52** 1995 High Precision GPS Processing in Kinematic Mode: M. Cocard. 139 Seiten.
- 53** 1995 Ambiguity Resolution Techniques in Geodetic and Geodynamic Applications of the Global Positioning System. L. Mervart. 155 Seiten.
- 54** 1997 SG 95: Das neue Schweregrundnetz der Schweiz: F. Arnet und E. Klingelé. 37 Seiten.
- 55** 1997 Combination of Solutions for Geodetic and Geodynamic Applications of the Global Positioning System (GPS). Elmar Brockmann, 211 Seiten.
- 56** 1997 Geoid der Schweiz 1997. Urs Marti, 140 Seiten.
- 57** 1998 Astrometry and Satellite Orbits: Theoretical Considerations and Typical Applications. Urs Hugentobler, 209 Seiten.
- 58** 1998 Systematic Investigations of Error- and System-Modelling of Satellite Based Flight Approaches and Landings in Switzerland. Maurizio Scaramuzza, 165 Seiten.
- 59** 1999 Mapping and Predicting the Earth’s Ionosphere Using the Global Positioning System. Stefan Schaer, 205 Seiten.
- 60** 2000 Modeling and Validating Orbits and Clocks Using the Global Positioning System. Timon Anton Springer, 154 Seiten.
- 61** 2001 Spatial and Temporal Distribution of Atmospheric Water Vapor using Space Geodetic Techniques. Lars Peter Kruse, 128 Seiten.
- 62** 2001 Solar Spectrometry for Determination of Tropospheric Water Vapor. Bernd Sierk, 212 Seiten.
- 63** 2001 Analysis of refraction influences in geodesy using image processing and turbulence models. Philipp Flach, 175 Seiten.
- 64** 2003 INS/GPS Integration for Pedestrian Navigation. V. Gabaglio, 161 Seiten.
- 65** 2003 Efficient Methods for Determining Precise Orbits of Low Earth Orbiters Using the Global Positioning System. Heike Bock, 214 Seiten.
- 66** 2003 Capteurs et Algorithmes pour la Localisation Autonome en Mode Pédestre. Quentin Ladetto, 121 Seiten.
- 67** 2004 GPS based Determination of the Integrated and Spatially Distributed Water Vapor in the Troposphere. Marc Troller, 172 Seiten.
- 68** 2005 Geodetic Mobile Solar Spectrometer. Alexander Somieski, 205 Seiten.
- 69** 2005 Absolute Airborne Gravimetry. Henri Baumann, 142 Seiten.
- 70** 2006 *The Swiss Trolley* – A Modular System for Track Surveying. Ralph Glaus, 184 Seiten.
- 71** 2006 Development of a Robotic Mobile Mapping System by Vision-Aided Inertial Navigation: A Geomatics Approach. Fadi Atef Bayoud, 157 Seiten.
- 72** 2007 Das neue Landeshöhennetz der Schweiz LHN95. Andreas Schlatter, 373 Seiten.
- 73** 2007 Pseudo-Stochastic Orbit Modeling of Low Earth Satellites Using the Global Positioning System. Adrian Jäggi, 214 Seiten.
- 74** 2008 Cartographie Mobile en Temps Réel. Hervé Gontran, 162 Seiten.
- 75** 2008 Mutual Validation of Satellite-Geodetic Techniques and its Impact on GNSS Orbit Modeling. Claudia Flohrer, 198 Seiten.